



HAL
open science

Modeling and simulation of damage in anisotropic materials by the phase-field method

Ba Thanh Vu

► **To cite this version:**

Ba Thanh Vu. Modeling and simulation of damage in anisotropic materials by the phase-field method. Other [cond-mat.other]. Université Paris-Est, 2021. English. NNT : 2021PESC2023 . tel-03391722

HAL Id: tel-03391722

<https://theses.hal.science/tel-03391722>

Submitted on 21 Oct 2021

HAL is a multi-disciplinary open access archive for the deposit and dissemination of scientific research documents, whether they are published or not. The documents may come from teaching and research institutions in France or abroad, or from public or private research centers.

L'archive ouverte pluridisciplinaire **HAL**, est destinée au dépôt et à la diffusion de documents scientifiques de niveau recherche, publiés ou non, émanant des établissements d'enseignement et de recherche français ou étrangers, des laboratoires publics ou privés.

UNIVERSITÉ PARIS EST
ÉCOLE DOCTORALE SCIENCE INGÉNIERIE ET ENVIRONNEMENT
ANNÉE 2021

THÈSE
pour obtenir le grade de

DOCTEUR DE L'UNIVERSITÉ PARIS EST

Discipline: Génie Civil

présentée par

VU Ba Thanh

Titre :

**Modélisation et simulation de l'endommagement dans
matériaux anisotropes par la méthode de champ de phase**

**Modeling and simulation of damage in
anisotropic materials by the phase-field method**

soutenue le 13 Janvier 2021 devant le jury composé de

M. Corrado MAURINI

Rapporteur

M. Dashnor HOXHA

Rapporteur

M. Salah RAMTANI

Examineur

M. Qi-Chang HE

Directeur de thèse

M. Hung LE QUANG

Co-directeur de thèse

Acknowledgments

First of all, I would like to express my sincere gratitude to my supervisor, Professor Qi-Chang HE who followed me during my PhD study and who gave me his scientific help and his time. Words can not express all that he has done for me, from my heart, I thank him.

I would also like to thank Mr. Hung LE QUANG, for his guidance and his availability as well as his kindness as a brother. I am grateful for his help and the endless discussions between us, not only about scientific research, but also about everyday life. I particularly appreciated his teaching skills that allowed me to progress in my research.

I extend my thanks to Professor Salah RAMTANI for agreeing to review my thesis and to chair the jury of the thesis defense as well as Professor Corrado MAURINI and Professor Dashnor HOXHA who accepted a difficult task of being the thesis reporters. Their very detailed reports as well as their very interesting comments and questions have given me a lot of perspectives to my work.

I also want to express my friendship to all colleagues and my friends who helped me during my PhD study as well as the Laboratoire Modélisation et Simulation Multi-Echelle (MSME) - UMR 8208 CNRS where I had a great time.

Finally, my special thanks to my family who supported me during my PhD study. In particular, thanks to my wife Ngoc Huyền and my son Thành An who are always at my side.

Abstract

Recently, the phase-field method has been intensively developed to model and simulate the nucleation and propagation of cracks in materials and structures in a variety of situations. In this development, many questions remain still open and a lot of problems have to be solved. Concerning brittle and quasi-brittle materials, one of the main difficulties comes from the fact that these materials behave differently in tension and in compression. To overcome this difficulty, the strain tensor is usually decomposed directly into a tensile part and a compressive part, while arguing that damage in brittle and quasi-brittle materials is essentially controlled by the tensile part. However, this direct decomposition is not consistent from an energy point of view, in particular when elastically anisotropic materials are in question. Another important problem in using the phase-field method and the finite element method to deal with cracks is that the mesh size must be sufficiently small in any zone where a crack is located or expected to be nucleated/ propagated, so that the resulting computational cost is high. The present work aims at contributing to the development of the phase-field method in modelling and simulating cracks in both isotropic and anisotropic brittle/ quasi-brittle materials. A novel family of degradation functions is used and implemented for these materials. New decompositions of the strain tensor based on an elastic energy preserving transformation are also employed and implemented for isotropic and anisotropic damage. Both bulk damage and interfacial damage are investigated. The proposed methods are systematically illustrated by numerical examples. The obtained results are compared with and validated by relevant available experimental/ numerical ones.

Key-words: Phase-field method; Damage; Crack; Fracture; Interfacial damage; Brittle materials; Isotropy; Anisotropy; Unilateral effects; Strain decomposition.

Résumé

Récemment, la méthode de champ de phase a été intensivement développée pour modéliser et simuler la nucléation et la propagation de fissures dans des matériaux et des structures dans diverses situations. Dans ce développement, de nombreuses questions restent encore ouvertes et de nombreux problèmes sont à résoudre. Concernant les matériaux fragiles et quasi-fragiles, l'une des principales difficultés vient du fait que ces matériaux se comportent différemment en traction et en compression. Pour surmonter cette difficulté, le tenseur des déformations est habituellement décomposé directement en une partie tendue et une partie compressive, tout en avançant l'argument que l'endommagement des matériaux fragile et quasi-fragile est essentiellement contrôlé par la partie tendue. Cependant, cette décomposition directe n'est pas cohérente d'un point de vue énergétique, en particulier lorsqu'il s'agit de matériaux élastiquement anisotropes. Un autre problème important lié à l'utilisation de la méthode de champ de phase et de la méthode des éléments finis pour traiter les fissures est que le maillage doit être suffisamment fin dans toute zone où une fissure est située ou devrait être nucléée/ propagée, de sorte que le coût de calcul résultant est élevé. Le présent travail vise à contribuer au développement de la méthode de champ de phase dans la modélisation et la simulation de fissures dans les matériaux fragiles/ quasi-fragiles isotropes et anisotropes. Une nouvelle famille de fonctions de dégradation est utilisée et implémenté pour ces matériaux. De nouvelles décompositions du tenseur des déformations basées sur une transformation préservant l'énergie élastique sont également employées et implémentées pour l'endommagement isotrope et l'endommagement anisotrope. Les endommagements volumiques et interfaciaux sont étudiés. Les méthodes proposées sont systématiquement illustrées par des exemples numériques. Les résultats obtenus sont comparés avec et validés par des résultats expérimentaux/ numériques disponibles.

Mots-clés: Méthode champ de phase; Endommagement ; Fissure ; Fracture ; Endommagement d'interface; Matériaux fragiles ; Isotropie ; Anisotropie ; Effets unilatéraux ; Décomposition des déformations.

Contents

General introduction	21
Notations and table of abbreviations	24
1 Phase-field modeling of the nucleation and propagation of cracks by using a new family of degradation functions for the experimental validation	27
1.1 Abstract	27
1.2 Introduction	28
1.3 Review of the phase field method	29
1.3.1 Regularized representation of free discontinuities	29
1.3.2 Energy functional	30
1.3.3 Phase field and displacement problems	32
1.4 Influence of input parameters in the numerical simulations	34
1.4.1 Determination of the regularization parameter l	35
1.4.2 Influence of the mesh size	38
1.4.3 Influence of the displacement increments	39
1.5 Numerical examples	39
1.5.1 Experimental validation: three-point bending test of un-notched beam	39
1.5.2 Experimental validation: single-hole plate compression test	41
1.5.3 Experimental validation: compression test of a plate containing a periodic distribution of cylindrical holes	44
1.5.4 Compression test of a microstructure with uniformly distributed holes	50
1.6 Conclusions	53
2 Phase-field modeling with strain orthogonal decompositions for the modeling and simulation of isotropic and anisotropic damage	54
2.1 Abstract	54

2.2	Introduction	55
2.3	Phase-field modeling for the fracture of brittle and quasi-brittle materials	57
2.3.1	Smearred approximation of free discontinuities	57
2.3.2	Phase field and displacement problems	58
2.4	Numerical examples	66
2.4.1	Single edge notched tension test	66
2.4.2	Single edge notched shear test	68
2.4.3	Symmetric three point bending test of a 3D beam	69
2.4.4	Single edge notched shear test for an orthotropic material plate	71
2.4.5	Single edge notched tension test for an orthotropic material plate	73
2.4.6	Bi-axial tension test of an orthotropic material plate made of a Glass-epoxy composite and containing an initial crack	75
2.4.7	Bi-axial tension test of an orthotropic material 3D plate made of a Glass-epoxy composite and containing an initial crack	82
2.4.8	Bi-axial tension test of an orthotropic material plate made of a Graphite-epoxy composite and containing an initial crack	84
2.5	Conclusions	91
3	Modeling and simulation of crack propagation in heterogeneous materials by phase-field method with interfacial damage	92
3.1	Introduction	92
3.2	Phase-field modeling of bulk crack and interfaces	94
3.2.1	Regularized representation of free discontinuous field	94
3.2.2	Energy functional	96
3.2.3	Resolution of the phase-field problem	99
3.2.4	Resolution of the displacement problem	100
3.3	Numerical examples	100
3.3.1	Symmetric three-point bending test	100
3.3.2	Delamination peel test	103
3.3.3	Tension test of a plate with a complex inclusion	105
3.3.4	Tension test of a plate containing randomly distributed inclusions	108
3.3.5	Tension test of a realistic microstructure obtained by X-ray microtomography image	113
3.4	Conclusions	115

4	Modeling and simulation of crack propagation in anisotropic two-phase composite materials by phase-field method with interfacial damage	117
4.1	Phase-field modeling for anisotropic two-phase composite materials	117
4.2	Numerical examples	119
4.2.1	Tension test of composites with two identical material phases and adhesive interface	119
4.2.2	Tension test of a polycrystalline microstructure containing 50 grains	122
4.2.3	Tension test of composites with two different orthotropic phases and adhesive interface	125
4.2.4	Symmetric three-point bending test of a composite beam consisting of two identical materials with adhesive interface	128
4.2.5	Symmetric three-point bending test of a composite beam consisting of two different anisotropic materials with adhesive interface	131
4.3	Conclusions	135
	Conclusions and perspectives	136
	Bibliography	136
	Appendix	144
A		145
A.1	Details about the solution of the displacement problem	145
A.2	The solution of the phase field problem in Chapter 4	149
B		151
B.1	Algorithm in chapter 1	151
B.2	Algorithms in chapter 2	151
B.3	Algorithm in chapter 3 and chapter 4	152

List of Figures

1.1	<i>Plots of: (a) the new degradation function $g(d)$, (b) the first-order derivative $g'(d)$, (c) the second-order derivative $g''(d)$ for different values of n in the influence of the correction term $f_c(d)$.</i>	32
1.2	<i>Analyze the influence of numerical parameters on the simulation by the compression test of the sample containing a hole: geometry and boundary conditions. . . .</i>	35
1.3	<i>Uniaxial tension test of a 1-dimensional homogeneous bar: dependence on the phase-field variable d when using the new family of degradation functions $g(d)$ of (a) strain and (b) stress.</i>	36
1.4	<i>Uniaxial tension test of a 1-dimensional homogeneous bar: relational curve of normalized peak stress and parameter n assuming uniform stress and damage. . . .</i>	37
1.5	<i>Convergence of the solution corresponds to the regularization parameter l: (a) Load-displacement curve; (b) σ^* for different values of l</i>	37
1.6	<i>Convergence of the solution corresponds to the different values of mesh size.</i>	38
1.7	<i>Convergence of the solution corresponds to the displacement increments: (a) load-displacement curve; (b) σ^* for different displacement increments Δu</i>	39
1.8	<i>Symmetric three-point bending test of un-notched beam: Geometry and boundary conditions.</i>	40
1.9	<i>Symmetric three-point bending test of un-notched beam: (a) Load-displacement curves; (b) Critical value of the tensile stress σ_c for the different values of l</i>	40
1.10	<i>Compression test of the sample containing a hole whose diameter D changes: geometry and boundary conditions</i>	41
1.11	<i>Crack onset of plaster sample containing one hole whose diameter D changes with using a pair of $l=0.1\text{mm}$ and $n=7$: (a) $D=3\text{mm}$, $U=0.055\text{mm}$; (b) $D=4\text{mm}$, $U=0.051\text{mm}$; (c) $D=5\text{mm}$, $U=0.041\text{mm}$; (d) $D=6\text{mm}$, $U=0.036\text{mm}$</i>	42
1.12	<i>Critical axial tress σ^* when the cracks onset corresponds to the hole diameter: comparison between experimental results and numerical results</i>	42

1.13	<i>Compression test of a plate containing a periodic distribution of the holes: geometry and boundary conditions (a) containing 45 holes with the surface fraction 12.2% and (b) containing 60 holes with surface fraction 13.5% (in [37])</i>	43
1.14	<i>Compression test of a plate containing a periodic distribution of 45 holes (surface fraction 12.2%): evolution of the crack onset in the first hole for the different regularization lengths l: (a) $l=0.1\text{mm}$, $U=0.0456\text{mm}$;(b) $l=0.14\text{mm}$, $U=0.044\text{mm}$; (c) $l=0.16\text{mm}$, $U=0.0439\text{mm}$; (d) $l=0.2\text{mm}$, $U=0.0446\text{mm}$</i>	43
1.15	<i>Compression test of a plate containing a periodic distribution of 45 holes (a surface fraction 12.2%): Propagation of the crack for the different regularization lengths l: (a) $l=0.1\text{mm}$, $U=0.0470\text{mm}$;(b) $l=0.14\text{mm}$, $U=0.0464\text{mm}$; (c) $l=0.16\text{mm}$, $U=0.0465\text{mm}$; (d) $l=0.2\text{mm}$, $U=0.0465\text{mm}$</i>	44
1.16	<i>Compression test of a plate containing a periodic distribution of 45 holes (a surface fraction 12.2%): Propagation of the crack for the different regularization lengths l: (a) $l=0.1\text{mm}$, $U=0.0545\text{mm}$;(b) $l=0.14\text{mm}$, $U=0.0542\text{mm}$; (c) $l=0.16\text{mm}$, $U=0.0534\text{mm}$; (d) $l=0.2\text{mm}$, $U=0.0530\text{mm}$; (e) [34].</i>	45
1.17	<i>Compression test of a plate containing a periodic distribution of 45 holes (surface fraction 12.2%): Propagation of the crack for the different regularization lengths l: (a) $l=0.1\text{mm}$, $U=0.056\text{mm}$;(b) $l=0.14\text{mm}$, $U=0.0552\text{mm}$; (c) $l=0.16\text{mm}$, $U=0.055\text{mm}$; (d) $l=0.2\text{mm}$, $U=0.0543\text{mm}$; (e) [34].</i>	46
1.18	<i>Compression test of a plate containing a periodic distribution of 45 holes (surface fraction 12.2%): Load- displacement curves for the different regularization length l</i>	47
1.19	<i>Compression test of a plate containing a periodic distribution of 60 holes (surface fraction 13.5%): evolution of the crack onset in the first hole for the different regularization lengths l: (a) $l=0.1\text{mm}$, $U=0.0442\text{mm}$;(b) $l=0.14\text{mm}$, $U=0.0443\text{mm}$; (c) $l=0.16\text{mm}$, $U=0.0450\text{mm}$; (d) $l=0.2\text{mm}$, $U=0.0452\text{mm}$</i>	47
1.20	<i>Compression test of a plate containing a periodic distribution of 60 holes (surface fraction 13.5%): Propagation of the crack for the different regularization lengths l: (a) $l=0.1\text{mm}$, $U=0.049\text{mm}$;(b) $l=0.14\text{mm}$, $U=0.049\text{mm}$; (c) $l=0.16\text{mm}$, $U=0.049\text{mm}$; (d) $l=0.2\text{mm}$, $U=0.0485\text{mm}$; (e) [34]; (f) provided in [37].</i>	48
1.21	<i>Compression test of a plate containing a periodic distribution of 60 holes (surface fraction 13.5%): evolution of the crack for the different regularization lengths l: (a) $l=0.1\text{mm}$, $U=0.0517\text{mm}$;(b) $l=0.14\text{mm}$, $U=0.0515\text{mm}$; (c) $l=0.16\text{mm}$, $U=0.0515\text{mm}$; (d) $l=0.2\text{mm}$, $U=0.0515\text{mm}$;</i>	49

1.22	<i>Compression test of a plate containing a periodic distribution of 60 holes (surface fraction 13.5%): Load- displacement curves for the different regularization lengths l</i>	49
1.23	<i>Critical axial tress σ^* when the cracks onset: comparison between experimental values and numerical values for two surface fractions of the holes (12.2% and 13.5%)</i>	50
1.24	<i>Compression test of a plate with uniformly distributed holes: geometry and loading conditions.</i>	51
1.25	<i>Compression test of a plate with uniformly distributed holes: evolution of the crack onset in the first hole: (a) $l=0.012\text{mm}$, $n=7$, $U=0.0053\text{mm}$; (b) $l=0.012\text{mm}$, the quadratic degradation function, $U=0.0055\text{mm}$;(c) [18]</i>	51
1.26	<i>Compression test of a plate with uniformly distributed holes: propagation of the crack: (a) $l=0.012\text{mm}$, $n=7$, $U=0.0068\text{mm}$; (b) $l=0.012\text{mm}$, the quadratic degradation function, $U=0.0068\text{mm}$; (c) [18]</i>	52
1.27	<i>Compression test of a plate with uniformly distributed holes: Propagation of the crack: (a) $l=0.012\text{mm}$, $n=7$, $U=0.00872\text{mm}$; (b) $l=0.012\text{mm}$, the quadratic degradation function, $U=0.008\text{mm}$; (c) in [18]; (d) solved by MFPA^{2D} simulation in [38]</i>	52
1.28	<i>Compression test of a plate with uniformly distributed holes: Load- displacement curves with a pair of $l=0.012\text{mm}$, $n=7$</i>	53
2.1	<i>Regularized representation of a crack: two-dimensional case: (a) sharp crack model; (b) regularized representation through phase field.</i>	57
2.2	<i>Regularized representation of a crack: (a) sharp cracks in an orthotropic material (dashed lines indicate material orthotropy direction), (b) regularized representation through phase field.</i>	58
2.3	<i>Single edge notched tension test: geometry and boundary conditions.</i>	66
2.4	<i>Single edge notched tension test: a) solution 1; b) solution 2; c) Miehe et al. [16]</i>	66
2.5	<i>Single edge notched tension test: comparison of the load-displacement curves with the length scale $l=0.015\text{mm}$ between solution 1, solution 2 and Miehe et al. [16].</i>	67
2.6	<i>Single edge notched shear test: geometry and boundary conditions.</i>	68
2.7	<i>Single edge notched shear test: a) solution 1; b) solution 2; c) Miehe et al. [16]</i>	68
2.8	<i>Single edge notched shear test: comparison of the load-displacement curves with the length scale $l=0.015\text{mm}$ between solution 1, solution 2 and Miehe et al. [16].</i>	69

2.9	<i>Symmetric three point bending test of a 3D beam (thickness $B=0.5\text{mm}$): geometry and boundary conditions.</i>	69
2.10	<i>Symmetric three point bending test of a 3D beam: a) solution 1; b) solution 2; c) [16]</i>	70
2.11	<i>Symmetric three point bending test of a 3D beam: comparison of the load-displacement curves between solution 1, solution 2 and [16].</i>	70
2.12	<i>Single-edge-notched shear test for orthotropic material plate: geometry and boundary conditions.</i>	71
2.13	<i>Comparison of the crack path which depends on the orthotropic direction orientations α for shear test: (a) with $\alpha = -45^\circ$ (d) with $\alpha = 0^\circ$ (g) with $\alpha = 45^\circ$ solution 1; (b) with $\alpha = -45^\circ$ (e) with $\alpha = 0^\circ$ (h) with $\alpha = 45^\circ$ solution 2; (c) with $\alpha = -45^\circ$ (f) with $\alpha = 0^\circ$ (i) with $\alpha = 45^\circ$ [61].</i>	72
2.14	<i>Single-edge-notched tension test for orthotropic material plate: geometry and boundary conditions.</i>	73
2.15	<i>Comparison of the crack path which depends on the orthotropic direction orientations α for tension test: (a) with $\alpha = 0^\circ$ (d) with $\alpha = 30^\circ$ solution 1; (b) with $\alpha = 0^\circ$ (e) with $\alpha = 30^\circ$ solution 2; (c) with $\alpha = 0^\circ$ (f) with $\alpha = 30^\circ$ [61].</i>	73
2.16	<i>Comparison of the crack path which depends on the orthotropic direction orientations α for tension test: (a) with $\alpha = 78^\circ$ (d) with $\alpha = 90^\circ$ solution 1; (b) with $\alpha = 78^\circ$ (e) with $\alpha = 90^\circ$ solution 2; (c) with $\alpha = 78^\circ$ (f) with $\alpha = 90^\circ$ [61].</i>	74
2.17	<i>Tension test in two directions of an orthotropic plate: geometry and boundary conditions.</i>	75
2.18	<i>Crack extension angle θ_0 vs. crack inclination angle α for various values of biaxial load parameter for the orthotropic material of Glass-epoxy (this figure in [47])</i>	75
2.19	<i>Crack extension angle θ_0 vs. crack inclination angle $\alpha=0^\circ$ for various values of biaxial load parameter for Glass-epoxy by phase field method of solution 1: a) $k = 0.1$, b) $k = 0.5$, c) $k = 1$, d) $k = 3$.</i>	76
2.20	<i>Crack extension angle θ_0 vs. crack inclination angle $\alpha=0^\circ$ for various values of biaxial load parameter for Glass-epoxy by phase field method of solution 2: a) $k = 0.1$, b) $k = 0.5$, c) $k = 1$, d) $k = 3$.</i>	76
2.21	<i>Crack extension angle θ_0 vs. crack inclination angle $\alpha=30^\circ$ for various values of biaxial load parameter for Glass-epoxy by phase field method of solution 1: a) $k = 0.1$, b) $k = 0.5$, c) $k = 1$, d) $k = 3$.</i>	77

2.22	<i>Crack extension angle θ_0 vs. crack inclination angle $\alpha=30^\circ$ for various values of biaxial load parameter for Glass-epoxy by phase field method of solution 2: a) $k = 0.1$, b) $k = 0.5$, c) $k = 1$, d) $k = 3$.</i>	77
2.23	<i>Crack extension angle θ_0 vs. crack inclination angle $\alpha=45^\circ$ for various values of biaxial load parameter for Glass-epoxy by phase field method of solution 1: a) $k = 0.1$, b) $k = 0.5$, c) $k = 1$, d) $k = 3$.</i>	78
2.24	<i>Crack extension angle θ_0 vs. crack inclination angle $\alpha=45^\circ$ for various values of biaxial load parameter for Glass-epoxy by phase field method of solution 2: a) $k = 0.1$, b) $k = 0.5$, c) $k = 1$, d) $k = 3$.</i>	78
2.25	<i>Crack extension angle θ_0 vs. crack inclination angle $\alpha=60^\circ$ for various values of biaxial load parameter for Glass-epoxy by phase field method of solution 1: a) $k = 0.1$, b) $k = 0.5$, c) $k = 1$, d) $k = 3$.</i>	79
2.26	<i>Crack extension angle θ_0 vs. crack inclination angle $\alpha=60^\circ$ for various values of biaxial load parameter for Glass-epoxy by phase field method of solution 2: a) $k = 0.1$, b) $k = 0.5$, c) $k = 1$, d) $k = 3$.</i>	79
2.27	<i>Crack extension angle θ_0 vs. crack inclination angle $\alpha=90^\circ$ for various values of biaxial load parameter for Glass-epoxy by phase field method of solution 1: a) $k = 0.1$, b) $k = 0.5$, c) $k = 1$, d) $k = 3$.</i>	80
2.28	<i>Crack extension angle θ_0 vs. crack inclination angle $\alpha=90^\circ$ for various values of biaxial load parameter for Glass-epoxy by phase field method of solution 2: a) $k = 0.1$, b) $k = 0.5$, c) $k = 1$, d) $k = 3$.</i>	80
2.29	<i>Comparison between the analytical method in [47] and the proposed solutions of the crack extension angles θ_0 which depends on the initial crack direction α with Glass-epoxy material</i>	81
2.30	<i>Crack extension angle θ_0 vs. crack inclination angle $\alpha=30^\circ$ for various values of biaxial load parameter for Glass-epoxy by phase field method of solution 1: a) $k = 0.1$, b) $k = 0.5$, c) $k = 1$, d) $k = 3$ (in the 3D case). Note that, the load-displacement curves are drawn corresponding to the displacement values of the vertical direction.</i>	83

2.31	<i>Crack extension angle θ_0 vs. crack inclination angle $\alpha=30^\circ$ for various values of biaxial load parameter for Glass-epoxy by phase field method of solution 2: a) $k = 0.1$, b) $k = 0.5$, c) $k = 1$, d) $k = 3$ (in the 3D case). Note that, the load-displacement curves are drawn corresponding to the displacement values of the vertical direction.</i>	84
2.32	<i>Crack extension angle θ_0 vs. crack inclination angle α for various values of biaxial load parameter for the orthotropic material of Graphite-epoxy (this figure in [47])</i>	85
2.33	<i>Crack extension angle θ_0 vs. crack inclination angle $\alpha=0^\circ$ for various values of biaxial load parameter for Graphite-epoxy by phase field method of solution 1: a) $k = 0.1$, b) $k = 0.5$, c) $k = 1$, d) $k = 3$.</i>	86
2.34	<i>Crack extension angle θ_0 vs. crack inclination angle $\alpha=0^\circ$ for various values of biaxial load parameter for Graphite-epoxy by phase field method of solution 2: a) $k = 0.1$, b) $k = 0.5$, c) $k = 1$, d) $k = 3$.</i>	86
2.35	<i>Crack extension angle θ_0 vs. crack inclination angle $\alpha=30^\circ$ for various values of biaxial load parameter for Graphite-epoxy by phase field method of solution 1: a) $k = 0.1$, b) $k = 0.5$, c) $k = 1$, d) $k = 3$.</i>	87
2.36	<i>Crack extension angle θ_0 vs. crack inclination angle $\alpha=30^\circ$ for various values of biaxial load parameter for Graphite-epoxy by phase field method of solution 2: a) $k = 0.1$, b) $k = 0.5$, c) $k = 1$, d) $k = 3$.</i>	87
2.37	<i>Crack extension angle θ_0 vs. crack inclination angle $\alpha=45^\circ$ for various values of biaxial load parameter for Graphite-epoxy by phase field method of solution 1: a) $k = 0.1$, b) $k = 0.5$, c) $k = 1$, d) $k = 3$.</i>	88
2.38	<i>Crack extension angle θ_0 vs. crack inclination angle $\alpha=45^\circ$ for various values of biaxial load parameter for Graphite-epoxy by phase field method of solution 2: a) $k = 0.1$, b) $k = 0.5$, c) $k = 1$, d) $k = 3$.</i>	88
2.39	<i>Crack extension angle θ_0 vs. crack inclination angle $\alpha=60^\circ$ for various values of biaxial load parameter for Graphite-epoxy by phase field method of solution 1: a) $k = 0.1$, b) $k = 0.5$, c) $k = 1$, d) $k = 3$.</i>	89
2.40	<i>Crack extension angle θ_0 vs. crack inclination angle $\alpha=60^\circ$ for various values of biaxial load parameter for Graphite-epoxy by phase field method of solution 2: a) $k = 0.1$, b) $k = 0.5$, c) $k = 1$, d) $k = 3$.</i>	89

2.41	<i>Crack extension angle θ_0 vs. crack inclination angle $\alpha=90^\circ$ for various values of biaxial load parameter for Graphite-epoxy by phase field method of solution 1: a) $k = 0.1$, b) $k = 0.5$, c) $k = 1$, d) $k = 3$.</i>	90
2.42	<i>Crack extension angle θ_0 vs. crack inclination angle $\alpha=90^\circ$ for various values of biaxial load parameter for Graphite-epoxy by phase field method of solution 2: a) $k = 0.1$, b) $k = 0.5$, c) $k = 1$, d) $k = 3$.</i>	90
2.43	<i>Comparison between the analytical method in [47] and the proposed solutions of the crack extension angles θ_0 which depends on the initial crack direction α with Graphite-epoxy material.</i>	91
3.1	<i>Regularized representation of a crack and an interface: (a) Solid containing an interface and a crack; (b) Regularized representation of the interface; (c) Regularized representation of the crack.</i>	95
3.2	<i>Symmetric three-point bending test: geometry and boundary conditions.</i>	101
3.3	<i>The evolution of the crack in symmetric three-point bending test: (a), (b) and (c) crack initiation and crack propagation for solution 1 corresponding to $U = 0$ mm, $U = 0.25$ mm, and $U = 0.35$ mm, respectively; (d), (e) and (f) crack initiation and crack propagation for solution 2 corresponding to $U = 0$ mm, $U = 0.25$ mm, and $U = 0.35$ mm, respectively; Figs. (g), (h) and (i) crack initiation and crack propagation presented in Nguyen et al. [19] corresponding to $U = 0$ mm, $U = 0.25$ mm, and $U = 0.35$ mm, respectively</i>	101
3.4	<i>Symmetric three-point bending test: comparison of the load-displacement curves between Wells et al.[78] with two solutions of strain decompositions (3.21) and (3.27).</i>	102
3.5	<i>Geometry and boundary conditions of the delamination peel test.</i>	103
3.6	<i>The crack evolution in the delamination peel test: (a), (b) and (c) crack nucleation and propagation for solution 1 of strain decomposition corresponding to $U = 0$ mm, $U = 0.4$ mm, and $U = 1$ mm, respectively;(d), (e) and (f) crack nucleation and propagation for solution 2 of strain decomposition corresponding to $U = 0$ mm, $U = 0.4$ mm, and $U = 1$ mm, respectively; (g), (h) and (i) crack nucleation and propagation in the work Nguyen et al. [19] corresponding to $U = 0$ mm, $U = 0.4$ mm, and $U = 1$ mm, respectively</i>	103

3.7	<i>Delamination peel test: comparison of the load-displacement curves between Verhoosel et al. [66], Nguyen et al. [19] and two solutions of strain decompositions (3.21) and (3.27).</i>	104
3.8	<i>Tension test of a plate containing a complex inclusion: geometry and boundary conditions.</i>	105
3.9	<i>Tension test of a plate containing a complex inclusion: crack propagation. (a), (b) and (c) crack initiation and propagation for solution 1 of strain decomposition corresponding to $U = 0.008$ mm, $U = 0.01$ mm, and $U = 0.012$ mm, respectively;(d), (e) and (f) crack initiation and propagation for solution 2 of strain decomposition corresponding to $U = 0.008$ mm, $U = 0.01$ mm, and $U = 0.012$ mm, respectively; (g), (h) and (i) crack initiation and propagation obtained by Nguyen et al. [19] corresponding to $U = 0.008$ mm, $U = 0.01$ mm, and $U = 0.012$ mm, respectively . .</i>	106
3.10	<i>Tension test of a plate containing a complex inclusion: comparison of the load-displacement curves between Nguyen et al. [19] with two solutions of strain decompositions (3.21) and (3.27).</i>	107
3.11	<i>Traction test of a microstructure containing randomly distributed inclusions: geometry and boundary conditions.</i>	107
3.12	<i>Crack evolution for 15 realizations of the microstructures containing randomly distributed inclusions (part 1): (a), (b) and (c) depict crack propagation of realization 1 corresponding to solutions 1 and 2 of strain decomposition (3.21) and (3.27), and Nguyen et al. [19], respectively; (d), (e) and (f) depict crack propagation of realization 2 corresponding to solutions 1 and 2 of strain decomposition (3.21) and (3.27), and Nguyen et al. [19], respectively; (g), (h) and (i) depict crack propagation of realization 3 corresponding to solutions 1 and 2 of strain decomposition (3.21) and (3.27) and Nguyen et al. [19], respectively</i>	108
3.13	<i>Crack evolution for 15 realizations of the microstructures containing randomly distributed inclusions (part 2): (a), (b) and (c) depict crack propagation of realization 4 corresponding to solutions 1 and 2 of strain decomposition (3.21) and (3.27), and Nguyen et al. [19], respectively; (d), (e) and (f) depict crack propagation of realization 5 corresponding to solutions 1 and 2 of strain decomposition (3.21) and (3.27), and Nguyen et al. [19], respectively; (g), (h) and (i) depict crack propagation of realization 6 corresponding to solutions 1 and 2 of strain decomposition (3.21) and (3.27), and Nguyen et al. [19], respectively</i>	109

3.14	<i>Crack evolution for 15 realizations of the microstructures containing randomly distributed inclusions (part 3): (a), (b) and (c) depict crack propagation of realization 7 corresponding to solutions 1 and 2 of strain decomposition (3.21) and (3.27), and Nguyen et al. [19], respectively; (d), (e) and (f) depict crack propagation of realization 8 corresponding to solutions 1 and 2 of strain decomposition (3.21) and (3.27), and Nguyen et al. [19], respectively; (g), (h) and (i) depict crack propagation of realization 9 corresponding to solutions 1 and 2 of strain decomposition (3.21) and (3.27), and Nguyen et al. [19], respectively</i>	110
3.15	<i>Crack evolution for 15 realizations of the microstructures containing randomly distributed inclusions (part 4): (a), (b) and (c) depict crack propagation of realization 10 corresponding to solutions 1 and 2 of strain decomposition (3.21) and (3.27), and Nguyen et al. [19], respectively; (d), (e) and (f) depict crack propagation of realization 11 corresponding to solutions 1 and 2 of strain decomposition (3.21) and (3.27), and Nguyen et al. [19], respectively; (g), (h) and (i) depict crack propagation of realization 12 corresponding to solutions 1 and 2 of strain decomposition (3.21) and (3.27), and Nguyen et al. [19], respectively</i>	111
3.16	<i>Crack evolution for 15 realizations of the microstructures containing randomly distributed inclusions (part 5): (a), (b) and (c) depict crack propagation of realization 13 corresponding to solutions 1 and 2 of strain decomposition (3.21) and (3.27), and Nguyen et al. [19], respectively; (d), (e) and (f) depict crack propagation of realization 14 corresponding to solutions 1 and 2 of strain decomposition (3.21) and (3.27), and Nguyen et al. [19], respectively; (g), (h) and (i) depict crack propagation of realization 15 corresponding to solutions 1 and 2 of strain decomposition (3.21) and (3.27), and Nguyen et al. [19], respectively</i>	112
3.17	<i>Traction test of a plate containing randomly distributed inclusions with interfacial damage (the red curve denotes the average response): a) load-displacement curve for 15 realizations with solution 1 of strain decomposition (3.21); b) load-displacement curve for 15 realizations with solution 2 of strain decomposition (3.27); c) load-displacement curve for 15 realizations with Nguyen et al. [19] . . .</i>	113
3.18	<i>Tension test of a realistic microstructure obtained by X-ray microtomography: geometry and loading conditions; a) X-ray microtomography image in Ren et al. [53], b) horizontal tension test, c) vertical tension test</i>	113

3.19	<i>Tension test of a realistic microstructure obtained by X-ray microtomography: a) zero isovalue of the constructed level-set, b) geometry of the domain after solve: mortar (blue), aggregates (black) and pores (white).</i>	114
3.20	<i>Horizotal tension test: cracks nucleation and propagation: (a), (b) and (c) depict crack propagation corresponding to two solutions of strain decompositions (3.21) and (3.27), and Ren et al. [53], respectively</i>	114
3.21	<i>Vertical tension test: cracks nucleation and propagation: (a), (b) and (c) depict crack propagation corresponding to two solutions of strain decompositions (3.21) and (3.27), and Ren et al. [53], respectively</i>	114
4.1	<i>Regularized representation of crack and interface in a composite: (a) composite material consisting of two anisotropic materials with interface Γ^I and crack Γ; (b) Regularized representation the interface Γ^I; (c) Regularized representation of the crack Γ</i>	118
4.2	<i>Geometry and boundary condition of tension tests for composites with two identical material phases and adhesive interface.</i>	120
4.3	<i>Tension test of composites with two identical material phases and adhesive interface: crack evolution due to bulk fracture and interfacial fracture with $U = 0.0105\text{mm}$: (a) and (d) solution 1 of strain decomposition (3.21) with $\varphi = 0^\circ, -20^\circ$; (b) and (e) solution 2 of strain decomposition (3.27) with $\varphi = 0^\circ, -20^\circ$; c) f) Nguyen et al. [81] with $\varphi = 0^\circ, -20^\circ$.</i>	120
4.4	<i>Tension test of composites with two identical material phases: crack evolution due to bulk fracture and interfacial fracture with $U = 0.0105\text{mm}$: a) d) g) solution 1 of strain decomposition (3.21) with $\varphi = -40^\circ, -60^\circ, -90^\circ$; b) e) h) solution 2 of strain decomposition (3.27) with $\varphi = -40^\circ, -60^\circ, -90^\circ$; c) f) i) Nguyen et al. [81] with $\varphi = -40^\circ, -60^\circ, -90^\circ$</i>	121
4.5	<i>Tension test of composites with two identical material phases: comparison of the stress-displacement curves with $\varphi = -45^\circ$ between two solutions of strain decompositions (3.21) and (3.27) and the results obtained in Nguyen et al. [81]</i>	122
4.6	<i>Tension test of a polycrystalline microstructure containing 50 grains: geometry and boundary conditions with dimensions in μm</i>	123
4.7	<i>Tension test of a polycrystalline microstructure: crack evolution with a) solution 1 of strain decomposition (3.21), b) solution 2 of strain decomposition (3.27) and c) results of Nguyen et al. [81]</i>	123

4.8	<i>Tension test of a polycrystalline microstructure: comparison of the stress-displacement curves between two solutions of strain decomposition (3.21) and (3.27) and Nguyen et al. [81]</i>	124
4.9	<i>Tension test of composites with two different orthotropic phases and adhesive interface: geometry, boundary condition and preferential orientation for each material.</i>	125
4.10	<i>Tension test of composites with two Carbon-epoxy materials used by De Morais et al. [49] and Robinson et al. [48]: a) d) crack evolution with solution 1 of strain decomposition (3.21) and $\varphi = -30^\circ, -45^\circ$; b) e) crack evolution with solution 2 of strain decomposition (3.27) and $\varphi = -30^\circ, -45^\circ$; c) f) comparisons of the stress-displacement curves</i>	126
4.11	<i>Tension test of composites with two Carbon-epoxy materials used by De Morais et al. [49] and Robinson et al. [48]: a) d) crack evolution with solution 1 of strain decomposition (3.21) and $\varphi = -60^\circ, -90^\circ$; b) e) crack evolution with solution 2 of strain decomposition (3.27) and $\varphi = -60^\circ, -90^\circ$; c) f) comparisons of the stress-displacement curves.</i>	127
4.12	<i>Symmetric three-point bending test of a composite beam consisting of two identical materials with adhesive interface: geometry, boundary condition and preferential orientation for each material.</i>	127
4.13	<i>Symmetric three-point bending test of a composite beam consisting of two identical materials with adhesive interface: a) d) g) crack evolution with solution 1 of strain decomposition (3.21) and $\varphi = 0^\circ, 30^\circ, 45^\circ$; b) e) h) crack evolution with solution 2 of strain decomposition (3.27) and $\varphi = 0^\circ, 30^\circ, 45^\circ$; c) f) i) comparison of the load-displacement curves.</i>	128
4.14	<i>Symmetric three-point bending test of a composite beam consisting of two identical materials with adhesive interface: a) d) g) crack evolution with solution 1 of strain decomposition (3.21) and $\varphi = 60^\circ, 90^\circ$; b) e) h) crack evolution with solution 2 of strain decomposition (3.27) and $\varphi = 60^\circ, 90^\circ$; c) f) i) comparison of the load-displacement curves.</i>	129
4.15	<i>Symmetric three-point bending test of a composite beam consisting of two identical materials with adhesive interface: a) d) g) crack evolution with solution 1 of strain decomposition (3.21) and $\varphi = 120^\circ, 135^\circ, 150^\circ$; b) e) h) crack evolution with solution 2 of strain decomposition (3.27) and $\varphi = 120^\circ, 135^\circ, 150^\circ$; c) f) i) comparison of the load-displacement curves.</i>	130

4.16	<i>Symmetric three-point bending test of a composite beam consisting of two different anisotropic materials with adhesive interface</i>	131
4.17	<i>Symmetric three-point bending test of a composite beam consisting of two Carbon-epoxy materials used by De Morais et al. [49] and Robinson et al. [48]: a) d) g) crack evolution corresponding to solution 1 of strain decomposition (3.21) with $\varphi = 0^\circ, 30^\circ, 45^\circ$; b) e) h) crack evolution corresponding to solution 2 of strain decomposition (3.27) with $\varphi = 0^\circ, 30^\circ, 45^\circ$; c) f) i) comparison of the load-displacement curves.</i>	132
4.18	<i>Symmetric three-point bending test of a composite beam consisting of two Carbon-epoxy materials used by De Morais et al. [49] and Robinson et al. [48]: a) d) g) crack evolution corresponding to solution 1 of strain decomposition (3.21) with $\varphi = 60^\circ, 90^\circ$; b) e) h) crack evolution corresponding to solution 2 of strain decomposition (3.27) with $\varphi = 60^\circ, 90^\circ$; c) f) i) comparison of the load-displacement curves.</i>	133
4.19	<i>Symmetric three-point bending test of a composite beam consisting of two Carbon-epoxy materials used by De Morais et al. [49] and Robinson et al. [48]: a) d) g) crack evolution corresponding to solution 1 of strain decomposition (3.21) with $\varphi = 120^\circ, 135^\circ, 150^\circ$; b) e) h) crack evolution corresponding to solution 2 of strain decomposition (3.27) with $\varphi = 120^\circ, 135^\circ, 150^\circ$; c) f) i) comparison of the load-displacement curves.</i>	134

General introduction

The problems related to the initiation and propagation of cracks in materials and structures are of prominent importance to engineering and, in particular, to civil engineering. The classical Linear Elastic Fracture Mechanics (LEFM) is based on the well-known work of Griffith [7] and Irwin *et al.* [40]. Apart from theoretical and analytical approaches developed to treat cracks in materials and structures, numerical methods have been proposed and have turned out to be indispensable and powerful when situations of practical interest are concerned. In particular, the eXtended Finite Element Method (XFEM) (see, e.g., Moes *et al.* [79] and Sukumar *et al.* [67]), capable of overcoming the difficulty of mesh dependence, is very efficient for numerically solving crack problems. The Cohesive Zone Model (CZM), which is popular and based on the pioneer works of Barenblatt [62] and Dugdale [63], has also been adopted and implemented within the framework of FEM (see, e.g., Tvergaard and Hutchinson [64], Xu and Needleman [65], Verhoosel and de Borst [66]). One main drawback of these methods is that they are in general unable to simulate crack nucleation and crack paths in complex situations, for example in three-dimensional cases.

Recently, the phase-field method has been widely developed to handle the nucleation and propagation of crack in many kinds of materials. This method relies on the pioneer work of Francfort and Marigo [8] on the variational formulation of crack problems (see, e.g., also Bourdin *et al.* [20, 31]) and finds its mathematical justification in Mumford and Shah [9]. Up to now, the phase-field method has been applied to: (i) describe very complex cracks topologies via a scalar damage variable (see e.g., [8, 13, 14, 15, 16, 18, 20, 34, 82, 83, 84, 85]); (ii) simulate quasi-static fracture (see e.g., [15, 16, 18, 86, 55, 82]); (iii) deal with dynamic crack propagation (see e.g., [1, 2, 3, 4, 84]); (iv) treat cohesive fracture (see e.g., [5, 66, 19, 81]); (v) investigate fracture in anisotropic materials cohesive fracture (see e.g., [56, 57, 58, 59, 81]).

In the development of the phase-field method, many problems remain to be solved. The present work aims to contribute to solving some of them. In the phase-field method, a regularization length is involved. Most of the works dedicated to the phase-field method interpret it as a material parameter. The requirement that the regularization length be small makes that the mesh discretization

in FEM must be very small so that the computational cost is high. Recently, Sargado *et al.*[6] provided a conceptual explanation of how the choice of a length scale can result in either delay or acceleration of failure under quasi-static conditions, and introduced a new family of degradation functions capable of correctly reproducing the onset of failure for a wide range of values of the regularization parameter. This new family of degradation functions, adopted and implemented in the present work, allows us to increase the mesh size in the area where a crack is expected to spread and thus reduce the computational cost.

Another important problem which remains to be solved is related to modelling and simulating cracks in brittle and quasi-brittle materials, such as ceramics, rocks and concrete. These materials of engineering importance behave differently in tension and in compression. It is commonly admitted that the initiation and propagation of cracks in these materials are controlled by tensile strains. How to define "tensile strains" in two- and three-dimensional cases is still an open problem, especially when anisotropic materials are in question. The usual way of directly decomposing the strain tensor into a tensile (or positive) part and a compressive (or negative) part is not consistent from the elastic energy point of view. Indeed, the tensile and compressive parts of the strain tensor obtained by the direct decomposition are not orthogonal in the sense of the inner product where the elastic stiffness (or compliance) tensor acts as the measure tensor; thus, the elastic energy cannot be split into two parts involving, respectively, the tensile and compressive parts of the strain tensor. In a recent work of He [39], a novel decomposition of the strain tensor into a tensile part and a compressive part was proposed. This decomposition, which is orthogonal in the sense of the inner product involving the elastic stiffness tensor, is adopted and implemented within the framework of the finite element method and the phase-field method.

This thesis is structured as follows. In chapter 1, the classical phase-field method is introduced in detail. Then, the steps toward building a new family of degradation functions are described. The quadratic degradation function and the new family of degradation functions are used in the classical phase-field method so as to predict the crack nucleation and propagation. The numerical results are compared with available experimental ones. In particular, we show the advantage of the method through several numerical examples: the regularization length does not depend on the mesh size. In chapter 2, the phase-field method is used to compute crack paths in isotropic and anisotropic materials. The aforementioned orthogonal strain decomposition of He [39] is adopted and implemented. Through proposing two solutions, we improve the accuracy of the phase-field methods in simulating the mechanical behavior of brittle and quasi-brittle materials. In addition, only one damage variable is employed instead of multiple ones in some previous works. In chapter

3, the phase-field method is extended so as to account for interfacial damage. This allows the modelling and simulation of cracks in complex multiphase materials and microstructures obtained by microtomography. Once more, the orthogonal strain decomposition of He [39] is applied to describe the bulk material behavior. Several examples are given, and the obtained numerical results are compared with some solutions of reference. In chapter 4, the damage of composite materials is investigated by the phase-field method. In particular, interfacial damage is taken into account. The interface effect on the propagation direction of cracks in a structure consisting of two different orthotropic materials connected by an adhesive layer is studied. Numerical examples are provided to illustrate the efficiency of the proposed solutions. Finally, some conclusions are drawn and a few perspectives are given.

Notations and table of abbreviations

- Tensor notations

a	scalar,	\mathbf{a}	vector,
\mathbf{A}	second-order tensor,	\otimes	tensor product,
\mathbb{A}	fourth-order tensor,	\otimes^s	symmetric tensor product,
\mathbf{I}	second-order identity tensor,	δ_{ij}	Kronecker symbol,
\mathbb{I}	fourth-order identity tensor,	\mathbf{n}	normal vector.

- Tensor calculus

$$\begin{aligned}
 \mathbf{a} \cdot \mathbf{b} &= a_i b_i, & (\mathbf{A}\mathbf{b})_i &= A_{ij} b_j, & (\mathbf{A}\mathbf{B})_{ij} &= A_{ik} b_{kj}, \\
 \mathbf{A} : \mathbf{B} &= A_{ij} B_{ij}, & (\mathbb{A}\mathbf{B})_{ij} &= A_{ijkl} B_{kl}, & (\mathbb{A}\mathbb{B})_{ijkl} &= A_{ijmn} B_{mnkl}, \\
 (\mathbf{a} \otimes \mathbf{b})_{ij} &= a_i b_j, & (\mathbf{A} \otimes \mathbf{B})_{ijkl} &= A_{ij} B_{kl}, & (\mathbf{A} \underline{\otimes} \mathbf{B})_{ijkl} &= \frac{1}{2}(A_{ik} B_{jl} + A_{il} B_{jk}).
 \end{aligned}$$

- Table of abbreviations in chapter 1, 2, 3, 4

d	phase field variable
l	regularization length
E	total energy of the body
W	free energy
γ	crack density function
g_c	fracture toughness
\mathbf{u}	displacement vector
ε	strain tensor
Γ	total crack length
$g(d)$	degradation function

\mathcal{A}	thermodynamic force associated with d
λ	Lamé's coefficient
μ	shear coefficient
κ	bulk modulus of the material
\mathcal{H}	strain history functional

- Table of abbreviations in chapter 1, 2

W_u	elastic strain energy density function
σ	Cauchy stress tensor
Ψ^+	strain energy density function associated with extension mode
Ψ^-	strain energy density function associated with compression mode
ε^+	extension part of the strain tensor
ε^-	compression part of the strain tensor
$\tilde{\varepsilon}$	bulk strain tensor which satisfies $\tilde{\varepsilon}^+$ be orthogonal to $\tilde{\varepsilon}^-$ (in chapter 2)

- Table of abbreviations in chapter 3, 4

β	fixed scalar phase field variable at the interface
l_β	regularization length of material at the interface
l_d	regularization length of smeared crack
W_u^e	bulk strain energy density function
Ψ_e^+	bulk strain energy density function associated with extension mode
Ψ_e^-	bulk strain energy density function associated with compression mode
g_c^I	fracture toughness at the interface
\mathbf{w}	displacement jump approximation
χ	history parameter of displacement jump across the interface
σ_e	Cauchy stress tensor
α	angle of fiber respect to the horizontal direction (in chapter 2 and 4)
Ψ^I	strain energy density function depending on the displacement jump across the interface
γ_d	crack density function
γ_β	crack density function at the interface

- ε_e bulk strain tensor
- $\bar{\varepsilon}$ strain tensor induced by the smoothed jump at the interface
- $\tilde{\varepsilon}_e$ bulk strain tensor which satisfies $\tilde{\varepsilon}_e^+$ be orthogonal to $\tilde{\varepsilon}_e^-$
- \mathbb{C} fourth-order elastic tensor
- \mathbb{L} fourth-order elastic compliance tensor

Chapter 1

Phase-field modeling of the nucleation and propagation of cracks by using a new family of degradation functions for the experimental validation

1.1 Abstract

The phase-field method, also referred to as the gradient damage or smeared crack method is a framework for modeling and simulating the initiation and propagation of complex crack networks. Most of the previous works require that the regularization length be interpreted as a material parameter. This problem makes the mesh discretization in the structure is very small and thus, the computational costs increase. In this work, we use a quadratic degradation function as Nguyen *et al.* [18] and a new family of degradation functions introduced by Sargado *et al.* [6] into the elastic strain energy density function to describe the damage state as well as predict critical loads associated with crack nucleation and propagation in plaster compression tests. The mesh size in the area where the crack passes through is coarser, thus the calculation cost is reduced without changing the path of the crack as well as the global and local mechanical behaviors in the structure. The classical phase field method using the proposed degradation function is compared with the one using the quadratic degradation function through several numerical examples. These numerical results are validated with the experimental ones in [36] and [37].

1.2 Introduction

The accurate simulation by computational method of crack initiation and propagation in brittle and quasi-brittle materials, such as concrete, cement, plaster or rocks, is necessary to predicting the strength and durability of structures made of these materials.

Linear Elastic Fracture Mechanics (LEFM) is based on the thermodynamic principles given by Griffith [7]. Elastic energy and damage dissipation are competing a novel variational approach generalizing Griffith's idea was elaborated by Francfort and Marigo [8].

The works [9, 10, 11, 12, 13, 14, 15, 16, 17] have proposed the phase field method based on a regularized description of discontinuities. This method allows an accurate prediction of the propagation of cracks in complex materials such as plaster, concrete [18, 19].

Bourdin *et al.* [20] have introduced an important parameter in the phase field method, i.e. is the regularization length l . The works [21, 22, 23] have studied the effects of this parameter so as to determine the convergence in the sense of Γ -convergence. In [24, 25], the gradient damage models with the regularization parameter l have been proposed. In [26, 27, 28, 29, 30], the regularization parameter l as a material's internal length, which is kept fixed. In [31, 32], it is shown that the regularization parameter l and mesh size are related to the relationship between the critical stress and toughness criterion for crack initiation.

The length parameter l related to the regularized representation of a crack is required in the phase field method. This regularization parameter often depends on the material parameters, and choosing the value of this parameter l greatly affects the peak load value. In [33, 34, 35], it has been shown that a relationship between l and at least two other material parameters need to be identified.

The work [6] has conceptually explained how the choice of the length scale parameter can result in either delay or acceleration of failure under quasi-static conditions and introduced a new family of degradation functions allowing exact reproduction of the beginning of fracture for arbitrary values of the length parameter l .

In the present work, we use is made of the phase-field modeling proposed in the work of [18] together with the new degradation function introduced by [6]. It aims at increasing the accuracy of the phase-field method in predicting crack nucleation and propagation in experimental materials.

The main advantages of the proposed method are listed as follows: (a) the regularization length is independent of the material parameters, so that mesh size can be coarser; (b) linear elastic behavior is preserved before damage even when applied to experimental materials; (c) the peak load and the crack path are accurately described in the experimental materials; (d) it is applied with respect to experimental materials both regarding global and local mechanical response.

To demonstrate the above advantages, in each numerical example, we choose several mesh size values in the expected crack propagation zone of a structure (the choice of mesh size is detailed in Section 1.3). Then, the simulation results are compared with the experimental results of [36]. Experimental parameters provided in [36] are used in all numerical examples. Several advantages are also given in comparison with [34].

This chapter is organized as follows: In Section 1.3, we introduce the phase-field method and a new degradation function. In Section 1.4, the influences of the main material parameters in the numerical modeling are investigated and the determination of the relationship between the regularization parameter l with some material parameters is carried out when using the new degradation function. In Section 1.5, several numerical examples are presented and the corresponding results are compared with available experimental results. Finally, conclusions and perspectives are given in Section 1.6.

1.3 Review of the phase field method

In this section, we give a review of the phase-field method as presented in [13, 14, 15, 16, 17, 18] together with the degradation functions of [6] and the quadratic degradation function in [18].

1.3.1 Regularized representation of free discontinuities

Let $\Omega \in \mathbb{R}^{\mathcal{D}}$ be an open domain occupied by a damaged solid, with $\mathcal{D} \in [2; 3]$ being the space dimension and $\partial\Omega \in \mathbb{R}^{\mathcal{D}-1}$ is the external boundary of Ω . Let Γ be the crack which spreads within Ω . Within a smeared framework, the discontinuity is approximated by a regularized representation obtained by a phase-field scalar variable $d(\mathbf{x})$ with $\mathbf{x} \in \Omega$. We can determine the damage variable $d(\mathbf{x})$ by solving the following equations in Ω (see e.g. [16]):

$$\begin{cases} d - l^2 \Delta d = 0 & \text{in } \Omega \\ d(\mathbf{x}) = 1 & \text{on } \Gamma \\ \nabla d(\mathbf{x}) \cdot \mathbf{n} = 0 & \text{on } \partial\Omega \end{cases} \quad (1.1)$$

where Δd is the Laplacian, l is the length parameter, and \mathbf{n} is the unit normal vector to the external boundary $\partial\Omega$. Eq.(1.1) can be seen as the Euler-Lagrange expression related to the variational problem

$$d(\mathbf{x}, t) = \text{Arg} \{ \inf_{d \in \mathcal{S}_d} \Gamma(d) \}, \quad \Gamma(d) = \int_{\Omega} \gamma(d, \nabla d) d\Omega, \quad (1.2)$$

where $\mathcal{S}_d = \{d | d(\mathbf{x}) = 1 \text{ on } \Gamma, \forall \mathbf{x} \in \Gamma\}$ and Γ represents the total crack length per unit area in the two-dimensional case and total crack area of per unit volume in the three-dimensional case. In (1.2), $\gamma(d, \nabla d)$ is defined by

$$\gamma(d, \nabla d) = \frac{d^2}{2l} + \frac{l}{2} \nabla d \cdot \nabla d. \quad (1.3)$$

1.3.2 Energy functional

The total energy of the solid body is introduced as follows:

$$E(\mathbf{u}, d) = \int_{\Omega} W_u(\boldsymbol{\varepsilon}(\mathbf{u}), d) d\Omega + \int_{\Omega} g_c \gamma(d, \nabla d) d\Omega \quad (1.4)$$

where g_c is the fracture toughness and the total energy is set as $E = \int_{\Omega} W d\Omega$ in which:

$$W(\mathbf{u}, d) = W_u(\boldsymbol{\varepsilon}(\mathbf{u}), d) + g_c \gamma(d, \nabla d). \quad (1.5)$$

The free energy W in (1.5) can be written as:

$$W_u(\boldsymbol{\varepsilon}(\mathbf{u}), d) = \Psi^+(\boldsymbol{\varepsilon}(\mathbf{u}))\{g(d) + k\} + \Psi^-(\boldsymbol{\varepsilon}(\mathbf{u})). \quad (1.6)$$

In this work, we choose the split proposed in [16]:

$$\Psi_{\pm}(\boldsymbol{\varepsilon}(\mathbf{u})) = \frac{\lambda}{2} (\langle \text{Tr}(\boldsymbol{\varepsilon}) \rangle_{\pm})^2 + \mu \text{Tr}\{(\boldsymbol{\varepsilon}_{\pm})^2\} \quad (1.7)$$

The strain is decomposed into the positive and negative parts corresponding to the extensive and compressive parts as:

$$\boldsymbol{\varepsilon} = \boldsymbol{\varepsilon}_+ + \boldsymbol{\varepsilon}_- \quad (1.8)$$

and

$$\boldsymbol{\varepsilon}_{\pm} = \sum_{i=1}^{\mathcal{D}} \langle \varepsilon_i \rangle_{\pm} \mathbf{n}_i \otimes \mathbf{n}_i \quad (1.9)$$

In (1.7) and (1.9), $\langle x \rangle_{\pm} = (x \pm |x|)/2$, ε_i and \mathbf{n}_i are the eigenvalues and unit eigenvectors of $\boldsymbol{\varepsilon}$, respectively. In (1.7), λ and μ are initial Lamé coefficients and, in (1.6) k is a very small value to maintain the well-posedness of structure behaviors.

Here, we used two types of degradation function: first, the quadratic degradation function as in [18] takes the form:

$$g_1(d) = (1 - d)^2 \quad (1.10)$$

second, the new family of degradation functions introduced in [6] is specified by:

$$g_2(d; n, w) = (1 - w) \frac{1 - e^{-m(n)}(1 - d)^n}{1 - e^{-m(n)}} + w f_c(d) \quad (1.11)$$

where m, n and w are real numbers such that $m > 0, n \geq 2$ and $w \in [0, 1]$.

In addition,

$$m(n) = \frac{(n-2)d^* + 1}{nd^*(1-d^*)^n} \quad (1.12)$$

where

$$d^* = \begin{cases} \frac{1}{3} & \text{if } n=2, \\ \frac{-(n+1) + \sqrt{5n^2 - 6n + 1}}{2(n^2 - 2n)} & \text{otherwise,} \end{cases} \quad (1.13)$$

and

$$f_c(d) = a_2(1-d)^2 + a_3(1-d)^3 \quad (1.14)$$

In order to fully determine the constants a_2 and a_3 , we impose two conditions. The first is that $f_c(d^*) - d^* f''_c(d^*) = 0$ in order to retain validity of expressions obtained based on d^* . The second is that $f_c(0) = 1$. This yields the following expressions for the constants:

$$a_2 = \frac{3(d^*)^2 - 3}{3(d^*)^2 - 1}; \quad a_3 = \frac{2}{3(d^*)^2 - 1}. \quad (1.15)$$

We note that $f_c(d)$ itself is not a degradation function since for sufficiently large d^* , it may be that $f_c(d) > 0$ at certain values of d . Thus w should be kept small to remain elastic linear before damage. Here, we set $w = 0.1$ to have a sufficient residual in the gradient of $g_2(d)$. The resulting plots for $g_2(d)$, $g'_2(d)$ and $g''_2(d)$ are detailed in Fig. 1.1.

A reduced Clausius-Duhem inequality expression for the evolution of the scalar variable d can be written as follows:

$$\mathcal{A}\dot{d} \geq 0 \text{ and } \mathcal{A} = -\frac{\partial W}{\partial d} \quad (1.16)$$

An assumption of a threshold function $\mathcal{F}(\mathcal{A})$ such that no damage occurs can be written as:

$$\mathcal{F}(\mathcal{A}) = \mathcal{A} \leq 0 \quad (1.17)$$

The concept of maximum dissipation requires that expression $\mathcal{A}\dot{d}$ must be satisfied the condition $\dot{d} > 0$ and $\mathcal{F} = 0$, it means:

$$\mathcal{F} = -\frac{\partial W}{\partial d} = -\frac{\partial W_{\mathbf{u}}}{\partial d} - g_c \delta_d \gamma(d) = 0 \quad (1.18)$$

with the functional derivative

$$\delta_d \gamma(d, \nabla d) = \frac{d}{l} - l \Delta d \quad (1.19)$$

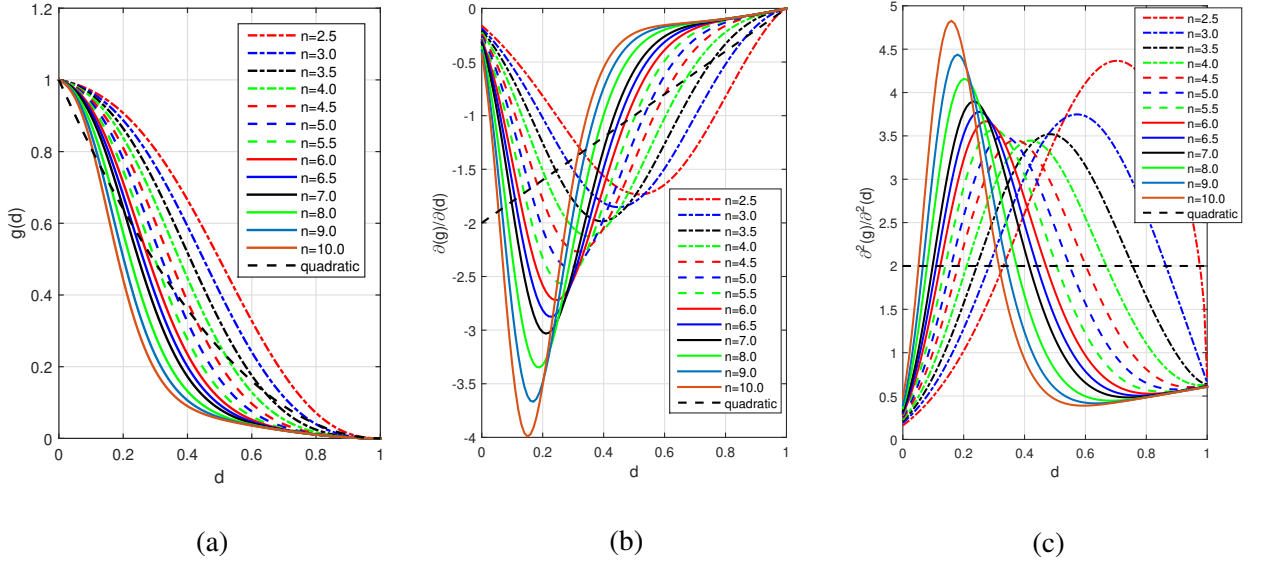


Figure 1.1: Plots of: (a) the new degradation function $g(d)$, (b) the first-order derivative $g'(d)$, (c) the second-order derivative $g''(d)$ for different values of n in the influence of the correction term $f_c(d)$.

It follows that, when $\dot{d} > 0$, then

$$\mathcal{F} = -\frac{\partial W}{\partial d} = -g'(d)\Psi^+ - g_c\delta_d\gamma(d) = 0 \quad (1.20)$$

To handle loading and unloading process, the strain history function introduced in the works [16] is adopted:

$$\mathcal{H} = \max_{\tau \in [0, t]} \{\Psi^+(\mathbf{x}, \tau)\}. \quad (1.21)$$

From (1.20) and (1.21), we have

$$g'(d)\mathcal{H} + g_c\delta_d\gamma(d) = 0. \quad (1.22)$$

1.3.3 Phase field and displacement problems

Weak form of the phase field problem

Using (1.19) and (1.22), the evaluation of the damage variable $d(\mathbf{x}, t)$ can be formulated as the following phase field problem:

$$\begin{cases} g'(d)\mathcal{H} + \frac{g_c}{l}(d - l^2\Delta d) = 0 & \text{in } \Omega \\ d(\mathbf{x}) = 1 & \text{on } \Gamma \\ \nabla d(\mathbf{x}) \cdot \mathbf{n} = 0 & \text{on } \delta\Omega \end{cases} \quad (1.23)$$

From [6], we have the second-order derivative $g''(d) = \frac{-g'(d)}{(1-d)}$ and using (1.23), the weak form of the phase-field problem can be written as:

$$\int_{\Omega} \left\{ \left(g''(d) \mathcal{H}_n + \frac{g_c}{l} \right) d_n \delta d + g_c l \nabla d_{n+1} \nabla (\delta d) \right\} d\Omega = \int_{\Omega} g''(d) \mathcal{H}_n \delta d d\Omega \quad (1.24)$$

FEM discretization of the phase field problem

Using FEM, the phase-field as well as its gradient are approximated by

$$d(\mathbf{x}) = \{\mathbf{N}_d(\mathbf{x})\} \{\mathbf{d}\} \text{ and } \nabla d(\mathbf{x}) = [\mathbf{B}_d(\mathbf{x})] \{\mathbf{d}\}, \quad (1.25)$$

$$\delta d(\mathbf{x}) = \{\mathbf{N}_d(\mathbf{x})\} \{\delta \mathbf{d}\} \text{ and } \nabla \delta d(\mathbf{x}) = [\mathbf{B}_d(\mathbf{x})] \{\delta \mathbf{d}\}, \quad (1.26)$$

where $\mathbf{N}_d(\mathbf{x})$ and $\mathbf{B}_d(\mathbf{x})$ are the matrix of shape functions and the matrix of shape function derivatives, respectively. Introducing (1.25) and (1.26) into the weak form (1.24), we obtain:

The stiffness matrix is determined:

$$[\mathbf{K}_d] = \int_{\Omega} \left\{ \left(\frac{g_c}{l} + g''(d) \mathcal{H}_n \right) \{\mathbf{N}_d\}^T \{\mathbf{N}_d\} + g_c l [\mathbf{B}_d]^T [\mathbf{B}_d] \right\} d\Omega \quad (1.27)$$

The force vector is written as:

$$\{\mathbf{F}_d\} = \int_{\Omega} g''(d) \{\mathbf{N}_d\}^T \mathcal{H}_n d\Omega \quad (1.28)$$

And the solution for the nodal values of the damage variable:

$$\{\mathbf{d}\} = [\mathbf{K}_d]^{-1} \cdot \{\mathbf{F}_d\} \quad (1.29)$$

Weak form of the displacement problem

Using the variational principle for minimizing the total energy E with respect to the displacement \mathbf{u} , the weak form for the displacement problem can be formulated as

$$\int_{\Omega} \frac{\partial W_u}{\partial \boldsymbol{\varepsilon}} : \boldsymbol{\varepsilon}(\delta \mathbf{u}) d\Omega = \int_{\Omega} \mathbf{f} \cdot \delta \mathbf{u} d\Omega + \int_{\partial \Omega_F} \bar{\mathbf{F}} \cdot \delta \mathbf{u} d\Gamma \quad (1.30)$$

where \mathbf{f} and $\bar{\mathbf{F}}$ are the body forces and the prescribed traction over the boundary $\partial \Omega_F$.

With the aforementioned expression of the strain energy function, the Cauchy stress now reads

$$\boldsymbol{\sigma} = \frac{\partial W_u}{\partial \boldsymbol{\varepsilon}} = \{g(d) + k\} \{\lambda \langle \text{Tr} \boldsymbol{\varepsilon} \rangle_+ \mathbf{1} + 2\mu \boldsymbol{\varepsilon}_+\} + \lambda \langle \text{Tr} \boldsymbol{\varepsilon} \rangle_- \mathbf{1} + 2\mu \boldsymbol{\varepsilon}_- \quad (1.31)$$

where $\langle \text{Tr} \boldsymbol{\varepsilon} \rangle_{\pm} = \mathbf{R}^{\pm}(\text{Tr} \boldsymbol{\varepsilon})$ (see, e.g., [18]).

FEM discretization of the displacement problem

We use FEM approximations for the displacement problem:

$$\mathbf{u}(\mathbf{x}) = [\mathbf{N}]\{\mathbf{u}\} \text{ and } \boldsymbol{\varepsilon}(\mathbf{u}) = [\mathbf{B}]\{\mathbf{u}\} \quad (1.32)$$

$$\delta \mathbf{u} = [\mathbf{N}]\{\delta \mathbf{u}\} \text{ and } \boldsymbol{\varepsilon}(\delta \mathbf{u}) = [\mathbf{B}]\{\delta \mathbf{u}\} \quad (1.33)$$

where \mathbf{N} and \mathbf{B} are the matrix of shape function and the matrix of shape functions derivatives for displacement vector, respectively. Inserting (1.32) and (1.33) into the weak form (1.31), we obtain:

The stiffness matrix is written as follows:

$$[\mathbf{K}_1(d_{n+1}, \mathbf{u}_n)] = \int_{\Omega} [\mathbf{B}]^T \{g(d) + k\} \{\lambda \mathbf{R}_n^+ [\mathbf{1}]^T [\mathbf{1}] + 2\mu \mathbf{P}_n^+\} [\mathbf{B}] d\Omega \quad (1.34)$$

$$[\mathbf{K}_2(d_{n+1}, \mathbf{u}_n)] = \int_{\Omega} [\mathbf{B}]^T \{\lambda \mathbf{R}_n^- [\mathbf{1}]^T [\mathbf{1}] + 2\mu \mathbf{P}_n^-\} [\mathbf{B}] d\Omega \quad (1.35)$$

with $\mathbf{R}^{\pm} = \frac{1}{2} \{\text{sign}\{\pm \text{Tr}(\boldsymbol{\varepsilon})\} + 1\}$ and $\mathbf{P}^{\pm} = \frac{\partial \boldsymbol{\varepsilon}^{\pm}}{\partial \boldsymbol{\varepsilon}}$ (see, e.g., [18]).

The force vector is obtained:

$$\{\mathbf{F}\}_{n+1} = \int_{\Omega} [\mathbf{N}]^T \{\mathbf{f}\} d\Omega + \int_{\partial\Omega_F} [\mathbf{N}]^T \{\bar{\mathbf{F}}\}_{n+1} d\Gamma \quad (1.36)$$

And the nodal displacements are solved:

$$\{\mathbf{u}\}_{n+1} = \{[\mathbf{K}_1] + [\mathbf{K}_2]\}^{-1} \cdot \{\mathbf{F}\}_{n+1} \quad (1.37)$$

1.4 Influence of input parameters in the numerical simulations

In this section, we investigate the influences of the numerical parameters on the simulation results as in [34] while using the degradation function suggested in [6]. We study the effects of three important parameters: (a) the regularization parameter l in (1.1), (b) the mesh size of structure and (c) the loading increments. For this purpose, we use a sample containing a hole as in Fig. 1.2 undergoing compression. In all examples of the present work, the triangle elements are used. The material parameters have been chosen from the experimental values as $E = 12\text{GPa}$, $\nu = 0.3$, $g_c = 1.4\text{N/m}$ and $\sigma_c = 3.9\text{MPa}$ provided in [36]. Plane strain assumption is adopted.

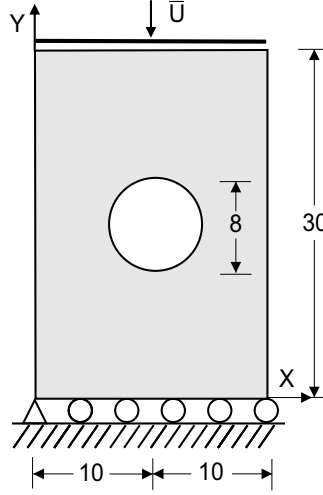


Figure 1.2: Analyze the influence of numerical parameters on the simulation by the compression test of the sample containing a hole: geometry and boundary conditions.

1.4.1 Determination of the regularization parameter I

We consider a bar under uniaxial tension. In this configuration and in the absence of initial defects, the damage distribution is assumed to be homogeneous, i.e. $\nabla d(\mathbf{x}) = 0$. For uniaxial tension, and assuming $k \simeq 0$, from (1.31) we have:

$$\sigma = g(d)E\varepsilon, \quad \Psi^+ = \frac{E\varepsilon^2}{2}, \quad (1.38)$$

with the degradation functions from (1.10) and (1.11). Then using (1.19) and (1.20), we have the relation:

$$\frac{g'(d)E\varepsilon^2}{2} = -\frac{g_c d}{l} \quad (1.39)$$

From (1.39) we obtain

$$\varepsilon = \sqrt{\frac{-2d}{g'(d)}} \sqrt{\frac{g_c}{lE}} \quad (1.40)$$

And then

$$\sigma = g(d)E\varepsilon = g(d) \sqrt{\frac{-2d}{g'(d)}} \sqrt{\frac{Eg_c}{l}} \quad (1.41)$$

From (1.40) and (1.41) we have the Fig. 1.3. Next, we find the maximum value of the stress with respect to d is given by

$$\sigma_c = \text{Arg} \left\{ \sup_{d \in [0;1]} \sigma(d, l) \right\} = \text{Arg} \left\{ \sup_{d \in [0;1]} \left(g(d) \sqrt{\frac{-2d}{g'(d)}} \sqrt{\frac{Eg_c}{l}} \right) \right\} \quad (1.42)$$

The critical value of the stress σ_c is reached when d corresponds to the maximum value of $\sigma \sqrt{\frac{l}{Eg_c}}$ obtained (see Fig. 1.3b). Thus we use the quadratic degradation function as (1.10), the value of

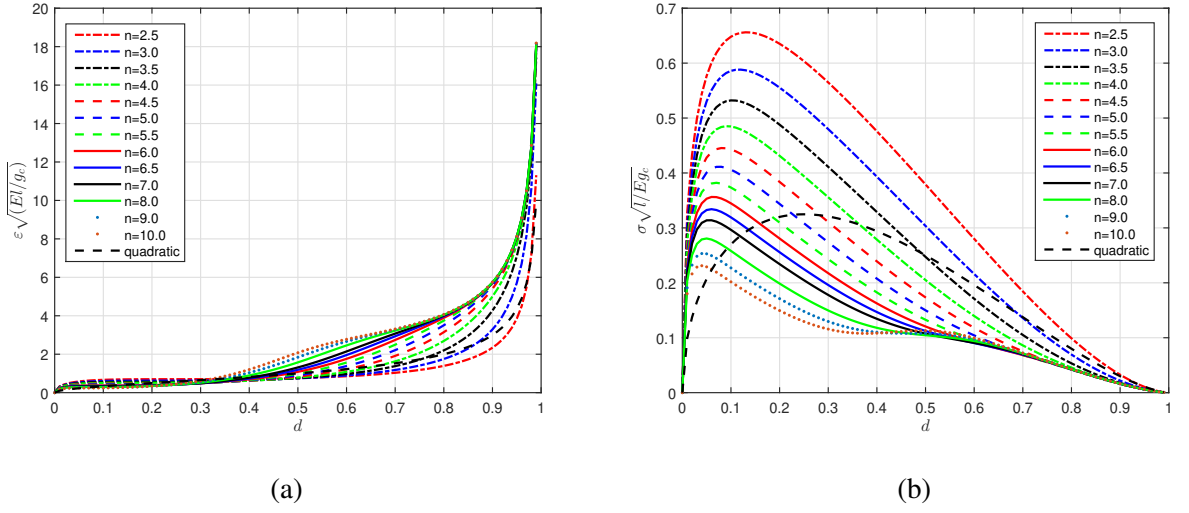


Figure 1.3: Uniaxial tension test of a 1-dimensional homogeneous bar: dependence on the phase-field variable d when using the new family of degradation functions $g(d)$ of (a) strain and (b) stress.

$d = \frac{1}{4}$ corresponds to the critical stress σ_c , and we have the regularization length l as in Nguyen *et al.* [34]:

$$l = \frac{27Eg_c}{256(\sigma_c)^2} \quad (1.43)$$

We can utilize a dimensionless function of $\sigma_{nd} = \sigma_c \sqrt{l/Eg_c}$ which is given by fitting a function to numerical evaluations of the peak stress for different values of n from Fig. 1.3b. The function of n , which depends on σ_{nd} , is provided by

$$n(\sigma_{nd}) = c_0 + \frac{c_1}{\sigma_{nd}} + \frac{c_2}{\sigma_{nd}^2} + \frac{c_3}{\sigma_{nd}^3} \quad (1.44)$$

From (1.44), given four values of σ_{nd} which are found in Fig. 1.3b and four corresponding values of n , we can determine the values of the coefficients c_0 to c_3 as follows:

$$\begin{cases} c_0 = -1.9683716827 \\ c_1 = 3.0725412764 \\ c_2 = -0.1019957566 \\ c_3 = 0.0071948119 \end{cases} \quad (1.45)$$

and we have the $\sigma_{nd} - n$ curve as plotted in Fig. 1.4.

In the first test, we use the mesh size $h_{min} = 0.01\text{mm}$ around the hole and in the expected crack propagation zone where the cracks should initiate and propagate, and the mesh size $h_{max} = 1\text{mm}$ in the remaining zone, such that mesh size ensures numerical convergence of the computations for all values of l considered. The displacement increment is chosen as $\Delta u = -10^{-4}$ mm. With the

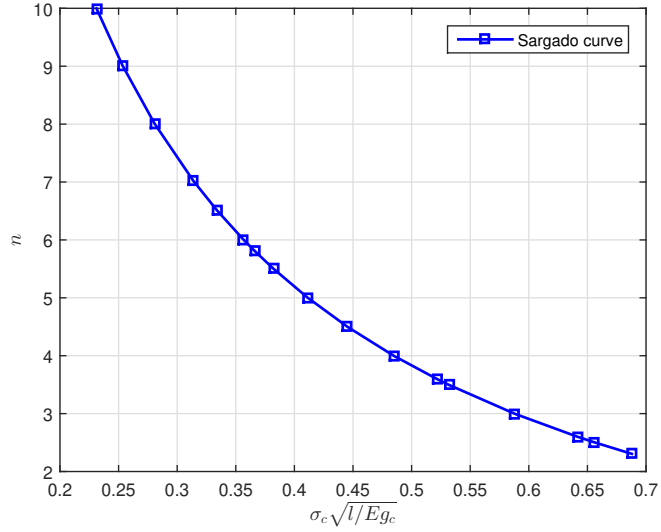


Figure 1.4: Uniaxial tension test of a 1-dimensional homogeneous bar: relational curve of normalized peak stress and parameter n assuming uniform stress and damage.

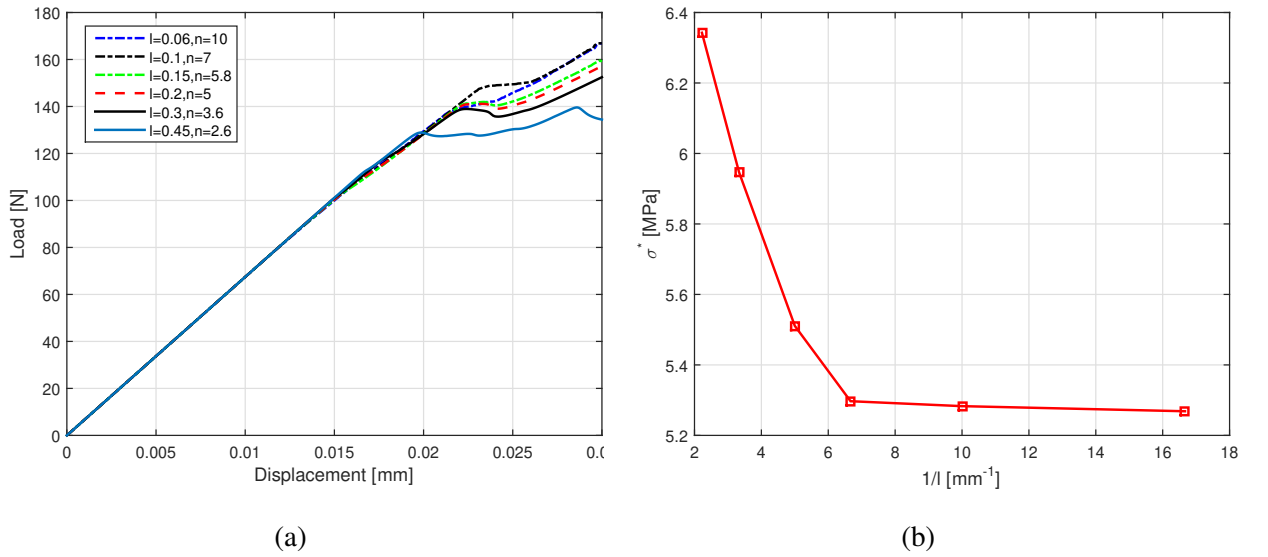


Figure 1.5: Convergence of the solution corresponds to the regularization parameter l : (a) Load-displacement curve; (b) σ^* for different values of l

new degradation function, we take six values of parameters $n = 10, 7, 5.8, 5, 3.6$ and 2.6 , and we calculate the corresponding values of the regularization lengths $l = 0.06\text{mm}, 0.1\text{mm}, 0.15\text{mm}, 0.2\text{mm}, 0.3\text{mm}$ and 0.45mm based on (1.44) and (1.45) as well as Fig. 1.4. In Fig. 1.5a, we can see the preservation of linear elastic response in the bulk material before fracture, and the peak loads are relatively similar when using six above values of l . In Fig. 1.5b, we show the related convergence: the variation of σ^* is 0.5%, 4.5%, 11.1%, and 17%, respectively, for $l \leq 0.15\text{mm}$,

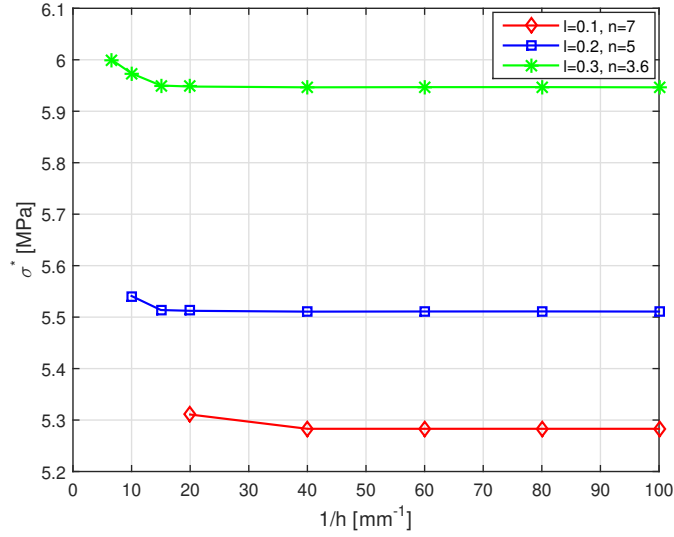


Figure 1.6: Convergence of the solution corresponds to the different values of mesh size.

0.2mm, 0.3mm and 0.45mm. Here, the numerical critical axial stress σ^* is taken as the ratio of the vertical component of the resultant force prescribed at the upper side of the sample to the area of its upper side, when damage reaches the value $d = 1$ for the first load increment at some node in the mesh (i.e. stress associated to the onset of the first crack). These results are acceptable in comparison with the quadratic degradation function.

1.4.2 Influence of the mesh size

In the second test, we investigate the convergence of the mechanical response with respect to mesh size. Here, it is made of the values of l and n : $l = 0.1\text{mm}$ and $n = 7$; $l = 0.2\text{mm}$ and $n = 5$; $l = 0.3\text{mm}$ and $n = 3.6$ together with the new degradation function. The constant compressive displacement increment of $\Delta u = -10^{-4}\text{ mm}$ is prescribed for 250 load increments. Then we perform several simulations using refined meshes, where the mesh sizes in expected crack propagation zone change from $h_{min} = 0.01\text{mm}$ to $h_{min} = 0.2\text{mm}$.

We show in Fig.1.6 the convergence of this quantity with respect to the mesh size. A clear convergence is observed, with results becoming mesh independent when condition $h_{min} \leq l/2$ is fulfilled with all of values of l . In other words, the convergence of σ^* is obtained with $h_{min} \leq 0.15\text{mm}$ when $l = 0.3\text{mm}$, $h_{min} \leq 0.1\text{mm}$ when $l = 0.2\text{mm}$ and $h_{min} \leq 0.05\text{mm}$ when using $l = 0.1\text{mm}$. This confirms the results of [16]. Note that, when $l = 0.1\text{mm}$, 0.2mm and 0.3mm , the corresponding convergence values of σ^* are 5.28 MPa, 5.51MPa and 5.94MPa. We can see that the variation of convergence values σ^* is about 11.1 %. These variations are acceptable when the minimal element

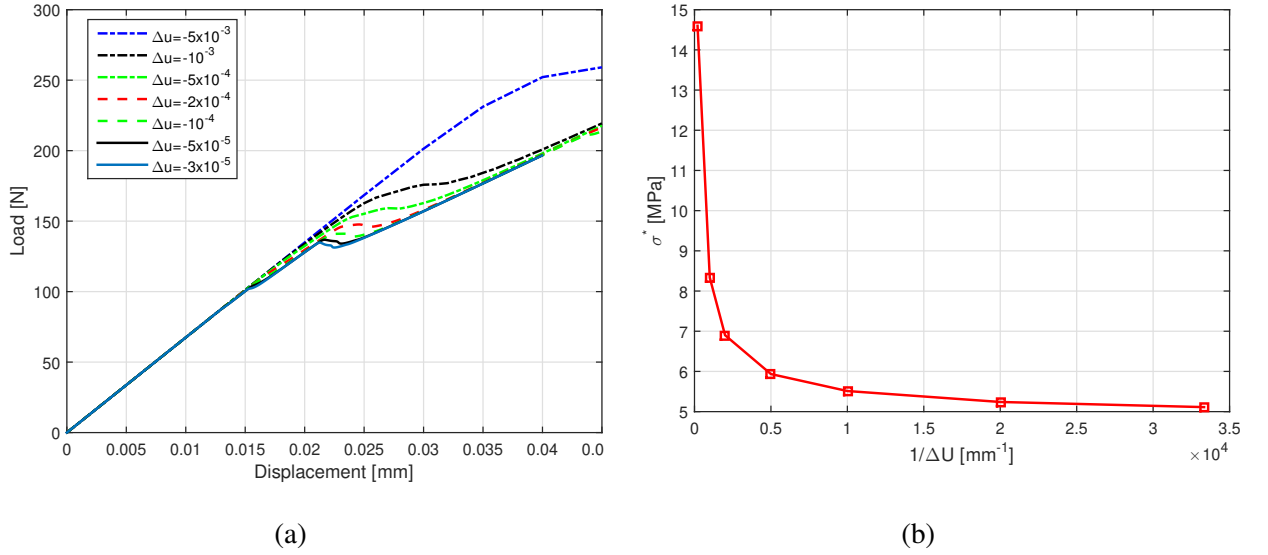


Figure 1.7: Convergence of the solution corresponds to the displacement increments: (a) load-displacement curve; (b) σ^* for different displacement increments Δu

size in the expected fracture propagation zone is increased by three times.

1.4.3 Influence of the displacement increments

In the next test, we investigate the influence of the displacement increment Δu during the numerical simulation on the mechanical behavior while using the new degradation function of [6]. Here, we use $l = 0.2\text{mm}$, $n = 5$ and several displacement increments from $\Delta u = -5 \times 10^{-3}\text{mm}$ to $\Delta u = -3 \times 10^{-5}\text{mm}$. Results are presented in Fig.1.7. The displacement-load curves are shown in Fig1.7a. We can see the peak loads are relatively similar when $\Delta u \geq -2 \times 10^{-4}\text{mm}$. In Fig.1.7b, we study the evolution of σ^* with respect to Δu and can see that the corresponding variations of σ^* is below 2% when the increment goes from -5×10^{-5} to $-3 \times 10^{-5}\text{mm}$. This confirms the results of [34] where $l = 0.1\text{mm}$. Thus, the larger displacement increments cause the hardening phenomena of material mechanical behavior and increase the peak load of a structure during the simulation. The content of chapter 1 is summarized as the algorithm provided in the Appendix B.1

1.5 Numerical examples

1.5.1 Experimental validation: three-point bending test of un-notched beam

Now, we use the phase-field method together with the quadratic degradation function as (1.10) and the new family of degradation functions as (1.11) to determine the numerical critical stress σ_c^{num}

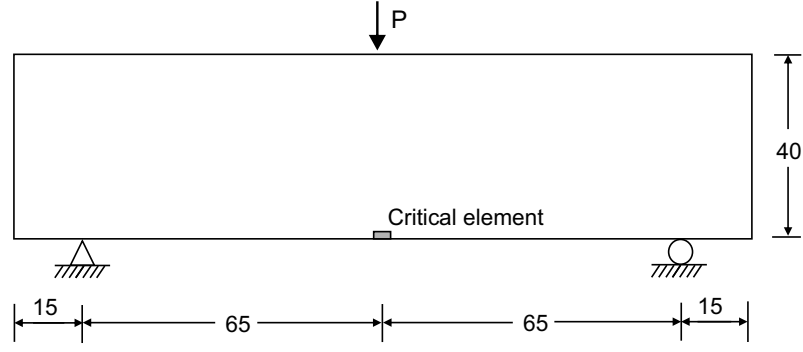


Figure 1.8: Symmetric three-point bending test of un-notched beam: Geometry and boundary conditions.

for the three-point bending test of an un-notched beam. And then, we compare the result with the experimental critical stress σ_c^{exp} obtained in the work of [36]. The geometric setup and the displacement conditions are depicted in Fig.1.8. The left bearing is fixed in two directions, while the vertical displacement of the right bearing is blocked, and the horizontal displacement is free. The constant compression displacement increments of $\Delta u = -5 \times 10^{-4}$ mm at the center of the beam on the upper side are for 120 increments.

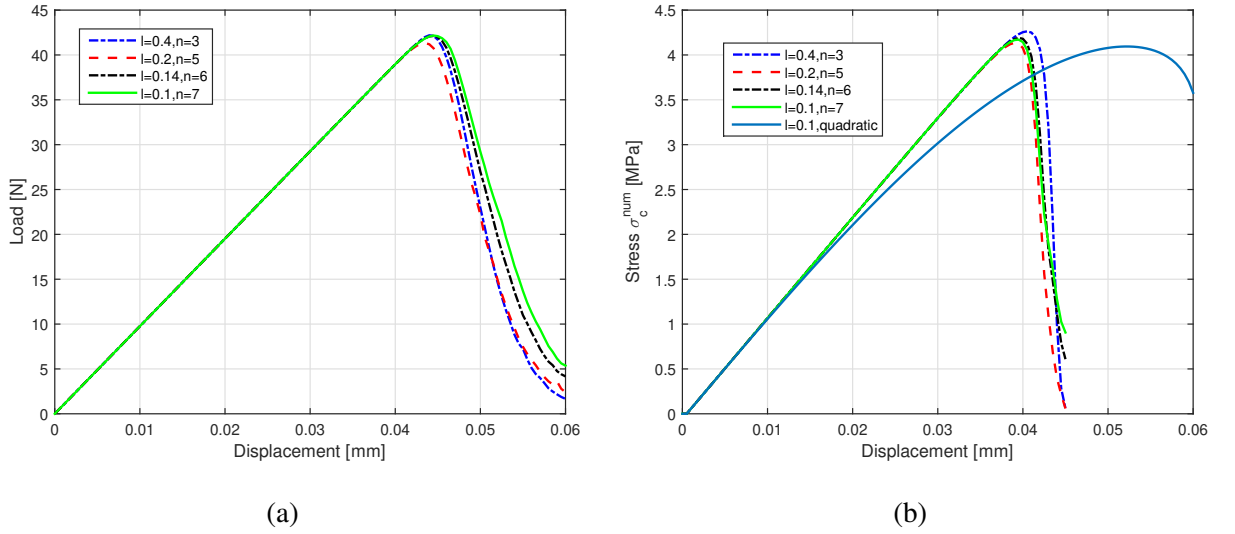


Figure 1.9: Symmetric three-point bending test of un-notched beam: (a) Load-displacement curves; (b) Critical value of the tensile stress σ_c for the different values of l

The numerical critical stress σ_c^{num} is defined as the maximal stress of the critical element at the center of the beam on the lower end in Fig.1.9b. With the new degradation functions in [6], use is made of four values of parameters $n = 3, 5, 6$ and 7 corresponding to the four values of the regularization lengths $l = 0.4$ mm, 0.2 mm, 0.14 mm, and 0.1 mm. In Fig.1.9, we observe the preservation

of linear elastic response in the bulk material prior to fracture. In Fig.1.9a, the load-displacement curves are similar when the values of regularization length l change. Next, in Fig1.9b, we show the numerical values of σ_c^{num} which are 4.26MPa, 4.13MPa, 4.19MPa, 4.17MPa corresponding the above four values of l , and 4.1MPa when using $l=0.1\text{mm}$ with the quadratic degradation function as (1.10). We have the experimental stress value reported in [36]: $\sigma_c^{exp} = 3.9\text{MPa}$. It is seen that the variation of σ_c^{num} with σ_c^{exp} is below 8%. In this example, the numerical critical stresses by using the different values of l are relatively similar to the experimental stress value.

1.5.2 Experimental validation: single-hole plate compression test

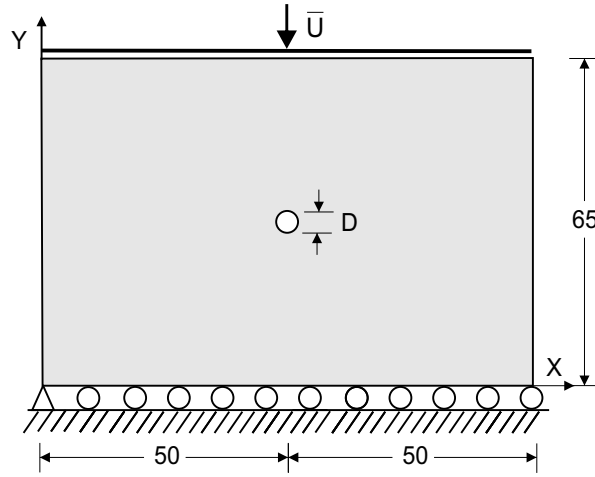


Figure 1.10: Compression test of the sample containing a hole whose diameter D changes: geometry and boundary conditions

This example aims to numerically determine the critical axial stress σ^* of the compression test of a plaster plate containing a hole whose diameter changes from $D = 3\text{mm}$ to $D = 6\text{mm}$. The numerical results obtained will be compared with experimental results in [36]. Moreover, we shall investigate the crack onset direction in the plaster sample. The geometry and boundary conditions of the plate are shown in Fig.1.10. The dimensions of the plate are 100x65mm. On the lower end, the vertical displacements are fixed, while the horizontal displacements are free and the left bottom nodes are fixed. On the upper end, the horizontal displacements are free, while the vertical displacements are prescribed via the displacement increments of Δu during the simulation. Constant compression displacement increments of $\Delta u = -10^{-4}\text{mm}$ are imposed for first load increments until d reaches 0.9 at the expected crack onset element, and then we use $\Delta u = -2 \times 10^{-5}\text{mm}$ until full fracture. We use element size $h_{min} = 0.05\text{mm}$ around the hole and the expected crack propagation zone, and $h_{max} = 0.25\text{mm}$ in the rest of zone.

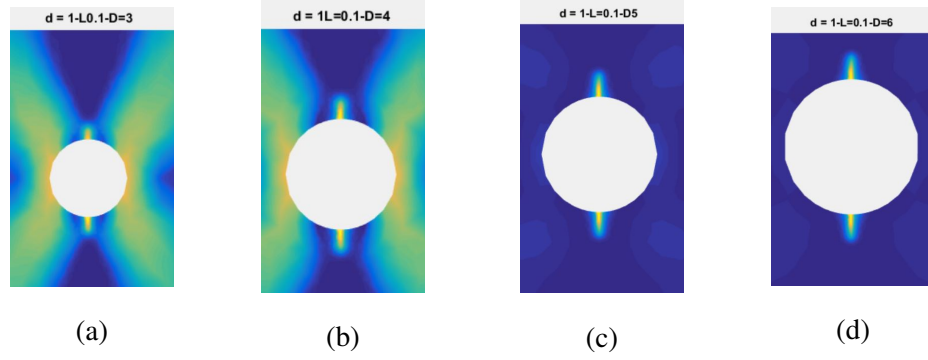


Figure 1.11: Crack onset of plaster sample containing one hole whose diameter D changes with using a pair of $l=0.1\text{mm}$ and $n=7$: (a) $D=3\text{mm}$, $U=0.055\text{mm}$; (b) $D=4\text{mm}$, $U=0.051\text{mm}$; (c) $D=5\text{mm}$, $U=0.041\text{mm}$; (d) $D=6\text{mm}$, $U=0.036\text{mm}$

In Fig. 1.11, we show the crack onset image of the plaster sample with different diameters $D=3\text{mm}$ to $D=6\text{mm}$ in the simulation while using $l=0.1\text{mm}$ and $n=7$. It can be seen that the stress state around the hole varies with the hole diameter.

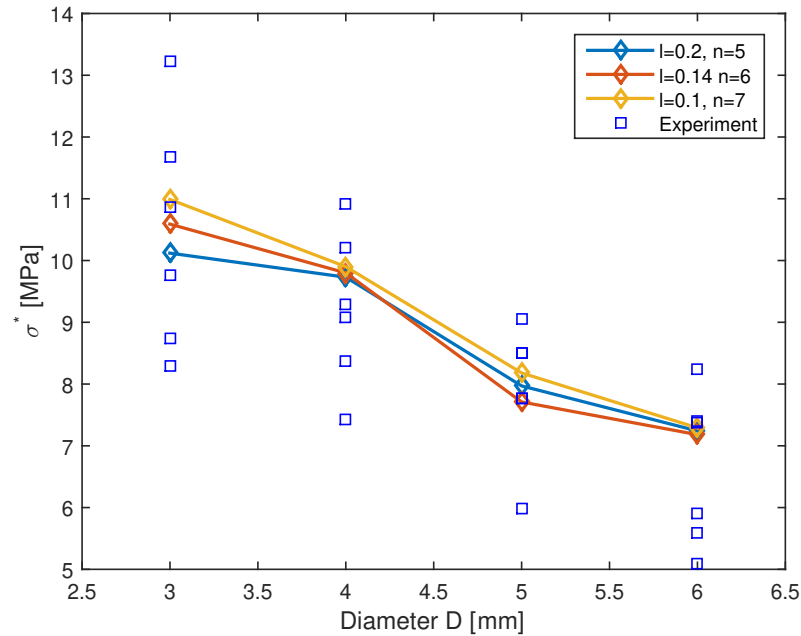


Figure 1.12: Critical axial stress σ^* when the cracks onset corresponds to the hole diameter: comparison between experimental results and numerical results

Comparison of the numerical stress values of σ^* with the experimental ones in [36] is shown in Fig.1.12. In the simulation, use is made of several pairs of l and n ($l=0.1\text{mm}$, $n=7$; $l=0.14\text{mm}$, $n=6$; $l=0.2\text{mm}$, $n=5$) for each hole diameter of the plate. All values of σ^* in simulation are seen to be within the experimental values in [36]. This implies that the present numerical method is

relatively reliable for determining the critical stress σ^* in single-hole plate compression tests.

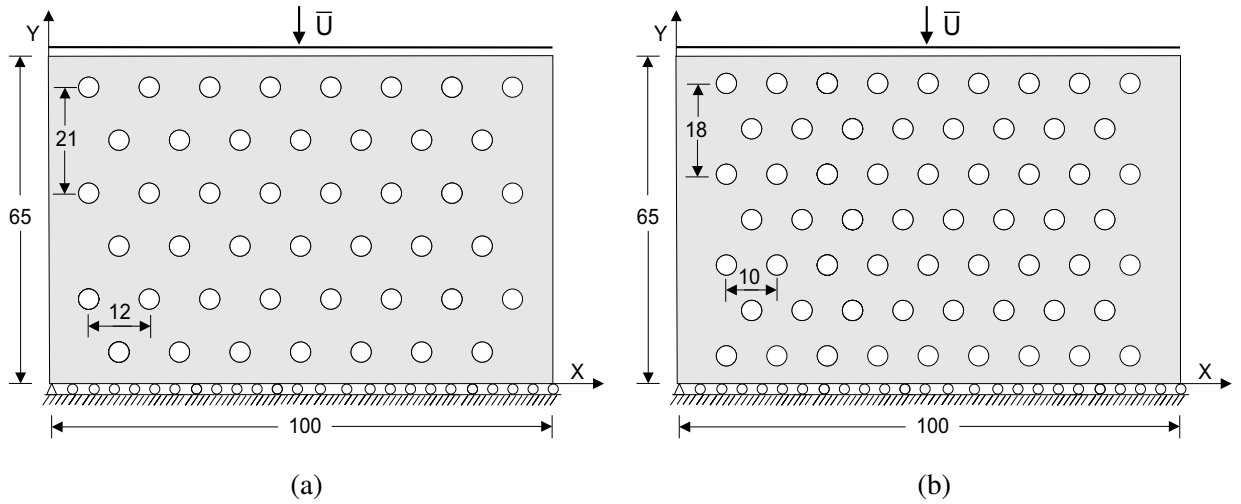


Figure 1.13: Compression test of a plate containing a periodic distribution of the holes: geometry and boundary conditions (a) containing 45 holes with the surface fraction 12.2% and (b) containing 60 holes with surface fraction 13.5% (in [37])

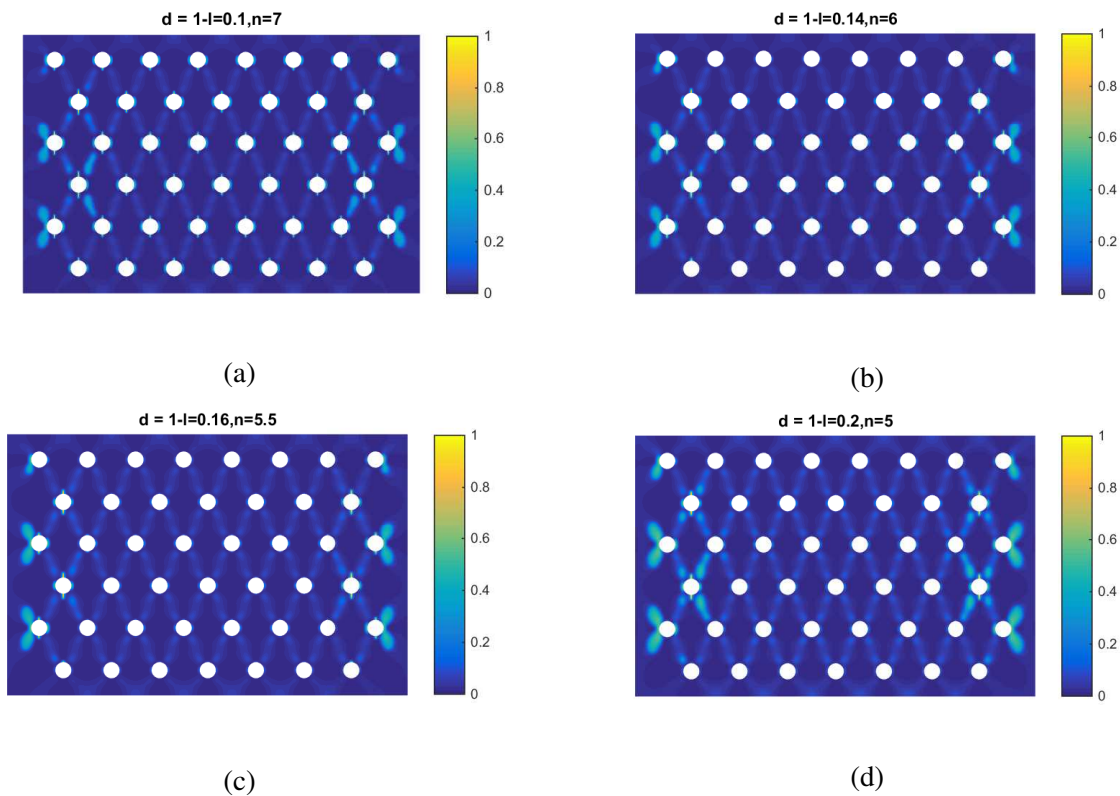


Figure 1.14: Compression test of a plate containing a periodic distribution of 45 holes (surface fraction 12.2%): evolution of the crack onset in the first hole for the different regularization lengths l : (a) $l=0.1\text{mm}$, $U=0.0456\text{mm}$; (b) $l=0.14\text{mm}$, $U=0.044\text{mm}$; (c) $l=0.16\text{mm}$, $U=0.0439\text{mm}$; (d) $l=0.2\text{mm}$, $U=0.0446\text{mm}$

1.5.3 Experimental validation: compression test of a plate containing a periodic distribution of cylindrical holes

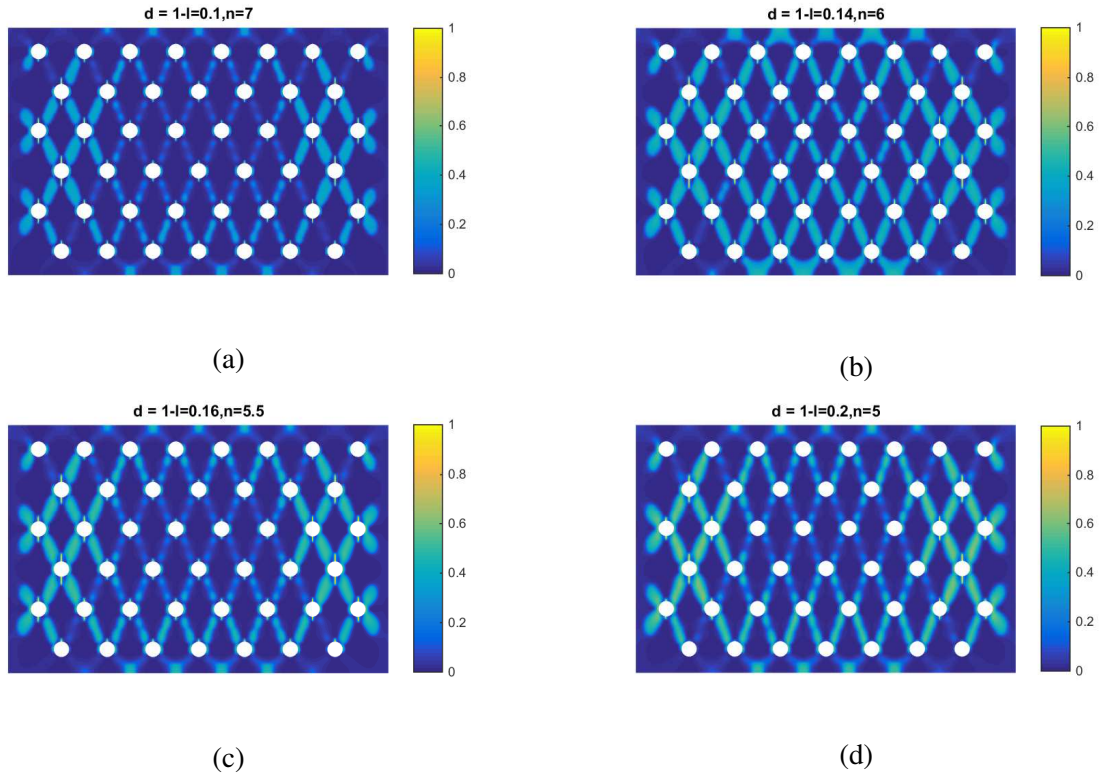


Figure 1.15: Compression test of a plate containing a periodic distribution of 45 holes (a surface fraction 12.2%): Propagation of the crack for the different regularization lengths l : (a) $l=0.1\text{mm}$, $U=0.0470\text{mm}$; (b) $l=0.14\text{mm}$, $U=0.0464\text{mm}$; (c) $l=0.16\text{mm}$, $U=0.0465\text{mm}$; (d) $l=0.2\text{mm}$, $U=0.0465\text{mm}$

The purpose of this example is to determine the numerical critical stress σ^* as well as the crack paths relative to the compression tests of a plate containing a periodic distribution of cylindrical holes. These numerical results will be compared with the experimental results in [37] and the numerical ones in [34]. The geometry and boundary conditions of the plate are presented in Fig.1.13a with 45 holes corresponding to a volume fraction of 12.2%, and in Fig.1.13b with 60 holes corresponding to a volume fraction of 13.5%. The dimensions of the plate are 100x65mm. The loading conditions are similar to those of the example 1.5.2. Monotonic compression displacement increments of $\Delta u = -10^{-4}\text{mm}$ are prescribed until d reaches 0.9 at the expected crack onset element, and then we impose $\Delta u = -2 \times 10^{-5}\text{mm}$ until full fracture. The element size $h_{min} = 0.05\text{mm}$ is applied around the hole and in the expected crack propagation zone while the element size $h_{max} = 0.5\text{mm}$ prevails in the remaining zone. Four pairs of values are employed for l and n : $l = 0.1\text{mm}$, $n = 7$; $l = 0.14\text{mm}$, $n = 6$; $l = 0.16\text{mm}$, $n = 5.5$ and $l = 0.2\text{mm}$, $n = 5$.

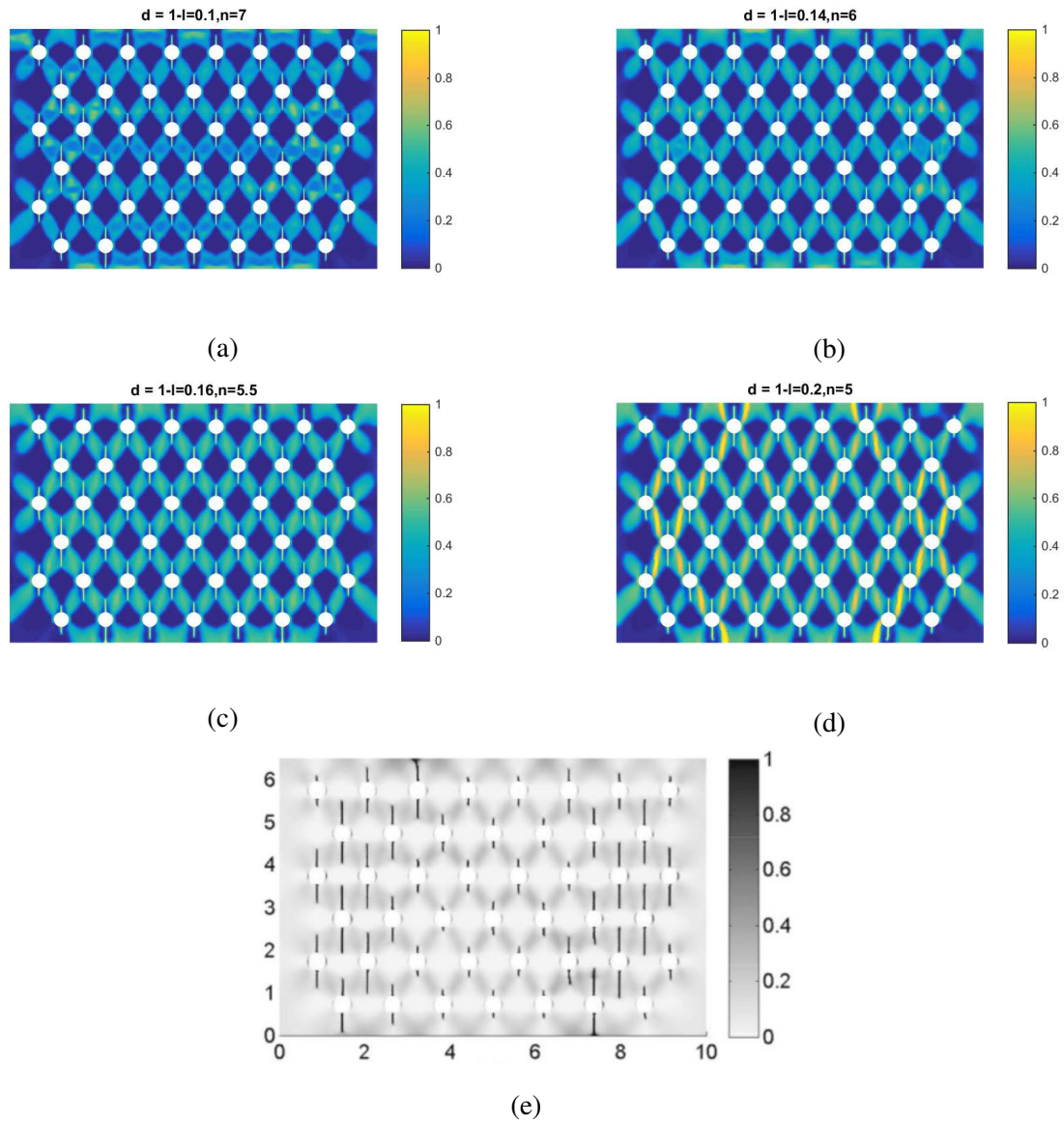


Figure 1.16: Compression test of a plate containing a periodic distribution of 45 holes (a surface fraction 12.2%): Propagation of the crack for the different regularization lengths l : (a) $l=0.1\text{mm}$, $U=0.0545\text{mm}$; (b) $l=0.14\text{mm}$, $U=0.0542\text{mm}$; (c) $l=0.16\text{mm}$, $U=0.0534\text{mm}$; (d) $l=0.2\text{mm}$, $U=0.0530\text{mm}$; (e) [34].

The evolutions of microcracking onset in the first holes for different values of l within the plate with 45 holes are depicted from Fig.1.14a to Fig.1.14d and those within the plate containing 60 holes are shown from Fig.1.19a to Fig.1.19d. In these plates, the cracks are initiated first from the holes near two free lateral sides of the plates and then from the holes in the central zone. This is probably because of the deformations near the left and right sides are larger than in the remaining zone. As can be seen, the directions of the cracks tend to develop vertically from holes, as shown in Fig.1.15 with the plate containing 45 holes and in Fig.1.20 with the plate containing 60 holes. Next, we analyze the cracks propagate until full fracture in the plate containing 45 holes. In Fig.1.16

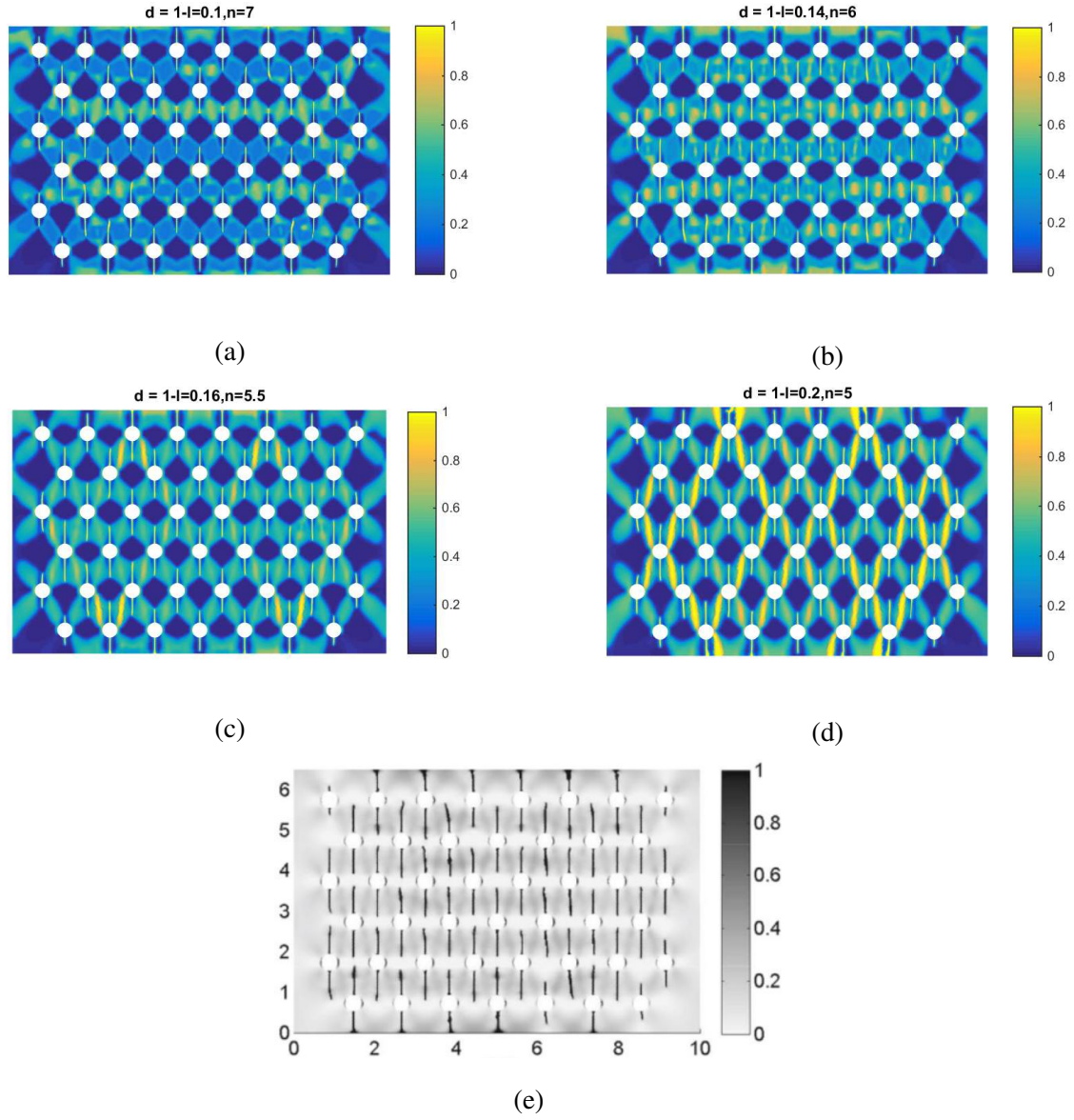


Figure 1.17: Compression test of a plate containing a periodic distribution of 45 holes (surface fraction 12.2%): Propagation of the crack for the different regularization lengths l : (a) $l=0.1\text{mm}$, $U=0.056\text{mm}$; (b) $l=0.14\text{mm}$, $U=0.0552\text{mm}$; (c) $l=0.16\text{mm}$, $U=0.055\text{mm}$; (d) $l=0.2\text{mm}$, $U=0.0543\text{mm}$; (e) [34].

and Fig.1.17, the microcrack propagation with the different values of l are similar to those reported by [34], which are depicted in Fig.1.16e and Fig.1.17e. But, when $l=0.2\text{mm}$, damage around holes propagates faster in comparison with the cases associated to the remaining values of l depicted in Fig. 16d and Fig.1.17d. This phenomenon also occurs similarly in the plate containing 60 holes (see in Fig.1.20 and Fig.1.21, respectively). The results in the Fig.1.20a to Fig.1.20d with the proposed numerical method are in very good agreement with the results of [34] in Fig.1.20e and digital image obtained of [37] in Fig.1.20f.

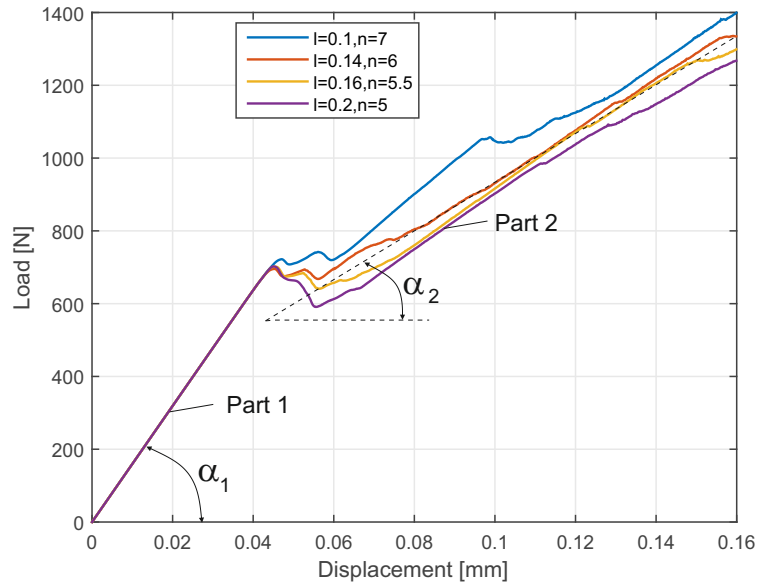


Figure 1.18: Compression test of a plate containing a periodic distribution of 45 holes (surface fraction 12.2%): Load- displacement curves for the different regularization length l

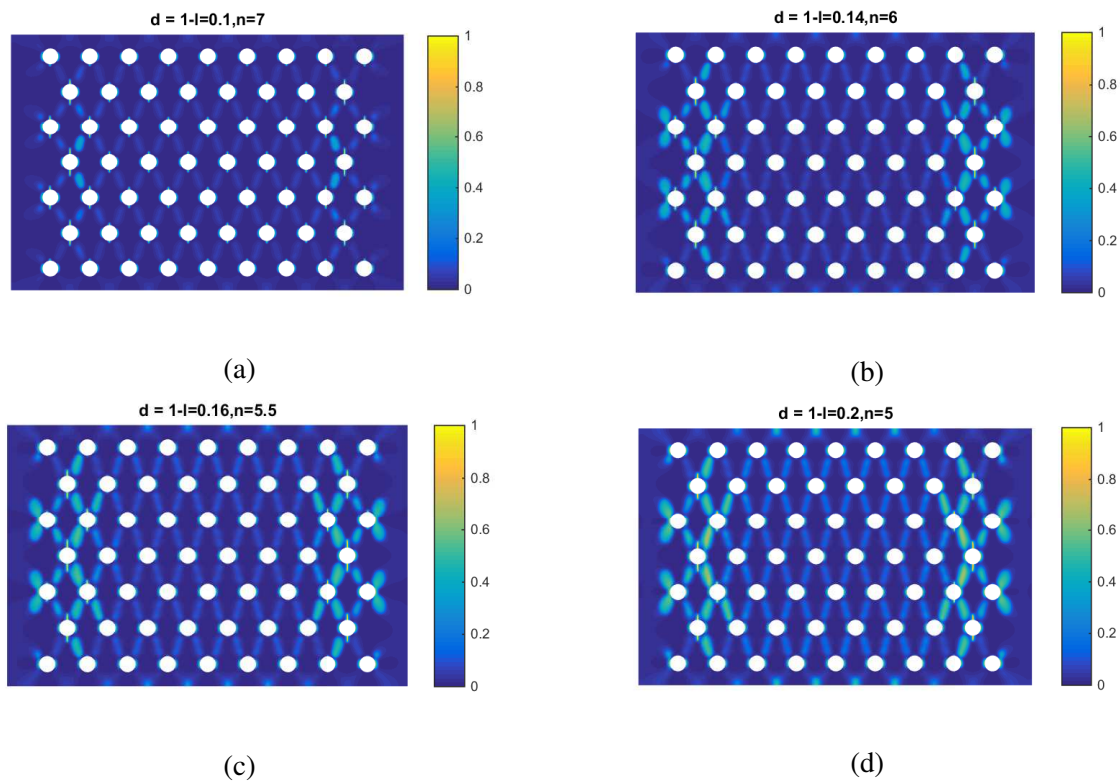


Figure 1.19: Compression test of a plate containing a periodic distribution of 60 holes (surface fraction 13.5%): evolution of the crack onset in the first hole for the different regularization lengths l : (a) $l=0.1\text{mm}$, $U=0.0442\text{mm}$; (b) $l=0.14\text{mm}$, $U=0.0443\text{mm}$; (c) $l=0.16\text{mm}$, $U=0.0450\text{mm}$; (d) $l=0.2\text{mm}$, $U=0.0452\text{mm}$

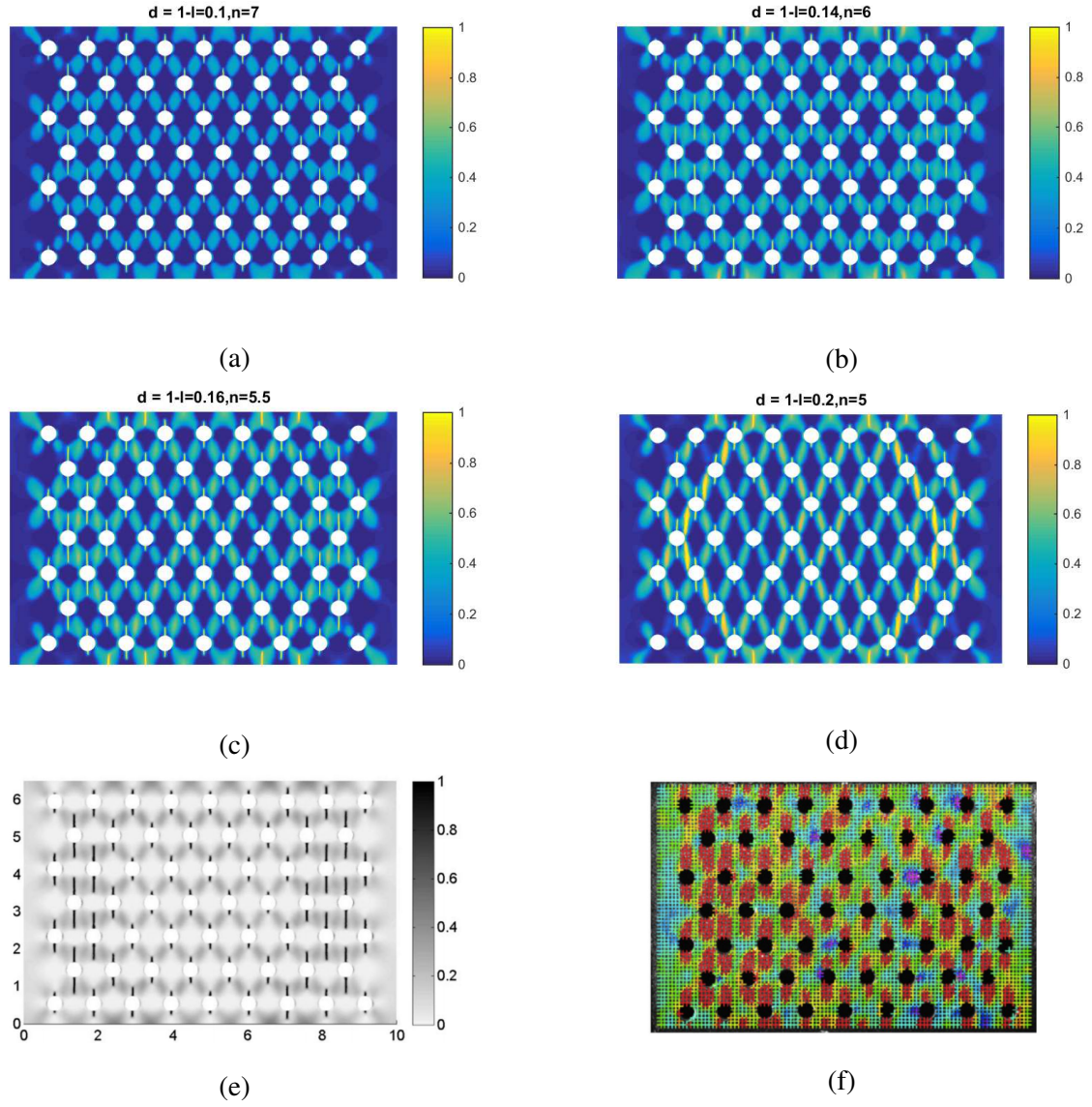


Figure 1.20: Compression test of a plate containing a periodic distribution of 60 holes (surface fraction 13.5%): Propagation of the crack for the different regularization lengths l : (a) $l=0.1\text{mm}$, $U=0.049\text{mm}$; (b) $l=0.14\text{mm}$, $U=0.049\text{mm}$; (c) $l=0.16\text{mm}$, $U=0.049\text{mm}$; (d) $l=0.2\text{mm}$, $U=0.0485\text{mm}$; (e) [34]; (f) provided in [37].

The load-displacement curves for different values of l are presented in Fig.1.18 for the specimen containing 45 holes and in Fig.1.22 for the specimen containing 60 holes. We can observe that the material mechanical behaviors are linearly elastic until the first crack appears. Then, the overall mechanical properties of the structure are reduced through the inclination angle α_2 of the second part of the load-displacement curve ($\alpha_2 < \alpha_1$). In other words, after the appearance of the first crack, the deformations of the structure during the loading process increase faster until full damage. These phenomena are relatively similar when using the different values of l .

Finally, we compare the numerical stress values of σ^* for two samples containing 45 holes and 60

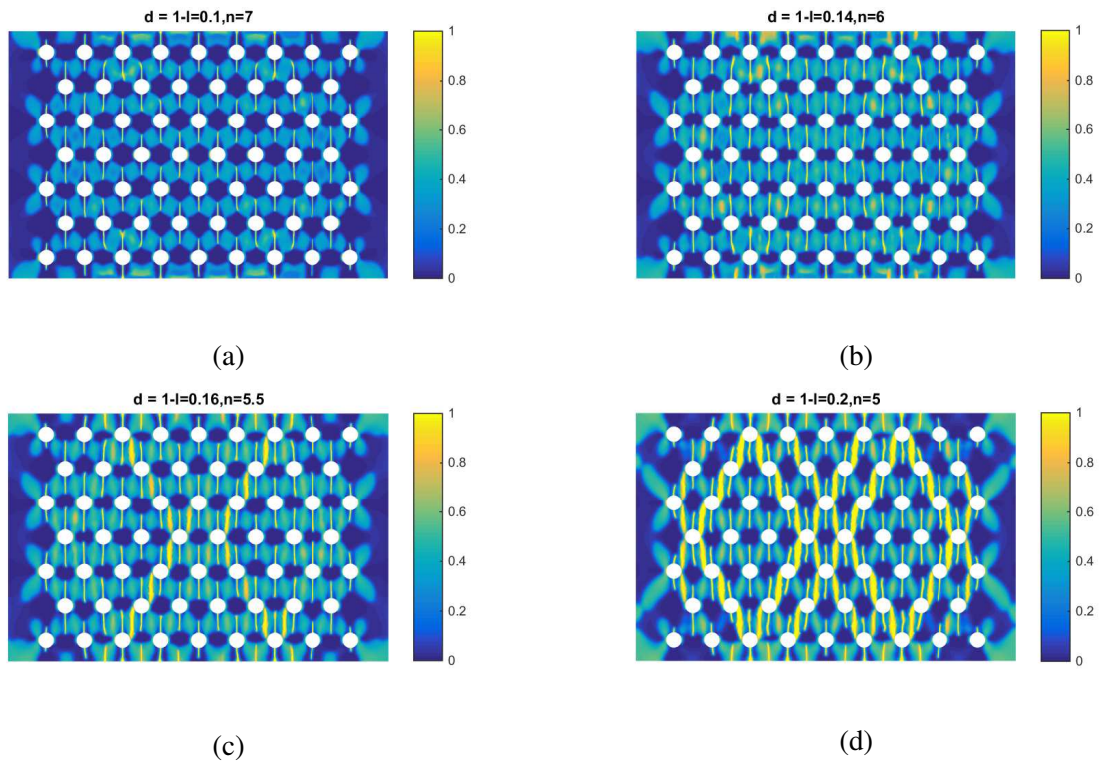


Figure 1.21: Compression test of a plate containing a periodic distribution of 60 holes (surface fraction 13.5%): evolution of the crack for the different regularization lengths l : (a) $l=0.1\text{mm}$, $U=0.0517\text{mm}$; (b) $l=0.14\text{mm}$, $U=0.0515\text{mm}$; (c) $l=0.16\text{mm}$, $U=0.0515\text{mm}$; (d) $l=0.2\text{mm}$, $U=0.0515\text{mm}$;

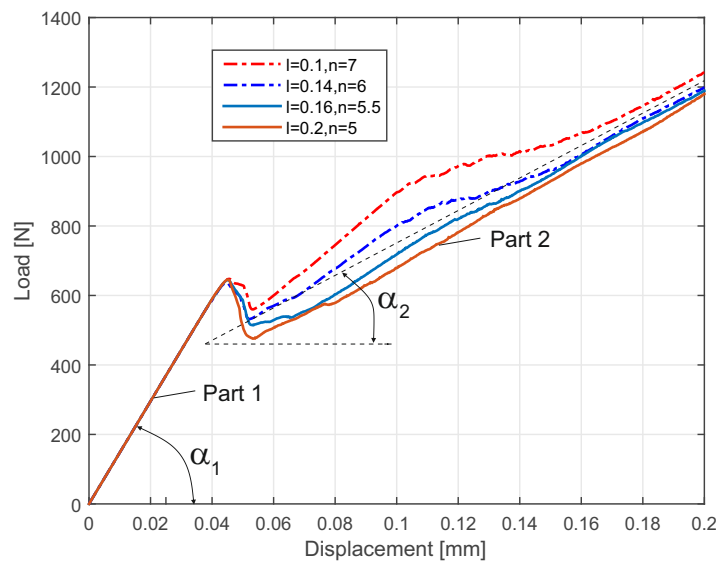


Figure 1.22: Compression test of a plate containing a periodic distribution of 60 holes (surface fraction 13.5%): Load- displacement curves for the different regularization lengths l

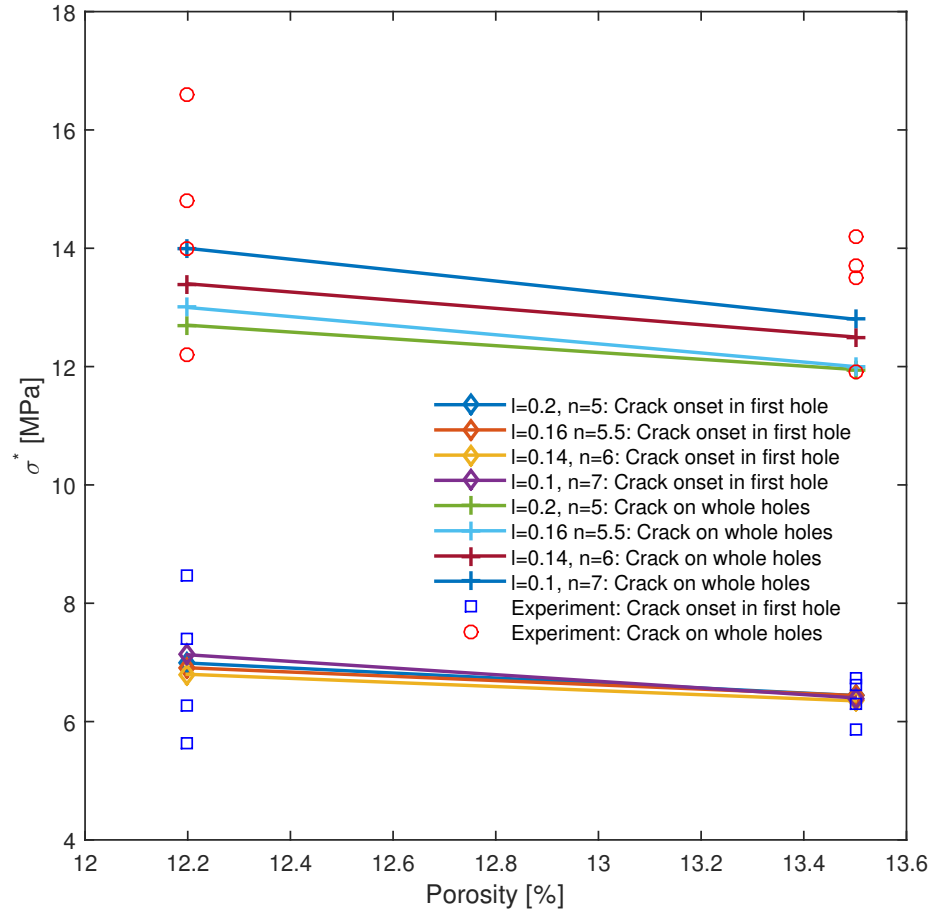


Figure 1.23: Critical axial stress σ^* when the cracks onset: comparison between experimental values and numerical values for two surface fractions of the holes (12.2% and 13.5%)

holes with the relevant experimental results provided in [37]. In the numerical simulations, use is made of four pairs of l and n for each sample. We can see that all the numerical values of σ^* obtained are in good agreement with the experimental values in [37]. Comparisons are provided in Fig.1.23. This demonstrates the present numerical method is valid for the samples containing a periodic distribution of holes.

1.5.4 Compression test of a microstructure with uniformly distributed holes

In the last example, the length parameter l is considered as a pure numerical parameter of the regularized model of brittle fracture instead of a material parameter for a gradient damage model. This consists in taking l as small as possible to fit the selected mesh size. For this purpose, we consider a microstructure whose dimensions are 3x2mm with the material parameters are provided

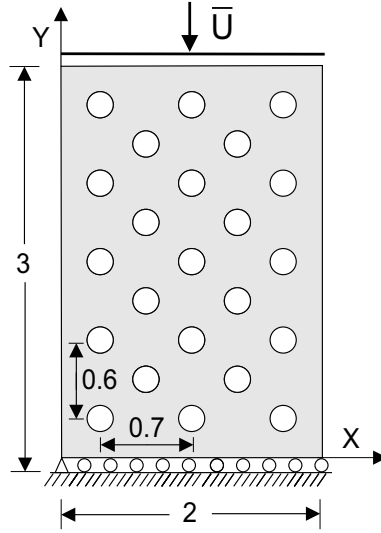


Figure 1.24: Compression test of a plate with uniformly distributed holes: geometry and loading conditions.

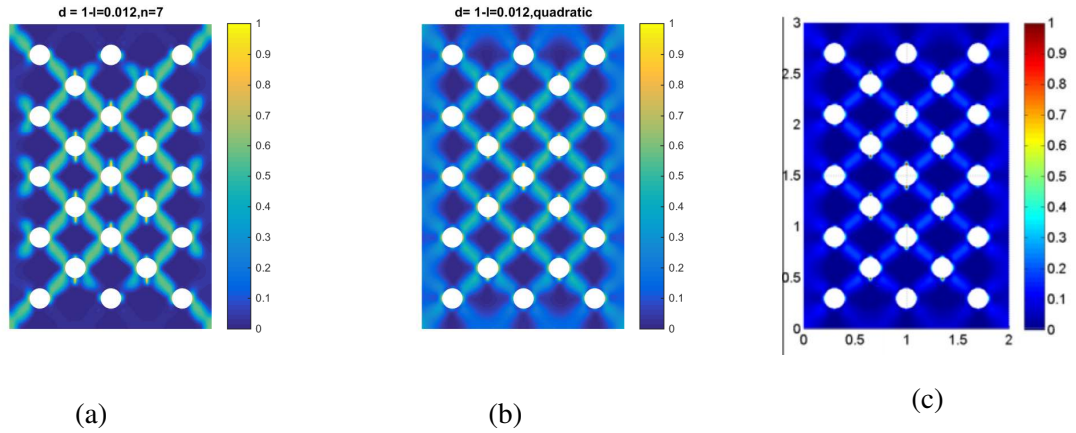


Figure 1.25: Compression test of a plate with uniformly distributed holes: evolution of the crack onset in the first hole: (a) $l=0.012\text{mm}$, $n=7$, $U=0.0053\text{mm}$; (b) $l=0.012\text{mm}$, the quadratic degradation function, $U=0.0055\text{mm}$; (c) [18]

in [36] and [37]. This structure contains 23 holes of diameter $D=0.2\text{mm}$ and the boundary conditions of the structure are presented in Fig.1.24. Constant compression displacement increments of $\Delta u=-10^{-4}\text{mm}$ are prescribed until d reaches 0.9 at the expected crack onset element, and then we use $\Delta u=-3\times 10^{-5}\text{mm}$ until full fracture. The element sizes vary from $h_{min}=0.006\text{mm}$ to $h_{max}=0.01\text{mm}$. Here, the value of $l=0.012\text{mm}$, $n=7$ for the new degradation functions and $l=0.012\text{mm}$ for the quadratic degradation function.

The crack nucleation and propagation are shown in Fig.1.25 to Fig.1.27 with the comparison of the crack paths when using the new degradation functions in [6], the quadratic degradation function in

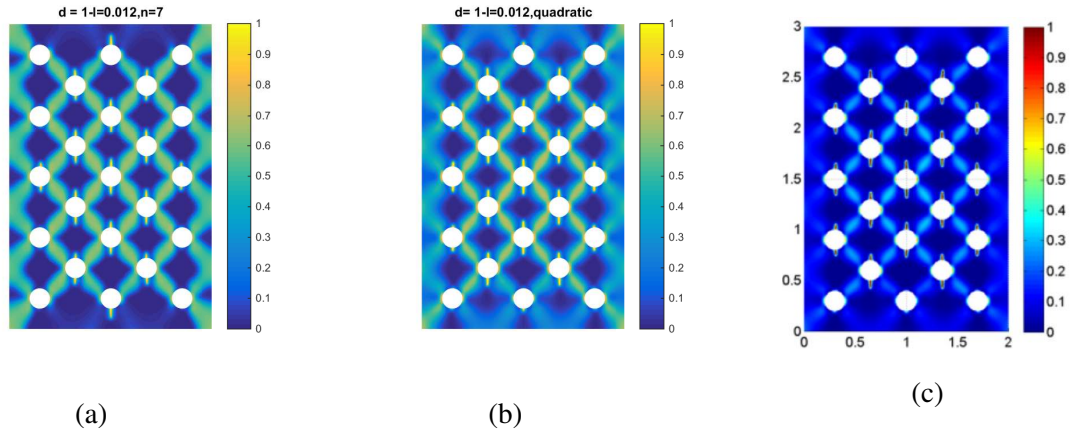


Figure 1.26: Compression test of a plate with uniformly distributed holes: propagation of the crack: (a) $l=0.012\text{mm}$, $n=7$, $U=0.0068\text{mm}$; (b) $l=0.012\text{mm}$, the quadratic degradation function, $U=0.0068\text{mm}$; (c) [18]

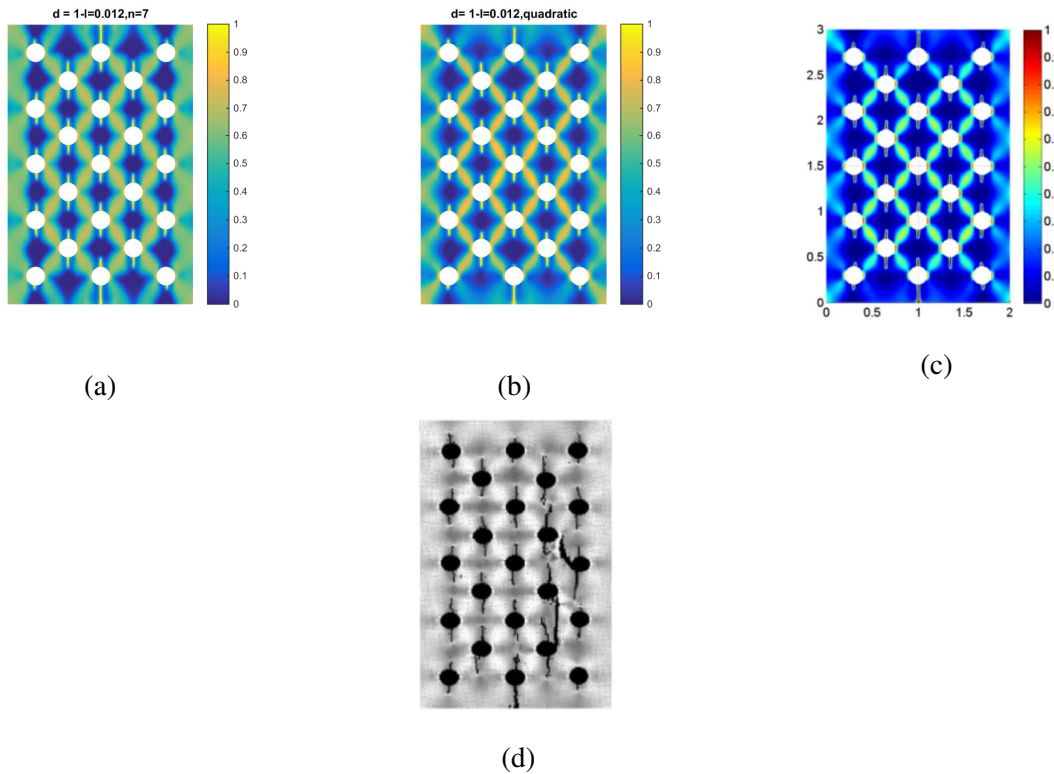


Figure 1.27: Compression test of a plate with uniformly distributed holes: Propagation of the crack: (a) $l=0.012\text{mm}$, $n=7$, $U=0.00872\text{mm}$; (b) $l=0.012\text{mm}$, the quadratic degradation function, $U=0.008\text{mm}$; (c) in [18]; (d) solved by $MFPA^{2D}$ simulation in [38]

[34] and the results in [18]. In particular, the results of three numerical modelings are compared to the $MFPA^{2D}$ simulation result in [38] (see Fig.1.27).

Fig.1.28 displays the load-displacement curves for $l = 0.012\text{mm}$, $n=7$ with the marked points corresponding to the steps depicted in Fig.1.25, Fig.1.26 and Fig.1.27. As expected the mechanical

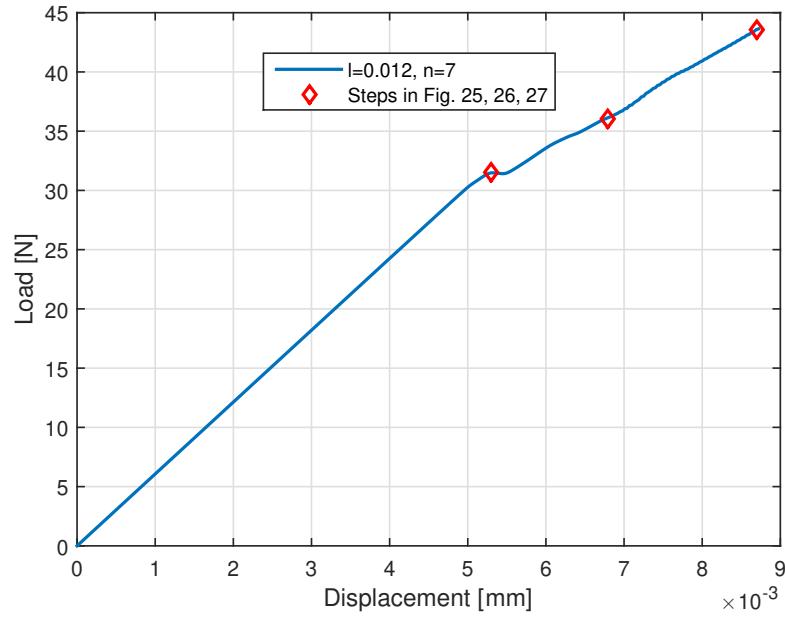


Figure 1.28: *Compression test of a plate with uniformly distributed holes: Load- displacement curves with a pair of $l=0.012\text{mm}$, $n=7$*

response is linearly elastic until the appearance of the first crack and the peak loads are similar to the relevant results reported in [37].

1.6 Conclusions

In this chapter, we use the phase-field method in combination with the new family of degradation functions in [6] to determine the regularization length l on the basis of the experimental results reported in [36] and [37]. Through several examples, the effects of the numerical parameters (loading step, mesh size) are studied. The determined values of l together with the specified parameters n give rise to relatively good convergent behavior.

By others examples such as three point bending un-notched beam and drilled holes samples of plaster in compression, with l satisfied $l \geq 0.1\text{mm}$, we have obtained the critical stresses and crack propagation similar to those in [34] and in good agreement with the experimental results [36] and [37]. Note that, in [34], only one value $l = 0.1\text{mm}$ was used. The greater value of l without affecting the material response allows saving computational time.

Thus, the phase-field method with the new family of degradation functions in [6] turns out to be efficient for predicting the initiation and propagation of cracks in brittle heterogeneous materials.

Chapter 2

Phase-field modeling with strain orthogonal decompositions for the modeling and simulation of isotropic and anisotropic damage

2.1 Abstract

The phase-field method is able to model and simulate complex cracks initiation, branching and propagation in solids. Concerning brittle and quasi-brittle materials, an important problem is to decompose the strain tensor into a positive part and a negative part so as to account the fact that they behave differently in tension and compression. To handle this problem, recent works have proposed some methods of splitting the total strain into two parts. But these decompositions have the shortcoming that they are not orthogonal in the sense of the strain-energy norm, even when the elastic tensor is isotropic. This problem leads, in particular, to the inaccuracy in modeling and simulating the damaged material mechanical response. To solve the problem, a recent theoretical study of He [39] proposed novel orthogonal decompositions for the strain and stress tensor, which preserve the strain- or stress-energy. Adopting the approach of He [39], we develop the phase field method so as to thoroughly solve the afoementioned drawback. In the present work, two proposed solutions related to the strain orthogonal decompositions are presented to model isotropic and anisotropic fracture through several numerical examples.

2.2 Introduction

Brittle and quasi-brittle materials constitute an important class of materials for civil engineering. Determination of the strength, as well as the initiation and propagation of cracks in these materials is very important.

Fracture mechanics, based on the pioneer work of Griffith [7] was in particularly developed by Irwin [40] and Rice [41]. The phase-field method proposed in the works such as [9, 10, 11, 13, 14, 15, 16] rely on a regularized description of discontinuities. The variational principle of fracture is based on a global minimization of the total free energy of materials with cracks proposed by Francfort and Marigo [8].

The length parameter l in the smeared approximation of discontinuities was proposed and determined in the works [20, 24, 25, 27, 34, 35]. The influence of length parameter l on the mechanical behavior of materials was studied. In [6, 16, 42, 43], the degradation functions were introduced to improve the accuracy of the phase-field method in predicting critical stress and crack nucleation in solid.

In fact, brittle and quasi-brittle materials in tension and compression behave differently in tension and compression. This problem appear clearly in masonry-like and ceramics-like materials [44, 45] and composite media such as glass-epoxy, graphite-epoxy composites [46, 47] as well as carbon-epoxy ones [48, 49]. Moreover, this tension-compression asymmetry is observed in other materials such as bones [50, 51], concrete [19, 52, 53], coke blend [54].

To model the asymmetric tension-compression behavior, decomposing the strain (or stress) tensor into a positive part and a negative part has been suggested in the recent works. In [33, 55], decomposition of the strain tensor into deviatoric and spheric parts was adopted. Precisely, this means that it mean when crack growth is driven also by the positive spherical part of the strain tensor. Typically, within the linear elasticity framework, the strain energy density function Ψ of a material at an undamaged state takes the classical form:

$$\Psi(\boldsymbol{\varepsilon}) = \frac{1}{2} \boldsymbol{\varepsilon} : (\mathbb{C} \boldsymbol{\varepsilon}) = \frac{1}{2} \varepsilon_{ij} : (C_{ijkl} \varepsilon_{kl}) \quad (2.1)$$

where $\boldsymbol{\varepsilon}$ is the infinitesimal strain tensor and \mathbb{C} is the forth-order elastic stiffness tensor of the undamaged material, which has the minor and major symmetries. Decomposition of the strain tensor $\boldsymbol{\varepsilon}$ into a positive part $\boldsymbol{\varepsilon}^+$ and a negative part $\boldsymbol{\varepsilon}^-$ gives:

$$\boldsymbol{\varepsilon} = \boldsymbol{\varepsilon}^+ + \boldsymbol{\varepsilon}^- \quad (2.2)$$

Introducing the decomposition (2.2) into (2.1) and accounting for the major symmetry of the elastic tensor of \mathbb{C} , we obtain

$$\Psi(\boldsymbol{\varepsilon}) = \Psi(\boldsymbol{\varepsilon}^+ + \boldsymbol{\varepsilon}^-) = \frac{1}{2}\boldsymbol{\varepsilon}^+ : (\mathbb{C}\boldsymbol{\varepsilon}^+) + \frac{1}{2}\boldsymbol{\varepsilon}^- : (\mathbb{C}\boldsymbol{\varepsilon}^-) + \boldsymbol{\varepsilon}^+ : (\mathbb{C}\boldsymbol{\varepsilon}^-). \quad (2.3)$$

From (2.3), it follows immediately that the strain energy decomposition

$$\Psi(\boldsymbol{\varepsilon}) = \Psi^+(\boldsymbol{\varepsilon}) + \Psi^-(\boldsymbol{\varepsilon}) = \Psi(\boldsymbol{\varepsilon}^+) + \Psi(\boldsymbol{\varepsilon}^-) = \frac{1}{2}\boldsymbol{\varepsilon}^+ : (\mathbb{C}\boldsymbol{\varepsilon}^+) + \frac{1}{2}\boldsymbol{\varepsilon}^- : (\mathbb{C}\boldsymbol{\varepsilon}^-) \quad (2.4)$$

holds if and only if

$$\boldsymbol{\varepsilon}^+ : (\mathbb{C}\boldsymbol{\varepsilon}^-) = 0 \quad \text{or} \quad (\mathbb{C}^{1/2}\boldsymbol{\varepsilon}^+) : (\mathbb{C}^{1/2}\boldsymbol{\varepsilon}^-) = 0 \quad (2.5)$$

shows that (2.4) is satisfied if and only if $\boldsymbol{\varepsilon}^+$ is orthogonal to $\boldsymbol{\varepsilon}^-$ in the sense of the inner product with \mathbb{C} acting as a metric tensor. Next, using a scalar phase-field variable d to describe the damage state of the material (see, e.g., [16]), the elastic strain energy density function W_u of the damaged material can be written as

$$W_u(\boldsymbol{\varepsilon}, d) = \Psi^+(\boldsymbol{\varepsilon})\{g(d) + k\} + \Psi^-(\boldsymbol{\varepsilon}) = \Psi(\boldsymbol{\varepsilon}^+)\{g(d) + k\} + \Psi(\boldsymbol{\varepsilon}^-) \quad (2.6)$$

where $g(d) = (1 - d)^2$ is the damage degradation function in the phase field methods for fracture and k is a very small value to maintain the well-posedness of the problem.

In most of the recent works of phase-field method on brittle and quasi-brittle materials (see, e.g., [8, 9, 10, 11, 13, 14, 15, 16, 18]), the decomposition of the strain tensor into a positive part and a negative part does not verify the orthogonality condition (2.5), even when the elastic stiffness tensor \mathbb{C} is isotropic. Further, when the elastic stiffness tensor \mathbb{C} is anisotropic (see, e.g., [56, 57, 58, 59]), few additive decompositions of $\boldsymbol{\varepsilon}$ into $\boldsymbol{\varepsilon}^+$ and $\boldsymbol{\varepsilon}^-$ have been proposed in the literature, and the orthogonality condition (2.5) is not verified in this case.

The principal features of the present work are listed as follows: (a) the orthogonality condition (2.5) holds: in the elastic isotropic case, and in the orthotropic case; (b) only one damage variable d instead of multiple damage variables d_i for anisotropic materials; (c) the crack patterns which are described by the phase field variable d are stable due to its inherent gradient-based expression.

The present chapter is organized as follows: Section 2.3 presents the phase-field method which is employed to simulate the crack propagation in isotropic and anisotropic materials. In Section 2.4, several numerical examples are provided. Finally, conclusions and perspectives are given in Section 2.5.

2.3 Phase-field modeling for the fracture of brittle and quasi-brittle materials

In this section, we describe the phase-field method for modeling and simulating the crack nucleation and propagation in isotropic and anisotropic materials with the use of the strain orthogonal decomposition method of [39].

2.3.1 Smearred approximation of free discontinuities

Let $\Omega \in \mathbb{R}^{\mathcal{D}}$ be an open domain describing a cracked solid, with $\mathcal{D} \in [2, 3]$ being the space dimension and $\partial\Omega \in \mathbb{R}^{\mathcal{D}-1}$ the external boundary of Ω . Let Γ be the crack propagating within Ω (see., Fig.2.1 and Fig.2.2). In a regularized framework, the geometry of a propagating crack is approximated by a scalar parameter $d(\mathbf{x})$, with $\mathbf{x} \in \Omega$. The scalar field $d(\mathbf{x})$ is governed by the following equations defined in Ω (see e.g. [16]):

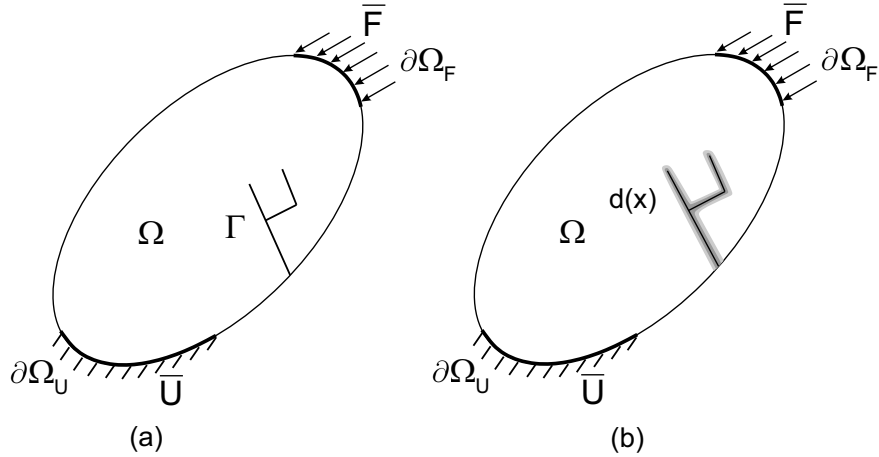


Figure 2.1: Regularized representation of a crack: two-dimensional case: (a) sharp crack model; (b) regularized representation through phase field.

$$\begin{cases} d - l^2 \Delta d = 0 & \text{in } \Omega \\ d(\mathbf{x}) = 1 & \text{on } \Gamma \\ \nabla d(\mathbf{x}) \cdot \mathbf{n} = 0 & \text{on } \partial\Omega \end{cases} \quad (2.7)$$

where Δd is the Laplacian operator, l is the length parameter, and \mathbf{n} is the unit outward normal vector to the external boundary $\partial\Omega$. Equations (2.7) can be seen as the Euler-lagrange ones associated

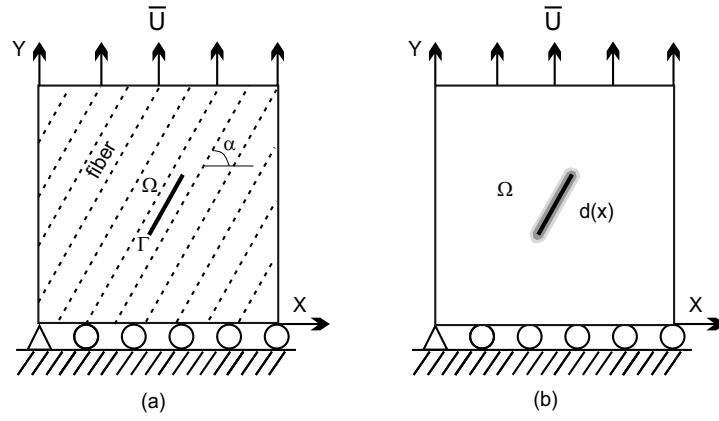


Figure 2.2: Regularized representation of a crack: (a) sharp cracks in an orthotropic material (dashed lines indicate material orthotropy direction), (b) regularized representation through phase field.

with the variational problem

$$d(\mathbf{x}, t) = \text{Arg}\{\inf_{d \in \mathcal{S}_d} \Gamma(d)\}, \quad \Gamma(d) = \int_{\Omega} \gamma(d, \nabla d, \boldsymbol{\omega}) d\Omega, \quad (2.8)$$

Above, $\Gamma(d)$ is the total crack length per unit area in the two-dimensional case (the 2D case) and total crack surface area per unit volume in the three-dimensional case (the 3D case), and $\mathcal{S}_d = \{d | d(\mathbf{x}) = 1 \text{ on } \Gamma, \forall \mathbf{x} \in \Gamma\}$. In (2.8), $\gamma(d, \nabla d, \boldsymbol{\omega})$ is the crack surface density function of per unit volume defined by

$$\gamma(d, \nabla d, \boldsymbol{\omega}) = \frac{d^2}{2l} + \frac{l}{2} \boldsymbol{\omega} : (\nabla d \otimes \nabla d). \quad (2.9)$$

where $\boldsymbol{\omega}$ is a second-order orientation tensor defined by

$$\boldsymbol{\omega} = \mathbf{I} + \eta(\mathbf{I} - \mathbf{m} \otimes \mathbf{m}) \quad (2.10)$$

here, $\boldsymbol{\omega}$ is calculated from (2.10) corresponding to each preferential cleavage plane (depending on the unit vector normal \mathbf{m} and anisotropic coefficient η), $\mathbf{I} = \mathbf{1} \otimes \mathbf{1}$ with $\mathbf{1}$ is the identity tensor. Here, $\eta \gg 0$ is used to penalize the damage on planes not normal to \mathbf{m} in the anisotropic material. Therefore, when let $\eta = 0$, we have the isotropic material.

2.3.2 Phase field and displacement problems

Energy functional

The total energy of the solid body is defined by:

$$E(\mathbf{u}, d) = \int_{\Omega} W_u(\boldsymbol{\varepsilon}(\mathbf{u}), d) d\Omega + \int_{\Omega} g_c \gamma(d, \nabla d, \boldsymbol{\omega}) d\Omega \quad (2.11)$$

where g_c is the fracture toughness. The total energy can be rewritten as $E = \int_{\Omega} W d\Omega$ with

$$W(\mathbf{u}, d) = W_u(\boldsymbol{\varepsilon}(\mathbf{u}), d) + g_c \gamma(d, \nabla d, \boldsymbol{\omega}). \quad (2.12)$$

The strain energy function W_u in (2.12) is given by:

$$W_u(\boldsymbol{\varepsilon}(\mathbf{u}), d) = \Psi^+(\boldsymbol{\varepsilon})\{g(d) + k\} + \Psi^-(\boldsymbol{\varepsilon}) = \Psi(\boldsymbol{\varepsilon}^+)\{g(d) + k\} + \Psi(\boldsymbol{\varepsilon}^-) \quad (2.13)$$

To satisfy the orthogonal condition (2.5), we shall use the general approach proposed recently [39].

Let the transformed strain space $\tilde{\mathcal{E}}$ be split into two convex subsets $\tilde{\mathcal{K}}^+$ and $\tilde{\mathcal{K}}^-$ such that

$$\tilde{\mathcal{E}} = \tilde{\mathcal{K}}^+ \oplus \tilde{\mathcal{K}}^- \quad (2.14)$$

This means that any element $\tilde{\boldsymbol{\varepsilon}} \in \tilde{\mathcal{E}}$ can be decomposed into a positive part $\tilde{\boldsymbol{\varepsilon}}^+ \in \tilde{\mathcal{K}}^+$ and a negative part $\tilde{\boldsymbol{\varepsilon}}^- \in \tilde{\mathcal{K}}^-$ such that

$$\tilde{\boldsymbol{\varepsilon}} = \tilde{\boldsymbol{\varepsilon}}^+ + \tilde{\boldsymbol{\varepsilon}}^- \quad (2.15)$$

$$\tilde{\boldsymbol{\varepsilon}}^+ : \tilde{\boldsymbol{\varepsilon}}^- = 0. \quad (2.16)$$

Moreover, we require that $\tilde{\boldsymbol{\varepsilon}}^+$ and $\tilde{\boldsymbol{\varepsilon}}^-$ be the projections of a given $\tilde{\boldsymbol{\varepsilon}} \in \tilde{\mathcal{E}}$ on $\tilde{\mathcal{K}}^+$ and $\tilde{\mathcal{K}}^-$ in the variational sense that

$$\|\tilde{\boldsymbol{\varepsilon}} - \tilde{\boldsymbol{\varepsilon}}^\pm\|^2 = \min_{\tilde{\boldsymbol{\varepsilon}} \in \tilde{\mathcal{K}}^\pm} (\tilde{\boldsymbol{\varepsilon}} - \tilde{\boldsymbol{\varepsilon}}) : (\tilde{\boldsymbol{\varepsilon}} - \tilde{\boldsymbol{\varepsilon}}). \quad (2.17)$$

The convex subsets $\tilde{\mathcal{K}}^+$ and $\tilde{\mathcal{K}}^-$ in the right part of (2.14) are not unique and have to be chosen according to what we mean by "tension" and "compression" in the two- or three-dimensional case.

We consider two following cases:

Case 1 : $\tilde{\mathcal{K}}^+$ and $\tilde{\mathcal{K}}^-$ are defined by:

$$\tilde{\mathcal{K}}^+ = \{\tilde{\boldsymbol{\varepsilon}} \in \tilde{\mathcal{E}} | \text{Tr}(\tilde{\boldsymbol{\varepsilon}}) \geq 0\} \quad \text{and} \quad \tilde{\mathcal{K}}^- = \{\tilde{\boldsymbol{\varepsilon}} \in \tilde{\mathcal{E}} | \tilde{\boldsymbol{\varepsilon}} = a\mathbf{1}, a \leq 0\} \quad (2.18)$$

It can be shown from (2.17) and (2.18) that

$$\tilde{\boldsymbol{\varepsilon}}^+ = \frac{1}{\mathcal{D}} \langle \text{Tr}(\tilde{\boldsymbol{\varepsilon}}) \rangle_+ \mathbf{1} + \tilde{\boldsymbol{\varepsilon}}^D, \quad \tilde{\boldsymbol{\varepsilon}}^- = \frac{1}{\mathcal{D}} \langle \text{Tr}(\tilde{\boldsymbol{\varepsilon}}) \rangle_- \mathbf{1} \quad (2.19)$$

where $\mathbf{1}$ denotes the \mathcal{D} -dimensional identity tensor, $\langle x \rangle_\pm = (x \pm |x|)/2$ and the deviatoric strain tensor is defined by

$$\tilde{\boldsymbol{\varepsilon}}^D = \tilde{\boldsymbol{\varepsilon}} - \frac{1}{\mathcal{D}} \text{Tr}(\tilde{\boldsymbol{\varepsilon}}) \mathbf{1}. \quad (2.20)$$

Once $\tilde{\varepsilon}^+$ and $\tilde{\varepsilon}^-$ have been obtained, ε^+ and ε^- can be directly determined by

$$\varepsilon^+ = \mathbf{C}^{-1/2} \tilde{\varepsilon}^+, \quad \varepsilon^- = \mathbf{C}^{-1/2} \tilde{\varepsilon}^- \quad (2.21)$$

and we obtain

$$\Psi^+(\varepsilon^+) = \frac{1}{2} \mathbf{C} : \varepsilon^+ : \varepsilon^+ = \frac{1}{2} \left\{ \frac{1}{\mathcal{D}} \langle \text{Tr}(\tilde{\varepsilon}) \rangle_{+1} + \tilde{\varepsilon}^D \right\} : \left\{ \frac{1}{\mathcal{D}} \langle \text{Tr}(\tilde{\varepsilon}) \rangle_{+1} + \tilde{\varepsilon}^D \right\}, \quad (2.22)$$

$$\Psi^-(\varepsilon^-) = \frac{1}{2} \mathbf{C} : \varepsilon^- : \varepsilon^- = \frac{1}{2} \left\{ \frac{1}{\mathcal{D}} \langle \text{Tr}(\tilde{\varepsilon}) \rangle_{-1} \right\} : \left\{ \frac{1}{\mathcal{D}} \langle \text{Tr}(\tilde{\varepsilon}) \rangle_{-1} \right\}. \quad (2.23)$$

where, \mathbf{C} is the elastic stiffness matrix form corresponding to the tensor \mathbb{C} . In our present work, we use matrix \mathbf{C} which respects to the Voigt notation.

Here, we have the relation between strain and stress tensor, i.e., $\boldsymbol{\sigma} = \mathbf{C} : \boldsymbol{\varepsilon}$ or $\boldsymbol{\varepsilon} = \mathbf{L} : \boldsymbol{\sigma}$, with \mathbf{L} is the elastic compliance matrix. Matrix \mathbf{C} or matrix \mathbf{L} is determined depending on the types of material as follows:

- Isotropic case

In the 3D case, the elastic stiffness matrix \mathbf{C} is defined by:

$$\begin{bmatrix} \sigma_{11} \\ \sigma_{22} \\ \sigma_{33} \\ \sigma_{23} \\ \sigma_{13} \\ \sigma_{12} \end{bmatrix} = \begin{bmatrix} \lambda + 2\mu & \lambda & \lambda & 0 & 0 & 0 \\ \lambda & \lambda + 2\mu & \lambda & 0 & 0 & 0 \\ \lambda & \lambda & \lambda + 2\mu & 0 & 0 & 0 \\ 0 & 0 & 0 & \mu & 0 & 0 \\ 0 & 0 & 0 & 0 & \mu & 0 \\ 0 & 0 & 0 & 0 & 0 & \mu \end{bmatrix} \begin{bmatrix} \varepsilon_{11} \\ \varepsilon_{22} \\ \varepsilon_{33} \\ 2\varepsilon_{23} \\ 2\varepsilon_{13} \\ 2\varepsilon_{12} \end{bmatrix} \quad (2.24)$$

In the 2D case, the elastic stiffness matrix \mathbf{C} is obtained:

$$\begin{bmatrix} \sigma_{11} \\ \sigma_{22} \\ \sigma_{12} \end{bmatrix} = \begin{bmatrix} \lambda + 2\mu & \lambda & 0 \\ \lambda & \lambda + 2\mu & 0 \\ 0 & 0 & \mu \end{bmatrix} \begin{bmatrix} \varepsilon_{11} \\ \varepsilon_{22} \\ 2\varepsilon_{12} \end{bmatrix} \quad (2.25)$$

Here, λ and μ are Lamé's coefficients.

- Orthotropic case

In the 3D case, the elastic compliance matrix \mathbf{L} is determined:

$$\begin{bmatrix} \varepsilon_{11} \\ \varepsilon_{22} \\ \varepsilon_{33} \\ 2\varepsilon_{23} \\ 2\varepsilon_{13} \\ 2\varepsilon_{12} \end{bmatrix} = \begin{bmatrix} \frac{1}{E_1} & -\frac{\nu_{21}}{E_2} & -\frac{\nu_{31}}{E_3} & 0 & 0 & 0 \\ -\frac{\nu_{12}}{E_1} & \frac{1}{E_2} & -\frac{\nu_{32}}{E_3} & 0 & 0 & 0 \\ -\frac{\nu_{13}}{E_1} & -\frac{\nu_{23}}{E_2} & \frac{1}{E_3} & 0 & 0 & 0 \\ 0 & 0 & 0 & \frac{1}{G_{23}} & 0 & 0 \\ 0 & 0 & 0 & 0 & \frac{1}{G_{13}} & 0 \\ 0 & 0 & 0 & 0 & 0 & \frac{1}{G_{12}} \end{bmatrix} \begin{bmatrix} \sigma_{11} \\ \sigma_{22} \\ \sigma_{33} \\ \sigma_{23} \\ \sigma_{13} \\ \sigma_{12} \end{bmatrix} \quad (2.26)$$

In the 2D case, the elastic compliance matrix \mathbf{L} is written:

$$\begin{bmatrix} \varepsilon_{11} \\ \varepsilon_{22} \\ 2\varepsilon_{12} \end{bmatrix} = \begin{bmatrix} \frac{1}{E_1} & -\frac{\nu_{21}}{E_2} & 0 \\ -\frac{\nu_{12}}{E_1} & \frac{1}{E_2} & 0 \\ 0 & 0 & \frac{1}{G_{12}} \end{bmatrix} \begin{bmatrix} \sigma_{11} \\ \sigma_{22} \\ \sigma_{12} \end{bmatrix} \quad (2.27)$$

In the orthotropic case, the elastic compliance matrix is written with respect to the symmetry planes defined by their unit normal vectors \mathbf{e}_1 , \mathbf{e}_2 and \mathbf{e}_3 . Here, in the case of a unidirectional fiber-reinforced composite ply (see., Fig.2.2), E_1 , E_2 and E_3 are the Young moduli along with the directions \mathbf{e}_1 , \mathbf{e}_2 and \mathbf{e}_3 , respectively; ν_{ij} are the Poisson's ratios and G_{ij} are the shear moduli.

According to [60], the transformation matrix \mathbf{P} in the 3D case is written:

$$\mathbf{P} = \begin{bmatrix} c^2 & s^2 & 0 & 0 & 0 & 2cs \\ s^2 & c^2 & 0 & 0 & 0 & -2cs \\ 0 & 0 & 1 & 0 & 0 & 0 \\ 0 & 0 & 0 & c & -s & 0 \\ 0 & 0 & 0 & s & c & 0 \\ -cs & cs & 0 & 0 & 0 & c^2 - s^2 \end{bmatrix} \quad (2.28)$$

And the matrix \mathbf{P} in the 2D case is set as:

$$\mathbf{P} = \begin{bmatrix} c^2 & s^2 & 2cs \\ s^2 & c^2 & -2cs \\ -cs & cs & c^2 - s^2 \end{bmatrix} \quad (2.29)$$

with $c = \cos(\alpha)$, $s = \sin(\alpha)$ and α is the angle of fiber in the orthotropic material. Then,

$$\mathbf{C} = \mathbf{C}_\alpha = \mathbf{P} \cdot \mathbf{C}_0 \cdot \mathbf{P}^T \quad (2.30)$$

Next, we can write the spectral decomposition

$$\mathbf{C} = \sum_{i=1}^n \xi_i \mathbf{a}_i \otimes \mathbf{a}_i = \sum_{i=1}^n \xi_i \mathbf{A}_i \quad (2.31)$$

Here, $\xi_i \geq 0$ ($i = 1, 2, \dots, n$) are the ordered eigenvalues of \mathbf{C} ; \mathbf{a}_i are orthonormal eigenvectors of \mathbf{C} associated with ξ_i , respectively, and $\mathbf{A}_i = \mathbf{a}_i \otimes \mathbf{a}_i$ are eigenprojectors, n is the order of the matrix \mathbf{C} .

The elastic compliance matrix decomposition \mathbf{L} associated with the tensor \mathbb{L} is defined by

$$\mathbf{L} = \mathbf{C}^{-1} = \xi_i^{-1} \mathbf{a}_i \otimes \mathbf{a}_i = \sum_{i=1}^n \xi_i^{-1} \mathbf{A}_i \quad (2.32)$$

and

$$\mathbf{C}^{1/2} = \sum_{i=1}^n \xi_i^{1/2} \mathbf{A}_i \quad (2.33)$$

$$\mathbf{C}^{-1/2} = \sum_{i=1}^n \xi_i^{-1/2} \mathbf{A}_i \quad (2.34)$$

Case 2 : $\tilde{\mathcal{K}}^+$ and $\tilde{\mathcal{K}}^-$ such that:

$$\tilde{\mathcal{K}}^+ = \{\tilde{\boldsymbol{\varepsilon}} \in \tilde{\mathcal{E}} | \mathbf{x} \cdot (\tilde{\boldsymbol{\varepsilon}} \mathbf{x}) \geq 0, \forall \mathbf{x} \in \mathbb{R}^{\mathcal{D}}\}; \quad \text{and} \quad \tilde{\mathcal{K}}^- = \{\tilde{\boldsymbol{\varepsilon}} \in \tilde{\mathcal{E}} | \mathbf{x} \cdot (\tilde{\boldsymbol{\varepsilon}} \mathbf{x}) \leq 0, \forall \mathbf{x} \in \mathbb{R}^{\mathcal{D}}\} \quad (2.35)$$

$$\tilde{\boldsymbol{\varepsilon}} = \mathbf{C}^{1/2} \boldsymbol{\varepsilon} = \tilde{\boldsymbol{\varepsilon}}^+ + \tilde{\boldsymbol{\varepsilon}}^- \quad (2.36)$$

Since (2.17) and (2.35), it can be demonstrated that

$$\tilde{\boldsymbol{\varepsilon}}^{\pm} = \sum_{i=1}^{\mathcal{D}} \langle \tilde{\boldsymbol{\varepsilon}}^i \rangle_{\pm} \tilde{\mathbf{n}}_i \otimes \tilde{\mathbf{n}}_i \quad (2.37)$$

where $\tilde{\boldsymbol{\varepsilon}}^i$ and $\tilde{\mathbf{n}}_i$ with $i = 1, \dots, \mathcal{D}$ are the ordered eigenvalues and unit eigenvectors of $\tilde{\boldsymbol{\varepsilon}}$ such that $\tilde{\boldsymbol{\varepsilon}}^1 \leq \tilde{\boldsymbol{\varepsilon}}^2 \leq \dots \leq \tilde{\boldsymbol{\varepsilon}}^{\mathcal{D}}$ and $\langle \tilde{\boldsymbol{\varepsilon}}^i \rangle_{\pm} = (\tilde{\boldsymbol{\varepsilon}}^i \pm |\tilde{\boldsymbol{\varepsilon}}^i|)/2$. This yields

$$\Psi^+(\boldsymbol{\varepsilon}) = \frac{1}{2} \tilde{\boldsymbol{\varepsilon}}^+ : \tilde{\boldsymbol{\varepsilon}}^+ = \frac{1}{2} \text{Tr}[(\tilde{\boldsymbol{\varepsilon}}^+)^2] \quad (2.38)$$

$$\Psi^-(\boldsymbol{\varepsilon}) = \frac{1}{2} \tilde{\boldsymbol{\varepsilon}}^- : \tilde{\boldsymbol{\varepsilon}}^- = \frac{1}{2} \text{Tr}[(\tilde{\boldsymbol{\varepsilon}}^-)^2] \quad (2.39)$$

A reduced Clausius-Duhem inequality expression associated with the evolution of the scalar variable d can be written as follows:

$$\mathcal{A} \dot{d} \geq 0 \quad \text{and} \quad \mathcal{A} = -\frac{\partial W}{\partial d} \quad (2.40)$$

An assumption of a threshold function $\mathcal{F}(\mathcal{A})$ within no damage occurs is written:

$$\mathcal{F}(\mathcal{A}) = \mathcal{A} \leq 0 \quad (2.41)$$

It can be shown that the condition $\mathcal{A} \dot{d} \geq 0$ will be satisfied if either $\mathcal{F} < 0$ and $\dot{d} = 0$ or $\mathcal{F} = 0$ and $\dot{d} > 0$. More precisely, the later condition leads that, when $\dot{d} > 0$, we have

$$\mathcal{F} = -\frac{\partial W}{\partial d} = -\frac{\partial W_u}{\partial d} - g_c \delta_d \gamma(d, \nabla d, \boldsymbol{\omega}) = 0 \quad (2.42)$$

where the functional derivative $\delta_d \gamma(d)$ is defined

$$\delta_d \gamma(d, \nabla d, \boldsymbol{\omega}) = \frac{d}{l} - l \{ \Delta d (1 + \eta) - \eta \mathbf{m} \otimes \mathbf{m} : \nabla \nabla d \} \quad (2.43)$$

Eq. (2.42) is now rewritten as follows:

$$\mathcal{F} = -\frac{\partial W}{\partial d} = 2(1 - d)\Psi^+ - g_c \delta_d \gamma(d, \nabla d, \boldsymbol{\omega}) = 0 \quad (2.44)$$

To deal with loading and unloading process, the strain history functional introduced in the works [18] is employed here:

$$\mathcal{H} = \max_{\tau \in [0, t]} \{ \Psi^+(\mathbf{x}, \tau) \} \quad (2.45)$$

and (2.44) is substituted by

$$2(1 - d)\mathcal{H} - g_c \delta_d \gamma(d, \nabla d, \boldsymbol{\omega}) = 0. \quad (2.46)$$

Weak form of the phase field problem

Using (2.44), the evaluation of the damage variable $d(\mathbf{x}, t)$ can be formulated as the following phase field problem:

$$\begin{cases} 2(1 - d)\mathcal{H} - g_c \delta_d \gamma(d, \nabla d, \boldsymbol{\omega}) = 0 & \text{in } \Omega \\ d(\mathbf{x}) = 1 & \text{on } \Gamma \\ \nabla d(\mathbf{x}) \cdot \mathbf{n} = 0 & \text{on } \delta\Omega \end{cases} \quad (2.47)$$

The associated weak form is obtained as

$$\int_{\Omega} \left\{ \left(2\mathcal{H}_n + \frac{g_c}{l} \right) d_{n+1} \delta d + g_c l \nabla d_{n+1} \boldsymbol{\omega} \nabla(\delta d) \right\} d\Omega = \int_{\Omega} 2\mathcal{H}_n \delta d d\Omega. \quad (2.48)$$

FEM discretization for the phase-field problem

Use FEM, the phase-field as well as phase-field gradient defined over element are approximated by:

$$d(\mathbf{x}) = \{\mathbf{N}_d(\mathbf{x})\}\{\mathbf{d}\} \text{ and } \nabla d(\mathbf{x}) = [\mathbf{B}_d(\mathbf{x})]\{\mathbf{d}\} \quad (2.49)$$

$$\delta d(\mathbf{x}) = \{\mathbf{N}_d(\mathbf{x})\}\{\delta \mathbf{d}\} \text{ and } \nabla \delta d(\mathbf{x}) = [\mathbf{B}_d(\mathbf{x})]\{\delta \mathbf{d}\} \quad (2.50)$$

where $\mathbf{N}_d(\mathbf{x})$ and $\mathbf{B}_d(\mathbf{x})$ are the matrices of shape functions and of shape function derivatives associated to the phase-field variable. Inserting (2.49) and (2.50) into the weak form (2.48), we have:

the rigid matrix is determined as:

$$[\mathbf{K}_d] = \int_{\Omega} \left\{ \left(\frac{g_c}{l} + 2\mathcal{H}_n \right) \{\mathbf{N}_d\}^T \{\mathbf{N}_d\} + g_{cl} [\mathbf{B}_d]^T \boldsymbol{\omega} [\mathbf{B}_d] \right\} d\Omega. \quad (2.51)$$

the vector of force given by:

$$\{\mathbf{F}_d\} = \int_{\Omega} 2\{\mathbf{N}_d\}^T \mathcal{H}_n d\Omega. \quad (2.52)$$

Formally, the solution is provided by:

$$\{\mathbf{d}\} = [\mathbf{K}_d]^{-1} \cdot \{\mathbf{F}_d\}. \quad (2.53)$$

Weak form of the displacement problem

Using the variational principle for minimizing the total energy E with respect to the displacement \mathbf{u} , the weak form for the displacement problem can be written as:

$$\int_{\Omega} \frac{\partial W_u}{\partial \boldsymbol{\varepsilon}} : \boldsymbol{\varepsilon}(\delta \mathbf{u}) d\Omega = \int_{\Omega} \mathbf{f} \cdot \delta \mathbf{u} d\Omega + \int_{\partial \Omega_F} \bar{\mathbf{F}} \cdot \delta \mathbf{u} d\Gamma \quad (2.54)$$

where \mathbf{f} and $\bar{\mathbf{F}}$ are the body forces and the prescribed traction vector on the part $\partial \Omega_F$ of the external boundary.

With the aforementioned expression of the elastic strain energy density function, we have:

Case 1, from (2.22), we have:

$$\Psi^+(\boldsymbol{\varepsilon}^+) = \frac{1}{2} \left\{ \frac{1}{\mathcal{D}} \tilde{\mathbf{R}}^+ [\text{Tr}(\tilde{\boldsymbol{\varepsilon}})] [\mathbf{1}] + \left(\tilde{\boldsymbol{\varepsilon}} - \frac{[\text{Tr}(\tilde{\boldsymbol{\varepsilon}})] [\mathbf{1}]}{\mathcal{D}} \right) \right\} \left\{ \frac{1}{\mathcal{D}} \tilde{\mathbf{R}}^+ [\text{Tr}(\tilde{\boldsymbol{\varepsilon}})] [\mathbf{1}] + \left(\tilde{\boldsymbol{\varepsilon}} - \frac{[\text{Tr}(\tilde{\boldsymbol{\varepsilon}})] [\mathbf{1}]}{\mathcal{D}} \right) \right\} \quad (2.55)$$

$$\Psi^+(\boldsymbol{\varepsilon}^+) = \frac{1}{2} \left\{ \frac{\tilde{\mathbf{R}}^+}{\mathcal{D}} [\mathbf{1}]^T [\mathbf{1}] + \left(\mathbf{I} - \frac{[\mathbf{1}]^T [\mathbf{1}]}{\mathcal{D}} \right) \right\} : \mathbf{C} : \left\{ \frac{\tilde{\mathbf{R}}^+}{\mathcal{D}} [\mathbf{1}]^T [\mathbf{1}] + \left(\mathbf{I} - \frac{[\mathbf{1}]^T [\mathbf{1}]}{\mathcal{D}} \right) \right\} : \boldsymbol{\varepsilon}^2 \quad (2.56)$$

and from (2.23), we obtain:

$$\Psi^-(\boldsymbol{\varepsilon}^-) = \frac{1}{2} \left\{ \frac{1}{\mathcal{D}} \tilde{\mathbf{R}}^- [\text{Tr}(\tilde{\boldsymbol{\varepsilon}})] [\mathbf{1}] \right\} \left\{ \frac{1}{\mathcal{D}} \tilde{\mathbf{R}}^- [\text{Tr}(\tilde{\boldsymbol{\varepsilon}})] [\mathbf{1}] \right\} \quad (2.57)$$

$$\Psi^-(\boldsymbol{\varepsilon}^-) = \frac{1}{2} \left\{ \frac{\tilde{\mathbf{R}}^-}{\mathcal{D}} [\mathbf{1}]^T [\mathbf{1}] \right\} : \mathbf{C} : \left\{ \frac{\tilde{\mathbf{R}}^-}{\mathcal{D}} [\mathbf{1}]^T [\mathbf{1}] \right\} : \boldsymbol{\varepsilon}^2 \quad (2.58)$$

we introduce: $\mathbf{R}^+ = \left\{ \frac{\tilde{\mathbf{R}}^+}{\mathcal{D}} [\mathbf{1}]^T [\mathbf{1}] + \left(\mathbf{I} - \frac{[\mathbf{1}]^T [\mathbf{1}]}{\mathcal{D}} \right) \right\}$ and $\mathbf{R}^- = \left\{ \frac{\tilde{\mathbf{R}}^-}{\mathcal{D}} [\mathbf{1}]^T [\mathbf{1}] \right\}$

with $\tilde{\mathbf{R}}^{\pm} = \frac{1}{2} \{ \text{sign}\{\pm \text{Tr}(\tilde{\boldsymbol{\varepsilon}})\} + 1 \}$ and $\langle \text{Tr}(\tilde{\boldsymbol{\varepsilon}}) \rangle_{\pm} = \tilde{\mathbf{R}}^{\pm} \text{Tr}(\tilde{\boldsymbol{\varepsilon}})$ (see [18]).

We have the Cauchy stress as:

$$\boldsymbol{\sigma} = \{g(d) + k\} \frac{\partial \Psi^+(\boldsymbol{\varepsilon}^+)}{\partial \boldsymbol{\varepsilon}} + \frac{\partial \Psi^-(\boldsymbol{\varepsilon}^-)}{\partial \boldsymbol{\varepsilon}} \quad (2.59)$$

$$\boldsymbol{\sigma} = \{ \{g(d) + k\} \mathbf{R}^+ : \mathbf{C} : \mathbf{R}^+ + \mathbf{R}^- : \mathbf{C} : \mathbf{R}^- \} : \boldsymbol{\varepsilon} = \mathbf{C}(d) : \boldsymbol{\varepsilon} \quad (2.60)$$

Case 2, from (2.38) and (2.39), we have:

$$\Psi^+(\boldsymbol{\varepsilon}^+) = \frac{1}{2} \tilde{\boldsymbol{\varepsilon}}^+ : \tilde{\boldsymbol{\varepsilon}}^+ = \frac{1}{2} \left(\tilde{\mathbf{P}}^+ : \mathbf{C}^{1/2} \right) : \left(\tilde{\mathbf{P}}^+ : \mathbf{C}^{1/2} \right) : \boldsymbol{\varepsilon}^2 \quad (2.61)$$

$$\Psi^-(\boldsymbol{\varepsilon}^-) = \frac{1}{2} \tilde{\boldsymbol{\varepsilon}}^- : \tilde{\boldsymbol{\varepsilon}}^- = \frac{1}{2} \left(\tilde{\mathbf{P}}^- : \mathbf{C}^{1/2} \right) : \left(\tilde{\mathbf{P}}^- : \mathbf{C}^{1/2} \right) : \boldsymbol{\varepsilon}^2 \quad (2.62)$$

Here, $\tilde{\mathbf{P}}^\pm = \frac{\partial \boldsymbol{\varepsilon}^\pm}{\partial \boldsymbol{\varepsilon}}$ can be expressed by [18]

Similar to (2.59), the Cauchy stress now can be analyzed such as:

$$\boldsymbol{\sigma} = \left\{ \{g(d) + k\} \left(\tilde{\mathbf{P}}^+ : \mathbf{C}^{1/2} \right) : \left(\tilde{\mathbf{P}}^+ : \mathbf{C}^{1/2} \right) + \left(\tilde{\mathbf{P}}^- : \mathbf{C}^{1/2} \right) : \left(\tilde{\mathbf{P}}^- : \mathbf{C}^{1/2} \right) \right\} : \boldsymbol{\varepsilon} = \mathbf{C}(d) : \boldsymbol{\varepsilon} \quad (2.63)$$

FEM discretization for the mechanical problem

Similarly, we use FEM approximations for the displacement problem in one element:

$$\mathbf{u}(\mathbf{x}) = [\mathbf{N}]\{\mathbf{u}\} \text{ and } \boldsymbol{\varepsilon}(\mathbf{u}) = [\mathbf{B}]\{\mathbf{u}\} \quad (2.64)$$

$$\delta \mathbf{u} = [\mathbf{N}]\{\delta \mathbf{u}\} \text{ and } \boldsymbol{\varepsilon}(\delta \mathbf{u}) = [\mathbf{B}]\{\delta \mathbf{u}\} \quad (2.65)$$

where \mathbf{N} and \mathbf{B} are the matrices of shape functions and of shape functions derivatives associated for the displacement vector. Introducing (2.64) and (2.65) into the weak form (2.60) for case 1 and (2.63) for case 2, we have:

For case 1:

The rigid matrix:

$$[\mathbf{K}_1(d_{n+1}, \mathbf{u}_n)] = \int_{\Omega} [\mathbf{B}]^T \{ \{g(d) + k\} \mathbf{R}_n^+ : \mathbf{C} : \mathbf{R}_n^+ \} [\mathbf{B}] d\Omega \quad (2.66)$$

$$[\mathbf{K}_2(d_{n+1}, \mathbf{u}_n)] = \int_{\Omega} [\mathbf{B}]^T \{ \mathbf{R}_n^- : \mathbf{C} : \mathbf{R}_n^- \} [\mathbf{B}] d\Omega \quad (2.67)$$

For case 2:

The rigid matrix:

$$[\mathbf{K}_1(d_{n+1}, \mathbf{u}_n)] = \int_{\Omega} [\mathbf{B}]^T \left\{ \{ (1-d)^2 + k \} \left(\tilde{\mathbf{P}}_n^+ : \mathbf{C}^{1/2} \right) : \left(\tilde{\mathbf{P}}_n^+ : \mathbf{C}^{1/2} \right) \right\} [\mathbf{B}] d\Omega \quad (2.68)$$

$$[\mathbf{K}_2(d_{n+1}, \mathbf{u}_n)] = \int_{\Omega} [\mathbf{B}]^T \left\{ \left(\tilde{\mathbf{P}}_n^- : \mathbf{C}^{1/2} \right) : \left(\tilde{\mathbf{P}}_n^- : \mathbf{C}^{1/2} \right) \right\} [\mathbf{B}] d\Omega \quad (2.69)$$

The force vector:

$$\{\mathbf{F}\}_{n+1} = \int_{\Omega} [\mathbf{N}]^T \{\mathbf{f}\} d\Omega + \int_{\partial\Omega_F} [\mathbf{N}]^T \{\bar{\mathbf{F}}\}_{n+1} d\Gamma \quad (2.70)$$

The solution is formally given by:

$$\{\mathbf{u}\}_{n+1} = \{[\mathbf{K}_1] + [\mathbf{K}_2]\}^{-1} \cdot \{\mathbf{F}\}_{n+1} \quad (2.71)$$

The content of chapter 2 is summarized as the algorithm provided in **Appendix B.2**

2.4 Numerical examples

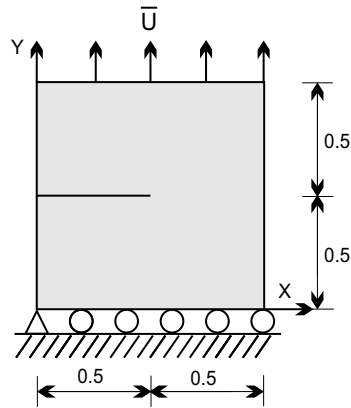


Figure 2.3: Single edge notched tension test: geometry and boundary conditions.

2.4.1 Single edge notched tension test

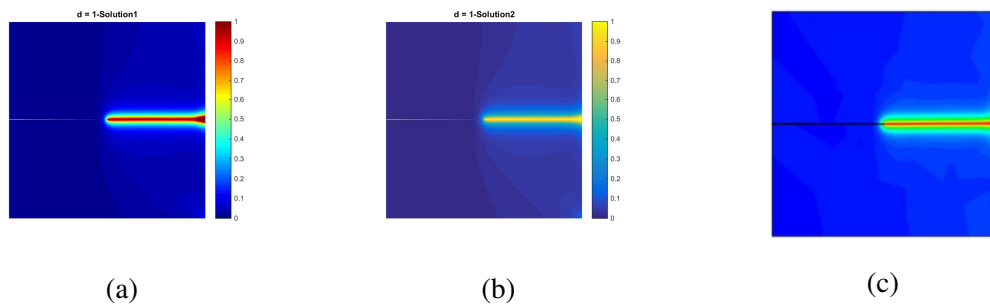


Figure 2.4: Single edge notched tension test: a) solution 1; b) solution 2; c) Miehe et al. [16]

The principal purpose of the first example is to predict the crack propagation in isotropic material by the two solutions of strain decompositions (2.18) and (2.35). For this purpose, we consider the problem introduced in [16]. A square domain contains an initial crack, the geometric setup

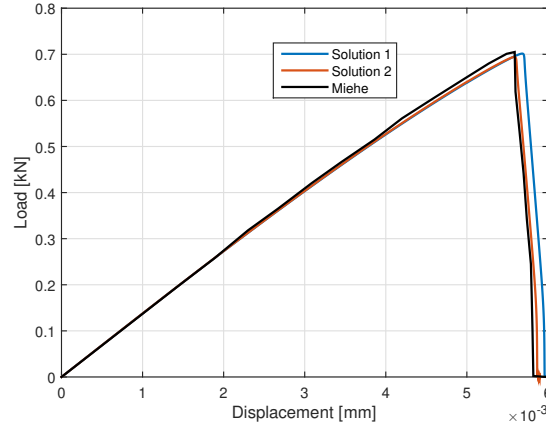


Figure 2.5: Single edge notched tension test: comparison of the load-displacement curves with the length scale $l=0.015\text{mm}$ between solution 1, solution 2 and Miehe et al. [16].

being depicted in Fig.2.3. On the lower side, the vertical displacements are blocked while the displacements of horizontal direction are free and the bottom left corner of the domain is blocked in two directions. On the upper side, the uniform vertical displacements are increased with time while the horizontal displacements are also free. Due to this tension loading, a curved crack nucleates and propagates. The mesh is refined in the expected crack propagation zone with 21684 elements. The typical size of an element is about $h_{min} = 0.001\text{mm}$ in the crack propagation zone and about $h_{min} = 0.02\text{mm}$ in the rest of the domain. Plane strain assumption is adopted. The plate is assumed to consist of an isotropic homogeneous material with Lamé's constants properties $\lambda = 121.15\text{GPa}$ and $\mu = 80.77\text{GPa}$. From (2.25), we have the elastic stiffness matrix as:

$$\mathbf{C} = \begin{bmatrix} 282.66 & 121.15 & 0 \\ 121.15 & 282.66 & 0 \\ 0 & 0 & 80.77 \end{bmatrix} \text{GPa}. \quad (2.72)$$

The fracture toughness is $g_c = 0.0027 \text{ kN/mm}$. Two displacement increments $\Delta u=10^{-5}$ in the first 500 loading steps and $\Delta u=10^{-6}\text{mm}$ in the next time steps are prescribed. The regularization length parameter is chosen as $l = 0.015 \text{ mm}$. The crack initiation and propagation during the simulations with solution 1, solution 2 and [16] are shown in Fig.2.4a, Fig.2.4b, and Fig.2.4c, respectively.

To demonstrate the strain orthogonal decomposition method, we have compared the two solutions provided by the two schemes defined in (2.18) and (2.35) with the solution provided in [16]. Then, we have shown the load - displacement curves of the two mentioned solutions (see Fig.2.5). We can note that when two mentioned solutions are used, the corresponding results are in agreement

with the reference result of [16].

2.4.2 Single edge notched shear test

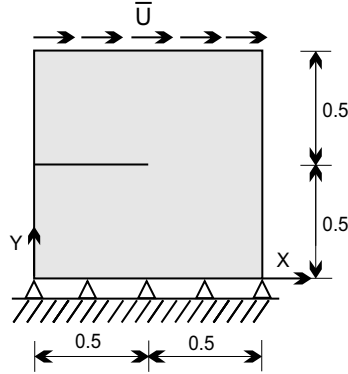


Figure 2.6: Single edge notched shear test: geometry and boundary conditions.

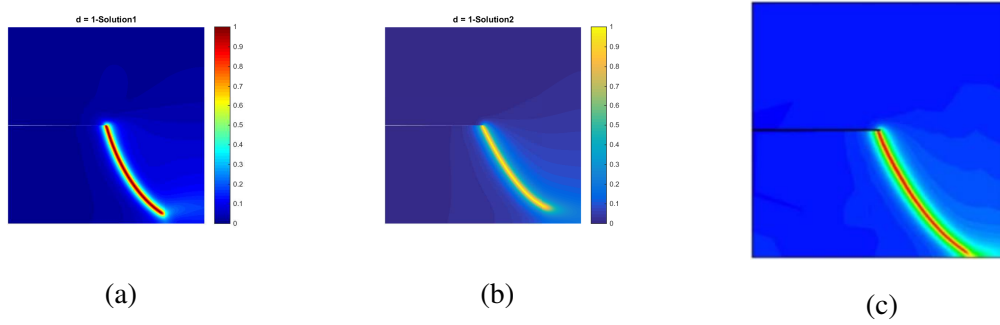


Figure 2.7: Single edge notched shear test: a) solution 1; b) solution 2; c) Miehe et al. [16]

In this example, we check the two solutions defined by the strain decompositions (2.18) and (2.35) for a plate undergoing pure shear. In this example, we are interested in the problem of crack nucleation and propagation of a single edge notched domain shear test as in [16]. The geometric setup is shown in Fig.2.6. The lower end is fixed in both directions. On the upper end, the displacements along vertical direction are fixed to zero, while the uniform horizontal displacements of $\Delta u = 10^{-5}$ mm are imposed. The crack initiates and propagates due to this shear loading. The domain contains 33245 triangle elements of two mesh sizes: $h_{min} = 0.002$ mm in the crack propagation zone and $h_{min} = 0.02$ mm in the remaining domain. Plane strain is assumed. The material properties in this problem are similar to the example 2.4.1: $\lambda = 121.15$ GPa, $\mu = 80.77$ GPa and the fracture toughness is $g_c = 0.0027$ kN/mm. We use also the length parameter $l = 0.015$ mm. The evolutions of the crack of solution 1, solution 2 and [16] are shown in Fig.2.7a, Fig.2.7b,

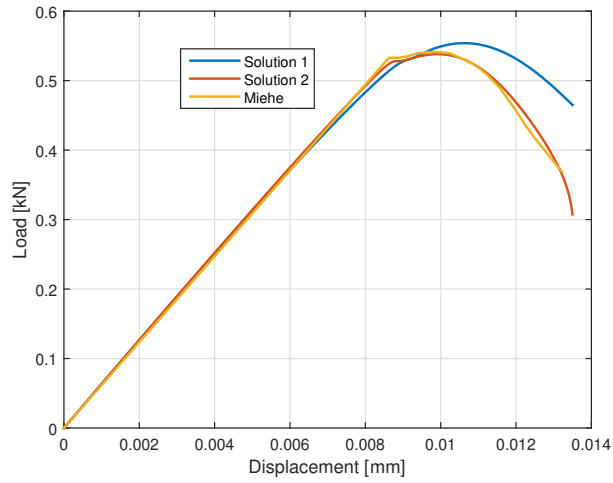


Figure 2.8: *Single edge notched shear test: comparison of the load-displacement curves with the length scale $l=0.015\text{mm}$ between solution 1, solution 2 and Miehe et al. [16].*

and Fig.2.7c, respectively. The load - displacement curves of our solutions and [16] are shown in Fig.2.8. We can see that, the crack propagation and material behavior curves of the two proposed solutions and the solution of [16] are the same.

2.4.3 Symmetric three point bending test of a 3D beam

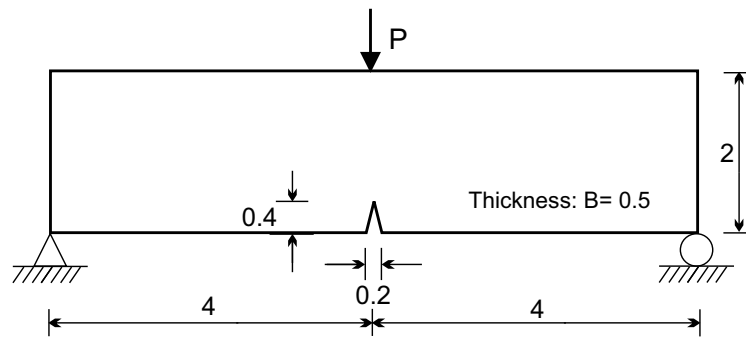


Figure 2.9: *Symmetric three point bending test of a 3D beam (thickness $B=0.5\text{mm}$): geometry and boundary conditions.*

We investigate the crack propagation in a three-point bending test of a 3D beam while using two aforementioned solutions in (2.18) and (2.35). The geometry as well as the loading conditions are depicted in Fig.2.9. In the present example, we consider a 3D beam whose dimensions as $L \times H \times B = 8 \times 2 \times 0.5\text{mm}$ while in [16] use was made of a 2D beam with the dimensions $L \times H = 8 \times 2\text{mm}$. The tetrahedral elements are adopted. The discretization is refined with the mesh size of $h_{min} =$

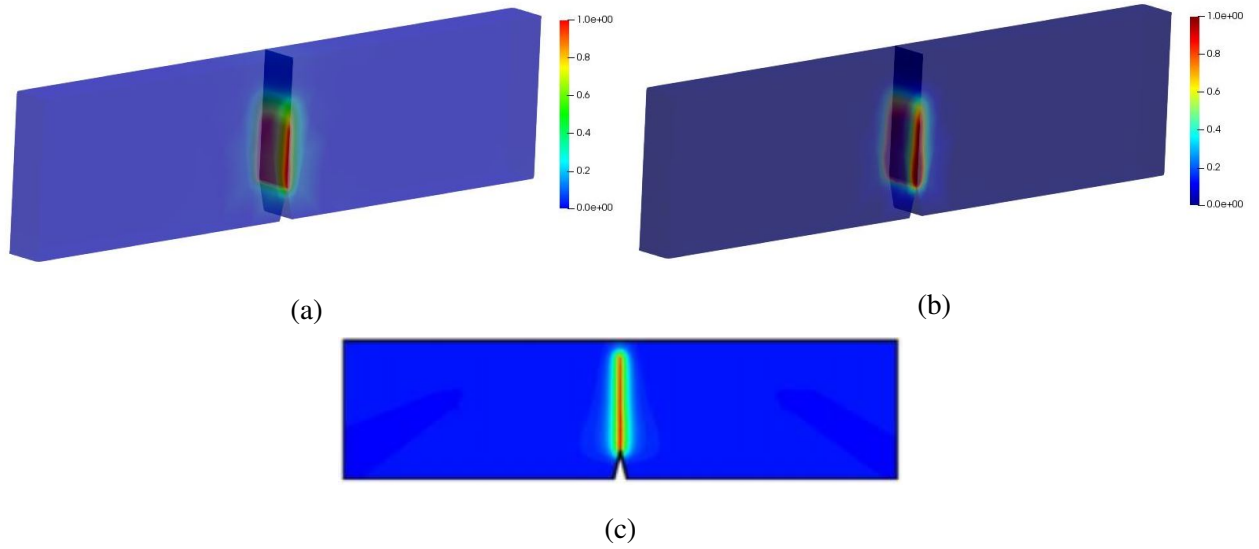


Figure 2.10: Symmetric three point bending test of a 3D beam: a) solution 1; b) solution 2; c) [16]

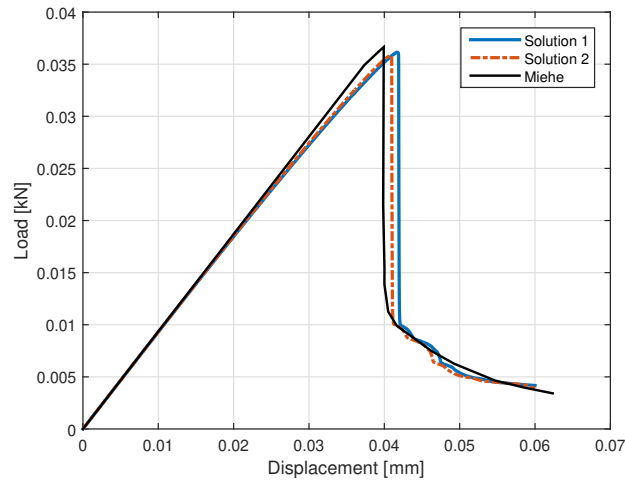


Figure 2.11: Symmetric three point bending test of a 3D beam: comparison of the load-displacement curves between solution 1, solution 2 and [16].

0.001mm in the expected crack propagation zone. The material properties are as follows: the elastic Lamé's constants are $\lambda = 12$ GPa and $\mu = 8$ GPa. The corresponding stiffness matrix is given by:

$$\mathbf{C} = \begin{bmatrix} 28 & 12 & 12 & 0 & 0 & 0 \\ 12 & 28 & 12 & 0 & 0 & 0 \\ 12 & 12 & 28 & 0 & 0 & 0 \\ 0 & 0 & 0 & 8 & 0 & 0 \\ 0 & 0 & 0 & 0 & 8 & 0 \\ 0 & 0 & 0 & 0 & 0 & 8 \end{bmatrix} \text{ GPa.} \quad (2.73)$$

The fracture toughness is equal to $g_c = 0.0005$ kN/mm. The displacement increment $\Delta u = 10^{-4}$ mm

is imposed in the first 360 loading steps while $\Delta u=10^{-6}$ mm is prescribed in the remaining time steps. The length parameter of $l = 0.06$ mm is chosen. The progresses of the crack computed with the two present solutions and [16] are shown in Fig.2.10a, Fig.2.10b and Fig.2.10c, respectively. The behavior curves are presented in Fig.2.11. We can see that, the results obtained by the two proposed solutions are in good agreement with the one of [16].

2.4.4 Single edge notched shear test for an orthotropic material plate

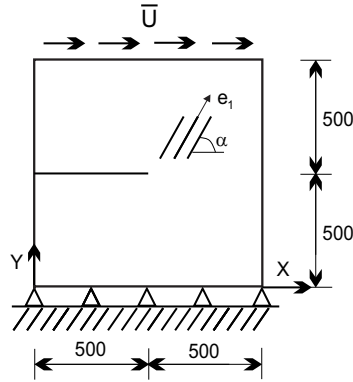


Figure 2.12: Single-edge-notched shear test for orthotropic material plate: geometry and boundary conditions.

The purpose of this sub-section is to investigate the crack propagation in an orthotropic single-edge-notched plate undergoing shear loading when changing the privileged directions α of the plate. We use the strain orthogonal decompositions proposed in (2.18) and (2.35) and only a unique damage variable d instead of multiple damage variables d_i . For this purpose, we consider the problem of crack propagation studied in [61]. In [61], use was made of a longitudinal damage variable d_1 and a transverse damage variable d_2 in to simulate the crack propagation in an orthotropic material plate. The geometric dimensions of the plate and the loading conditions are shown in Fig.2.12. The lower end is fixed in both directions. On the upper end, the displacement along the vertical direction is equal to zero, while the uniform horizontal displacement is prescribed. Due to this shear loading, the development of cracks depends on the change of fiber direction in the plate. The material parameters are: $E_1 = 150$ GPa, $E_2 = 10$ GPa, $G_{12} = 5$ GPa, $\nu_{12} = \nu_{13} = \nu_{23} = 0.25$. The toughness is $g_c=200$ N/m. The elastic compliance matrix \mathbf{L} is defined by (2.27). Then, we can determine the elastic stiffness matrix according to the 0° direction as $\mathbf{C}_0 = \mathbf{L}^{-1}$:

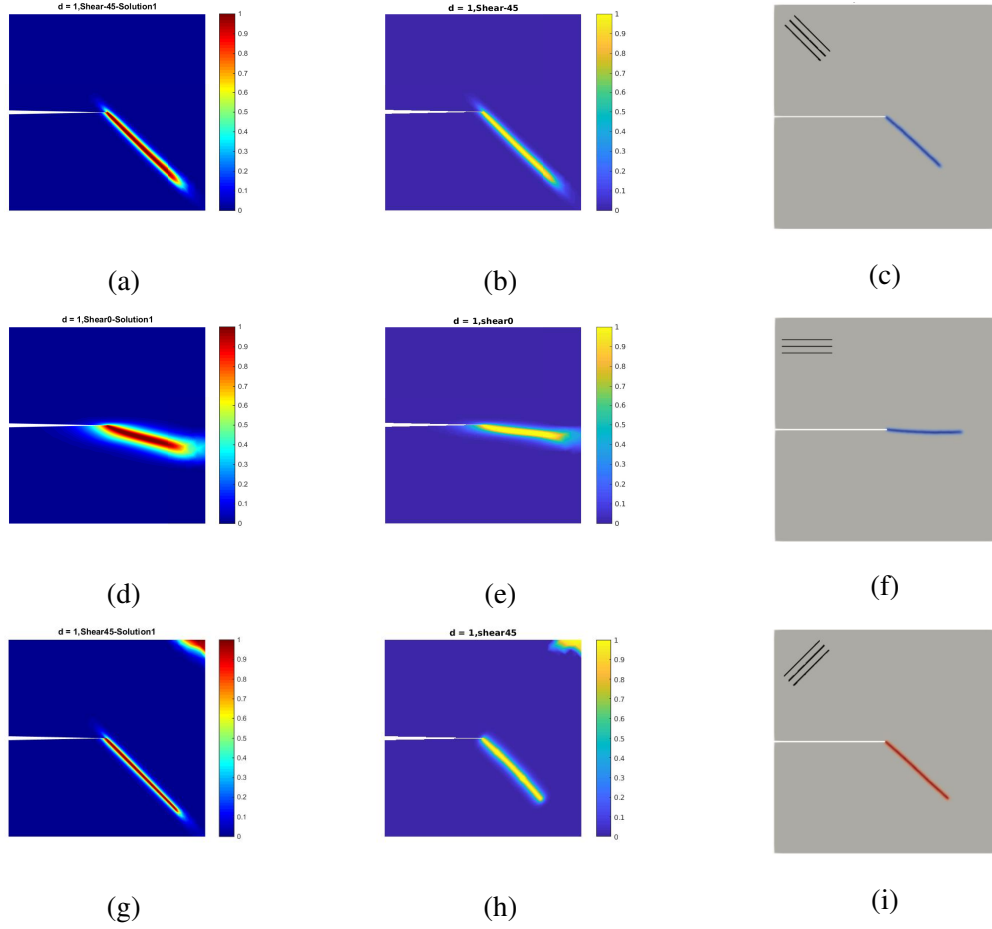


Figure 2.13: Comparison of the crack path which depends on the orthotropic direction orientations α for shear test: (a) with $\alpha = -45^\circ$ (d) with $\alpha = 0^\circ$ (g) with $\alpha = 45^\circ$ solution 1; (b) with $\alpha = -45^\circ$ (e) with $\alpha = 0^\circ$ (h) with $\alpha = 45^\circ$ solution 2; (c) with $\alpha = -45^\circ$ (f) with $\alpha = 0^\circ$ (i) with $\alpha = 45^\circ$ [61].

$$\mathbf{C}_0 = \begin{bmatrix} 150.63 & 2.51 & 0 \\ 2.51 & 10.04 & 0 \\ 0 & 0 & 5 \end{bmatrix} GPa \quad (2.74)$$

Then, we can determine the elastic matrix \mathbf{C} in relation to the angle α of one privileged direction by (2.30) (see e.g. fiber direction), where the transformation matrix \mathbf{P} is defined through (2.29). In this example, the value of the anisotropy coefficient is given by $\eta = 20$. The regularization length parameter is chosen as $l = 10\text{mm}$. The constant displacement increment is equal to $\Delta u = 0.001\text{mm}$. In this example, we vary the angle α with respect to the horizontal direction (see Fig.2.12). The crack propagations for $\alpha = -45^\circ$, $\alpha = 0^\circ$ and $\alpha = 45^\circ$ given by the two proposed solution, and [61] shown in Fig.2.13. We can see, in the results of [61], Fig.2.13c and Fig.2.13f corresponds to $\alpha = -45^\circ$ and $\alpha = 0^\circ$, the crack direction is preferred according to the longitudinal damage

variable d_1 and when $\alpha = 45^\circ$, the crack direction is preferred according to the transverse damage variable d_2 . We note the our results involving only one damage variable d and concerning, the crack propagation directions in the orthotropic plate are similar to those of [61] where two damage variables d_1 and d_2 are used.

2.4.5 Single edge notched tension test for an orthotropic material plate

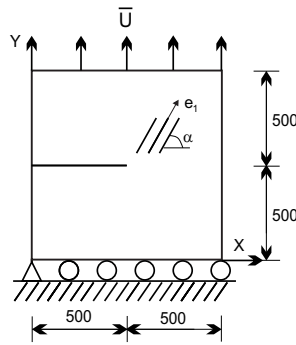


Figure 2.14: Single-edge-notched tension test for orthotropic material plate: geometry and boundary conditions.

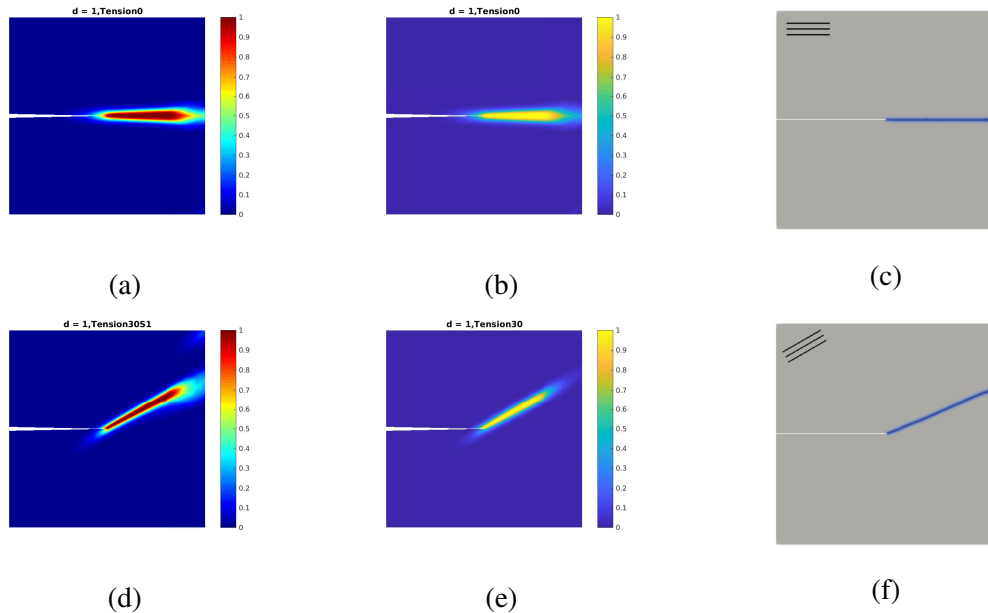


Figure 2.15: Comparison of the crack path which depends on the orthotropic direction orientations α for tension test: (a) with $\alpha = 0^\circ$ (d) with $\alpha = 30^\circ$ solution 1; (b) with $\alpha = 0^\circ$ (e) with $\alpha = 30^\circ$ solution 2; (c) with $\alpha = 0^\circ$ (f) with $\alpha = 30^\circ$ [61].

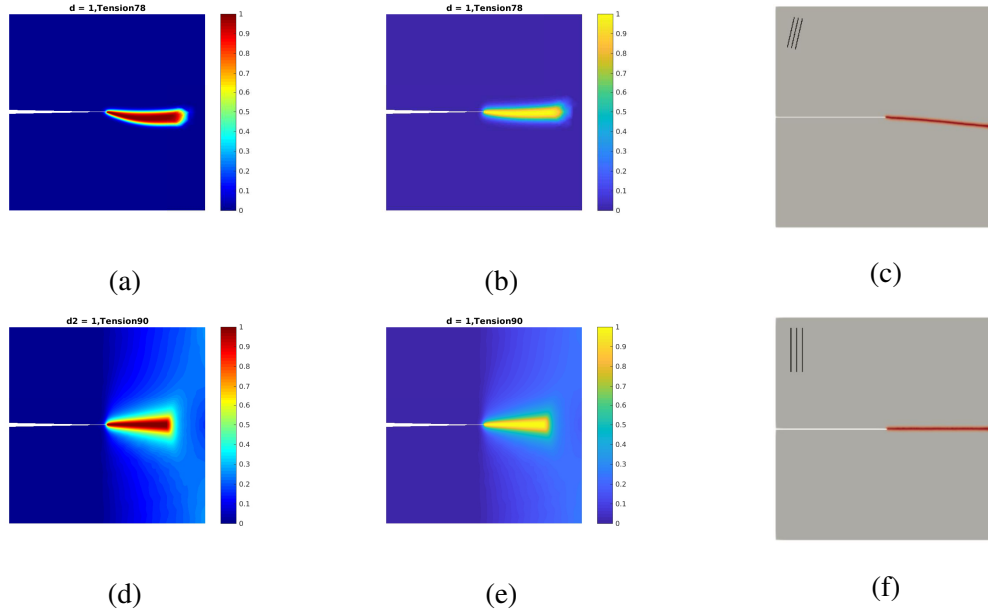


Figure 2.16: Comparison of the crack path which depends on the orthotropic direction orientations α for tension test: (a) with $\alpha = 78^\circ$ (d) with $\alpha = 90^\circ$ solution 1; (b) with $\alpha = 78^\circ$ (e) with $\alpha = 90^\circ$ solution 2; (c) with $\alpha = 78^\circ$ (f) with $\alpha = 90^\circ$ [61].

We now investigate the same square plate as in the example 2.4.4 for a tension test. The plate dimensions and the applied load are illustrated in Fig.2.14. The boundary conditions are as follows: on the lower end, the vertical displacements are fixed, while the horizontal displacements are free and the left bottom node is fixed. On the upper end, the horizontal displacements are free, while the vertical displacements are prescribed with an increasing constant value of $\Delta u = 0.001\text{mm}$ during the simulation. The material parameters are as example 2.4.4. We use the value of the anisotropy coefficient $\eta = 20$. The length parameter of l is set to 10mm. Here, we adopt only one damage variable d instead of two damage variables d_1 and d_2 as [61]. We use also the values of α as in [61]. The comparisons of the crack propagation directions between our results and those of [61] are shown in Fig.2.15 and Fig.2.16. In [61], Fig.2.15c and Fig.2.15f corresponds to $\alpha = 0^\circ$ and $\alpha = 30^\circ$, and the crack direction is developed according to the longitudinal damage variable d_1 , when $\alpha = 78^\circ$ and $\alpha = 90^\circ$ the crack propagation and directions are governed by the transverse damage variable d_2 (see Fig.2.16c and Fig.2.16f). Thus, we can see, when $\alpha \geq 78^\circ$, the crack tend to propagate in the direction perpendicular to the fiber direction and when $\alpha < 78^\circ$ the crack develop almost in the direction parallel to the fiber direction. From the obtained results, we see that, when using the two present solutions in (2.18) and (2.35) combined with only one damage variable d , the prediction of the crack development in the tension test problem for an orthotropic material plate is quite well.

2.4.6 Bi-axial tension test of an orthotropic material plate made of a Glass-epoxy composite and containing an initial crack

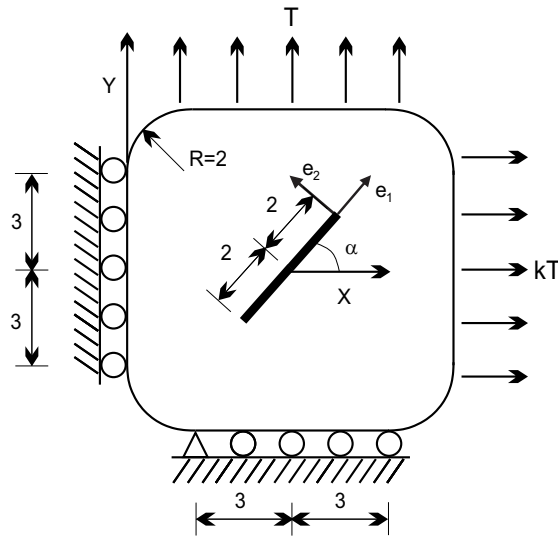


Figure 2.17: Tension test in two directions of an orthotropic plate: geometry and boundary conditions.

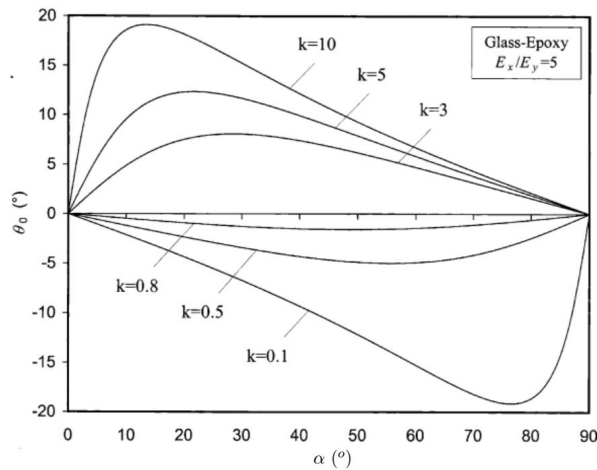


Figure 2.18: Crack extension angle θ_0 vs. crack inclination angle α for various values of biaxial load parameter for the orthotropic material of Glass-epoxy (this figure in [47])

An orthotropic glass-epoxy plate contains an initial crack which forms an angle α with respect to the horizontal direction and this initial crack is orientated along the fiber direction. The initial crack length is set to 4mm. This plate is pulled in both horizontal and vertical directions. The geometry and the boundary conditions are described in Fig.2.17. The boundary conditions are as follows: on

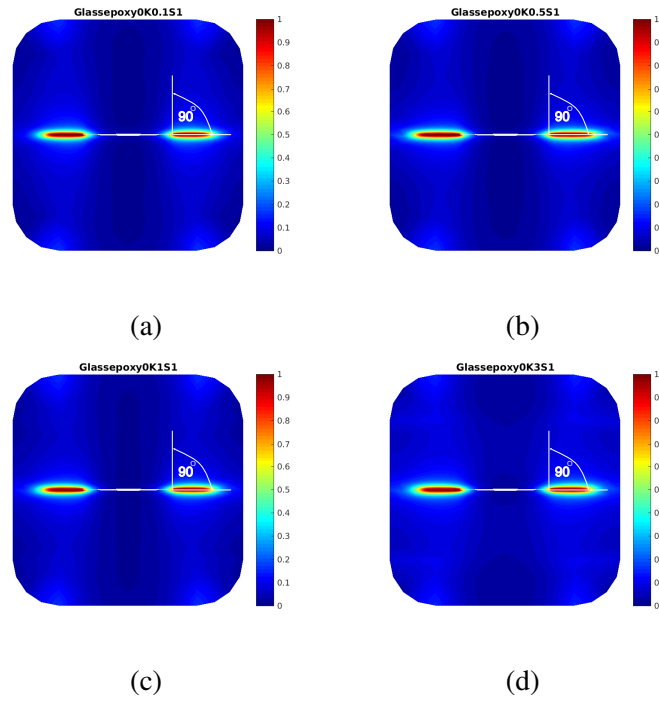


Figure 2.19: Crack extension angle θ_0 vs. crack inclination angle $\alpha=0^\circ$ for various values of biaxial load parameter for Glass-epoxy by phase field method of solution 1: a) $k = 0.1$, b) $k = 0.5$, c) $k = 1$, d) $k = 3$.

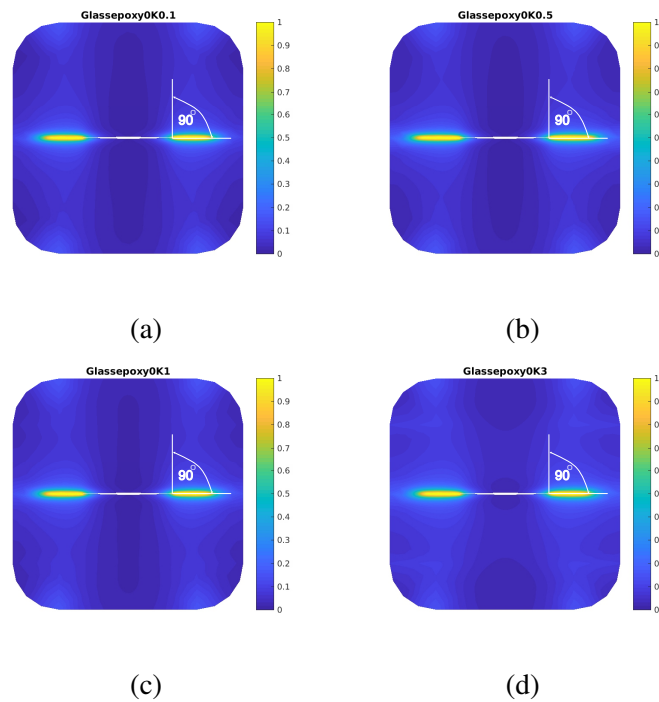


Figure 2.20: Crack extension angle θ_0 vs. crack inclination angle $\alpha=0^\circ$ for various values of biaxial load parameter for Glass-epoxy by phase field method of solution 2: a) $k = 0.1$, b) $k = 0.5$, c) $k = 1$, d) $k = 3$.

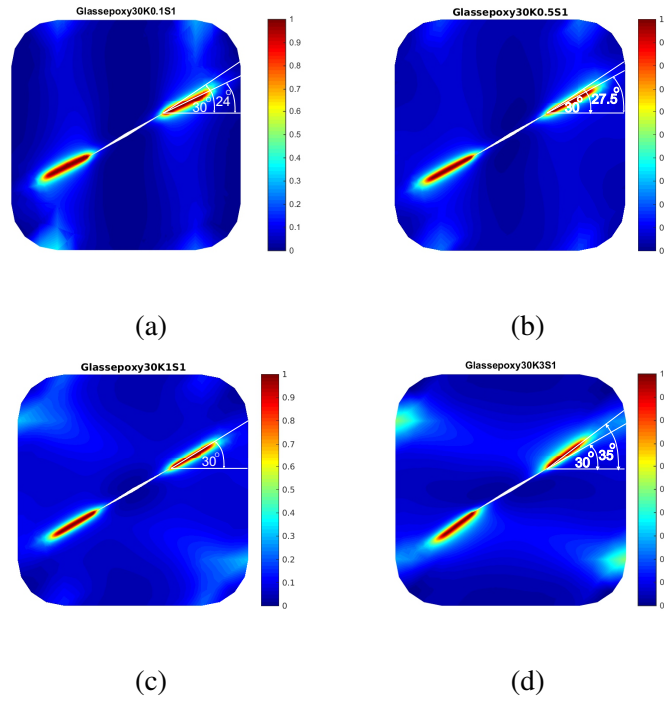


Figure 2.21: Crack extension angle θ_0 vs. crack inclination angle $\alpha=30^\circ$ for various values of biaxial load parameter for Glass-epoxy by phase field method of solution 1: a) $k = 0.1$, b) $k = 0.5$, c) $k = 1$, d) $k = 3$.

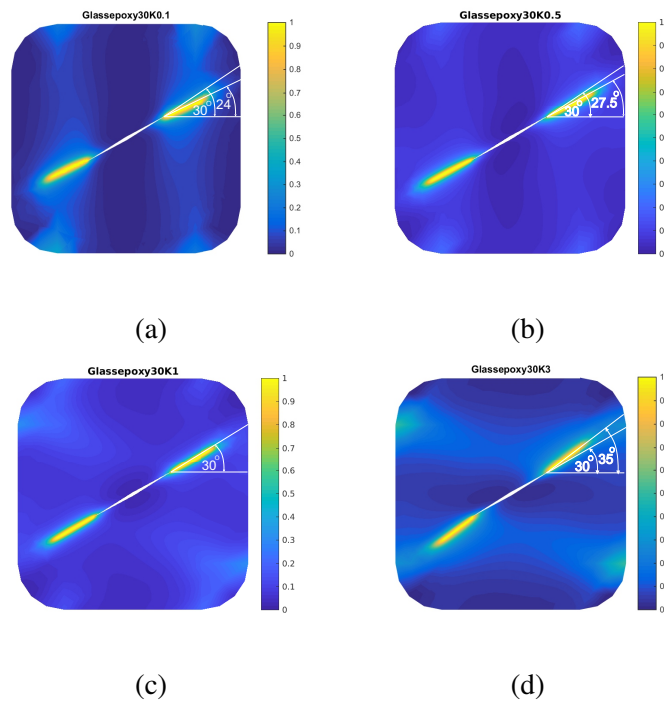


Figure 2.22: Crack extension angle θ_0 vs. crack inclination angle $\alpha=30^\circ$ for various values of biaxial load parameter for Glass-epoxy by phase field method of solution 2: a) $k = 0.1$, b) $k = 0.5$, c) $k = 1$, d) $k = 3$.

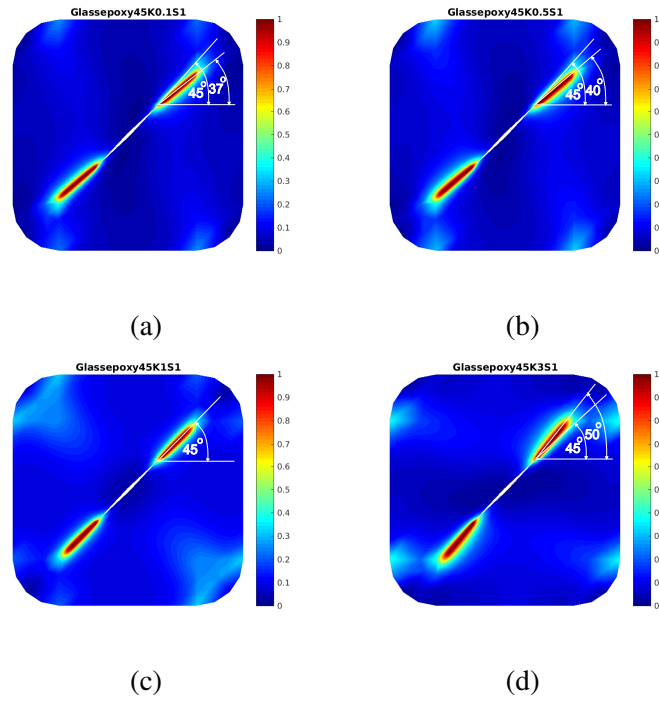


Figure 2.23: Crack extension angle θ_0 vs. crack inclination angle $\alpha=45^\circ$ for various values of biaxial load parameter for Glass-epoxy by phase field method of solution 1: a) $k = 0.1$, b) $k = 0.5$, c) $k = 1$, d) $k = 3$.

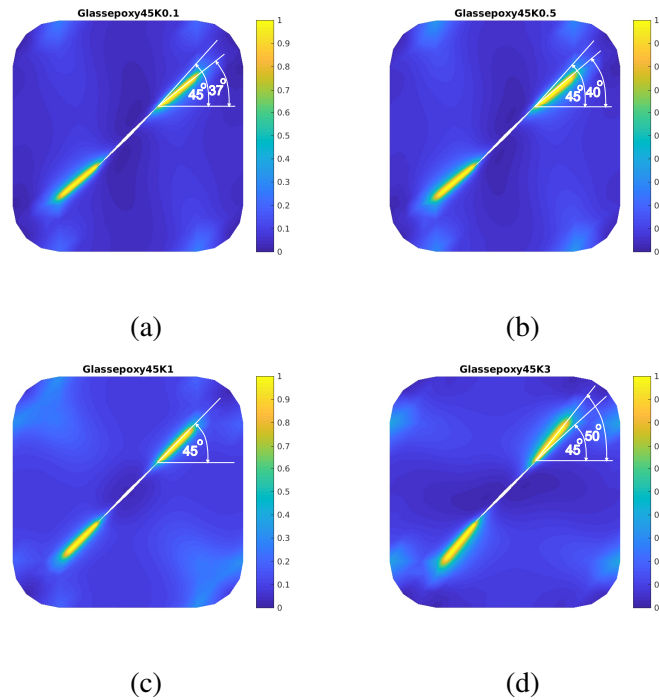


Figure 2.24: Crack extension angle θ_0 vs. crack inclination angle $\alpha=45^\circ$ for various values of biaxial load parameter for Glass-epoxy by phase field method of solution 2: a) $k = 0.1$, b) $k = 0.5$, c) $k = 1$, d) $k = 3$.

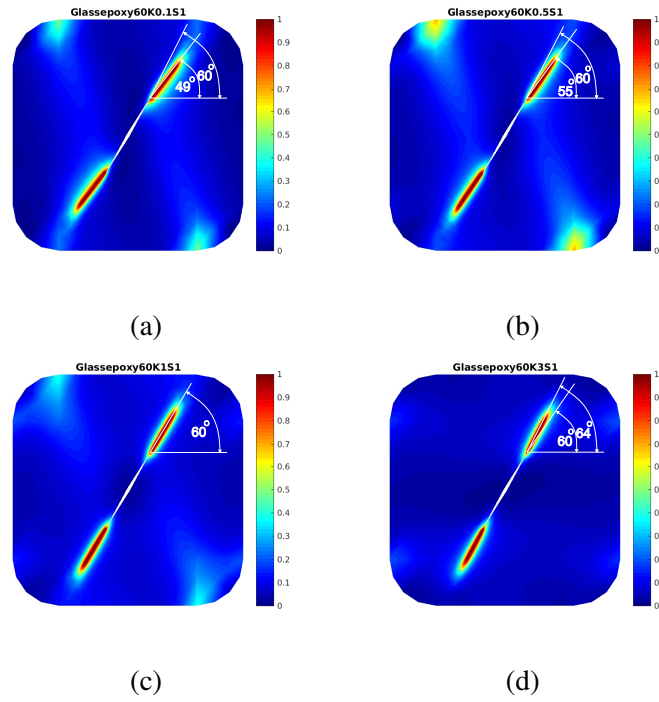


Figure 2.25: Crack extension angle θ_0 vs. crack inclination angle $\alpha=60^\circ$ for various values of biaxial load parameter for Glass-epoxy by phase field method of solution 1: a) $k = 0.1$, b) $k = 0.5$, c) $k = 1$, d) $k = 3$.

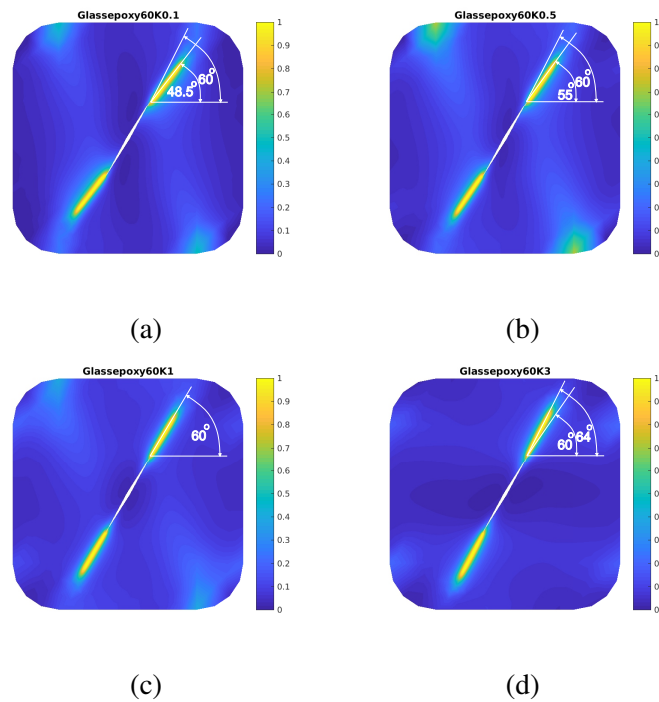


Figure 2.26: Crack extension angle θ_0 vs. crack inclination angle $\alpha=60^\circ$ for various values of biaxial load parameter for Glass-epoxy by phase field method of solution 2: a) $k = 0.1$, b) $k = 0.5$, c) $k = 1$, d) $k = 3$.

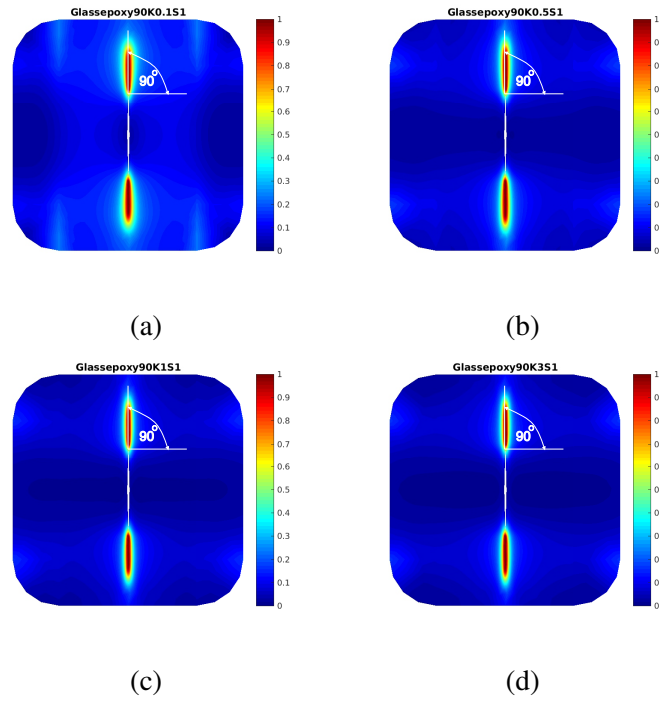


Figure 2.27: Crack extension angle θ_0 vs. crack inclination angle $\alpha=90^\circ$ for various values of biaxial load parameter for Glass-epoxy by phase field method of solution 1: a) $k = 0.1$, b) $k = 0.5$, c) $k = 1$, d) $k = 3$.

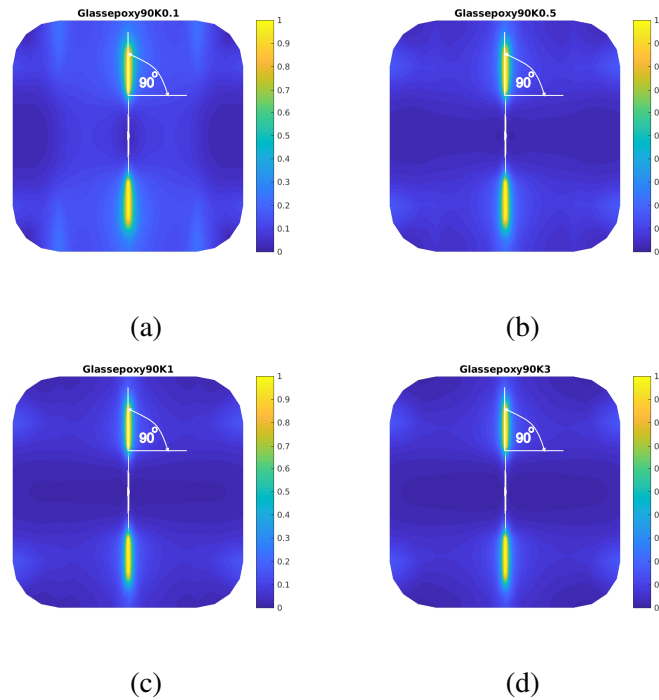


Figure 2.28: Crack extension angle θ_0 vs. crack inclination angle $\alpha=90^\circ$ for various values of biaxial load parameter for Glass-epoxy by phase field method of solution 2: a) $k = 0.1$, b) $k = 0.5$, c) $k = 1$, d) $k = 3$.

Comparison of the crack extension angles $\theta(\alpha)$ between the analytical method and the proposed solutions of Glass-epoxy material							
α (o)	k	Analytical method $\theta(\alpha)$	Simulation of Solution 1 $\theta(\alpha)$	Simulation of Solution 2 $\theta(\alpha)$	Correction 1(%)	Correction 2(%)	
0	0,1	0	0	0	0	0,0	0,0
	0,5	0	0	0	0	0,0	0,0
	1	0	0	0	0	0,0	0,0
	3	0	0	0	0	0,0	0,0
30	0,1	-7	-6	-6	-6	14,3	14,3
	0,5	-2,5	-2,5	-2,5	-2,5	0,0	0,0
	1	0	0	0	0	0,0	0,0
	3	5	5	5	5	0,0	0,0
45	0,1	-9	-8	-8	-8	11,1	11,1
	0,5	-5	-5	-5	-5	0,0	0,0
	1	0	0	0	0	0,0	0,0
	3	6	5	5	5	16,7	16,7
60	0,1	-14	-11	-11,5	-11,5	21,4	17,9
	0,5	-5	-5	-5	-5	0,0	0,0
	1	0	0	0	0	0,0	0,0
	3	5	4	4	4	20,0	20,0
90	0,1	0	0	0	0	0,0	0,0
	0,5	0	0	0	0	0,0	0,0
	1	0	0	0	0	0,0	0,0
	3	0	0	0	0	0,0	0,0

Figure 2.29: Comparison between the analytical method in [47] and the proposed solutions of the crack extension angles θ_0 which depends on the initial crack direction α with Glass-epoxy material

the lower end, the vertical displacements are fixed, while the horizontal displacements are free and one node at the lower end is fixed in both directions. On the upper end, the horizontal displacements are free, while the vertical displacements are prescribed with an increasing uniform value of Δu_y . On the left end, the horizontal displacements are fixed, while the vertical displacements are free. On the right end, the vertical displacements are free, while the horizontal displacements are prescribed with an increasing uniform value of Δu_x . Four corners of the plate are rounded with a radius of $R = 2\text{mm}$ to avoid concentration stress when tension in two dimensions. The computation is performed in a monotonic displacement increments Δu_y and $\Delta u_x = k_1 \Delta u_y$ to have $T_x = kT_y$. For each specific value of α , we use the different values of Δu_y and coefficients k_1 to obtain the values of $k = 0.1, 0.5, 1$ and 3 , respectively.

The glass-epoxy material parameters (see [46]) are as: $E_1 = 42.8\text{GPa}$, $E_2 = 9.9\text{GPa}$, $G_{12} = 3.7\text{GPa}$, $\nu_{12} = \nu_{13} = 0.27$, $\nu_{31} = \nu_{21} = \frac{E_2}{E_1} \nu_{12}$, $\nu_{23} = 0.34$. The toughness is $g_c = 0.2\text{N/mm}$. Similarly, the elastic compliance matrix \mathbf{L} is written as (2.27). Then, we can determine the elastic stiffness matrix according to the 0° direction as $\mathbf{C}_0 = \mathbf{L}^{-1}$:

$$\mathbf{C}_0 = \begin{bmatrix} 45.1 & 4.27 & 0 \\ 4.27 & 11.6 & 0 \\ 0 & 0 & 3.7 \end{bmatrix} \text{GPa} \quad (2.75)$$

We can also determine the elastic matrix \mathbf{C} according to the angle α of the fiber as (2.30) where the matrix \mathbf{P} is defined by (2.29). The anisotropy coefficient $\eta = 20$ and the length parameter $l = 0.1\text{mm}$ are taken.

Here, we use only a unique damage variable d and the strain orthogonal decompositions in (2.18) and (2.35). We use several values of angle α to determine the development direction of the crack when the displacements are applied along two directions at the plate sides.

In the work of [47], the analytical results of crack extension angle θ_0 with the angle of initial crack α with several various values of k of biaxial load ratio in the orthotropic material of glass-epoxy are shown in Fig.2.18.

The resulting crack propagations for the values of α which change from 0° to 90° and some values of k vary change from 0.1 to 3 are shown in from Fig.2.19 to Fig.2.28.

Concerning the crack extension angle θ_0 comparison between the analytical results of [47] and the simulation results according to the two present solutions as in Fig.2.29. We can see, the results of two solutions are in good agreement with the analytical results of [47]. Thus, the present solutions are able to predict very well the crack propagation of the orthotropic plate containing an initial crack when the plate is pulled in two directions.

2.4.7 Bi-axial tension test of an orthotropic material 3D plate made of a Glass-epoxy composite and containing an initial crack

The purpose of this example is to extend the example 2.4.6 by modeling the structure in the 3D case. The dimensions of plate in the (e_1, e_2) plane and the boundary conditions are given in Fig.2.17 with the thickness of plate according to the direction e_3 which is perpendicular to the (e_1, e_2) plane as $B=0.5\text{mm}$. In particular, the Young's moduli associated with any direction in the (e_2, e_3) plane is the same, $E = E_2 = E_3 = 9.9\text{GPa}$, and the Poisson's ratio $\nu = \nu_{23} = \nu_{32} = 0.34$. In addition, $E_1 = 42.8\text{GPa}$, $\nu_{12} = \nu_{13} = 0.27$ and $\nu_1 = \nu_{31} = \nu_{21} = \frac{E}{E_1}\nu_{12}$. From (2.26), we can determine the elastic compliance matrix \mathbf{L} in the 3D case. Then, we can find the elastic stiffness 3D matrix of 0° orientation $\mathbf{C}_0 = \mathbf{L}^{-1}$ as follows:

$$\mathbf{C}_0 = \begin{bmatrix} 45.1 & 4.27 & 4.27 & 0 & 0 & 0 \\ 4.27 & 11.6 & 4.21 & 0 & 0 & 0 \\ 4.27 & 4.21 & 11.6 & 0 & 0 & 0 \\ 0 & 0 & 0 & 3.69 & 0 & 0 \\ 0 & 0 & 0 & 0 & 3.7 & 0 \\ 0 & 0 & 0 & 0 & 0 & 3.7 \end{bmatrix} \quad (2.76)$$

Then, we can determine the elastic matrix \mathbf{C} relative to the angle α of the fiber as (2.30). Here, the transformation matrix is determined according by (2.28).

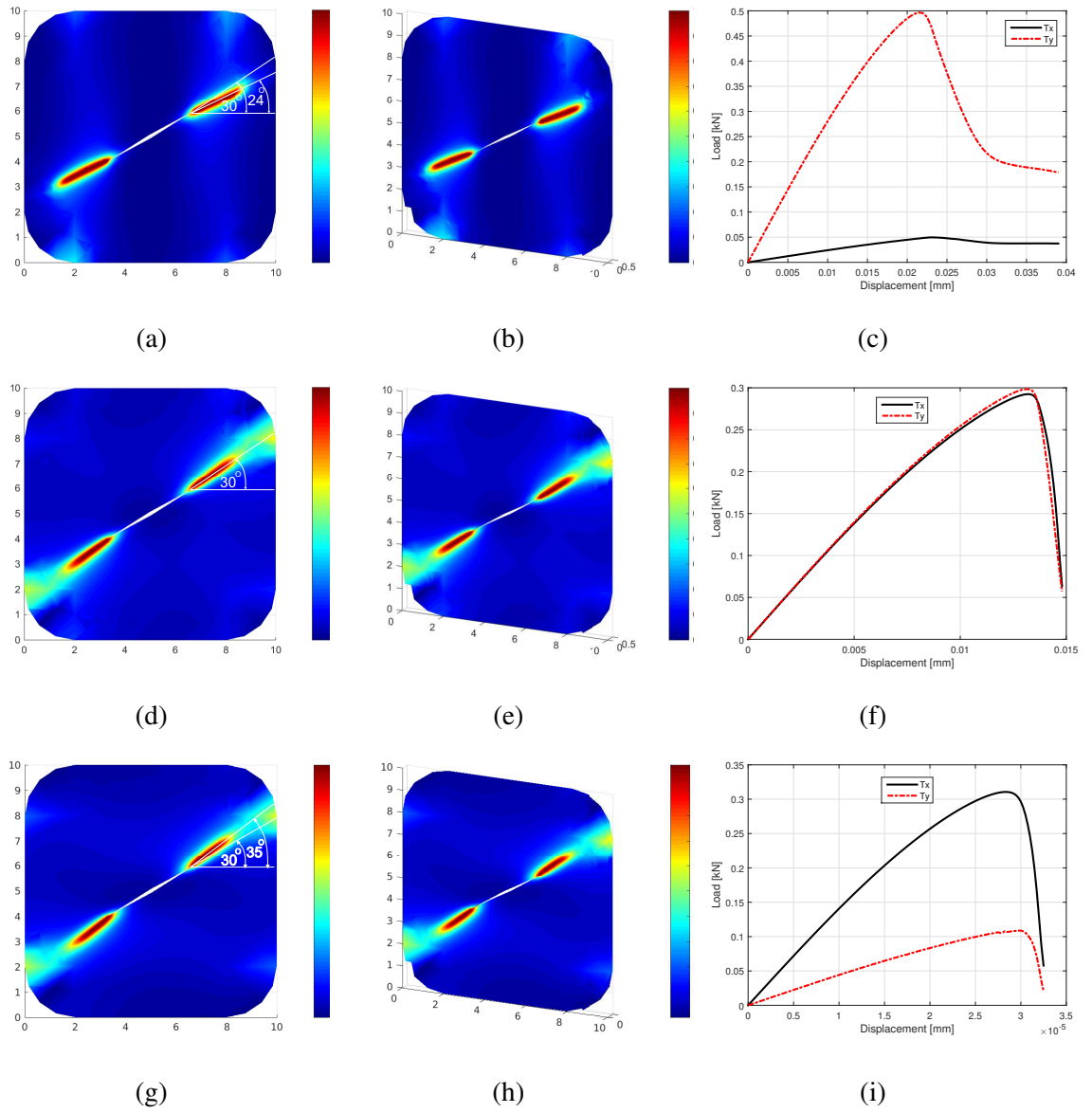


Figure 2.30: Crack extension angle θ_0 vs. crack inclination angle $\alpha=30^\circ$ for various values of biaxial load parameter for Glass-epoxy by phase field method of solution 1: a) $k = 0.1$, b) $k = 0.5$, c) $k = 1$, d) $k = 3$ (in the 3D case). Note that, the load-displacement curves are drawn corresponding to the displacement values of the vertical direction.

The toughness $g_c=0.2\text{N/mm}$, the anisotropy coefficient $\eta = 20$ and the length parameter $l = 0.1$ mm. We use the two proposed solutions to investigate the direction of the crack propagation with only one value of $\alpha = 30^\circ$ and the values of coefficient $k = 0.1, 1$ and 3 in the relation $T_x = kT_y$. The resulting crack propagations for these values with the two present solutions are shown in Fig.2.30 to Fig.2.31, respectively.

It can be seen that the results of the solutions in the 3D case are similar to the results in the 2D case as well as the analytical results of [47]. This proves that the two proposed solutions work well for

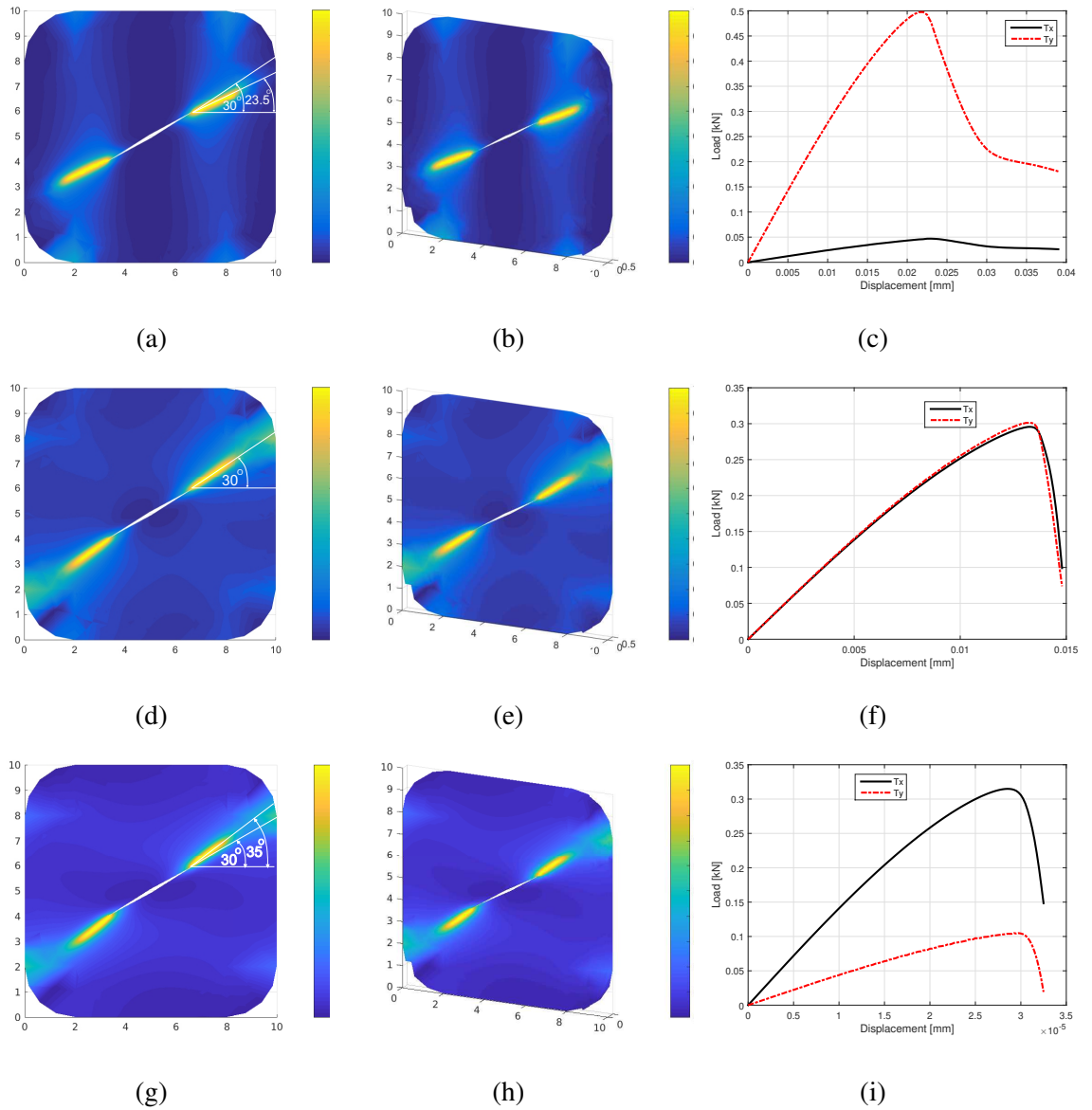


Figure 2.31: Crack extension angle θ_0 vs. crack inclination angle $\alpha=30^\circ$ for various values of biaxial load parameter for Glass-epoxy by phase field method of solution 2: a) $k = 0.1$, b) $k = 0.5$, c) $k = 1$, d) $k = 3$ (in the 3D case). Note that, the load-displacement curves are drawn corresponding to the displacement values of the vertical direction.

solving the problem of predicting crack propagation in orthotropic materials.

2.4.8 Bi-axial tension test of an orthotropic material plate made of a Graphite-epoxy composite and containing an initial crack

An orthotropic Graphite-epoxy plate is pulled in both horizontal direction and vertical direction. The geometric dimensions as well as the loading conditions are also depicted in Fig.2.17.

The Graphite-epoxy material parameters (see [46]) are as: $E_1 = 160\text{GPa}$, $E_2 = 15.5\text{GPa}$, $G_{12} =$

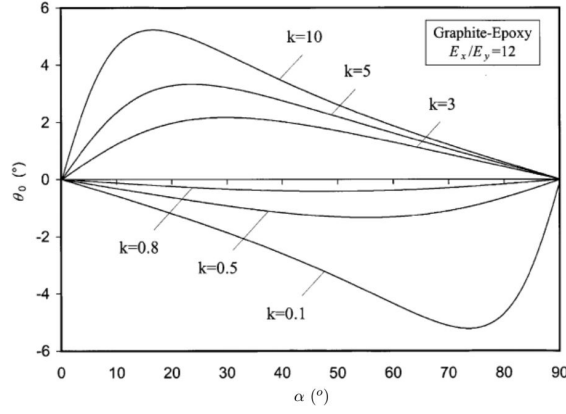


Figure 2.32: Crack extension angle θ_0 vs. crack inclination angle α for various values of biaxial load parameter for the orthotropic material of Graphite-epoxy (this figure in [47])

5.6GPa, $\nu_{12} = \nu_{13} = 0.34$, $\nu_{31} = \nu_{21} = \frac{E_2}{E_1}\nu_{12}$, $\nu_{23} = 0.43$. The toughness is $g_c=0.2\text{N/mm}$. Similarly, from the equation (2.27) and the relation $\mathbf{C}_0 = \mathbf{L}^{-1}$, we have:

$$\mathbf{C}_0 = \begin{bmatrix} 166.5 & 9.62 & 0 \\ 9.62 & 19.57 & 0 \\ 0 & 0 & 5.6 \end{bmatrix} \text{ GPa} \quad (2.77)$$

From (2.30), we have the elastic matrix \mathbf{C} according to the angle α of the fiber and \mathbf{P} is specified as (2.29). The anisotropy coefficient $\eta = 20$ and the length parameter $l = 0.1$ mm. During the simulation progress, we use a monotonic displacement driven loading with constant displacement increments Δu_y and $\Delta u_x = k_1 \Delta u_y$ to create the effect of force $T_x = kT_y$. In this problem, we use also one damage variable d and the strain orthogonal decomposition in (2.18) and (2.35).

Fig.2.32 shows the analytical results of the crack extension angle θ_0 for the angle of initial crack α and several various values of the biaxial load ratio k in the orthotropic Graphite-epoxy material in [47].

The resulting crack propagations for the different values of α and k with the two present solutions are shown in Fig.2.33 to Fig.2.42, respectively.

Similarly, for the crack extension angle θ_0 , we make comparisons between the analytical results of [47] and the simulation results obtained by the two proposed solutions as in Fig.2.43 with graphite-epoxy material. From this table, we note that, the results of the two present solutions and [47] are the same.

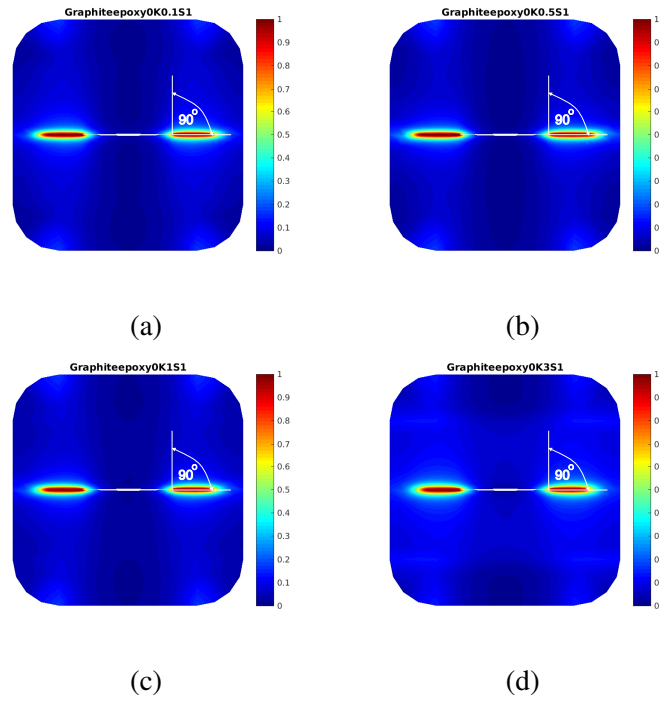


Figure 2.33: Crack extension angle θ_0 vs. crack inclination angle $\alpha=0^\circ$ for various values of biaxial load parameter for Graphite-epoxy by phase field method of solution 1: a) $k = 0.1$, b) $k = 0.5$, c) $k = 1$, d) $k = 3$.

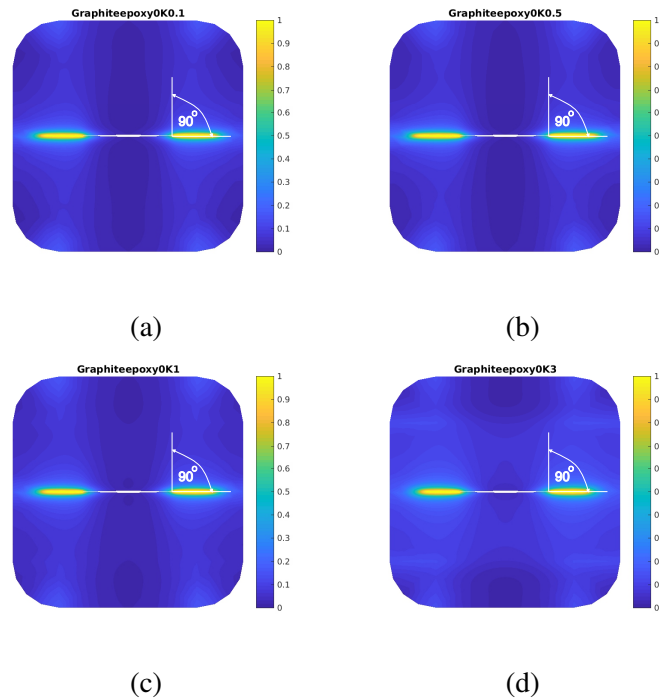


Figure 2.34: Crack extension angle θ_0 vs. crack inclination angle $\alpha=0^\circ$ for various values of biaxial load parameter for Graphite-epoxy by phase field method of solution 2: a) $k = 0.1$, b) $k = 0.5$, c) $k = 1$, d) $k = 3$.

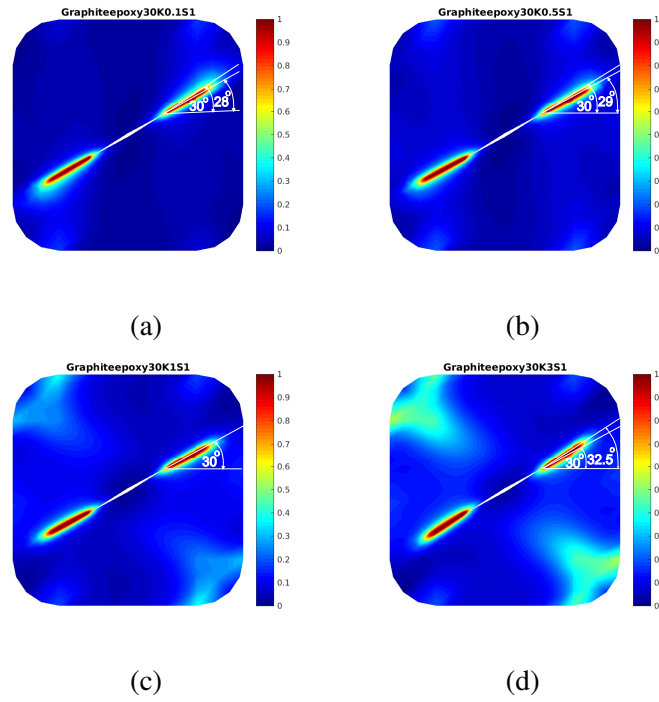


Figure 2.35: Crack extension angle θ_0 vs. crack inclination angle $\alpha=30^\circ$ for various values of biaxial load parameter for Graphite-epoxy by phase field method of solution 1: a) $k = 0.1$, b) $k = 0.5$, c) $k = 1$, d) $k = 3$.

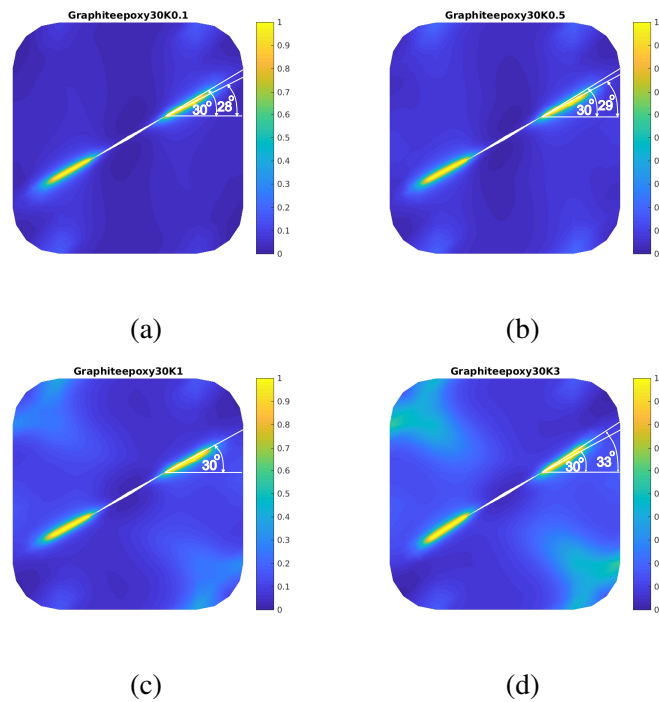


Figure 2.36: Crack extension angle θ_0 vs. crack inclination angle $\alpha=30^\circ$ for various values of biaxial load parameter for Graphite-epoxy by phase field method of solution 2: a) $k = 0.1$, b) $k = 0.5$, c) $k = 1$, d) $k = 3$.

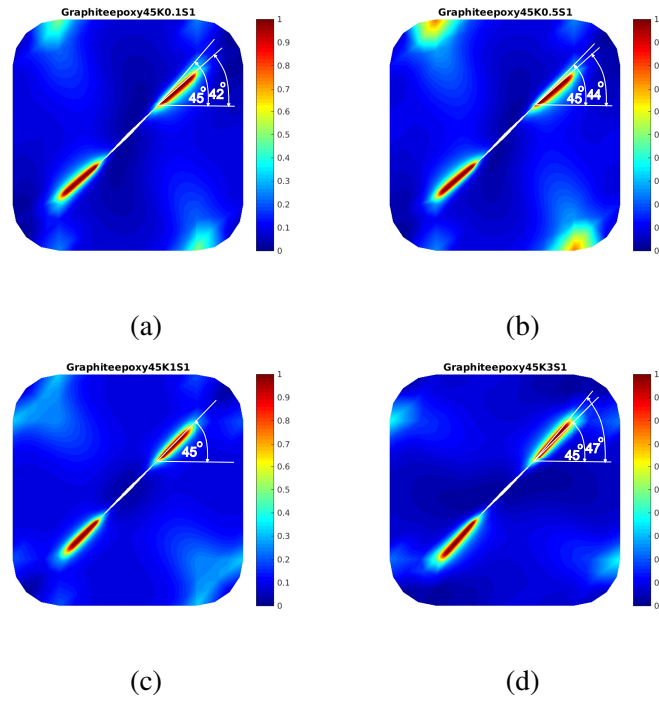


Figure 2.37: Crack extension angle θ_0 vs. crack inclination angle $\alpha=45^\circ$ for various values of biaxial load parameter for Graphite-epoxy by phase field method of solution 1: a) $k = 0.1$, b) $k = 0.5$, c) $k = 1$, d) $k = 3$.

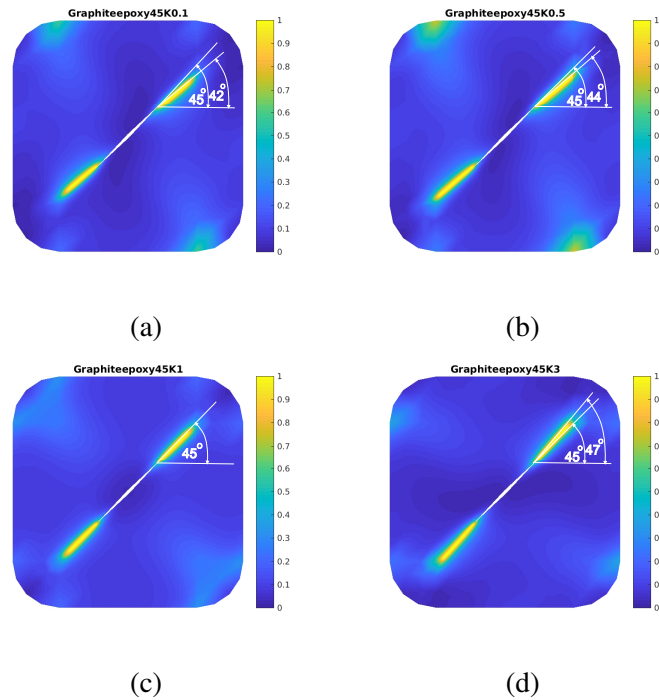


Figure 2.38: Crack extension angle θ_0 vs. crack inclination angle $\alpha=45^\circ$ for various values of biaxial load parameter for Graphite-epoxy by phase field method of solution 2: a) $k = 0.1$, b) $k = 0.5$, c) $k = 1$, d) $k = 3$.

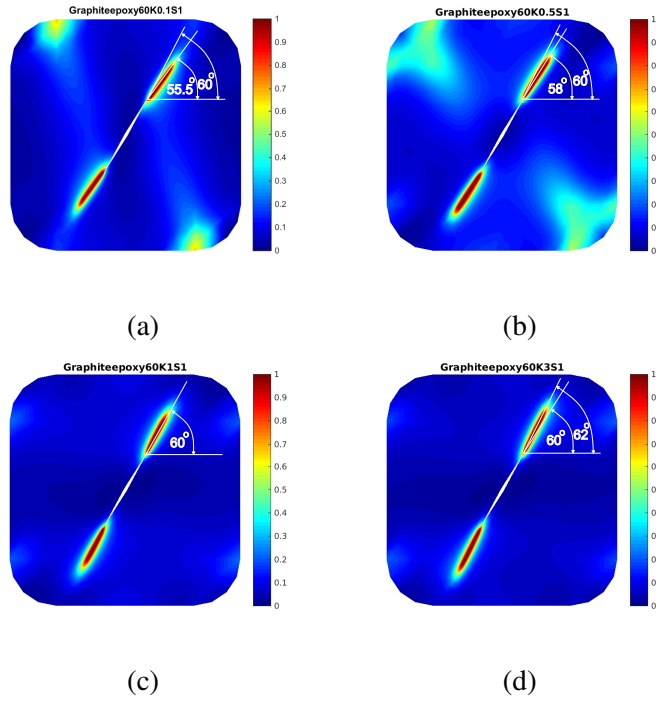


Figure 2.39: Crack extension angle θ_0 vs. crack inclination angle $\alpha=60^\circ$ for various values of biaxial load parameter for Graphite-epoxy by phase field method of solution 1: a) $k = 0.1$, b) $k = 0.5$, c) $k = 1$, d) $k = 3$.

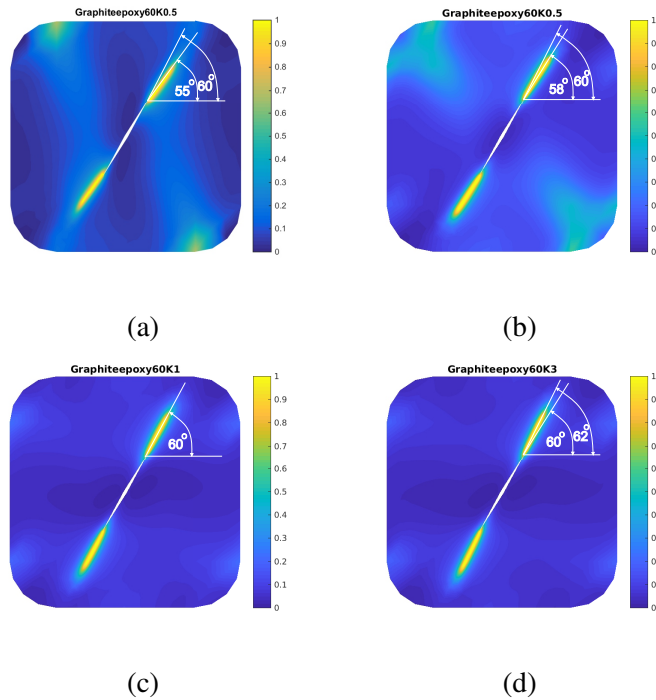


Figure 2.40: Crack extension angle θ_0 vs. crack inclination angle $\alpha=60^\circ$ for various values of biaxial load parameter for Graphite-epoxy by phase field method of solution 2: a) $k = 0.1$, b) $k = 0.5$, c) $k = 1$, d) $k = 3$.

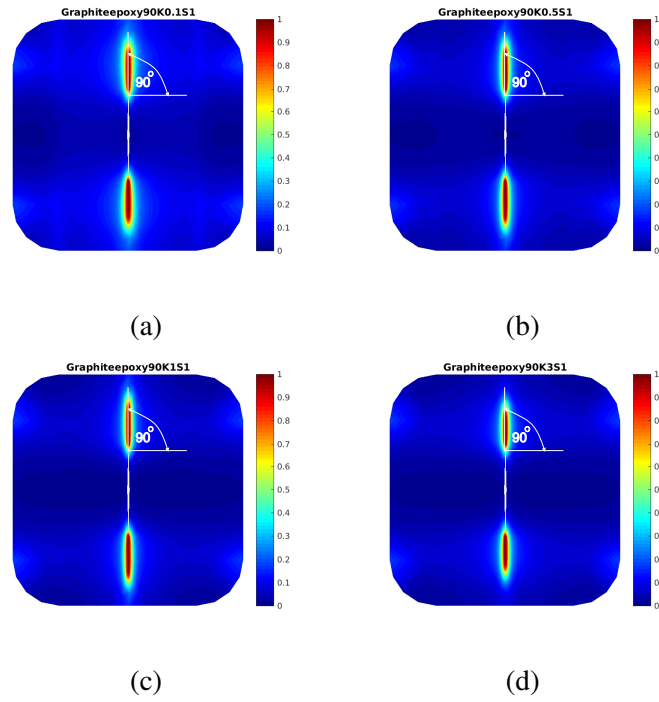


Figure 2.41: Crack extension angle θ_0 vs. crack inclination angle $\alpha=90^\circ$ for various values of biaxial load parameter for Graphite-epoxy by phase field method of solution 1: a) $k = 0.1$, b) $k = 0.5$, c) $k = 1$, d) $k = 3$.

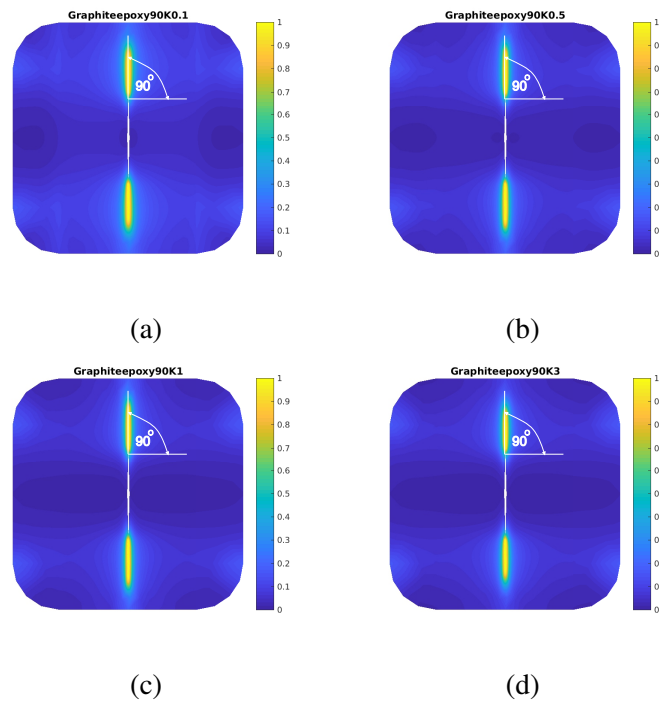


Figure 2.42: Crack extension angle θ_0 vs. crack inclination angle $\alpha=90^\circ$ for various values of biaxial load parameter for Graphite-epoxy by phase field method of solution 2: a) $k = 0.1$, b) $k = 0.5$, c) $k = 1$, d) $k = 3$.

Comparison of the crack extension angles $\theta(\alpha)$ between the analytical method and the proposed solutions of Graphite-epoxy material						
α (o)	k	Analytical method $\theta(\alpha)$	Simulation of Solution 1 $\theta(\alpha)$	Simulation of Solution 2 $\theta(\alpha)$	Correction 1(%)	Correction 2(%)
0	0,1	0	0	0	0,0	0,0
	0,5	0	0	0	0,0	0,0
	1	0	0	0	0,0	0,0
	3	0	0	0	0,0	0,0
30	0,1	-2	-2	-2	0,0	0,0
	0,5	-1	-1	-1	0,0	0,0
	1	0	0	0	0,0	0,0
	3	2,5	2,5	3	0,0	20,0
45	0,1	-3	-3	-3	0,0	0,0
	0,5	-1	-1	-1	0,0	0,0
	1	0	0	0	0,0	0,0
	3	2	2	2	0,0	0,0
60	0,1	-5	-4,5	-5	10,0	0,0
	0,5	-2	-2	-2	0,0	0,0
	1	0	0	0	0,0	0,0
	3	2	2	2	0,0	0,0
90	0,1	0	0	0	0,0	0,0
	0,5	0	0	0	0,0	0,0
	1	0	0	0	0,0	0,0
	3	0	0	0	0,0	0,0

Figure 2.43: Comparison between the analytical method in [47] and the proposed solutions of the crack extension angles θ_0 which depends on the initial crack direction α with Graphite-epoxy material.

2.5 Conclusions

In the present work, the strain orthogonal decompositions of [39], successfully applied in the phase field modeling to model and simulate isotropic and orthotropic damage.

The first three examples in both 2D and 3D cases for the modeling and simulation of the crack propagation in isotropic material. We can see that two proposed solutions give the very reliable results and they are good tools to predict the crack evolution.

Next, the two aforementioned solutions by using only one damage variable d instead of multiple damage variables d_i and using the strain orthogonal decompositions to model the crack path in orthotropic material through the next some numerical results. Our present solutions are able to provide the good results which respect to the reference ones.

Chapter 3

Modeling and simulation of crack propagation in heterogeneous materials by phase-field method with interfacial damage

The phase-field method has become a robust tool to describe the complex crack nucleation and propagation in heterogeneous materials. In these materials, an interaction between bulk brittle damage and interfacial damage through the splitting the strain tensor into a bulk strain part and a jump strain part at the interfaces introduced in Nguyen *et al.* [19]. Moreover, the material response of the heterogeneous materials in tension and compression, the bulk strain part needs to be decomposed into a positive part and a negative part (see, e.g, [19]). Most of the previous works, these decompositions do not verify the negative part be orthogonal the positive part, which lead to the inaccuracy in the material mechanical behavior. To solve the shortcomings, a recent theoretical study of He [39] proposed the strain orthogonal decompositions problem that is applied to decompose the bulk strain in our work. In the present work, we combine the phase-field modeling taking into account interfacial damage with the problem of the bulk strain orthogonal decompositions by two proposed solutions. The successful prediction of the crack propagation for two phases materials and X-ray microtomography image-based multi-phases materials by the proposed solutions will be demonstrated in several numerical examples.

3.1 Introduction

One of the main objectives of fracture mechanics is to predict the crack nucleation and propagation of materials. Many previous works have been done in both experimental and numerical approaches

to reach this goal. Griffith [7] and Irwin [40] have placed an important milestone in the problem of predicting the crack nucleation by developing the Linear Elastic Fracture Mechanic (LEFM) theory in which the stress field is calculated using the theory of elasticity. From the stress field obtained, the stress intensity factor (SIF) is defined and the crack will grow when this stress intensity factor exceeds the material fracture toughness. Based on this theory, Francfort and Marigo [8] and Bourdin et al. [20] proposed the variational approach to fracture relative to a global minimization of the total energy allowing to numerically solve the problem determining the crack nucleation and propagation for complex structures. Then, Pham et al. [27] used the variational framework for brittle fracture with the principles of irreversibility, stability and energy balance into the phase-field method to solve a homogeneous one-dimensional bar. Next, the authors of the works [9, 10, 11, 16] proposed a regularized description of discontinuities to replace the surface of the crack to improve the phase-field modeling.

In multi-phase materials, in order to model the spread of complex cracks, especially in the interfacial zone between two phases, many previous studies have been given the Cohesive Zone Model (CZM) concept which was proposed in first by Barenblatt [62] and Dugdale [63]. Then, in the works [64, 65, 66], the CZM have been applied into Finite Element Method (FEM) to handle the fracture at the crack tip in brittle and ductile materials. In the CZM framework, one of the softening curves describing the relation between the traction and displacement jump across the cohesive surface as linear, exponential, hyperbolic and Cornelissen's curves can be used to determine the separation state of the cohesive surface.

To simulate a network of the complex cracks as well as the interface between the matrix and inclusion phases, we need to smooth the mesh size to determine accurately the direction of the normal vectors at the nodes of elements. Several methods can find and refine the mesh size at the interfacial zone while the remaining zone can place the coarser meshes by additional functions such as viewpoint method presented in [67] and Extended Isogeometric Analysis (XIGA) in [68].

In the materials which have the highly complex microstructures and the random distribution of the multi-phases, the problem of determining the interfaces between the phases is necessary to identify their phase components. An experimental method based on the pixel-image as X-ray microtomography is widely applied to solve this problem (see, e.g, [69, 70, 71, 72, 73, 74, 75, 76, 77]). The phase-field modeling proposed by [19] to predict the crack propagation in realistic microstructures obtained by X-ray microtomography gave the very reliable results.

In a recent theoretical study presented in [39], the authors proposed the strain decomposition into a negative and positive parts which are orthogonal in the sense of an inner product where the elastic

stiffness tensor acts as a metric tensor. This described realistic and accuracy in mechanical behaviors of materials. In this work, we used the strain decomposition proposed in [39] associated with the work [19] to improve accuracy in terms of mechanical behaviors into account interfacial damage. The principal advantages of this method are: (a) the orthogonality condition is satisfied in the bulk strain decomposition; (b) multiple complex crack nucleation and propagation can be easily solving without mesh independent; (c) two solutions based on orthogonality condition are applied for numerical simulation.

The overview of the chapter is as follows: Section 3.2 gives the detailed phase-field framework taking into account the interfacial damage associated with the strain orthogonal decompositions. The FEM discretization for the phase-field problem and for the displacement problem are detailed. In Section 3.3, several numerical examples using two solutions are presented. Finally, conclusions and perspectives are drawn in Section 3.4.

3.2 Phase-field modeling of bulk crack and interfaces

In this section, we introduce a numerical modeling based on the phase-field modeling taking into account the interfacial damage. The combination allows predicting crack propagations and improving the accuracy in the mechanical response of heterogeneous materials. The main concept is introduced in the following.

3.2.1 Regularized representation of free discontinuous field

We consider a domain $\Omega \in \mathbb{R}^{\mathcal{D}}$ occupied by a heterogeneous solid, with $\mathcal{D} \in [2, 3]$ being the space dimension and $\partial\Omega \in \mathbb{R}^{\mathcal{D}-1}$ is the external boundary of domain Ω . The interface between the component phases of $\Omega \in \mathbb{R}^{\mathcal{D}}$ is denoted by Γ^I and the crack surface is denoted by Γ (see Fig. 3.1a). In a regularized framework, the geometry of interface between different phases is described by a fixed scalar parameter $\beta(\mathbf{x})$ (see Fig. 3.1b), and the geometry of propagating crack is approximately defined by a scalar parameter $d(\mathbf{x}, t)$, with $\mathbf{x} \in \Omega$ (see Fig. 3.1c). Here, l_d and l_β are the regularization lengths describing the actual widths of the smeared cracks and material interfaces, respectively. In what follows, we make the assumption that $l = l_d = l_\beta$ for the sake of simplicity in the simulation. In the initial state, i.e. $t = 0$, the phase-field $d(\mathbf{x}) = d(\mathbf{x}, 0)$ can be obtained by solving the following equations in Ω (see, e.g, [16]):

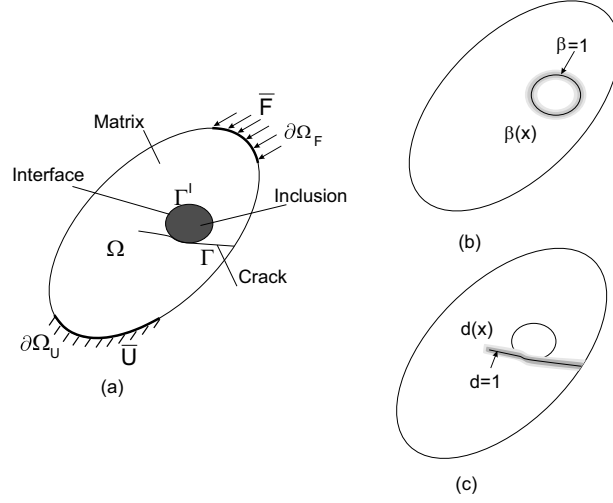


Figure 3.1: Regularized representation of a crack and an interface: (a) Solid containing an interface and a crack; (b) Regularized representation of the interface; (c) Regularized representation of the crack.

$$\begin{cases} d - l^2 \Delta d = 0 & \text{in } \Omega \\ d(\mathbf{x}) = 1 & \text{on } \Gamma \\ \nabla d(\mathbf{x}) \cdot \mathbf{n} = 0 & \text{on } \partial\Omega \end{cases} \quad (3.1)$$

where Δd is the Laplacian operator, when $l \rightarrow 0$ which will lead to the exact sharp crack on Γ ; and \mathbf{n} is the unit normal vector to the external boundary $\partial\Omega$. The problem described by Eq. (3.1) is equivalent to the following variational problem:

$$d(\mathbf{x}) = \text{Arg}\{\inf_{d \in \mathcal{S}_d} \Gamma_d(d)\} \quad \text{with} \quad \Gamma_d(d) = \int_{\Omega} \gamma_d(d, \nabla d) d\Omega, \quad (3.2)$$

where $\mathcal{S}_d = \{d(\mathbf{x}) \mid d(\mathbf{x}) = 1, \forall \mathbf{x} \in \Gamma\}$; Γ_d represents the total crack length per unit area in the two-dimensional case and total crack area of per unit volume in the three-dimensional case, and $\gamma_d(d, \nabla d)$ is defined by

$$\gamma_d(d, \nabla d) = \gamma(d, \nabla d) = \frac{d^2}{2l} + \frac{l}{2} \nabla d \nabla d. \quad (3.3)$$

The interface phase-field $\beta(\mathbf{x})$ describing the damage of interfaces is obtained by:

$$\begin{cases} \beta(\mathbf{x}) - l^2 \Delta \beta(\mathbf{x}) = 0 & \text{in } \Omega \\ \beta(\mathbf{x}) = 1 & \text{on } \Gamma^I \\ \nabla \beta(\mathbf{x}) \cdot \mathbf{n} = 0 & \text{on } \partial\Omega \end{cases} \quad (3.4)$$

Moreover, it can be shown that Eq. (3.4) corresponds to the Euler-Lagrange expression related to the variational problem as follows:

$$\beta(\mathbf{x}, t) = \text{Arg}\{\inf_{\beta \in \mathcal{S}_\beta} \Gamma_\beta(\beta)\} \quad \text{with} \quad \Gamma_\beta(\beta) = \int_{\Omega} \gamma_\beta(\beta, \nabla \beta) d\Omega, \quad (3.5)$$

where $\mathcal{S}_\beta = \{\beta(\mathbf{x}) \mid \beta(\mathbf{x}) = 1, \forall \mathbf{x} \in \Gamma^I\}$ and Γ_β represents the total interface length per unit area in the two-dimensional case and total interface area of per unit volume in the three-dimensional case, and $\gamma_\beta(\beta, \nabla\beta)$ is defined by

$$\gamma_\beta(\beta, \nabla\beta) = \frac{\beta^2}{2l} + \frac{l}{2} \nabla\beta \nabla\beta. \quad (3.6)$$

It is important to notice that, unlike the crack phase-field $d(\mathbf{x}, t)$, the value of the interface phase-field $\beta(\mathbf{x})$ does not evolve during the simulation.

An approximation for the displacement jump at the interfaces is proposed by using the Taylor's expansion of the displacement field around a point \mathbf{x} located on the interface:

$$\llbracket \mathbf{u}(\mathbf{x}) \rrbracket \simeq \mathbf{w}(\mathbf{x}) = \mathbf{u} \left(\mathbf{x} + \frac{h}{2} \mathbf{n}^I \right) - \mathbf{u} \left(\mathbf{x} - \frac{h}{2} \mathbf{n}^I \right) = h \nabla \mathbf{u}(\mathbf{x}) \frac{\nabla \phi(\mathbf{x})}{\|\nabla \phi(\mathbf{x})\|} \quad (3.7)$$

where $\mathbf{w}(\mathbf{x})$ denotes the smoothed displacement jump approximation; $\mathbf{n}^I(\mathbf{x})$ is an approximation of the normal to the interface Γ^I at the point \mathbf{x} ; and $\phi(\mathbf{x})$ is the level-set function which is used to describe the interface Γ^I (see e.g. [19, 66]).

3.2.2 Energy functional

The total energy in the cracked solid containing interfaces can be expressed by:

$$E(\mathbf{u}, d) = \int_{\Omega} W_u^e(\boldsymbol{\varepsilon}_e(\mathbf{u}), d) d\Omega + \int_{\Omega} \{1 - \beta(\mathbf{x})\} g_c \gamma(d, \nabla d) d\Omega + \int_{\Omega} \Psi^I(\mathbf{w}(\mathbf{u}), \boldsymbol{\chi}) \gamma_\beta(\beta, \nabla\beta) d\Omega \quad (3.8)$$

where g_c is the fracture toughness, Ψ^I is a strain density function related to the displacement jump across the interface Γ^I and $\boldsymbol{\chi}$ is a history parameter. The strain tensor $\boldsymbol{\varepsilon}(\mathbf{u}(\mathbf{x}))$ is split into two parts, $\boldsymbol{\varepsilon}_e$ and $\bar{\boldsymbol{\varepsilon}}(\mathbf{w}(\mathbf{x}))$, corresponding to the strain tensor of the bulk and the strain tensor induced by the smoothed jump at the interfaces such that $\bar{\boldsymbol{\varepsilon}} \rightarrow 0$ away from the interfaces (see e.g. [19]):

$$\boldsymbol{\varepsilon}(\mathbf{u}(\mathbf{x})) = \boldsymbol{\varepsilon}_e(\mathbf{u}(\mathbf{x})) + \bar{\boldsymbol{\varepsilon}}(\mathbf{w}(\mathbf{x})) \quad (3.9)$$

From Eq. (3.8), the total free energy W can be written therefore as follows:

$$W(\mathbf{u}, d) = W_u^e(\boldsymbol{\varepsilon}_e(\mathbf{u}), d) + \{1 - \beta(\mathbf{x})\} g_c \gamma(d, \nabla d) + \Psi^I(\mathbf{w}(\mathbf{u}), \boldsymbol{\chi}) \gamma_\beta(\beta, \nabla\beta) \quad (3.10)$$

By accounting for the asymmetric tensile-compressive behavior, the strain tensor is now decomposed into a positive part and negative part and the damage is assumed to be only developed by the positive part. Following the work of [39], the bulk strain $\boldsymbol{\varepsilon}_e$ is decomposed as follows:

$$\boldsymbol{\varepsilon}_e = \boldsymbol{\varepsilon}_e^+ + \boldsymbol{\varepsilon}_e^- \quad (3.11)$$

and the elastic energy function at the undamaged state is written as:

$$\Psi^e(\boldsymbol{\varepsilon}_e) = \Psi^e(\boldsymbol{\varepsilon}_e^+ + \boldsymbol{\varepsilon}_e^-) = \frac{1}{2}\boldsymbol{\varepsilon}_e^+ : (\mathbb{C}\boldsymbol{\varepsilon}_e^+) + \frac{1}{2}\boldsymbol{\varepsilon}_e^- : (\mathbb{C}\boldsymbol{\varepsilon}_e^-) + \boldsymbol{\varepsilon}_e^+ : (\mathbb{C}\boldsymbol{\varepsilon}_e^-). \quad (3.12)$$

From (3.12), we have immediately that the elastic energy decomposition

$$\Psi_e(\boldsymbol{\varepsilon}_e) = \Psi_e^+(\boldsymbol{\varepsilon}_e^+) + \Psi_e^-(\boldsymbol{\varepsilon}_e^-) \quad (3.13)$$

with

$$\Psi_e^+(\boldsymbol{\varepsilon}_e^+) = \frac{1}{2}\boldsymbol{\varepsilon}_e^+ : (\mathbb{C}\boldsymbol{\varepsilon}_e^+) \quad \text{and} \quad \Psi_e^-(\boldsymbol{\varepsilon}_e^-) = \frac{1}{2}\boldsymbol{\varepsilon}_e^- : (\mathbb{C}\boldsymbol{\varepsilon}_e^-), \quad (3.14)$$

holds if and only if

$$\boldsymbol{\varepsilon}_e^+ : (\mathbb{C}\boldsymbol{\varepsilon}_e^-) = 0. \quad (3.15)$$

This necessary and sufficient condition is satisfied if $\boldsymbol{\varepsilon}_e^+$ be orthogonal to $\boldsymbol{\varepsilon}_e^-$ in the sense of the inner product with \mathbb{C} acting as a metric tensor. Next, by choosing the scalar phase-field d to describe the damage state of the material, the elastic energy function W_u^e of the damaged material becomes

$$W_u^e(\boldsymbol{\varepsilon}_e(\mathbf{u}), d) = \{g(d) + k\}\Psi_e^+(\boldsymbol{\varepsilon}_e^+) + \Psi_e^-(\boldsymbol{\varepsilon}_e^-) \quad (3.16)$$

where the degradation function $g(d)$ in phase-field method takes the form of $g(d) = (1 - d)^2$ (see, e.g., [16]) and k is a very small value to maintain the well-posedness of the structure behaviors.

To satisfy the orthogonal condition (3.15), the general approach proposed recently in [39] is adopted.

By defining the transformed strain space $\tilde{\mathcal{E}}_e$ of the strain space \mathcal{E}_e such as $\tilde{\mathcal{E}}_e = \{\tilde{\boldsymbol{\varepsilon}}_e \mid \tilde{\boldsymbol{\varepsilon}}_e = \mathbb{C}^{1/2}\boldsymbol{\varepsilon}_e, \forall \boldsymbol{\varepsilon}_e \in \mathcal{E}_e\}$, this transformed strain space $\tilde{\mathcal{E}}_e$ is now separated into two convex subsets $\tilde{\mathcal{K}}_e^+$ and $\tilde{\mathcal{K}}_e^-$ such that

$$\tilde{\mathcal{E}}_e = \tilde{\mathcal{K}}_e^+ \oplus \tilde{\mathcal{K}}_e^-. \quad (3.17)$$

Thus, any element $\tilde{\boldsymbol{\varepsilon}}_e \in \tilde{\mathcal{E}}_e$ can be split into a positive part $\tilde{\boldsymbol{\varepsilon}}_e^+ \in \tilde{\mathcal{K}}_e^+$ and a negative part $\tilde{\boldsymbol{\varepsilon}}_e^- \in \tilde{\mathcal{K}}_e^-$ such that

$$\tilde{\boldsymbol{\varepsilon}}_e = \tilde{\boldsymbol{\varepsilon}}_e^+ + \tilde{\boldsymbol{\varepsilon}}_e^- \quad (3.18)$$

and

$$\tilde{\boldsymbol{\varepsilon}}_e^+ : \tilde{\boldsymbol{\varepsilon}}_e^- = 0. \quad (3.19)$$

Moreover, we demande that $\tilde{\boldsymbol{\varepsilon}}_e^+$ and $\tilde{\boldsymbol{\varepsilon}}_e^-$ correspond therefore the projections of a given $\tilde{\boldsymbol{\varepsilon}}_e \in \tilde{\mathcal{E}}_e$ on $\tilde{\mathcal{K}}_e^+$ and $\tilde{\mathcal{K}}_e^-$ in the variational sense that

$$\|\tilde{\boldsymbol{\varepsilon}}_e - \tilde{\boldsymbol{\varepsilon}}_e^\pm\|^2 = \min_{\tilde{\boldsymbol{\varepsilon}} \in \tilde{\mathcal{K}}_e^\pm} (\tilde{\boldsymbol{\varepsilon}}_e - \tilde{\boldsymbol{\varepsilon}}) : (\tilde{\boldsymbol{\varepsilon}}_e - \tilde{\boldsymbol{\varepsilon}}). \quad (3.20)$$

The choice of the convex subsets $\tilde{\mathcal{K}}_e^+$ and $\tilde{\mathcal{K}}_e^-$ is not unique. We now consider two following cases:

Case 1: The choice for $\tilde{\mathcal{K}}_e^+$ and $\tilde{\mathcal{K}}_e^-$ is such as:

$$\tilde{\mathcal{K}}_e^+ = \{\tilde{\boldsymbol{\varepsilon}}_e \in \tilde{\mathcal{E}}_e | \text{Tr}(\tilde{\boldsymbol{\varepsilon}}_e) \geq 0\} \quad \text{and} \quad \tilde{\mathcal{K}}_e^- = \{\tilde{\boldsymbol{\varepsilon}}_e \in \tilde{\mathcal{E}}_e | \tilde{\boldsymbol{\varepsilon}}_e = a\mathbf{1}, a \leq 0\}. \quad (3.21)$$

It can be shown from (3.20) and (3.21) that

$$\tilde{\boldsymbol{\varepsilon}}_e^+ = \frac{1}{\mathcal{D}} \langle \text{Tr}(\tilde{\boldsymbol{\varepsilon}}_e) \rangle_+ \mathbf{1} + \tilde{\boldsymbol{\varepsilon}}_e^D, \quad \tilde{\boldsymbol{\varepsilon}}_e^- = \frac{1}{\mathcal{D}} \langle \text{Tr}(\tilde{\boldsymbol{\varepsilon}}_e) \rangle_- \mathbf{1} \quad (3.22)$$

where $\mathbf{1}$ denotes the \mathcal{D} -dimensional identity tensor, $\langle x \rangle_{\pm} = (x \pm |x|)/2$ and the deviatoric strain tensor is defined by

$$\tilde{\boldsymbol{\varepsilon}}_e^D = \tilde{\boldsymbol{\varepsilon}}_e - \frac{1}{\mathcal{D}} \text{Tr}(\tilde{\boldsymbol{\varepsilon}}_e) \mathbf{1}. \quad (3.23)$$

Once $\tilde{\boldsymbol{\varepsilon}}_e^+$ and $\tilde{\boldsymbol{\varepsilon}}_e^-$ have been obtained, $\boldsymbol{\varepsilon}_e^+$ and $\boldsymbol{\varepsilon}_e^-$ can be directly determined by

$$\boldsymbol{\varepsilon}_e^+ = \mathbf{C}^{-1/2} \tilde{\boldsymbol{\varepsilon}}_e^+, \quad \boldsymbol{\varepsilon}_e^- = \mathbf{C}^{-1/2} \tilde{\boldsymbol{\varepsilon}}_e^- \quad (3.24)$$

and we obtain

$$\Psi_e^+(\boldsymbol{\varepsilon}_e^+) = \frac{1}{2} \mathbf{C} : \boldsymbol{\varepsilon}_e^+ : \boldsymbol{\varepsilon}_e^+ = \frac{1}{2} \left\{ \frac{1}{\mathcal{D}} \langle \text{Tr}(\tilde{\boldsymbol{\varepsilon}}_e) \rangle_+ \mathbf{1} + \tilde{\boldsymbol{\varepsilon}}_e^D \right\} : \left\{ \frac{1}{\mathcal{D}} \langle \text{Tr}(\tilde{\boldsymbol{\varepsilon}}_e) \rangle_+ \mathbf{1} + \tilde{\boldsymbol{\varepsilon}}_e^D \right\}, \quad (3.25)$$

$$\Psi_e^-(\boldsymbol{\varepsilon}_e^-) = \frac{1}{2} \mathbf{C} : \boldsymbol{\varepsilon}_e^- : \boldsymbol{\varepsilon}_e^- = \frac{1}{2} \left\{ \frac{1}{\mathcal{D}} \langle \text{Tr}(\tilde{\boldsymbol{\varepsilon}}_e) \rangle_- \mathbf{1} \right\} : \left\{ \frac{1}{\mathcal{D}} \langle \text{Tr}(\tilde{\boldsymbol{\varepsilon}}_e) \rangle_- \mathbf{1} \right\}. \quad (3.26)$$

Case 2: The choice for $\tilde{\mathcal{K}}_e^+$ and $\tilde{\mathcal{K}}_e^-$ is such as:

$$\tilde{\mathcal{K}}_e^+ = \{\tilde{\boldsymbol{\varepsilon}}_e \in \tilde{\mathcal{E}}_e | \mathbf{x}(\tilde{\boldsymbol{\varepsilon}}_e \mathbf{x}) \geq 0, \forall \mathbf{x} \in \mathbb{R}^{\mathcal{D}}\} \quad \text{and} \quad \tilde{\mathcal{K}}_e^- = \{\tilde{\boldsymbol{\varepsilon}}_e \in \tilde{\mathcal{E}}_e | \mathbf{x}(\tilde{\boldsymbol{\varepsilon}}_e \mathbf{x}) \leq 0 \forall \mathbf{x} \in \mathbb{R}^{\mathcal{D}}\}. \quad (3.27)$$

Since (3.20) and (3.27), it can be demonstrated that

$$\tilde{\boldsymbol{\varepsilon}}_e^{\pm} = \sum_{i=1}^{\mathcal{D}} \langle \tilde{\boldsymbol{\varepsilon}}_e^i \rangle_{\pm} \tilde{\mathbf{n}}_i \otimes \tilde{\mathbf{n}}_i \quad (3.28)$$

where $\tilde{\boldsymbol{\varepsilon}}_e^i$ and $\tilde{\mathbf{n}}_i$ with $i = 1, \dots, \mathcal{D}$ are the ordered eigenvalues and eigenvectors of $\tilde{\boldsymbol{\varepsilon}}_e$ such that $\tilde{\boldsymbol{\varepsilon}}_e^1 \leq \tilde{\boldsymbol{\varepsilon}}_e^2 \leq \dots \leq \tilde{\boldsymbol{\varepsilon}}_e^{\mathcal{D}}$ and $\langle \tilde{\boldsymbol{\varepsilon}}_e^i \rangle_{\pm} = (\tilde{\boldsymbol{\varepsilon}}_e^i \pm |\tilde{\boldsymbol{\varepsilon}}_e^i|)/2$. This yields

$$\Psi_e^+(\boldsymbol{\varepsilon}_e^+) = \frac{1}{2} \tilde{\boldsymbol{\varepsilon}}_e^+ : \tilde{\boldsymbol{\varepsilon}}_e^+ = \frac{1}{2} \text{Tr}[(\tilde{\boldsymbol{\varepsilon}}_e^+)^2] \quad (3.29)$$

$$\Psi_e^-(\boldsymbol{\varepsilon}_e^-) = \frac{1}{2} \tilde{\boldsymbol{\varepsilon}}_e^- : \tilde{\boldsymbol{\varepsilon}}_e^- = \frac{1}{2} \text{Tr}[(\tilde{\boldsymbol{\varepsilon}}_e^-)^2]. \quad (3.30)$$

The evolution of the scalar phase-field variable d must satisfy the following reduced Clausius-Duhem inequality:

$$\mathcal{A} \dot{d} \geq 0 \quad \text{and} \quad \mathcal{A} = -\frac{\partial W}{\partial d}. \quad (3.31)$$

An assumption of a threshold function $\mathcal{F}(\mathcal{A})$ within no damage occurs is expressed as:

$$\mathcal{F}(\mathcal{A}) = \mathcal{A} \leq 0. \quad (3.32)$$

It can be shown that the condition $\mathcal{A}\dot{d} \geq 0$ will be satisfied if either $\mathcal{F} < 0$ and $\dot{d} = 0$ or $\mathcal{F} = 0$ and $\dot{d} > 0$. More precisely, the latter condition leads that, when $\dot{d} > 0$, we have

$$\mathcal{F} = -\frac{\partial W}{\partial d} = 2(1-d)\Psi_e^+ - (1-\beta)g_c\delta_d\gamma(d, \nabla d) = 0 \quad (3.33)$$

where the functional derivative $\delta_d\gamma(d)$ is defined by (see, e.g., [18])

$$\delta_d\gamma(d, \nabla d) = \frac{d}{l} - l\Delta d. \quad (3.34)$$

By introducing the strain history function introduced (see e.g. [19])

$$\mathcal{H}^e(\mathbf{x}, t) = \max_{\tau \in [0, t]} \{\Psi_e^+(\mathbf{x}, \tau)\} \quad (3.35)$$

Eq. (3.33) is now rewritten as follows:

$$2(1-d)\mathcal{H}^e - (1-\beta)g_c\delta_d\gamma(d, \nabla d) = 0. \quad (3.36)$$

Finally, the crack field $d(\mathbf{x}, t)$ can be computed by solving the following phase field problem:

$$\begin{cases} 2(1-d)\mathcal{H}^e - \frac{g_c}{l}(1-\beta)(d - l^2\Delta d) = 0 & \text{in } \Omega; \\ d(\mathbf{x}) = 1 & \text{on } \Gamma; \\ \nabla d(\mathbf{x}) \cdot \mathbf{n} = 0 & \text{on } \partial\Omega. \end{cases} \quad (3.37)$$

3.2.3 Resolution of the phase-field problem

Weak form of the phase-field problem

To compute the scalar phase-field parameter $d(\mathbf{x}, t)$, a temporal discretization is carried out at times $0, t_1, \dots, t_n, t_{n+1}, \dots$. By assuming that, at time $t = t_n$, the scalar phase-field parameter $d_n = d(\mathbf{x}, t_n)$ is known, the weak form used to compute $d_{n+1} = d(\mathbf{x}, t_{n+1})$ is expressed as follows:

$$\int_{\Omega} \left\{ \left(2\mathcal{H}_n^e + (1-\beta)\frac{g_c}{l} \right) d_{n+1}\delta d + (1-\beta)g_cl\nabla d_{n+1}\nabla(\delta d) \right\} d\Omega = \int_{\Omega} 2\mathcal{H}_n^e\delta d d\Omega. \quad (3.38)$$

FEM discretization of the phase-field problem

By applying the FEM, the phase field as well as the phase-field gradient are approximately calculated by:

$$d(\mathbf{x}) = \{\mathbf{N}_d(\mathbf{x})\}\{\mathbf{d}\} \text{ and } \nabla d(\mathbf{x}) = [\mathbf{B}_d(\mathbf{x})]\{\mathbf{d}\} \quad (3.39)$$

$$\delta d(\mathbf{x}) = \{\mathbf{N}_d(\mathbf{x})\}\{\delta \mathbf{d}\} \text{ and } \nabla \delta d(\mathbf{x}) = [\mathbf{B}_d(\mathbf{x})]\{\delta \mathbf{d}\} \quad (3.40)$$

where $\mathbf{N}_d(\mathbf{x})$ and $\mathbf{B}_d(\mathbf{x})$ are the matrix of shape function and matrix of shape function derivative associated with phase-field variable, respectively. By introducing the aforementioned FEM discretization into the weak form (3.38), the phase-field variable $d_{n+1} = d(\mathbf{x}, t_{n+1})$ can be calculated by:

$$\{\mathbf{d}\} = [\mathbf{K}_d]^{-1} \cdot \{\mathbf{F}_d\} \quad (3.41)$$

where the rigid matrix is determined by

$$[\mathbf{K}_d] = \int_{\Omega} \left\{ \left(\frac{g_c}{l} (1 - \beta) + 2\mathcal{H}_n^e \right) \{\mathbf{N}_d\}^T \{\mathbf{N}_d\} + g_c l (1 - \beta) [\mathbf{B}_d]^T [\mathbf{B}_d] \right\} d\Omega \quad (3.42)$$

and the force vector is defined by

$$\{\mathbf{F}_d\} = \int_{\Omega} 2\{\mathbf{N}_d\}^T \mathcal{H}_n^e d\Omega. \quad (3.43)$$

3.2.4 Resolution of the displacement problem

Weak form of the displacement problem

Using the variational principle for minimizing the total energy E with respect to the displacement \mathbf{u} , the weak form associated with the displacement problem can be formulated as

$$\int_{\Omega} \frac{\partial W_u^e}{\partial \boldsymbol{\varepsilon}_e} : \boldsymbol{\varepsilon}_e(\delta \mathbf{u}) d\Omega + \int_{\Omega} \frac{\partial \Psi^I(\mathbf{w}, \boldsymbol{\chi})}{\partial \mathbf{w}} \delta \mathbf{w} \gamma_{\beta}(\beta, \nabla \beta) d\Omega = \int_{\Omega} \mathbf{f} \cdot \delta \mathbf{u} d\Omega + \int_{\partial \Omega_F} \bar{\mathbf{F}} \cdot \delta \mathbf{u} d\Gamma \quad (3.44)$$

The detail about the weak form of the displacement problem, the FEM discretization of the displacement problem and the numerical framework are presented in **Appendix A.1**. The algorithm used in chapter 3 is summarized and provided in **Appendix B.3**.

3.3 Numerical examples

3.3.1 Symmetric three-point bending test

This example aims to study the crack propagation within a beam during a three-point bending test. Furthermore, two solutions of strain decompositions (3.21) and (3.27) are investigated in

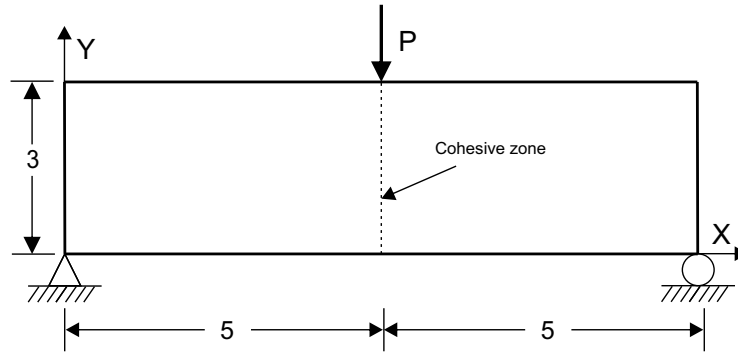


Figure 3.2: Symmetric three-point bending test: geometry and boundary conditions.

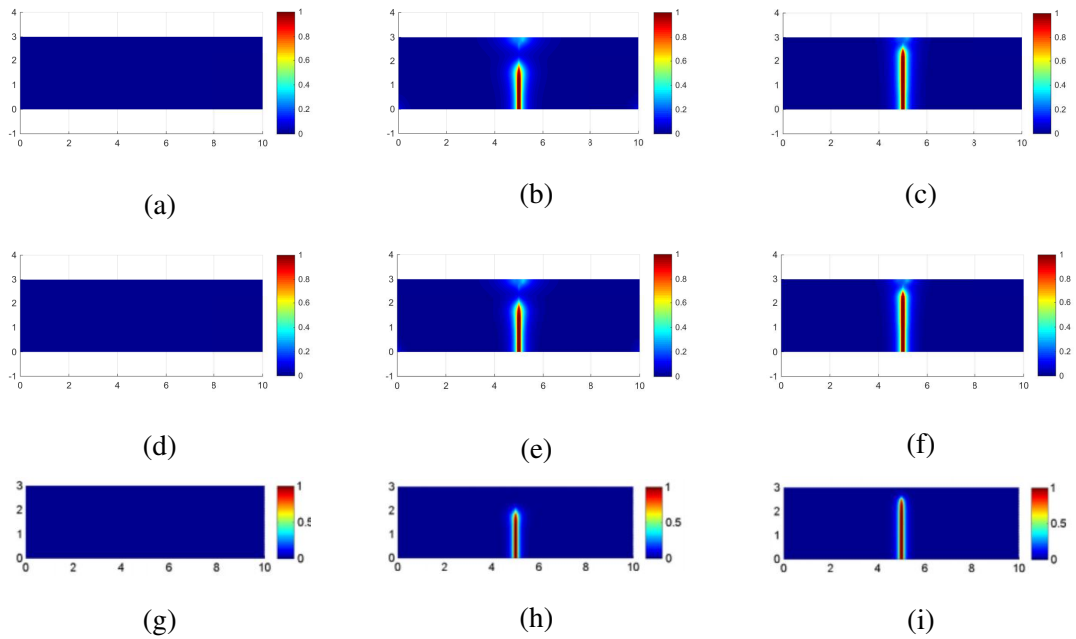


Figure 3.3: The evolution of the crack in symmetric three-point bending test: (a), (b) and (c) crack initiation and crack propagation for solution 1 corresponding to $U = 0$ mm, $U = 0.25$ mm, and $U = 0.35$ mm, respectively; (d), (e) and (f) crack initiation and crack propagation for solution 2 corresponding to $U = 0$ mm, $U = 0.25$ mm, and $U = 0.35$ mm, respectively; Figs. (g), (h) and (i) crack initiation and crack propagation presented in Nguyen et al. [19] corresponding to $U = 0$ mm, $U = 0.25$ mm, and $U = 0.35$ mm, respectively

this study. The beam under consideration in this study is assumed to have the same dimensions as the one used in [19] and [78]. The geometry of the structure and the loading conditions are depicted in Fig.3.2. The domain has an initial cohesive interface to validate the cohesive model. The dimensions of the beam are 10x3mm. The domain occupied by the beam is uniformly meshed into 200x60 quadrilateral elements. The boundary conditions are as follows: the left bottom corner

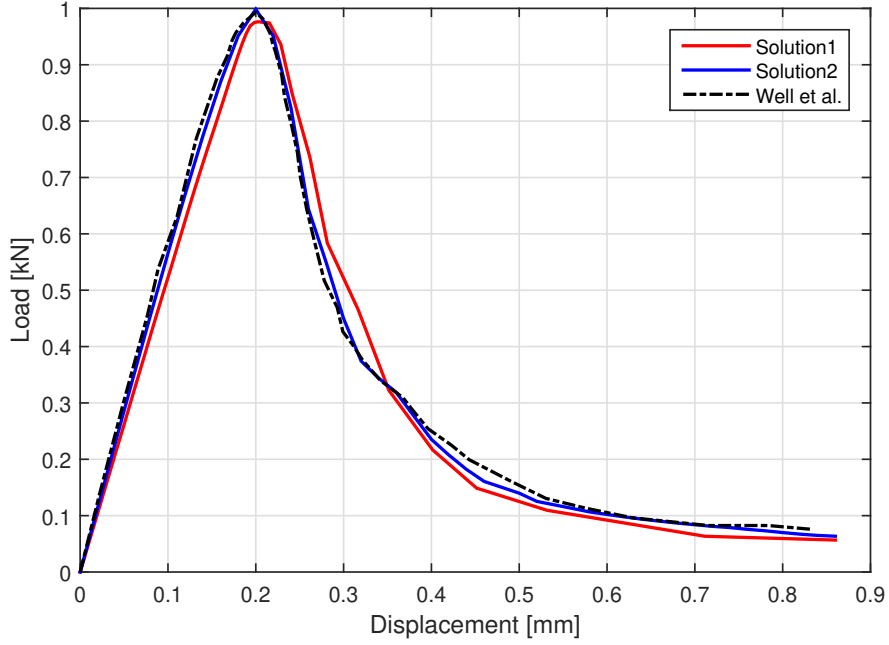


Figure 3.4: Symmetric three-point bending test: comparison of the load-displacement curves between Wells et al.[78] with two solutions of strain decompositions (3.21) and (3.27).

is fixed in two directions, while the right bottom corner the vertical displacement is fixed, and the horizontal displacement is free. The displacement is prescribed at the center on the upper end of the beam with monotonic increments of the displacement $\Delta u = -0.005\text{mm}$ for 170 load increments. The material properties of the beam are chosen as $E = 100\text{MPa}$, $\nu = 0.3$, the fracture toughness $g_c = g_c^I = 0.1\text{ N/mm}$ and the fracture strength $t_u = 1\text{ MPa}$. The regularization parameter l is chosen as $l = 0.15\text{mm}$. The plane strain assumption is adopted in our calculations.

By applying two solutions of strain decompositions (3.21) and (3.27), the evolutions of the crack are shown in Fig. 3.3(a-c) and Fig. 3.3(d-f) with different values of the prescribed displacement at the center on the upper end of the beam. These crack evolutions obtained in the work [19] are also presented in Fig. 3.3(g-i). The comparison of the load-displacement curves between two solutions of strain decompositions (3.21) and (3.27) with the result derived in [78] is shown in Fig. 3.4. In Nguyen *et al.* [19], we can find the comparison of the behavior curves between [19] and [78]. From the comparison of both the evolution of the crack and the mechanical behavior in Fig. 3.3 and Fig. 3.4, we can see that our computations with two proposed strain decompositions (3.21) and (3.27) are practically efficient and accurate to simulate the crack propagation taking into account the interfacial damage.

3.3.2 Delamination peel test

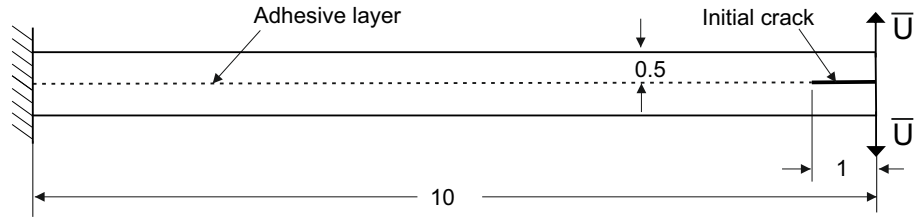


Figure 3.5: Geometry and boundary conditions of the delamination peel test.

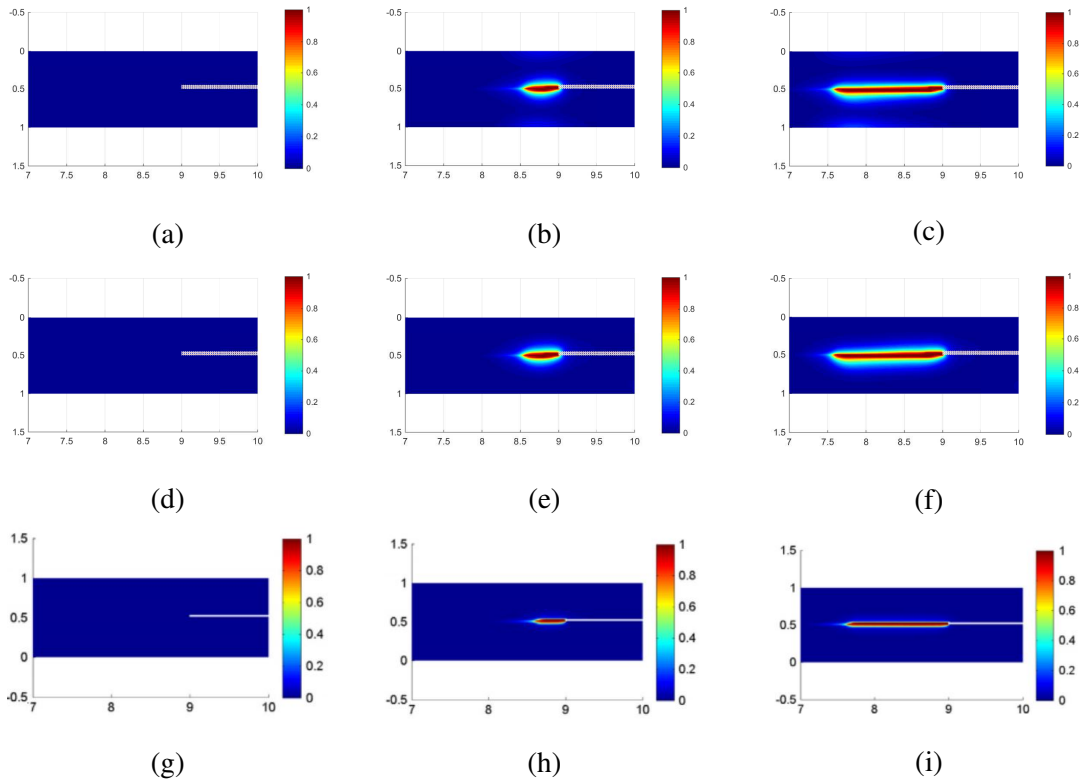


Figure 3.6: The crack evolution in the delamination peel test: (a), (b) and (c) crack nucleation and propagation for solution 1 of strain decomposition corresponding to $U = 0$ mm, $U = 0.4$ mm, and $U = 1$ mm, respectively; (d), (e) and (f) crack nucleation and propagation for solution 2 of strain decomposition corresponding to $U = 0$ mm, $U = 0.4$ mm, and $U = 1$ mm, respectively; (g), (h) and (i) crack nucleation and propagation in the work Nguyen et al. [19] corresponding to $U = 0$ mm, $U = 0.4$ mm, and $U = 1$ mm, respectively

The purpose of this example is to investigate the crack propagation during a peel test in which two cantilever elastic beams are assembled together via an adhesive layer. In this example, two solutions of strain decompositions (3.21) and (3.27) are used. The geometry of cantilever elastic

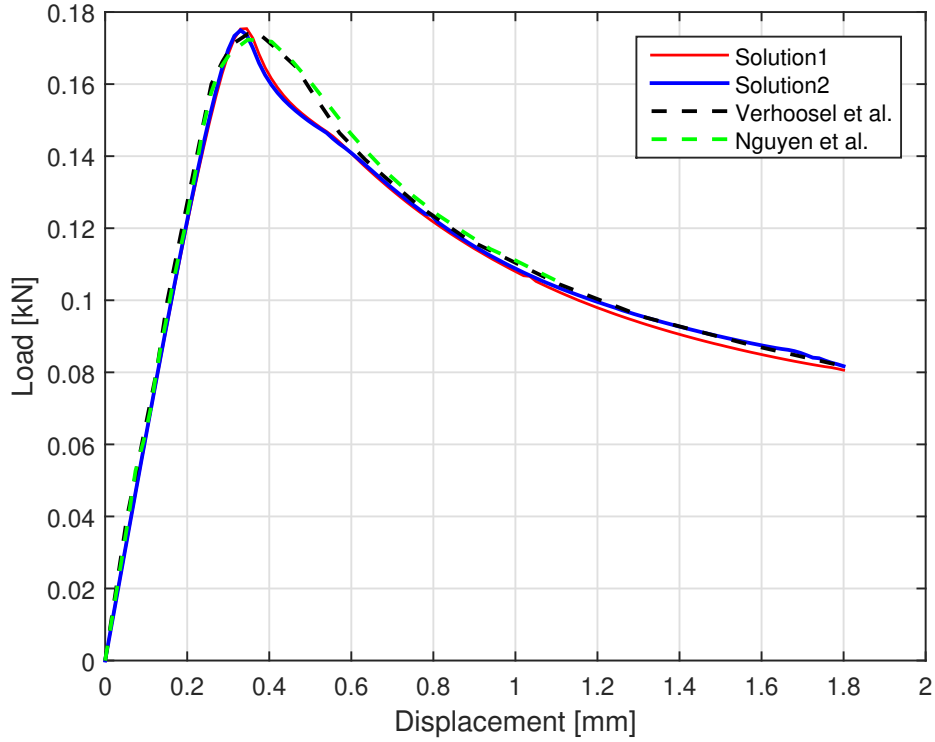


Figure 3.7: Delamination peel test: comparison of the load-displacement curves between Verhoosel et al. [66], Nguyen et al. [19] and two solutions of strain decompositions (3.21) and (3.27).

beams and the boundary conditions are described in Fig. 3.5. The dimensions of each beam are 10x0.5mm with over 90 % of the length is connected. Each beam is uniformly meshed into 400x20 quadrilateral elements. The left end of cantilever elastic beams is fixed in two directions. The displacement is prescribed at the right upper end and right bottom end of structure with monotonic increments of $\Delta u = 0.005\text{mm}$. The material properties are chosen as follows: $E = 100\text{ MPa}$ and Poisson's ratio $\nu = 0.3$. The fracture strength are taken as $t_u = 1\text{ MPa}$ and $g_c = g_c^I = 0.1\text{ N/mm}$, respectively. The length scale parameter l is chosen as $l = 0.05\text{ mm}$. The plane strain assumption is considered. The evolutions of the interfacial damage with two solutions of strain decompositions (3.21) and (3.27) as well as the results provided in [19] are shown in Fig. 3.6(a-c), Fig. 3.6(d-f) and Fig.3.6(g-i), respectively. We compare in Fig. 3.7 the load-displacement curves for two solutions of strain decompositions (3.21) and (3.27) with the results obtained and presented in [19] and [66]. From these comparisons, we can see that the crack propagation and the load-displacement relation with two solutions of strain decompositions (3.21) and (3.27) exhibit a good agreement with ones provided in [19] and [66].

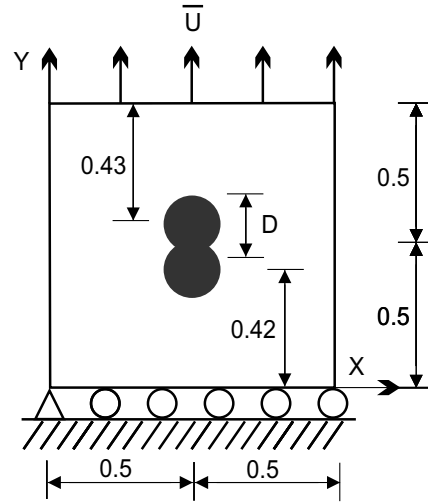


Figure 3.8: Tension test of a plate containing a complex inclusion: geometry and boundary conditions.

3.3.3 Tension test of a plate with a complex inclusion

In the example, we consider a plate containing an inclusion with complex geometry. In order to describe interfacial damage and bulk damage, two solutions of strain decompositions (3.21) and (3.27) are employed. Fig. 3.8 show the geometry and loading conditions applied to the plate under consideration. The dimensions of the plate are 1x1mm and the inclusion has the diameter $D = 0.2\text{mm}$. On the lower end, the vertical displacements are fixed, while the horizontal displacements are free and the left bottom node is fixed. On the upper end, the horizontal displacements are free, while the vertical displacements are prescribed to an increasing constant value of $\Delta u = 0.0001\text{mm}$ during the simulation process.

The plane strain condition is assumed in this study. The material properties of the inclusion phase are chosen as: $E_i = 52\text{ GPa}$ and $\nu_i = 0.3$ while the material properties of the matrix phase are $E_m = 10.4\text{ GPa}$ and $\nu_m = 0.3$. The fracture toughness is $g_c = g_c^I = 0.1\text{ N/mm}$ and the fracture strength $t_u = 0.01\text{ GPa}$. The plate is uniformly meshed into 400x400 quadrilateral elements. The regularization parameter l is chosen as $l = 0.005\text{ mm}$.

The evolutions of crack in the plate with two solutions of strain decompositions (3.21) and (3.27) and the results provided in [19] are shown in Fig. 3.9(a-c), Fig. 3.9(d-f) and Fig. 3.9(g-i), respectively. We can see that, in all of these models, the cracks appear initially at the interface and propagate then into the matrix until the full damage during the increment of the prescribed displacement. The load-displacement curves are presented in Fig. 3.10.

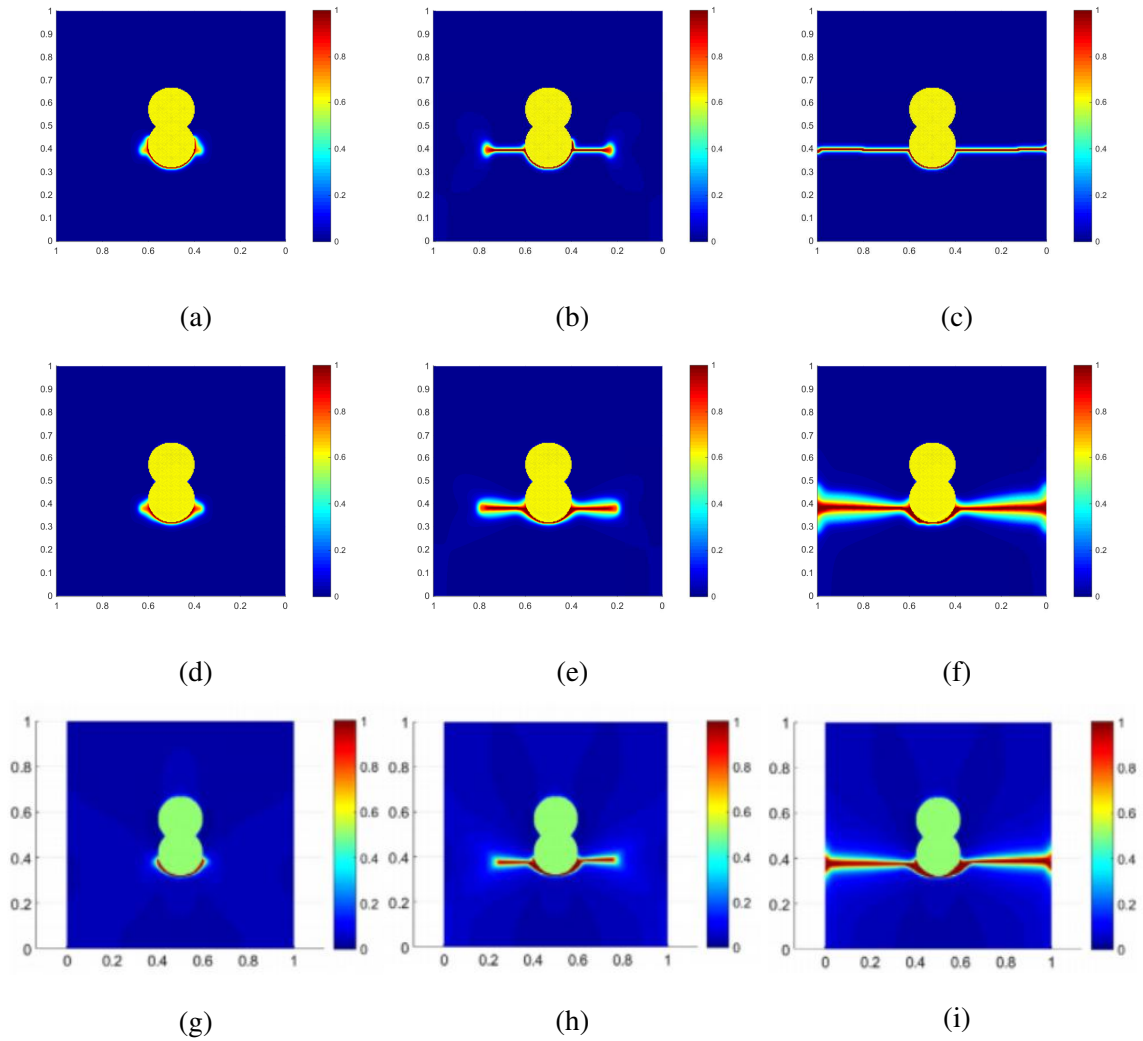


Figure 3.9: Tension test of a plate containing a complex inclusion: crack propagation. (a), (b) and (c) crack initiation and propagation for solution 1 of strain decomposition corresponding to $U = 0.008$ mm, $U = 0.01$ mm, and $U = 0.012$ mm, respectively; (d), (e) and (f) crack initiation and propagation for solution 2 of strain decomposition corresponding to $U = 0.008$ mm, $U = 0.01$ mm, and $U = 0.012$ mm, respectively; (g), (h) and (i) crack initiation and propagation obtained by Nguyen et al. [19] corresponding to $U = 0.008$ mm, $U = 0.01$ mm, and $U = 0.012$ mm, respectively

From the results observed in Fig. 3.9 and Fig. 3.10, two proposed strain decompositions (3.21) and (3.27) seem to be very efficient and accurate to predict the crack propagation related to interfacial damage in the plate containing a complex inclusion.

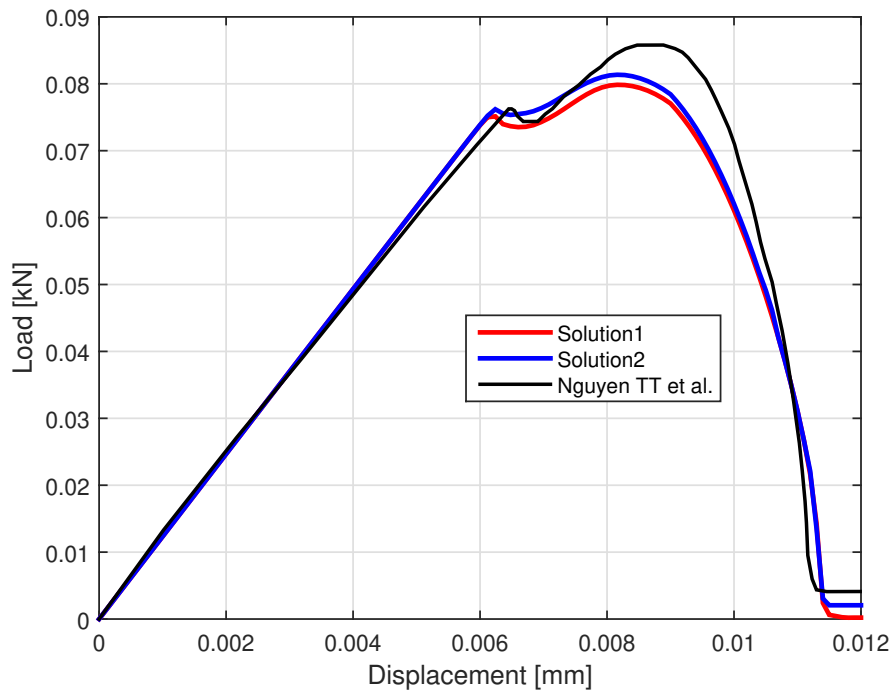


Figure 3.10: Tension test of a plate containing a complex inclusion: comparison of the load-displacement curves between Nguyen et al. [19] with two solutions of strain decompositions (3.21) and (3.27).

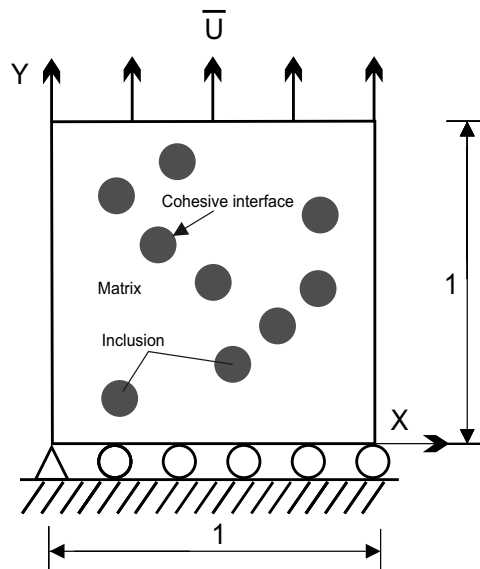


Figure 3.11: Traction test of a microstructure containing randomly distributed inclusions: geometry and boundary conditions.

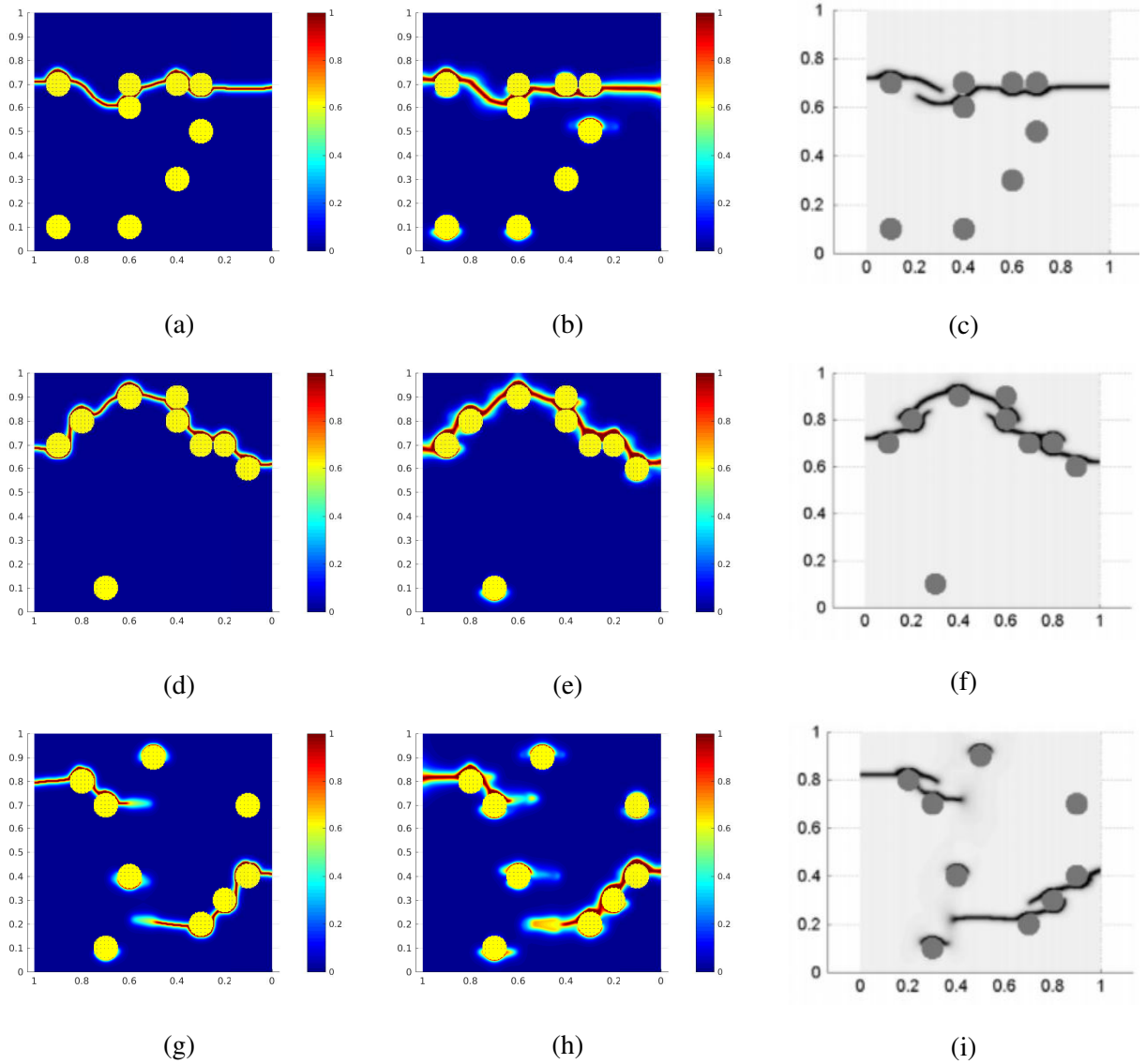


Figure 3.12: Crack evolution for 15 realizations of the microstructures containing randomly distributed inclusions (part 1): (a), (b) and (c) depict crack propagation of realization 1 corresponding to solutions 1 and 2 of strain decomposition (3.21) and (3.27), and Nguyen et al. [19], respectively; (d), (e) and (f) depict crack propagation of realization 2 corresponding to solutions 1 and 2 of strain decomposition (3.21) and (3.27), and Nguyen et al. [19], respectively; (g), (h) and (i) depict crack propagation of realization 3 corresponding to solutions 1 and 2 of strain decomposition (3.21) and (3.27) and Nguyen et al. [19], respectively

3.3.4 Tension test of a plate containing randomly distributed inclusions

This example aims to simulate the development of the interfacial damage situated between the randomly distributed inclusions and matrix phases. For this purpose, we use a plate containing 9 randomly distributed circular inclusions whose volume fraction is equal to 0.07 (see., Fig. 3.11). The dimensions of the plate are 1x1mm. The material properties of the matrix and inclusion phases

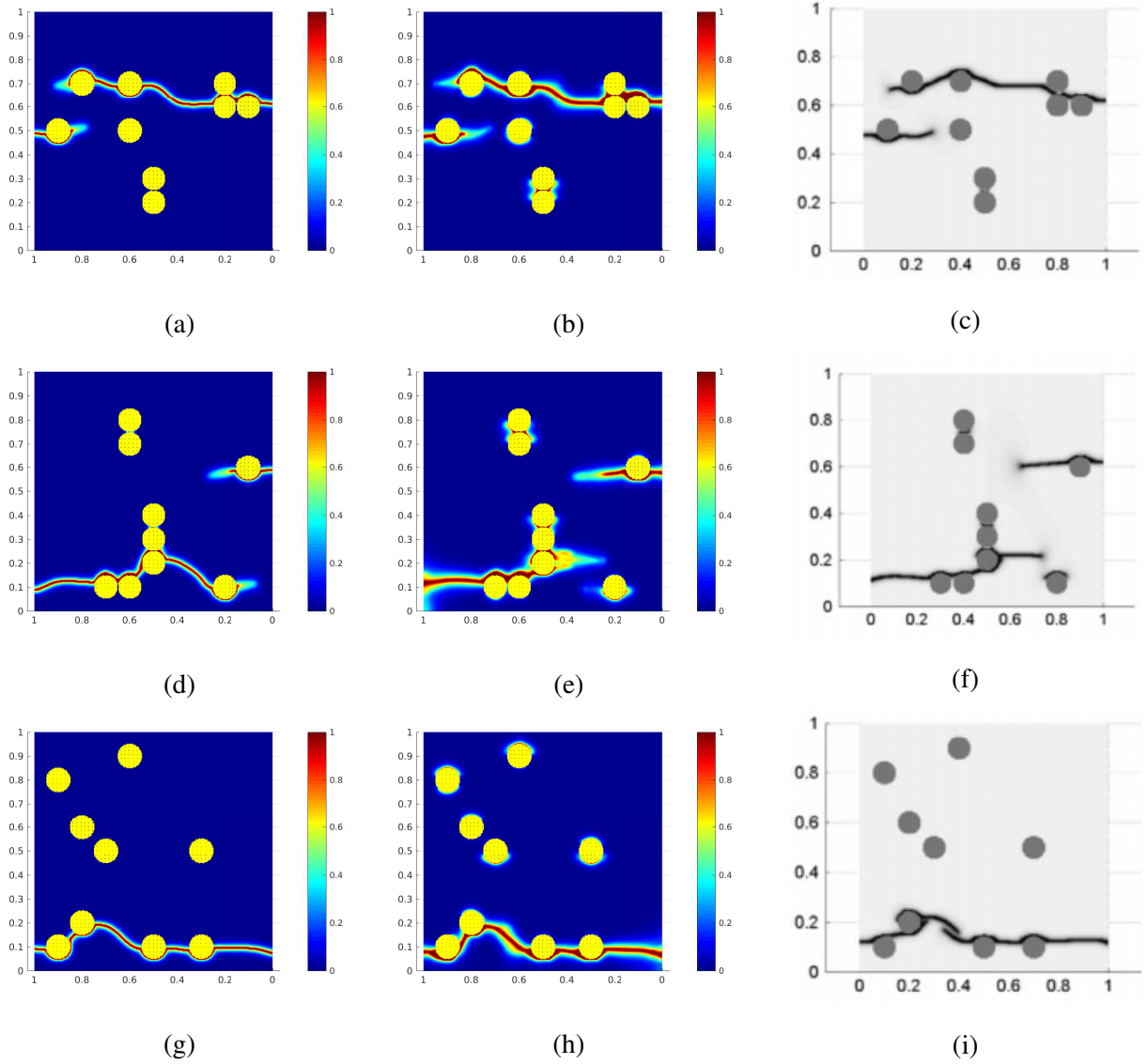


Figure 3.13: Crack evolution for 15 realizations of the microstructures containing randomly distributed inclusions (part 2): (a), (b) and (c) depict crack propagation of realization 4 corresponding to solutions 1 and 2 of strain decomposition (3.21) and (3.27), and Nguyen et al. [19], respectively; (d), (e) and (f) depict crack propagation of realization 5 corresponding to solutions 1 and 2 of strain decomposition (3.21) and (3.27), and Nguyen et al. [19], respectively; (g), (h) and (i) depict crack propagation of realization 6 corresponding to solutions 1 and 2 of strain decomposition (3.21) and (3.27), and Nguyen et al. [19], respectively

are chosen such as $E_i = 52$ GPa, $\nu_i = 0.3$, $E_m = 10.4$ GPa, $\nu_m = 0.3$, $t_u = 0.01$ GPa. The toughnesses of both phases are taken as $g_c = 0.27$ N/mm and $g_c^I = g_c$. The boundary conditions are identical to the previous example. The plane strain assumption is considered. On the upper end, the vertical displacements are prescribed in such a way that their values increase monotonically with $\Delta u = 0.00005$ mm during 200 load increments. The structure is discretized into 300×300 quadri-

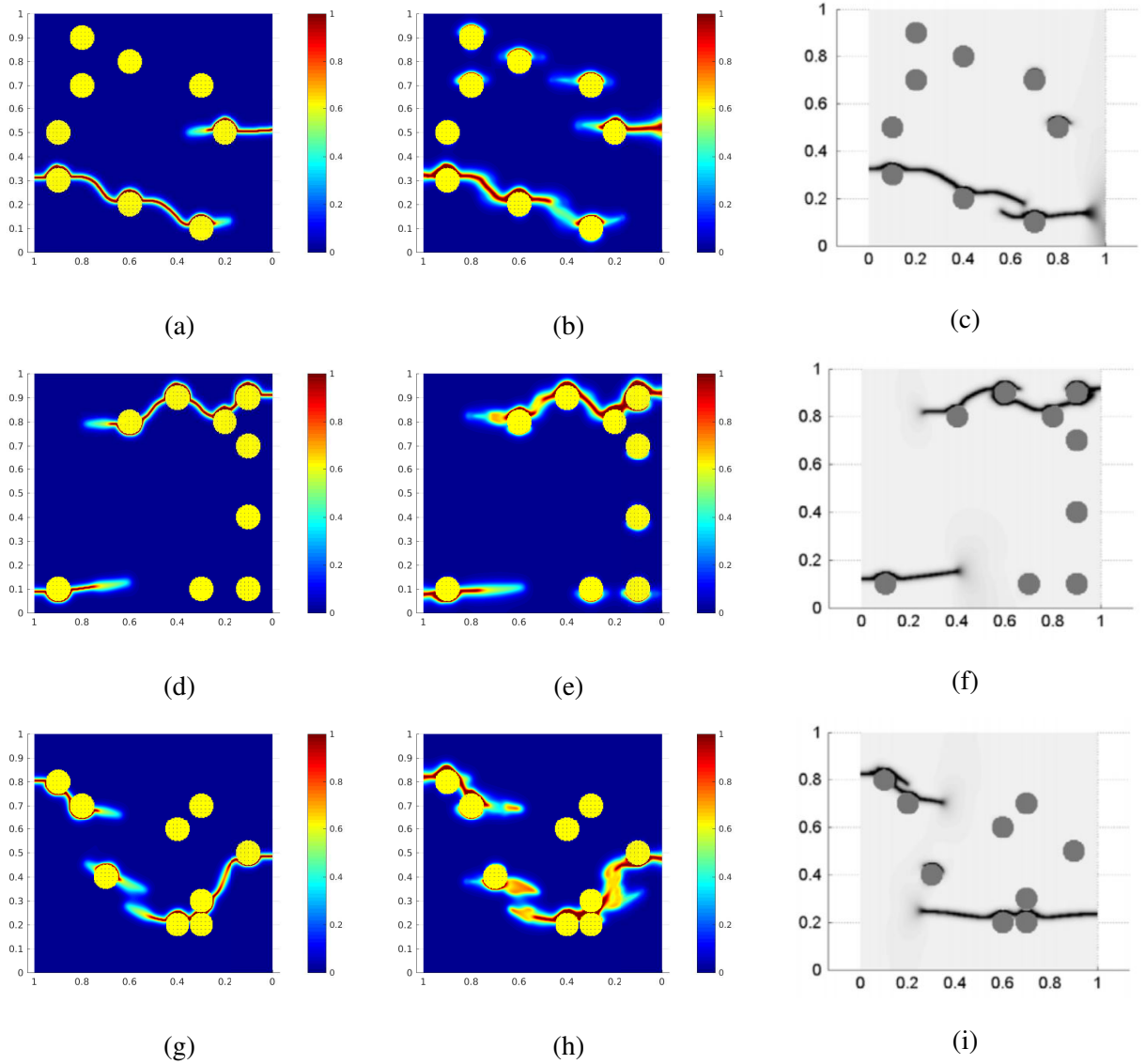


Figure 3.14: Crack evolution for 15 realizations of the microstructures containing randomly distributed inclusions (part 3): (a), (b) and (c) depict crack propagation of realization 7 corresponding to solutions 1 and 2 of strain decomposition (3.21) and (3.27), and Nguyen et al. [19], respectively; (d), (e) and (f) depict crack propagation of realization 8 corresponding to solutions 1 and 2 of strain decomposition (3.21) and (3.27), and Nguyen et al. [19], respectively; (g), (h) and (i) depict crack propagation of realization 9 corresponding to solutions 1 and 2 of strain decomposition (3.21) and (3.27), and Nguyen et al. [19], respectively

lateral elements. The regularization parameter is chosen as $l = 0.0075$ mm. The microcracking propagations in the plate containing randomly distributed inclusions with 15 realizations are shown in Fig. 3.12-3.16. It can be seen that, the evolutions of the crack are very various: when the inclusions in contact with each other, the crack path is formed between the inclusions where mechanical behavior seems to be the weakest, in the contrast when the inclusions are not in contact, the crack

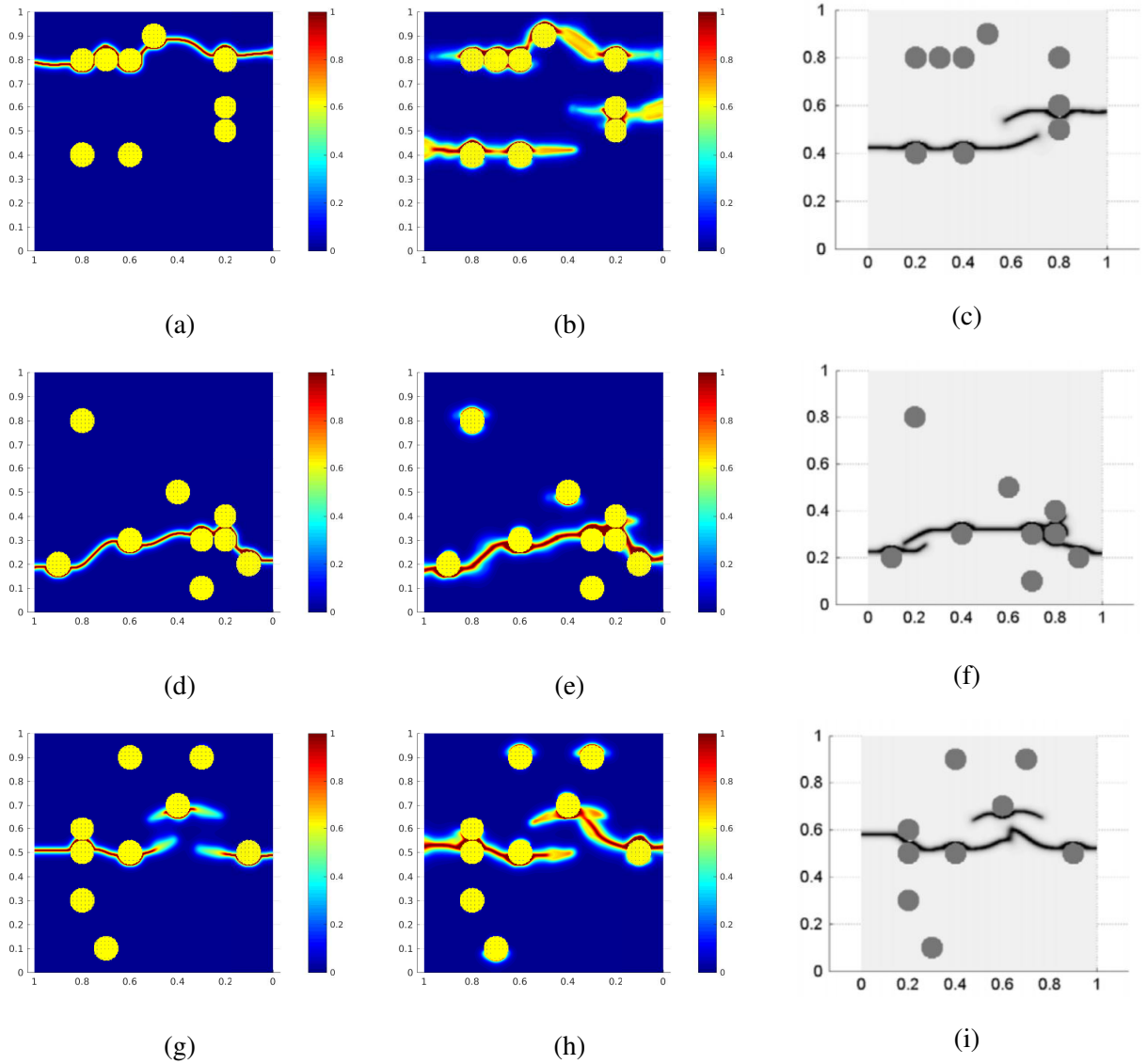


Figure 3.15: Crack evolution for 15 realizations of the microstructures containing randomly distributed inclusions (part 4): (a), (b) and (c) depict crack propagation of realization 10 corresponding to solutions 1 and 2 of strain decomposition (3.21) and (3.27), and Nguyen et al. [19], respectively; (d), (e) and (f) depict crack propagation of realization 11 corresponding to solutions 1 and 2 of strain decomposition (3.21) and (3.27), and Nguyen et al. [19], respectively; (g), (h) and (i) depict crack propagation of realization 12 corresponding to solutions 1 and 2 of strain decomposition (3.21) and (3.27), and Nguyen et al. [19], respectively

path can be created at the interface between the matrix and the inclusions, and then propagate into the matrix until the full rupture.

The force-displacement curves are plotted in Fig. 3.17a, Fig. 3.17b and Fig. 3.17c for 15 realizations. The average of these curves for 15 realizations is shown in red line. From the obtained results of both the crack propagation and the mechanical behaviors in the simulation for 15 realizations,

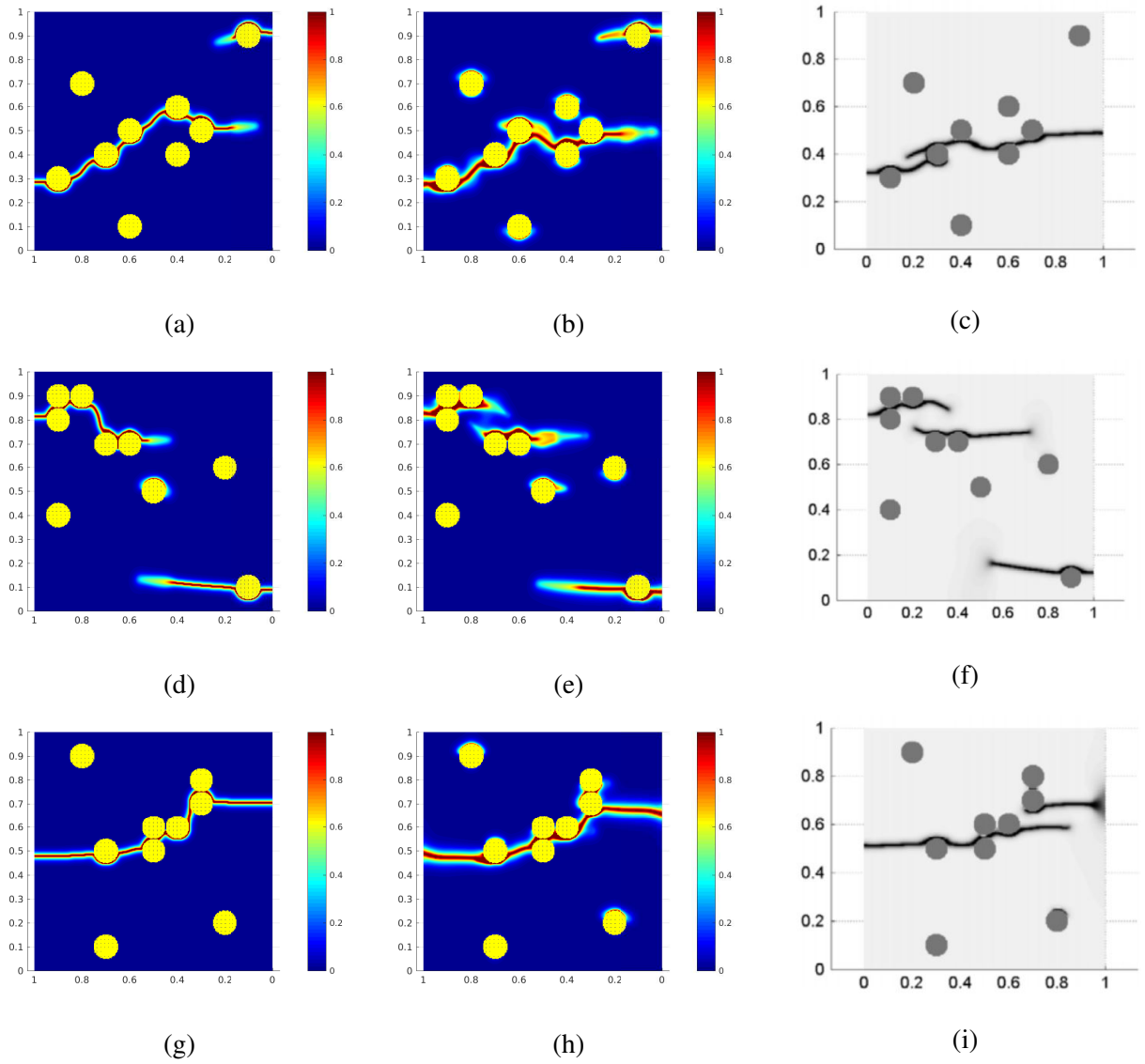


Figure 3.16: Crack evolution for 15 realizations of the microstructures containing randomly distributed inclusions (part 5): (a), (b) and (c) depict crack propagation of realization 13 corresponding to solutions 1 and 2 of strain decomposition (3.21) and (3.27), and Nguyen et al. [19], respectively; (d), (e) and (f) depict crack propagation of realization 14 corresponding to solutions 1 and 2 of strain decomposition (3.21) and (3.27), and Nguyen et al. [19], respectively; (g), (h) and (i) depict crack propagation of realization 15 corresponding to solutions 1 and 2 of strain decomposition (3.21) and (3.27), and Nguyen et al. [19], respectively

two proposed solutions of strain decompositions can provide a promising tool to investigate the damage of more complex structures.

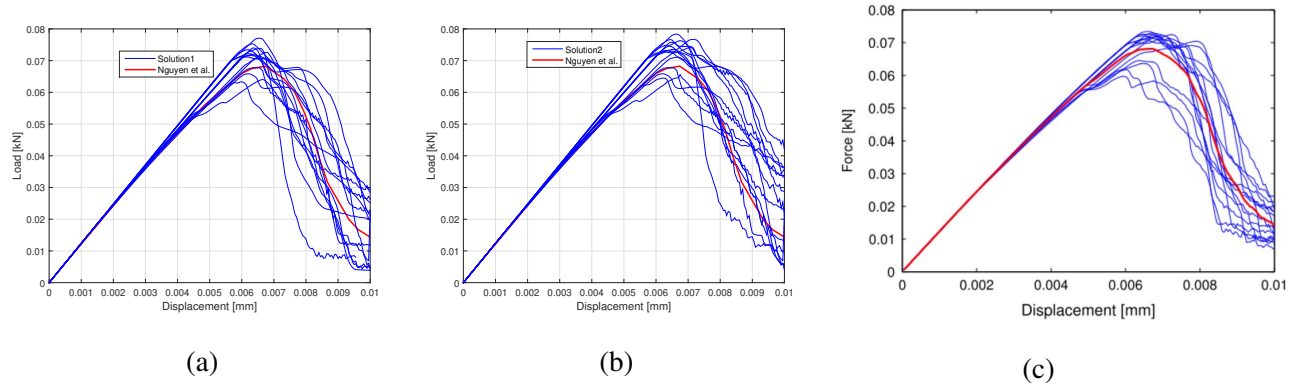


Figure 3.17: Traction test of a plate containing randomly distributed inclusions with interfacial damage (the red curve denotes the average response): a) load-displacement curve for 15 realizations with solution 1 of strain decomposition (3.21); b) load-displacement curve for 15 realizations with solution 2 of strain decomposition (3.27); c) load-displacement curve for 15 realizations with Nguyen et al. [19]

3.3.5 Tension test of a realistic microstructure obtained by X-ray microtomography image

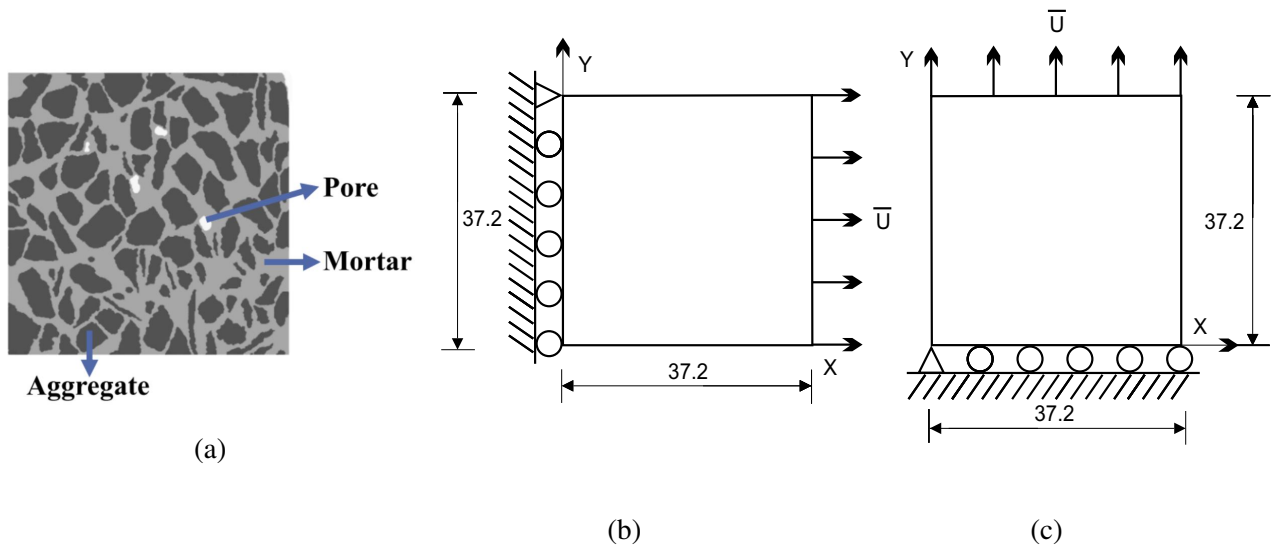


Figure 3.18: Tension test of a realistic microstructure obtained by X-ray microtomography: geometry and loading conditions; a) X-ray microtomography image in Ren et al. [53], b) horizontal tension test, c) vertical tension test

In this example, we use two proposed strain decompositions (3.21) and (3.27), to predict the microcrack propagation with both interfacial damage and bulk damage of a realistic microstructure obtained by X-ray microtomography image. We consider a 2D microstructure of dimensions

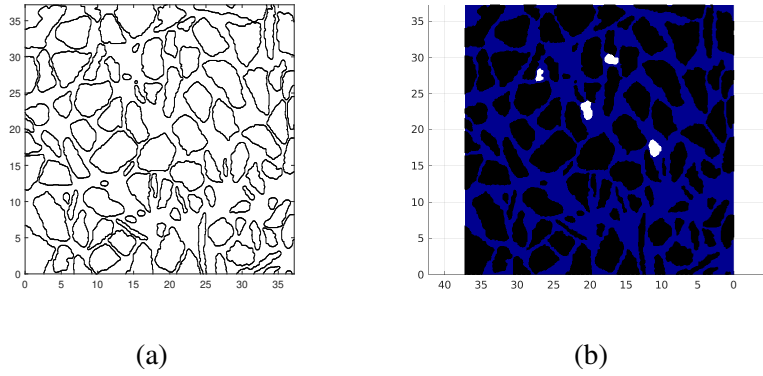


Figure 3.19: Tension test of a realistic microstructure obtained by X-ray microtomography: (a) zero isovalue of the constructed level-set, (b) geometry of the domain after solve: mortar (blue), aggregates (black) and pores (white).

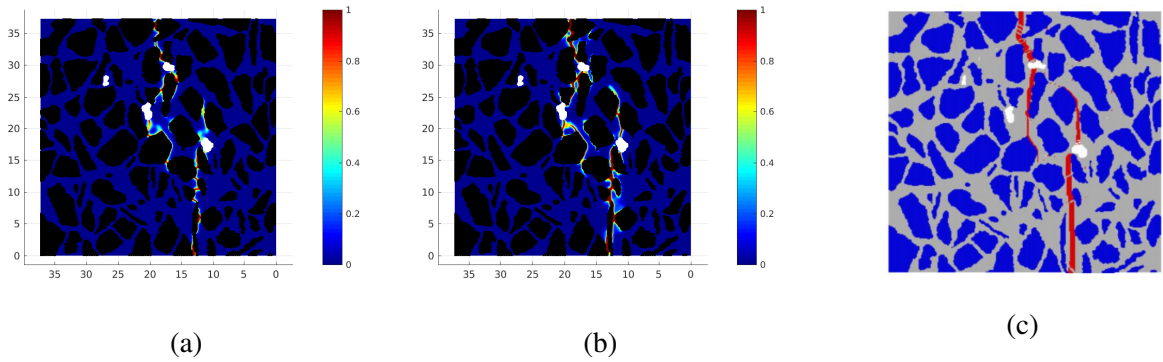


Figure 3.20: Horizontal tension test: cracks nucleation and propagation: (a), (b) and (c) depict crack propagation corresponding to two solutions of strain decompositions (3.21) and (3.27), and Ren et al. [53], respectively

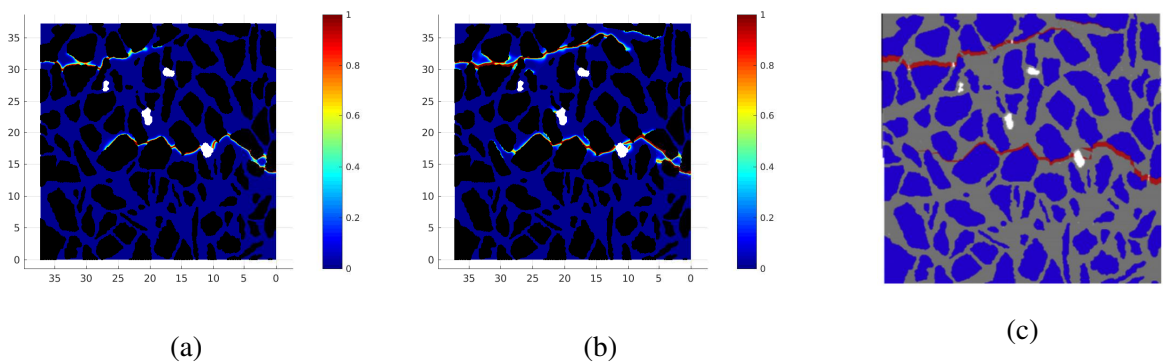


Figure 3.21: Vertical tension test: cracks nucleation and propagation: (a), (b) and (c) depict crack propagation corresponding to two solutions of strain decompositions (3.21) and (3.27), and Ren et al. [53], respectively

37.2x37.2mm. By using the microtomography image of a real cementitious material provided in [53], the geometry of this structure is described in Fig. 3.18a. The real material consists three phases: mortar (grey), gravel aggregates (black) and pore (white). The loading conditions in the horizontal and vertical directions are illustrated in Fig. 3.18b and Fig. 3.18c, respectively. A numerical technique such as a level set function is used to determine the interface of the aggregate and mortar. The interface shapes after the processing are shown in Fig. 3.19a. The shapes of three phases after the processing: mortar (blue), gravel aggregates (black) and pore (white) are presented in Fig. 3.19b.

After mesh smoothing by the numerical technique, the corresponding volume fractions of pores, aggregates and cement paste are 0.48%, 51.27% and 48.25%, which are within the range of the volume fractions from 0.47% to 0.50% for pores, from 50.72% to 51.84% for aggregates, and 48.81% to 47.66% for cement paste in [53]. These values are acceptable to simulate the crack propagation in the microstructure. The material parameters of aggregate and mortar are $E_i = 70$ GPa, $\nu_i = 0.2$, $E_m = 25$ GPa and $\nu_m = 0.2$. The toughness $g_c = 30$ N/m is assumed to be identical for the different phases and $g_c^I = g_c$. The fracture strength is taken as $t_u = 3$ MPa (see in [53]). We can choose the very compliant properties for the pore as $E_p = 10^{-6}$ GPa, $\nu_p = 0.3$. Each simulation is carried out with constant displacement increments $\Delta u = 10^{-6}$ mm during 240 load increments. The structure is discretized into 600x600 quadrilateral elements. The regularization parameter is chosen as $l = 0.12$ mm. The evolutions of crack for the horizontal tension test with two solutions of strain decompositions (3.21) and (3.27) and the ones obtained in [53] are shown in Fig. 3.20a, Fig. 3.20b and Fig. 3.20c, respectively. The crack evolutions for the vertical tension test are presented in Fig. 3.21. We can see that, with two proposed strain decompositions (3.21) and (3.27), several cracks nucleate at the pores, while another cracks initiate at the interface of the phases and then spread into the matrix until the full damage during the displacement increments. The obtained results are very similar to the experimental results presented in [53]. This demonstrates the present numerical models are the robust tools to predict the complex crack paths in the interaction of the microcrack taking into account interfacial damage in the realistic microstructure obtained by X-ray microtomography with heterogeneous material and very complex shapes of the interfaces.

3.4 Conclusions

In this work, the strain decomposition into a negative part and a positive part which are orthogonal in the sense of an inner product where the elastic stiffness tensor acts as a metric role is successfully

applied in the phase-field modeling taking into account interfacial damage to simulate the fracture in the very complex and heterogeneous material.

Starting firstly with some examples in which the shape of the interface between two structures or between two phases is assumed to be simple and smooth, the simulation of the crack nucleation and propagation obtained seems to be very efficient and accurate.

In the structure containing randomly distributed inclusions, due to the various shapes of the interface and their randomly occurrence densities, the microcrack is created not only by interfacial damage and but also by the bulk damage. The simulation of the crack nucleation and propagation with two solutions of strain decompositions shows that they are good tools to predict the crack propagation in composites with complex microstructures.

In the last example, a realistic microstructure obtained by X-ray microtomography and containing multi-phases: mortar, aggregate, and pore is studied. A numerical technique such as a level set function is used to determine the arbitrary shape of the interfaces. Moreover, we demonstrated the capability of two solutions of strain decompositions in the simulation of crack propagation in the heterogeneous material with both interfacial and bulk damage through the simulation results.

Chapter 4

Modeling and simulation of crack propagation in anisotropic two-phase composite materials by phase-field method with interfacial damage

4.1 Phase-field modeling for anisotropic two-phase composite materials

We consider in this chapter a composite structure consisting of two anisotropic phases (Fig. 4.1). The interface between these two component phases is denoted by Γ^I while the crack surface is denoted by Γ (see Fig. 4.1a). In a regularized framework, as presented in Chapter 3 that the geometry of interface between the component phases of the composite material is described by a fixed scalar parameter $\beta(\mathbf{x})$ (see Fig. 4.1b) and the geometry of propagating crack is approximately defined by a scalar parameter $d(\mathbf{x}, t)$ (see Fig. 4.1c).

In the case where the component phases of the composite under consideration are anisotropic, Eq. (3.3) is rewritten by replacing $\gamma_d(d, \nabla d)$ by an anisotropic crack surface density function defined by:

$$\gamma^{(p)}(d, \nabla d, \boldsymbol{\omega}^{(p)}) = \frac{d^2}{2l} + \frac{l}{2} \boldsymbol{\omega}^{(p)} : (\nabla d \otimes \nabla d) \quad (4.1)$$

where $p = 1$ or 2 denotes the phase 1 or 2 and $\boldsymbol{\omega}^{(p)}$ is a second-order orientation tensor defined by

$$\boldsymbol{\omega}^{(p)} = \mathbf{I} + \eta^{(p)} (\mathbf{I} - \mathbf{m}^{(p)} \otimes \mathbf{m}^{(p)}) \quad (4.2)$$

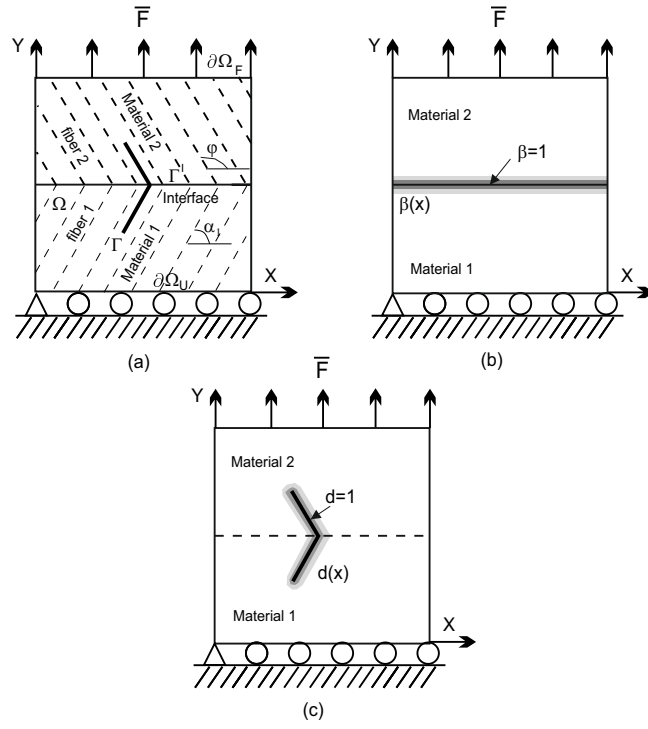


Figure 4.1: Regularized representation of crack and interface in a composite: (a) composite material consisting of two anisotropic materials with interface Γ^I and crack Γ ; (b) Regularized representation the interface Γ^I ; (c) Regularized representation of the crack Γ

where $\mathbf{m}^{(p)}$ and $\eta^{(p)}$ characterize the preferential cleavage plane of phase p . In particular, $\eta^{(p)} = 0$ corresponds to the case of isotropic material. The total crack length in phase p of the composite material is rewritten as:

$$\Gamma_d^{(p)}(d, \boldsymbol{\omega}^{(p)}) = \int_{\Omega^{(p)}} \gamma^{(p)}(d, \nabla d, \boldsymbol{\omega}^{(p)}) d\Omega. \quad (4.3)$$

where the functional derivative $\delta_d \gamma^{(p)}(d, \nabla d, \boldsymbol{\omega}^{(p)})$ is determined by

$$\delta_d \gamma^{(p)}(d, \nabla d, \boldsymbol{\omega}^{(p)}) = \frac{d}{l} - l \{ \Delta d (1 + \eta^{(p)}) - \eta^{(p)} \mathbf{m}^{(p)} \otimes \mathbf{m}^{(p)} : \nabla \nabla d \} \quad (4.4)$$

Although in the rest of this Chapter, we consider the 2D case in which the two component phases of the composites under investigation are assumed to be both orthotropic. More precisely, associated with the orthonormal basis $\{\mathbf{e}_1, \mathbf{e}_2\}$ whose the basis vectors \mathbf{e}_1 and \mathbf{e}_2 coincide with the privileged directions of materials, the strain matrix components and the stress matrix components are related by the following 2D Hooke law

$$\begin{bmatrix} \varepsilon_{11} \\ \varepsilon_{22} \\ 2\varepsilon_{12} \end{bmatrix} = \mathbf{L}_0 \begin{bmatrix} \sigma_{11} \\ \sigma_{22} \\ \sigma_{12} \end{bmatrix} \quad \text{or} \quad \begin{bmatrix} \sigma_{11} \\ \sigma_{22} \\ \sigma_{12} \end{bmatrix} = \mathbf{C}_0 \begin{bmatrix} \varepsilon_{11} \\ \varepsilon_{22} \\ 2\varepsilon_{12} \end{bmatrix} \quad (4.5)$$

where \mathbf{C}_0 and \mathbf{L}_0 are respectively the elastic stiffness and compliance matrices which are given by

$$\mathbf{L}_0 = (\mathbf{C}_0)^{-1} = \begin{bmatrix} \frac{1}{E_1} & -\frac{\nu_{21}}{E_2} & 0 \\ -\frac{\nu_{12}}{E_1} & \frac{1}{E_2} & 0 \\ 0 & 0 & \frac{1}{G_{12}} \end{bmatrix}. \quad (4.6)$$

Here, E_1 and E_2 are respectively the Young modulus associated with the fibrous and transversal directions, ν_{12} and ν_{21} are the Poisson's ratios and G_{12} denotes the shear modulus. In the case of unidirectional fiber-reinforced composite ply (see., Fig.4.1), since the fact that the fracture occurs within the matrix phase, the only fracture toughness g_c and only the fracture energy contribution of the matrix phase are taken into account. When the fiber direction of composite makes an angle α with the basis vector \mathbf{e}_1 , relative to the orthonormal basis $\{\mathbf{e}_1, \mathbf{e}_2\}$, the elastic stiffness matrix is expressed in the form

$$\mathbf{C} = \mathbf{P}\mathbf{C}_0\mathbf{P}^T \quad (4.7)$$

where

$$\mathbf{P} = \begin{bmatrix} c^2 & s^2 & 2cs \\ s^2 & c^2 & -2cs \\ -cs & cs & c^2 - s^2 \end{bmatrix} \quad (4.8)$$

with $c = \cos(\alpha)$ and $s = \sin(\alpha)$.

Next, applying the resolution of the phase-field problem and the resolution of the displacement problem which have been presented in Chapter 3 and in **Appendix A.2** allows us to predict the crack nucleation and propagation of the anisotropic two-phase composite material under consideration. The algorithm is provided in **Appendix B.3**.

4.2 Numerical examples

4.2.1 Tension test of composites with two identical material phases and adhesive interface

By applying two solutions of strain decompositions (3.21) and (3.27) and by taking into account interfacial damage into an anisotropic phase-field modeling, this first numerical example aims to predict the crack evolution during the tension test of two identical material phases containing an adhesive layer. In addition, we use only one damage variable d for the preferential cleavage direction instead of using multiple damage variables d_i for this problem. The geometry of the domain occupied by the composite is described in Fig.4.2. In addition, the domain of dimensions 1x1mm

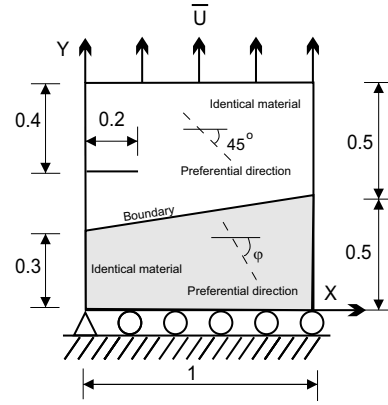


Figure 4.2: Geometry and boundary condition of tension tests for composites with two identical material phases and adhesive interface.

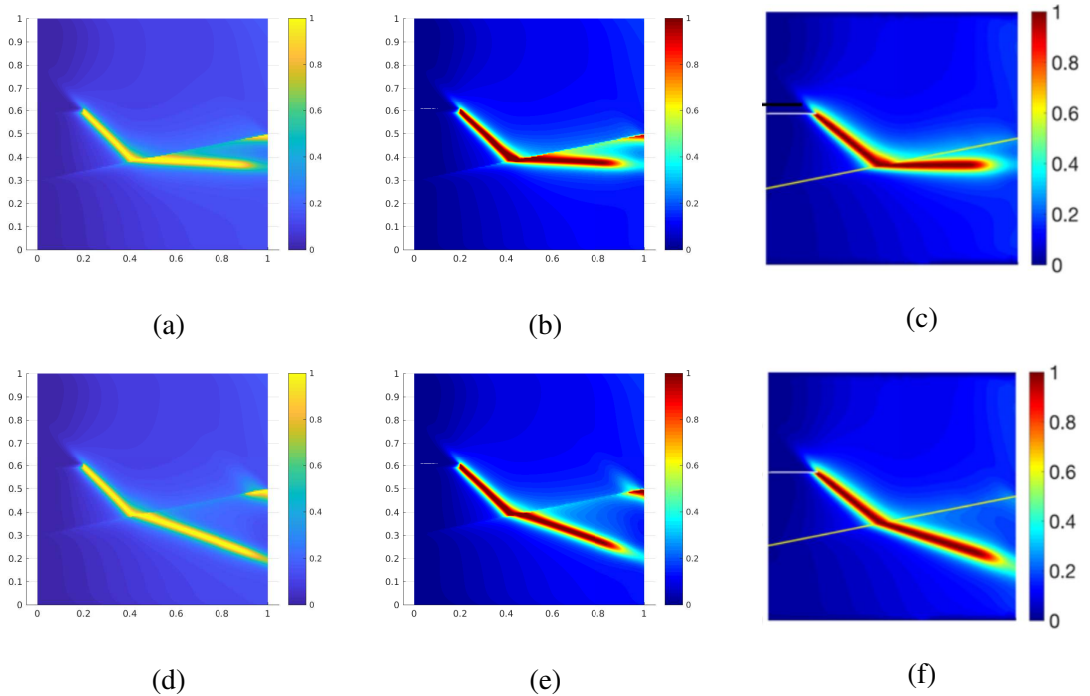


Figure 4.3: Tension test of composites with two identical material phases and adhesive interface: crack evolution due to bulk fracture and interfacial fracture with $U = 0.0105\text{mm}$: (a) and (d) solution 1 of strain decomposition (3.21) with $\varphi = 0^\circ, -20^\circ$; (b) and (e) solution 2 of strain decomposition (3.27) with $\varphi = 0^\circ, -20^\circ$; c) f) Nguyen et al. [81] with $\varphi = 0^\circ, -20^\circ$.

has an initial crack with length of 0.2mm and contains two subdomains consisting of the same material. The interface between two phases is described by an adhesive layer. This domain is uniformly meshed into 200x200 quadrilateral elements. The boundary and loading conditions are as follows: on the bottom side, the vertical displacement is fixed while the horizontal displacement is

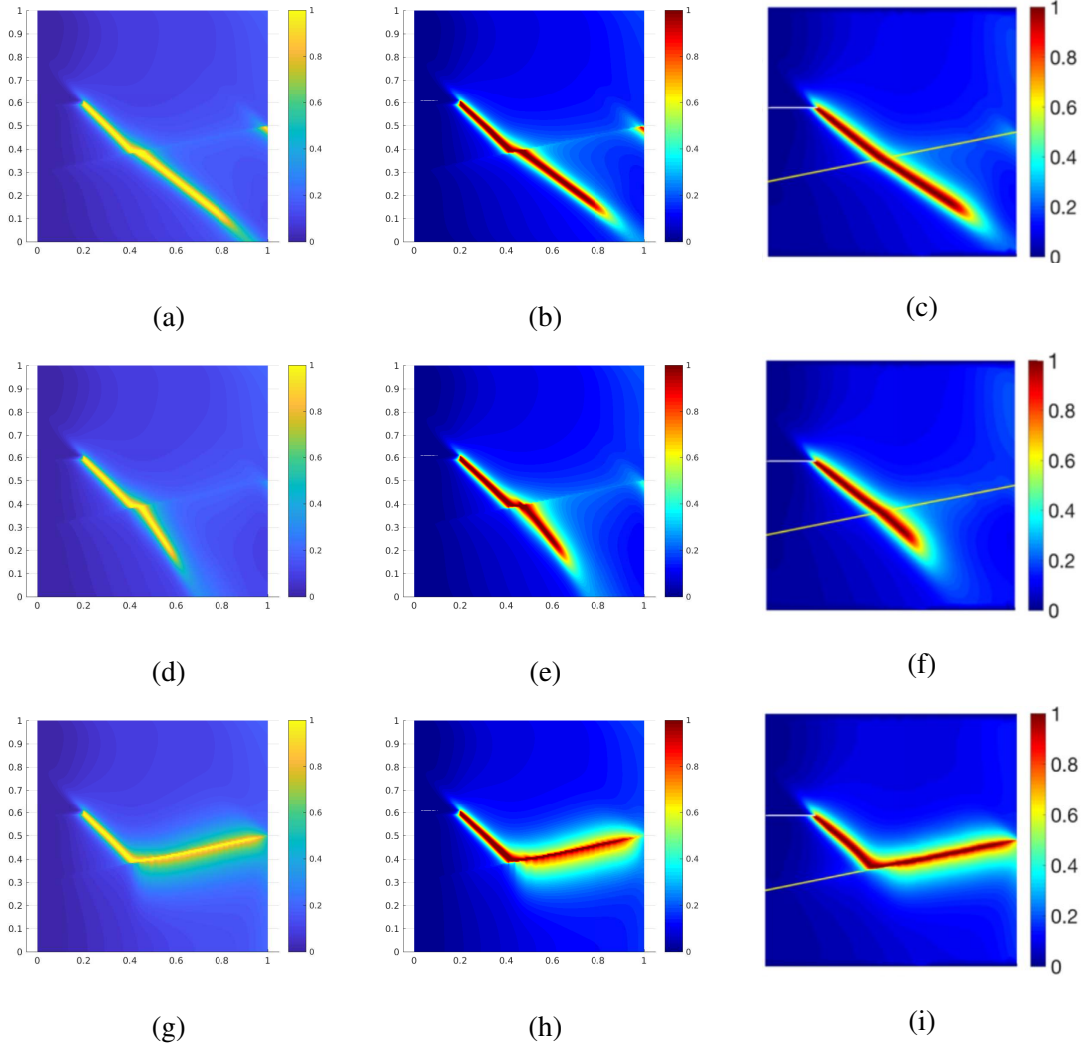


Figure 4.4: *Tension test of composites with two identical material phases: crack evolution due to bulk fracture and interfacial fracture with $U = 0.0105\text{mm}$: a) d) g) solution 1 of strain decomposition (3.21) with $\varphi = -40^\circ, -60^\circ, -90^\circ$; b) e) h) solution 2 of strain decomposition (3.27) with $\varphi = -40^\circ, -60^\circ, -90^\circ$; c) f) i) Nguyen et al. [81] with $\varphi = -40^\circ, -60^\circ, -90^\circ$*

free and the left bottom node is fixed. On the top side, the horizontal displacement is free, while the vertical displacement is prescribed to an increasing constant value of $\Delta u = 0.0001\text{mm}$ for 120 load increments. The plane strain assumption is assumed. The elastic stiffness matrix for the case of $\alpha = 0^\circ$ is:

$$\mathbf{C}_0 = \begin{bmatrix} 280 & 120 & 0 \\ 120 & 280 & 0 \\ 0 & 0 & 80 \end{bmatrix} \text{GPa} \quad (4.9)$$

Then, we can determine by using Eq. (4.7) the elastic stiffness matrix \mathbf{C} corresponding to the angle α with respect to \mathbf{e}_1 . The fracture strength is set to be $t_u = 0.1 \text{ GPa}$ at the interface. The fracture toughness within the interface and in the bulk material are given by $g_c^I = 1.45 \text{ N/mm}$ and $g_c = 1.5$

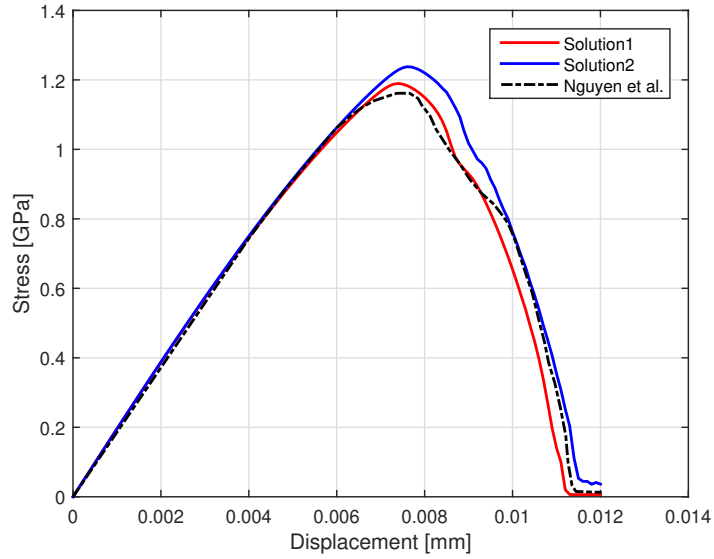


Figure 4.5: *Tension test of composites with two identical material phases: comparison of the stress-displacement curves with $\varphi = -45^\circ$ between two solutions of strain decompositions (3.21) and (3.27) and the results obtained in Nguyen et al. [81]*

N/mm. The preferential cleavage direction is oriented at -45° with respect to the horizontal axis in the upper domain, while in the lower domain, the preferential direction φ is set to vary from 0° to -90° to study the influence of preferential orientation and interfacial damage on the globe fracture. In this example, the value of the anisotropic coefficient is chosen such as $\eta = 20$. The regularization length is set to be as $l = l_\beta = 0.012\text{mm}$.

The evolutions of the crack for the case of $\varphi = 0^\circ$ and $\varphi = -20^\circ$ with $U = 0.0105\text{mm}$ and with two solutions of strain decompositions (3.21) and (3.27) are shown in Fig. 4.3. Similarly, the evolutions of the crack with $\varphi = -40^\circ$, $\varphi = -60^\circ$ and $\alpha = -90^\circ$ and $U = 0.0105\text{mm}$ are presented in Fig. 4.4. We can see that the crack propagations corresponding to two solutions of strain decompositions (3.21) and (3.27) are similar to the ones observed in the work [81].

The comparison of the force-displacement curves between two solutions of strain decompositions (3.21) and (3.27) and the work [81] with $\varphi = -45^\circ$ is shown in Fig. 4.5. We can see that the results provided from two solutions of strain decompositions (3.21) and (3.27) are good agreement with the ones derived in [81].

4.2.2 Tension test of a polycrystalline microstructure containing 50 grains

In this example, we solve the fracture problem with interfacial damage and bulk damage in a polycrystalline microstructure. We consider a domain whose dimensions are $10 \times 10 \mu\text{m}$. This domain

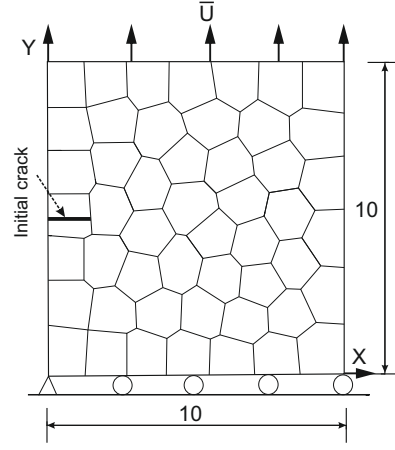


Figure 4.6: *Tension test of a polycrystalline microstructure containing 50 grains: geometry and boundary conditions with dimensions in μm*

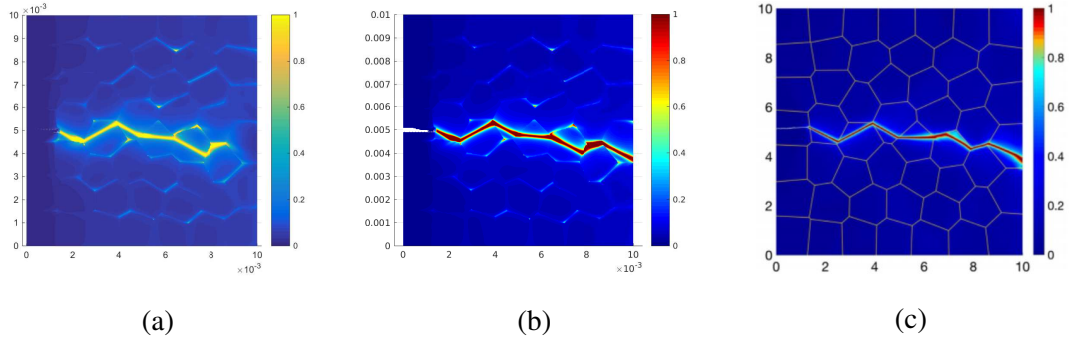


Figure 4.7: *Tension test of a polycrystalline microstructure: crack evolution with a) solution 1 of strain decomposition (3.21), b) solution 2 of strain decomposition (3.27) and c) results of Nguyen et al. [81]*

contains 50 grains and an initial crack on the left side. The geometric setup and the loading conditions are represented in Fig. 4.6 or in [81]. The left bottom node is fixed in two directions. The remaining points of the bottom side are fixed in the vertical direction, while the horizontal direction is free. The points of the top side are prescribed with constant displacement increment $\Delta u = 6 \times 10^{-7} \text{mm}$ during 130 load increments. The microstructure is uniformly discretized into 460×460 quadrilateral elements. In each grain, both directions of anisotropy and preferential damage are generated randomly. The elastic stiffness matrix corresponding to $\alpha = 0^\circ$ is given by:

$$\mathbf{C}_0 = \begin{bmatrix} 320 & 110 & 0 \\ 110 & 320 & 0 \\ 0 & 0 & 120 \end{bmatrix} \text{MPa} \quad (4.10)$$

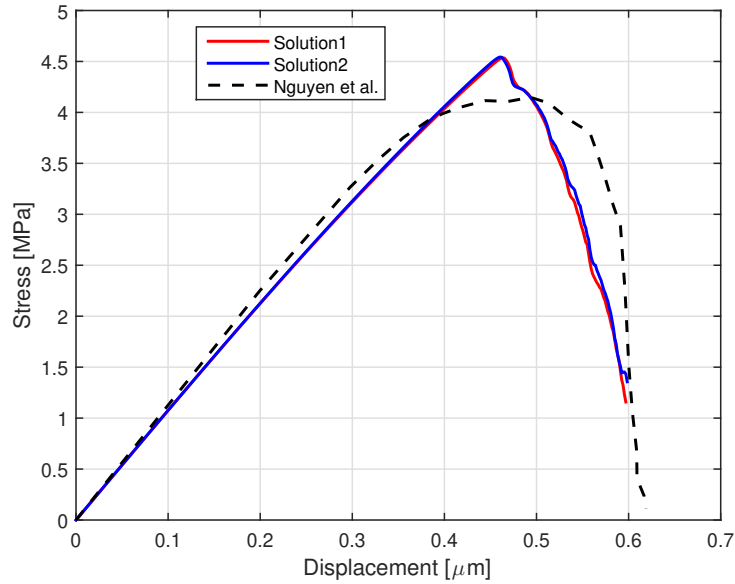


Figure 4.8: *Tension test of a polycrystalline microstructure: comparison of the stress-displacement curves between two solutions of strain decomposition (3.21) and (3.27) and Nguyen et al. [81]*

The elastic stiffness matrix \mathbf{C} corresponding to an arbitrary angle α is related to \mathbf{C}_0 by Eq. (4.7). The fracture strength is $t_u = 1.5$ MPa at the interface. The fracture toughness at the grain boundaries and in the bulk material are $g_c^I = 0.09$ N/m and $g_c = 0.1$ N/m. The anisotropy coefficient is chosen $\eta = 50$ as in [81] to promote for the bulk damage in the grains. The regularization length parameter is set to be as $l = l_\beta = 0.03\mu m$.

The evolution of the crack during the tension test with two solutions of strain decompositions (3.21) and (3.27) are shown in Fig. 4.7a, 4.7b and 4.7c. It can be seen from these figures that the crack initiates at the initial crack, then passes the grain boundary to propagate within the grain until the full fracture. The crack paths in two solutions of strain decomposition (3.21) and (3.27) are good agreement with the results in [81].

The curves of the displacement-stress relations are compared in Fig. 4.8. The values of the peak stress and the displacement when the full damage occurs are similar in all cases. Thus, the phase-field method taking into account the two solutions of strain decompositions (3.21) and (3.27) can be considered as an efficient and accurate tool to solve the fracture problem of polycrystalline microstructure where the interaction between interfacial fracture and grains fracture is very strong.

4.2.3 Tension test of composites with two different orthotropic phases and adhesive interface

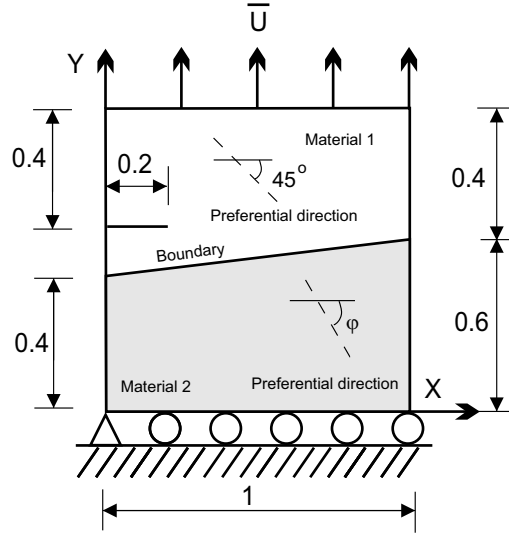


Figure 4.9: Tension test of composites with two different orthotropic phases and adhesive interface: geometry, boundary condition and preferential orientation for each material.

Unlike the example presented in Section 4.2.1, we consider in this example a tension test of a composite with two different orthotropic phases and adhesive interface. The geometric setup and the loading conditions are shown in Fig. 4.9. The domain of dimensions 1x1mm occupied by the composite possesses an initial crack of length 0.2mm. The domain is divided into two equal parts where each part is made of a different orthotropic material. The interface between two parts is described by an adhesive layer to illustrate the interfacial damage. The domain is meshed with 200x200 uniform quadrilateral elements. On the upper end and the vertical displacements are prescribed to an increasing monotonic value of $\Delta u = 0.0001\text{mm}$ during the simulation. The material parameters of the upper part are provided by [49] as follows: $E_1 = 150\text{GPa}$, $E_2 = 11\text{GPa}$, $G_{12} = 6\text{GPa}$, $\nu_{12} = \nu_{13} = 0.25$, $\nu_{31} = \nu_{21} = E_2\nu_{12}/E_1$, $\nu_{23} = 0.25$. The fracture toughness of this material is $g_{c1}=0.352\text{N/mm}$. The elastic compliance matrix \mathbf{L}_0^M is written as (4.6). The elastic stiffness matrix corresponding to $\alpha = 0^\circ$ is determined by $\mathbf{C}_0^M = (\mathbf{L}_0^M)^{-1}$ and given by

$$\mathbf{C}_0^M = \begin{bmatrix} 150.69 & 2.76 & 0 \\ 2.76 & 11.05 & 0 \\ 0 & 0 & 6 \end{bmatrix} \text{GPa}. \quad (4.11)$$

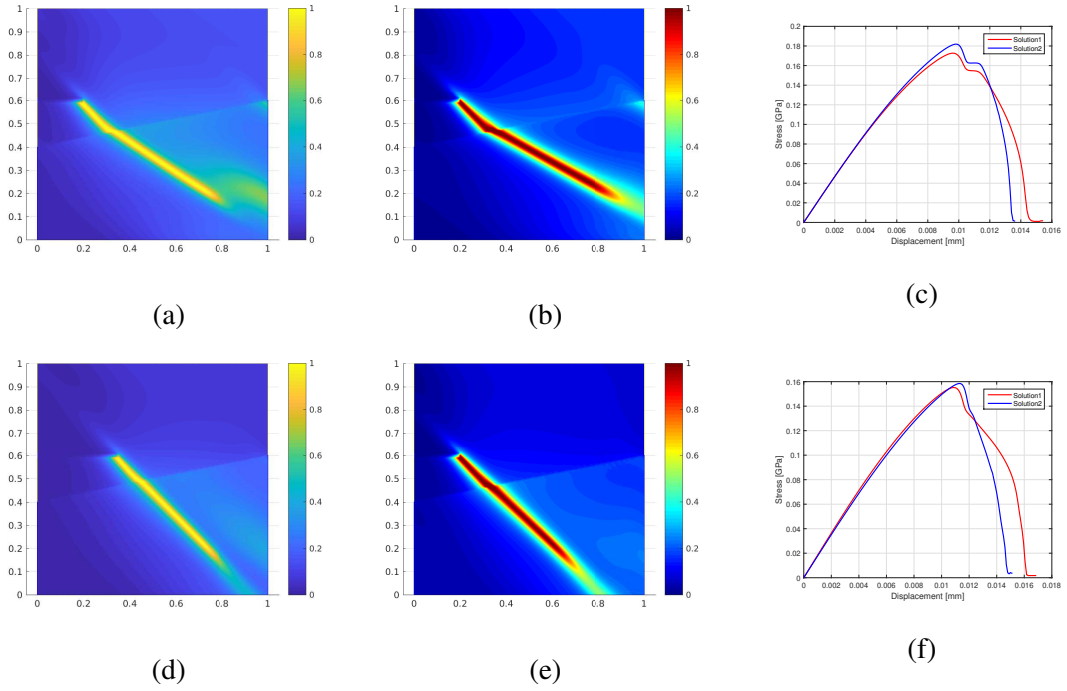


Figure 4.10: *Tension test of composites with two Carbon-epoxy materials used by De Morais et al. [49] and Robinson et al. [48]: a) d) crack evolution with solution 1 of strain decomposition (3.21) and $\varphi = -30^\circ, -45^\circ$; b) e) crack evolution with solution 2 of strain decomposition (3.27) and $\varphi = -30^\circ, -45^\circ$; c) f) comparisons of the stress-displacement curves*

The material parameters of the lower part are provided by [48] as follows: $E_1 = 115GPa$, $E_2 = 8.5GPa$, $G_{12} = 4.5GPa$, $\nu_{12} = \nu_{13} = 0.29$, $\nu_{31} = \nu_{21} = E_2\nu_{12}/E_1$, $\nu_{23} = 0.3$. The toughness is $g_{c2} = 0.33 N/mm$. The elastic compliance matrix \mathbf{L}_0^R is expressed as (4.6). The elastic stiffness matrix corresponding to $\alpha = 0^\circ$ is calculated by $\mathbf{C}_0^R = (\mathbf{L}_0^R)^{-1}$ and provided by :

$$\mathbf{C}_0^R = \begin{bmatrix} 115.72 & 2.48 & 0 \\ 2.48 & 8.55 & 0 \\ 0 & 0 & 4.5 \end{bmatrix} GPa. \quad (4.12)$$

The elastic stiffness matrices \mathbf{C}^R and \mathbf{C}^M with an arbitrary angle α of the fiber direction with respect to the direction \mathbf{e}_1 can be determined by using Eq. (4.7). The fracture strength is $t_u = 0.01 GPa$ at the interface and the fracture toughness is given by $g_c^I = g_{c2} = 0.33 N/mm$. The preferential cleavage direction is oriented at -45° in the upper part, while in the lower part, the preferential direction φ takes different values such as $-30^\circ, -45^\circ, -60^\circ$ and -90° to investigate the influences of preferential orientation and interfacial damage on the global fracture. In this example, we takes the value of the anisotropic coefficient as $\eta = 20$. The regularization length is chosen as $l = l_\beta = 0.012 mm$. The evolutions of the crack and the comparison of the force-displacement curves for the solutions of $\varphi = -30^\circ$ and $\varphi = -45^\circ$, with two solutions of strain

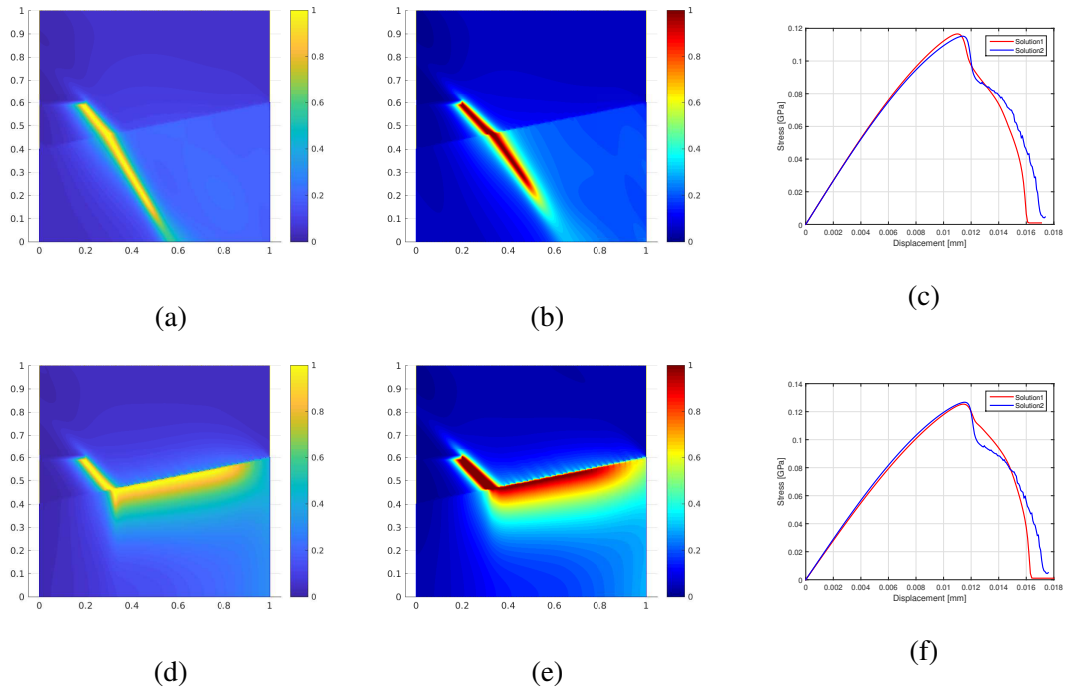


Figure 4.11: Tension test of composites with two Carbon-epoxy materials used by De Morais et al. [49] and Robinson et al. [48]: a) d) crack evolution with solution 1 of strain decomposition (3.21) and $\varphi = -60^\circ, -90^\circ$; b) e) crack evolution with solution 2 of strain decomposition (3.27) and $\varphi = -60^\circ, -90^\circ$; c) f) comparisons of the stress-displacement curves.

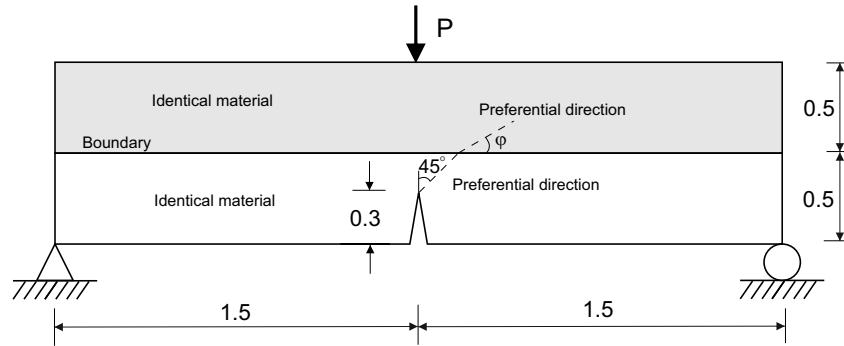


Figure 4.12: Symmetric three-point bending test of a composite beam consisting of two identical materials with adhesive interface: geometry, boundary condition and preferential orientation for each material.

decompositions (3.21) and (3.27) are presented in Fig. 4.10. And, the evolutions of the crack and the comparison of the force-displacement curves for the cases of $\varphi = -60^\circ$ and $\varphi = -90^\circ$ are detailed in Fig. 4.11. We can see from Figs. 4.10 and 4.11 that the crack propagation and the

force-displacement behavior of the solution 1 with (3.21) are similar to the ones of the solution 2 with (3.27). The crack nucleates at the initial crack and propagates within the material 1 respect to the preferential direction of -45° , then crosses the interface to spread within the material 2 respect to the preferential direction of φ when $\varphi = -30^\circ, -45^\circ$ and -60° . For $\varphi = -90^\circ$, the crack cannot cross the interface and it propagates along this interface (see Fig. 4.11d and Fig. 4.11e).

4.2.4 Symmetric three-point bending test of a composite beam consisting of two identical materials with adhesive interface

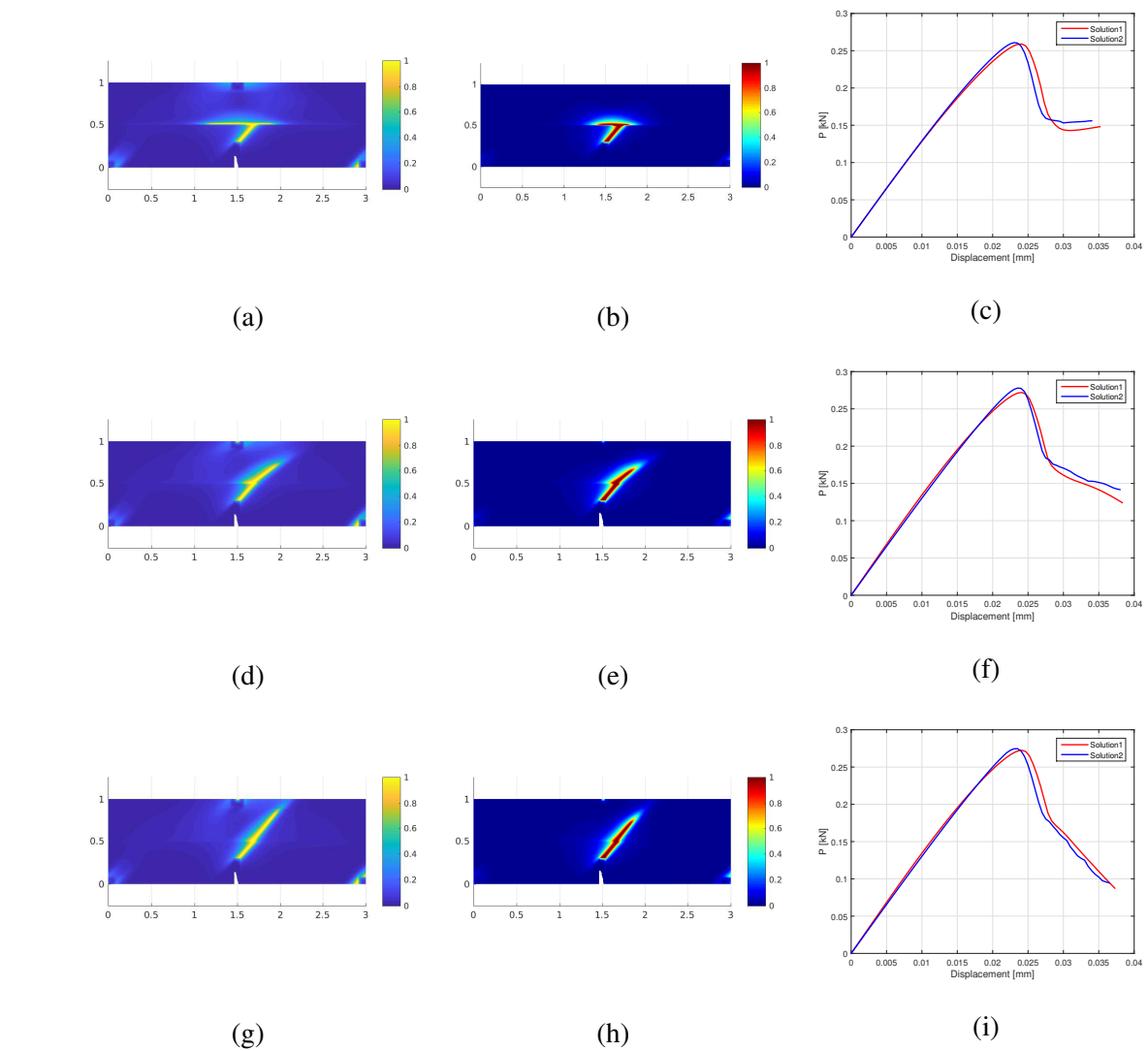


Figure 4.13: Symmetric three-point bending test of a composite beam consisting of two identical materials with adhesive interface: a) d) g) crack evolution with solution 1 of strain decomposition (3.21) and $\varphi = 0^\circ, 30^\circ, 45^\circ$; b) e) h) crack evolution with solution 2 of strain decomposition (3.27) and $\varphi = 0^\circ, 30^\circ, 45^\circ$; c) f) i) comparison of the load-displacement curves.

In this example, we consider a damage problem in which a symmetric three-point bending test of a beam consisting of two layers made of two identical materials. These two layers are connected via an adhesive layer as shown in Fig. 4.12. The dimensions of each layer are chosen as 3x0.5mm. Each layer is meshed into 75x450 uniform quadrilateral elements. The lower layer contains an initial crack whose length is 0.3mm. The boundary conditions are described as follows: the left bottom corner is blocked in two directions, the vertical displacement of the right bottom node is blocked while its horizontal displacement is free. At the center on the upper end, the displacement is prescribed with constant displacement increment $\Delta u = -0.0005\text{mm}$ during the simulation. The fracture strength is $t_u = 0.1\text{GPa}$. The values of the fracture toughness are $g_c^I = 1.45\text{ N/mm}$ and $g_c = 1.5\text{ N/mm}$. The elastic stiffness matrix corresponding to the case of $\alpha = 0^\circ$ is given by

$$\mathbf{C}_0 = \begin{bmatrix} 280 & 120 & 0 \\ 120 & 280 & 0 \\ 0 & 0 & 80 \end{bmatrix} \text{ GPa}. \quad (4.13)$$

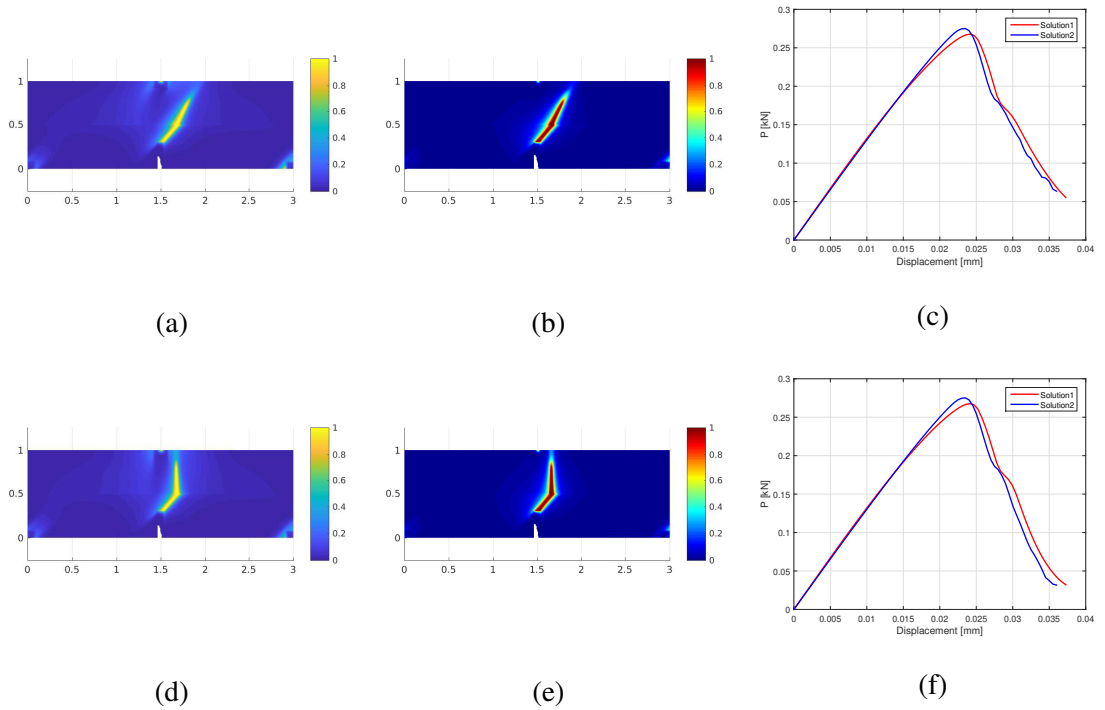


Figure 4.14: *Symmetric three-point bending test of a composite beam consisting of two identical materials with adhesive interface: a) d) g) crack evolution with solution 1 of strain decomposition (3.21) and $\varphi = 60^\circ, 90^\circ$; b) e) h) crack evolution with solution 2 of strain decomposition (3.27) and $\varphi = 60^\circ, 90^\circ$; c) f) i) comparison of the load-displacement curves.*

The value of the anisotropy coefficient is chosen as $\eta = 20$. The length scale parameter is taken as $l = l_\beta = 0.015\text{ mm}$. The preferential direction of lower layer is set to be equal to 45° , while the

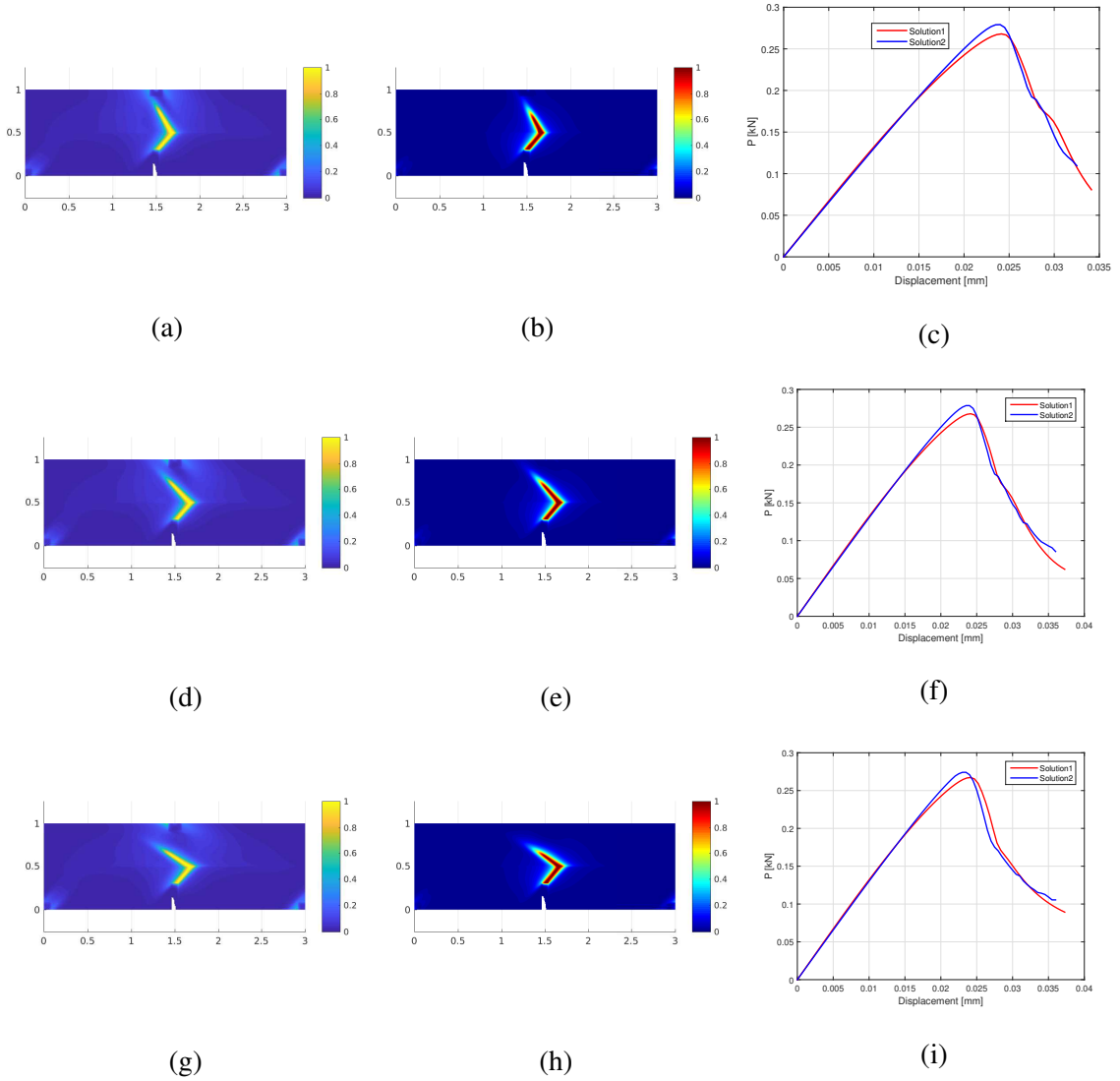


Figure 4.15: *Symmetric three-point bending test of a composite beam consisting of two identical materials with adhesive interface: a) d) g) crack evolution with solution 1 of strain decomposition (3.21) and $\varphi = 120^\circ, 135^\circ, 150^\circ$; b) e) h) crack evolution with solution 2 of strain decomposition (3.27) and $\varphi = 120^\circ, 135^\circ, 150^\circ$; c) f) i) comparison of the load-displacement curves..*

preferential directions φ of upper layer is set to vary from 0° to 150° . The evolution of the crack and the comparison of the force-displacement curves for the cases of $\varphi = 0^\circ$, $\varphi = 30^\circ$ and $\varphi = 45^\circ$, with two proposed strain decompositions (3.21) and (3.27) are presented in Fig. 4.13. Similarly, the evolutions of the crack and the comparison of the force-displacement curves when $\varphi = 60^\circ$ and $\varphi = 90^\circ$ are detailed in Fig. 4.14. For $\varphi = 120^\circ$ and $\varphi = 135^\circ$ and $\varphi = 150^\circ$, the evolutions of the crack and the comparison of the force-displacement curves are shown in Fig. 4.15.

It can be seen from Figs. 4.13, 4.14 and 4.15, the crack propagation and the force-displacement behavior obtained in two solutions of strain decompositions are similar. More precisely, the crack nucleates at the initial crack and propagates within the lower layer respect to the preferential direc-

tion of 45° , when $\varphi = 0^\circ$ the crack only propagates along the interface between two layers without causing damage to the upper layer (see Fig. 4.13a and Fig. 4.13b), while for remaining cases, the crack continues to cross the interface to spread within the upper layer respect to the preferential directions of φ . For the $\varphi = 0^\circ$ case, two layers of the composite beam seem to be detached at the interface when the load is increased. At this time, the interfacial damage is promoted in the competition with the bulk damage. This demonstrates the role of computational modeling taking into account interfacial fracture which is used with two proposed strain decompositions. It is important to observe from the force-displacement curve that the values of the peak load are almost the same in all cases. This may be due to the globe behavior of the structure related to the formation of the first crack.

4.2.5 Symmetric three-point bending test of a composite beam consisting of two different anisotropic materials with adhesive interface

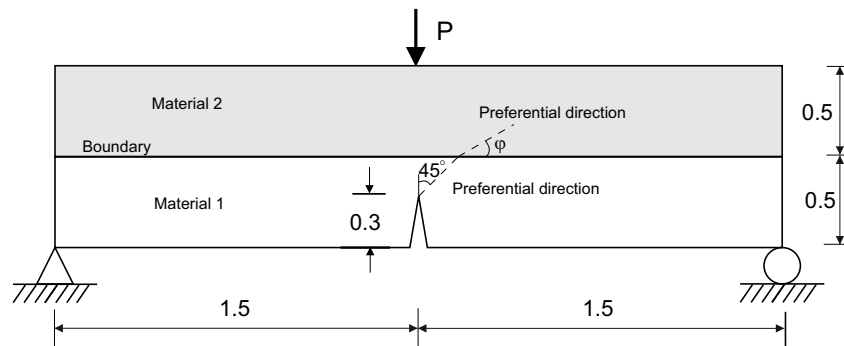


Figure 4.16: Symmetric three-point bending test of a composite beam consisting of two different anisotropic materials with adhesive interface

We consider in this example a beam which is similar to the one presented in Section 4.2.4. However, in this example, the beam under consideration is assumed to be made of two different orthotropic materials. The dimensions of each layer are 3×0.5 mm. Each layer is also uniformly discretized into 75×450 quadrilateral elements. The geometric setup and the loading conditions are described in Fig. 4.16. More precisely, the left bottom corner is blocked in two directions, the vertical displacement of the right bottom node is blocked while its horizontal displacement is free. The computation is carried out with constant displacement increment $\Delta u = -0.0005$ mm prescribed at the center of the upper end. The fracture strength is given as $t_u = 0.01$ GPa. The material properties of

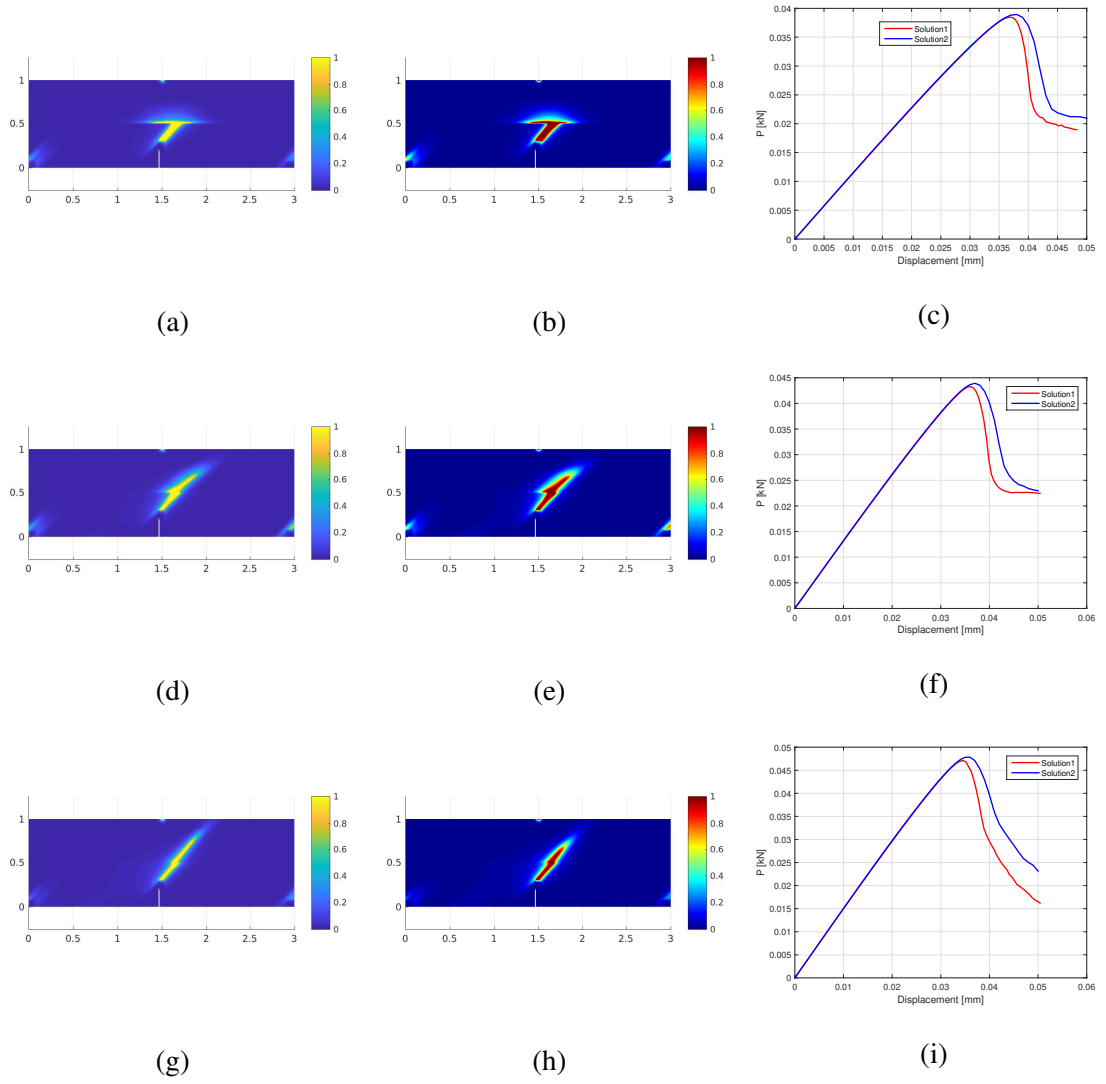


Figure 4.17: Symmetric three-point bending test of a composite beam consisting of two Carbon-epoxy materials used by De Morais *et al.* [49] and Robinson *et al.* [48]: a) d) g) crack evolution corresponding to solution 1 of strain decomposition (3.21) with $\varphi = 0^\circ, 30^\circ, 45^\circ$; b) e) h) crack evolution corresponding to solution 2 of strain decomposition (3.27) with $\varphi = 0^\circ, 30^\circ, 45^\circ$; c) f) i) comparison of the load-displacement curves.

the lower layer are chosen as in the work of De Morais *et al.* [49] with $E_1 = 150\text{GPa}$, $E_2 = 11\text{GPa}$, $G_{12} = 6\text{GPa}$, $\nu_{12} = \nu_{13} = 0.25$, $\nu_{31} = \nu_{21} = E_1\nu_{12}/E_2$ and $\nu_{23} = 0.25$. The fracture toughness of this material is given as $g_{c1}=0.352\text{N/mm}$. By using the elastic compliance matrix \mathbf{L}_0^M as in (4.6), the elastic stiffness matrix corresponding to $\alpha = 0^\circ$ can be calculated with $\mathbf{C}_0^M = (\mathbf{L}_0^M)^{-1}$ and given by

$$\mathbf{C}_0^M = \begin{bmatrix} 150.69 & 2.76 & 0 \\ 2.76 & 11.05 & 0 \\ 0 & 0 & 6 \end{bmatrix} \text{GPa}. \quad (4.14)$$

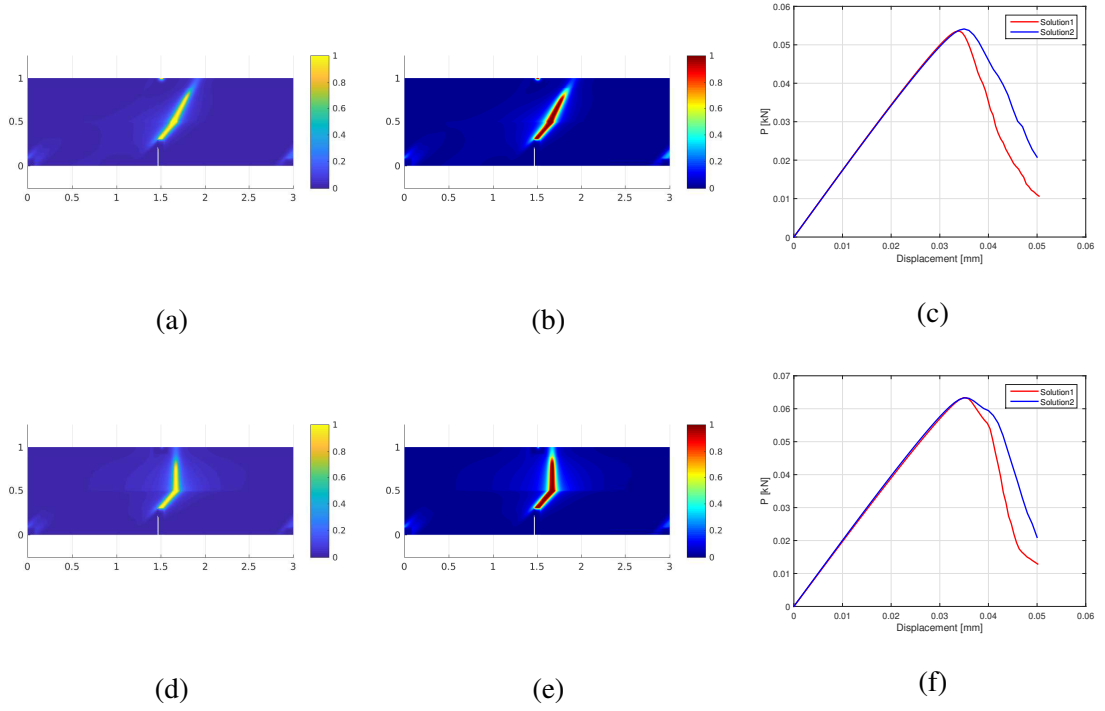


Figure 4.18: Symmetric three-point bending test of a composite beam consisting of two Carbon epoxy materials used by De Morais *et al.* [49] and Robinson *et al.* [48]: a) d) g) crack evolution corresponding to solution 1 of strain decomposition (3.21) with $\varphi = 60^\circ, 90^\circ$; b) e) h) crack evolution corresponding to solution 2 of strain decomposition (3.27) with $\varphi = 60^\circ, 90^\circ$; c) f) i) comparison of the load-displacement curves.

For the upper layer, we use the material properties which have been used by Robinson *et al.* [48] as $E_1 = 115\text{GPa}$, $E_2 = 8.5\text{GPa}$, $G_{12} = 4.5\text{GPa}$, $\nu_{12} = \nu_{13} = 0.29$, $\nu_{31} = \nu_{21} = E_1\nu_{12}/E_2$, $\nu_{23} = 0.3$. The toughness is $g_{c2}=0.33\text{N/mm}$. Similarly, the elastic stiffness matrix according to the 0° direction is calculated by using $\mathbf{C}_0^R = (\mathbf{L}_0^R)^{-1}$ and provided by:

$$\mathbf{C}_0^R = \begin{bmatrix} 115.72 & 2.48 & 0 \\ 2.48 & 8.55 & 0 \\ 0 & 0 & 4.5 \end{bmatrix} \text{ GPa}. \quad (4.15)$$

The elastic stiffness matrices \mathbf{C}^R and \mathbf{C}^M with an arbitrary angle α of the fiber can be determined by applying Eq. (4.7). The fracture toughness at the interface is given by $g_c^I = 0.33\text{N/mm}$ and the anisotropic coefficient is set to be equal to $\eta = 20$ and $l = l_\beta = 0.015\text{mm}$. In order to investigate the influence of preferential direction on the fracture response, we set the preferential direction of the lower layer is fixed as 45° while the preferential directions φ of the upper layer is set to vary from 0° to 150° . The evolutions of the crack and the comparison of the force-displacement curves when the values of φ change from 0° to 150° with two solutions of strain decompositions (3.21)

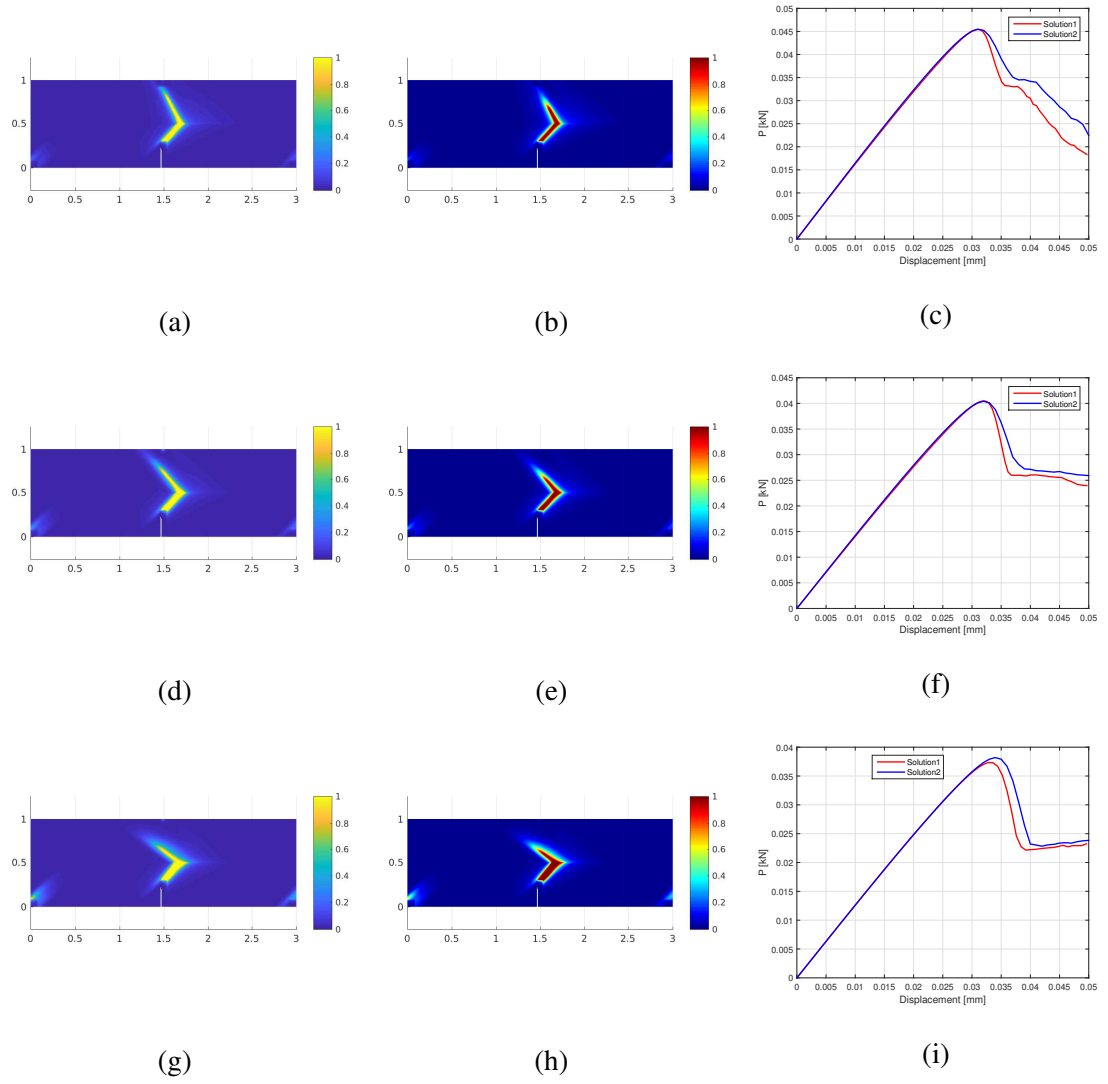


Figure 4.19: Symmetric three-point bending test of a composite beam consisting of two Carbon-epoxy materials used by De Morais et al. [49] and Robinson et al. [48]: a) d) g) crack evolution corresponding to solution 1 of strain decomposition (3.21) with $\varphi = 120^\circ, 135^\circ, 150^\circ$; b) e) h) crack evolution corresponding to solution 2 of strain decomposition (3.27) with $\varphi = 120^\circ, 135^\circ, 150^\circ$; c) f) i) comparison of the load-displacement curves.

and (3.27) are illustrated in Figs. 4.17, 4.18 and 4.19. We can see that the results obtained with two solutions of strain decompositions are relatively similar. When $\varphi = 0^\circ$, the crack propagates within the lower layer and continues to spread along the interface, while in the remaining cases, the crack crosses the interface and propagates into the upper layer. It can be observed from the force-displacement curves that the value of peak load increases when the value of φ increases from 0° to 90° . In contrary, the value of the peak load decreases when the value of φ increases from 90° to 150° . Thus, the peak load achieves the maximum value when $\varphi = 90^\circ$.

4.3 Conclusions

In this chapter, we demonstrate that the phase-field method, with interfacial damage and with orthogonal strain decompositions, developed in Chapter 3 is not only applicable to composite materials consisting of isotropic phases but can be extended also to the case of composite materials made of anisotropic multiphase. Moreover, unlike phase-field methods reported in the literature to model anisotropic materials in which multiple phase-field variables d_i has been introduced in the formulation, the phase-field method proposed in this chapter use only one damage variable d . Different numerical examples show that the phase-field method proposed is an efficient and accurate numerical tool capable of modeling and simulation of crack propagation in anisotropic multiphase composite materials.

Conclusions and perspectives

• *Conclusions*

The present thesis has contributed to developing the phase-field method by solving some open problems in modelling and simulating the initiation and propagation of cracks in brittle and quasi-brittle materials. Both bulk damage and interfacial damage have been taken into account, while considering isotropic and anisotropic multi-phase materials with realistic microstructure. The obtained numerical results have been compared with available experimental data.

First, we have adopted and implemented a new family of degradation functions in the phase-field method. In particular, we have shown that the regularization length does not depend on the mesh size in FEM. Second, the novel strain decompositions of He [39], which are orthogonal in the sense of the inner product with the elastic stiffness tensor as the measure, have been used and implemented in the phase-field method while accounting for bulk damage and interfacial damage. A number of numerical examples have been provided to illustrate the correctness and efficiency of the method developed. Finally, we have shown that it is possible to use a single damage variable instead of multiple ones to correctly model and simulate the crack path in strongly anisotropic materials.

• *Perspectives*

However, all the numerical examples given in this thesis are two-dimensional, and the materials considered are brittle or quasi-brittle. In principle, the methods developed in this thesis are valid in the three-dimensional situation but this should be carried out in a near future. The extension of our work beyond brittle or quasi-brittle materials necessitates more effort. For example, considering viscoelasticity and plasticity is challenging, especially in the anisotropic case.

Bibliography

- [1] M.J. Borden, T.J.R Hughes, C.M. Landis, C.V. Verhoosel. A higher-order phase-field model for brittle fracture: Formulation and analysis within the isogeometric analysis framework, *Comput. Methods Appl. Mech. Eng*, 273 (2014) 100-118.
- [2] V.P. Nguyen, J.Y. WU. Modeling dynamic fracture of solids with a phase-field regularized cohesive zone model, *Comput. Methods Appl. Mech. Eng*, 340 (2018) 1000-1022.
- [3] B. Bourdin, C.J. Larsen, C.L. Richardson. A time-discrete model for dynamic fracture based on crack regularization. *Int. J. Fract*, 168 (2011) 133-143.
- [4] A. Schluter, A. Willenbacher, C. Kuhn R. Muller. Phase-field approximation of dynamic brittle fracture. *Comput. Mech*, 54 (2014) 1141-1161.
- [5] J. Vignollet, S. May, R. De Borst, and C.V. Verhoosel. Phase-field models for brittle and cohesive fracture. *Meccanica*, 49 (2014) 2587-2601.
- [6] J. M. Sargado, E.Keilegavlen, I. Berre, J.M. Nordbottenn, High-accuracy phase-field models for brittle fracture based on a new family of degradation functions. *J. Mech. Phys. Solids*, 111 (2018) 458-489.
- [7] G.A. Griffith, The phenomena of rupture and flow in solid. *Philosophical Transaction of the Royal Society London Series A*. 221 (1921) 163-198.
- [8] G.A. Francfort, J.J. Marigo, Revisiting brittle fracture as an energy minimization problem. *J. Mech. Phys. Solids*, 46 (1998) 1319-1342.
- [9] D. Mumford, J. Shah, Optimal approximations by piecewise smooth functions and associated variational problems. *Commun. Pure. Appl. Math*, 42 (1989) 577-685.
- [10] L. Ambrosio, V.M. Tortorelli, Approximation of functionals depending on jumps by elliptic functionals via Γ -convergence. *Commun. Pure. Appl. Math*, 43 (1990) 999-1036.

- [11] L. Ambrosio, V.M. Tortorelli, On the approximation of free discontinuity problems. *Boll. UMI. 6B* (1992) 105-123.
- [12] L.O. Eastgate, J.P. Sethna, M. Rauscher, T. Creteigny , Fracture in mode I using a conserved phase-field model. *Phy. Rev. E*, 65(3) (2002) 036117.
- [13] V. Hakim, A. Karma, Laws of crack motion and phase-field models of fracture. *J. Mech. Phys. Solids*, 15(2) (2009) 342-368.
- [14] M. Hofacker, C. Miehe, A phase field model of dynamic fracture: robust field updates for the analysis of complex crack patterns. *Int. J. Numer. Meth. Eng*, 93(3) (2013) 276-301.
- [15] C. Kuhn, R. Muller, A continuum phase field model for fracture. *Eng. Fract. Mech*, 77(18) (2010) 3625-3634.
- [16] C. Miehe, M. Hofacker, F. Welschinger, A phase field model for rate-independent crack propagation: robust algorithmic implementation based on operator splits. *Comput. Methods Appl. Mech. Eng*, 199 (2010a) 2765-2778.
- [17] R. Spatschek, M. Hartmann, E. Brener, K.H. Muller, K. Kassner, Phase field modeling of fast crack propagation. *Phys. Rev. Lett*, 96(1) (2006) 015502.
- [18] T.T. Nguyen, J. Yvonnet, Q.Z. Zhu, M. Bornert, C. Chateau, A phase field method to simulate crack nucleation and propagation in strongly heterogeneous materials from direct imaging of their microstructure. *Eng. Fract. Mech*, 139 (2015a) 18-39.
- [19] T.T. Nguyen, J. Yvonnet, Q.Z. Zhu, M. Bornert, C. Chateau, A phase-field method for computational modeling of interfacial damage interacting with crack propagation in realistic microstructures obtained by microtomography. *Comput. Methods. Appl. Mech. Eng*, 312 (2015b) 567-595.
- [20] B. Bourdin, G.A. Francfort, J.J. Marigo, Numerical experiments in revisited brittle fracture. *J. Mech. Phys. Solids*, 48 (2000) 797-826.
- [21] A. Braides, Approximation of free discontinuity problems. Berlin. Springer Verlag. (1998).
- [22] A. Braides, Γ -Convergence for beginners, New York. Oxford University Press (2002).
- [23] G. Dal Maso, An introduction to Γ -convergence, Boston: Birkhauser Verlag (1993).

- [24] M. Prémond, B. Nedjar, Damage, gradient of damage and principle of virtual power. *Int. J. Sol. Struct.*, 33 (1996) 1083-1103.
- [25] E. Lorentz, S. Andrieux, Analysis of non-local models through energetic formulations. *Int. J. Solids Struct.*, 40 (2003) 2905-2936.
- [26] F. Freddi, C. Royer Carfagni, Regularized variational theories of fracture: a unified approach. *J. Mech. Phys. Solids*, 58 (2010) 1154-1174.
- [27] K. Pham, J.J. Marigo, C. Maurini, The issues of the uniqueness and the stability of the homogeneous response in uniaxial tests with gradient damage models. *J. Mech. Phys. Solids*, 59(6) (2011b) 1163-1190.
- [28] G. Del Piero, A variational approach to fracture and other inelastic phenomena. *J. Elasticity*, 112(1) (2013) 3-77.
- [29] K. Pham, J.J. Marigo, Approche variationnelle de l'endommagement: I. Les concepts fondamentaux. The variational approach to damage: I. The foundation. *C.R. Mécanique*, 338(4) (2010a) 191-198.
- [30] K. Pham, J.J. Marigo, Approche variationnelle de l'endommagement: II. Les modèles à gradient. The variational approach to damage: II. The gradient damage models. *C.R. Mécanique*, 338(4) (2010b) 199-206.
- [31] B. Bourdin, J.J. Marigo, C. Maurini, P. Sicsic, Morphogenesis and propagation of complex cracks induced by thermal shocks. *Phys. Rev. Lett.*, 112(1) (2014) 014301.
- [32] K.H. Pham, K. Ravi Chandar, C.M. Landis, Experimental validation of a phase-field model for fracture. *Int. J. Fract.*, 205(1) (2017) 83-101.
- [33] H. Amor, J.J. Marigo, C. Maurini, Regularized formulation of the variational brittle fracture with unilateral contact: numerical experiments. *J. Mech. Phys. Solids*, 57(8) (2009) 1209-1229.
- [34] T.T. Nguyen, J. Yvonnet, M. Bornert, C. Chateau, K. Sab, R. Romani, R. Le Roy, On the choice of parameters in the phase field method for simulating crack initiation with experimental validation. *Int. J. Fracture*, 197(2) (2016a) 213-226.
- [35] D. Leguillon, Strength or toughness? A criterion for crack onset at a notch. *Eur. J. Mech. A Solids*, 21(1) (2002) 61-72.

- [36] R. Romani, M. Bornert, D. Leguillon, R.L. Roy, K. Sab, Detection of crack onset in double cleavage drilled specimens of plaster under compression by digital image correlation-theoretical predictions based on a coupled criterion. *Eur. J. Mech. A Solids*, 51 (2015) 172-182.
- [37] R. Romani, Rupture en compression des structures hétérogènes à base de matériaux quasi-fragiles. PhD thesis, Université Pierre et Marie Curie.
- [38] C.A. Tang, R.H.C Wong, K.T. Chau, P. Lin, Modeling of compression-induced splitting failure in heterogeneous brittle porous solids. *Eng. Fract. Mech*, 72 (2005) 597-615.
- [39] Q.C. He, 2018, Three-Dimensional Strain and Stress Orthogonal Decompositions Via an Elastic Energy Preserving Transformation. 2018.
- [40] G.R. Irwin, Analysis of stress and strains near the end of a crack traversing a plate. *J. Appl. Mech*, 24 (1957) 361-364.
- [41] J.R. Rice, A path independent integral and the approximate analysis of strain concentration by notches and crack. *J. Appl. Mech*, 35 (1968) 379-386.
- [42] A. Karma, D.A. Kessler, H. Levine, Phase-field model of mode III dynamic fracture. *Phys. Rev. Lett*, 87 (2001), 045501.
- [43] M.J. Borden, Isogeometric analysis of phase-field models for dynamic brittle and ductile fracture. University of Texas at Austin Ph.D. Thesis.
- [44] G. Del Piero, Constitutive equation and compatibility of the external loads for linear elastic masonry-like materials. *Meccanica*, 24 (1989) 150-162.
- [45] H.C. Mattos, M. Fremond, E. Mamiya, A simple model of the mechanical behavior of ceramic-like materials. *Int. J. Solids Struct*, 29 (1992) 3185-3200.
- [46] M. Arcisz, G.C. Sih, Effect of orthotropy on crack propagation. *Theor. Appl. Fract. Mech*, 1 (1984) 225-238 .
- [47] L. Nobile, C. Carloni, Fracture analysis for orthotropic cracked plates. *Composite Structures*, 68 (2005) 285-293.
- [48] P. Robinson, T. Besant, D. Hitchings, Delamination Growth Prediction Using a Finite Element Approach. *Eur. Struct. Integrity Soc*, 27 (2000) 135-147.

- [49] A. De Morais, M. De Moura, A. Marques, P. De Castro, Mode-I Inter-laminar Fracture of Carbon/Epoxy Cross-Ply Composites. *Compos. Sci. Technol*, 62(5) (2002) 679-686.
- [50] C. Sandino, P. Kroliczek, D.D. McErlain, S.K. Boyd, Predicting the permeability of trabecular bone by micro-computed tomography and finite element modeling. *J. biomechanics*, 47 (2014) 3129-3134
- [51] Y. Chen, M. Pani, F. Taddei, C. Mazza, Large-scale finite element analysis of human cancellous bone tissue micro computer tomography data: a convergence study. *J. Biomech. Engg*, 136 (10) (2014) 101013.
- [52] J. Yvonnet, A fast method for solving microstructural problems defined by digital images: a Space Lippmann-Schwinger scheme. *Int. J. Numer. Methods Eng*, 92 (2) (2012) 178-205.
- [53] W. Ren, Z. Yang, R. Sharma, C.H. Zhang, P.J. Withers, Two-dimensional X-ray ct image based mesoscale fracture modelling of concrete. *Eng. Fract. Mech*, 133 (2015) 24-39.
- [54] N. Tsafnat, G. Tsafnat, A.S. Jones, Micro-finite element modelling of oke blends using X-ray microtomography. *Fuel* 87 (13-14) (2008) 2983-2987.
- [55] G. Lancioni, G. Royer-Carfagni, The variational approach to fracture mechanics. A practical application to the French Panthéon in Paris. *J. of Elas*, 95 (2009) 1-30.
- [56] J. Clayton, J. Knap, Nonlinear phase field theory for fracture and twinning with analysis of simple shear. *Philosophical Magazine*, 95(2015),2661-2696.
- [57] J. Clayton, J. Knap, Phase field modeling and simulation of coupled fracture and twinning in single crystals and polycrystals. *Comput. Methods Appl. Mech. Engg*, 312 (2016) 447-467.
- [58] T.T. Nguyen, J. Réthoré, M.C. Bainetto, Phase field modelling of anisotropic crack propagation. *Eur. J. Mech. A/Solids*, 65 (2017b) 279-288.
- [59] S. Teichtmeister, D. Kienle, F. Aldakheel, M.A. Keip, Phase field modeling of fracture in anisotropic brittle solids. *Int. J. Non-Linear Mech*, 97 (2017) 1-21.
- [60] B. Li, C. Peco, D. Millan, I. Arias, M. Arroyo, Phase-field modeling and simulation of fracture in brittle materials with strongly anisotropic surface energy. *Int. J. Numer. Methods Eng*, 102 (2015) 711-727.
- [61] J. Bleyer, R. Alessi, Phase-field modeling of anisotropic brittle fracture including several damage mechanisms. *Comput. Methods Appl. Mech. Engg*, 336 (2018) 213-236.

- [62] G.I. Barenblatt, The formation of equilibrium cracks during brittle fracture. General ideas and hypotheses. axially-symmetric cracks. *J. Appl. Math. Mech*, 23 (3) (1959) 622-636.
- [63] D.S. Dugdale, Yielding of steel sheets containing slits. *J. Mech. Phys. Solids*, 8 (2) (1960) 100-104.
- [64] V. Tvergaard, J.W. Hutchinson, The influence of plasticity on mixed mode interface toughness. *J. Mech. Phys. Solids*, 41 (6) (1993) 1119-1135.
- [65] X.P. Xu, A. Needleman, Numerical simulations of fast crack growth in brittle solids. *J. Mech. Phys. Solids*, 42 (9) (1994) 1397-1434.
- [66] C.V. Verhoosel, R. de Borst, A phase-field model for cohesive fracture. *Internat. J. Numer. Methods Engg*, 96 (1) (2013) 43-62.
- [67] N. Sukumar, N. Moes, B. Moran, T. Belytschko, Extended finite element method for three-dimensional crack modelling. *Internat. J. Numer. Methods Engg*, 48 (2000) 1549-1570.
- [68] J. Gu, T. Yu, V.L. Le, T.T. Nguyen, S. Tanaka, Q.T. Bui, Multi-inclusions modeling by adaptive XIGA based on LR B-splines and multiple level sets. *Finite Elem. Anal. Des*, 148 (2018) 48-66.
- [69] W.D. Carlson, Three-dimensional imaging of earth and planetary materials. *Earth Planet Sci. Lett*, 249 (2006) 133-147.
- [70] L. Babout, T.J. Marrow, D. Engelberg, P.J. Withers, X-ray microtomographic observation of intergranular stress corrosion cracking in sensitised austenitic stainless steel. *Mater. Sci. Technol*, 22 (2006) 1068-1075.
- [71] T.J. Marrow, L. Babout, A.P. Jivkov, P. Wood, et al, Three dimensional observations and modelling of intergranular stress corrosion cracking in austenitic stainless steel. *J. Nucl. Mater*, 352 (2006) 62-74.
- [72] L. Qian, H. Toda, K. Uesugi, M. Kobayashi, T. Kobayashi, Three-dimensional visualization of ductile fracture in an Al-Si alloy by high-resolution synchrotron X-ray microtomography. *Mater. Sci. Engg*, (2008) 293-296.
- [73] G. Kerckhofs, J. Schrooten, T. Van Cleynenbreugel, S.V. Lomov, M. Wevers, Validation of X-ray microfocus computed tomography as an imaging tool for porous structures. *Rev. Sci. Instrum*, 79 (2008) 013711.

- [74] J.L. Drummond, F. De Carlo, B.J. Super, Three-dimensional tomography of composite fracture surfaces. *J. Biomed. Mater. Res. B Appl. Biomater*, 74B (2005) 669-675.
- [75] S. Song, G. Paulino, W. Buttlar, Simulation of crack propagation in asphalt concrete using an intrinsic cohesive zone model. *J. Engng. Mech*, 132 (2006) 1215-1223.
- [76] E.J. Garboczi, Three-dimensional mathematical analysis of particle shape using X-ray tomography and spherical harmonics: application to aggregates used in concrete. *Cem. Concr. Res*, 32 (2002) 1621-1638.
- [77] L.B. Wang, J.D. Frost, G.Z. Voyiadjis, T.P. Harman, Quantification of damage parameters using X-ray tomography images. *Mech. Mater*, 35 (2003) 777-790.
- [78] G.N. Wells, L.J. Sluys, A new method for modelling cohesive cracks using finite elements. *Int. J. Numer. Methods Engg*, 50 (12) (2001) 2667-2682.
- [79] N. Moes, J. Dolbow, T. Belytschko, A finite element method for crack growth without remeshing. *Int. J. Numer. Methods Engrg*, 46 (1999) 131-150.
- [80] C. Miehe, M. Lambrecht, Algorithms for computation of stresses and elasticity moduli in terms of Seth-Hill's family of generalized strain tensors. *Commun. Numer. Meth. Engng*, 17 (2001) 337-353.
- [81] T.T. Nguyen, J. Rethore, J. Yvonnet, M. C. Baietto, Multi-phase-field modeling of anisotropic crack propagation for polycrystalline materials. *Comput. Mech*, 60 (2017) 289-314.
- [82] C. Miehe, F. Welschinger, M. Hofacker, Thermodynamically consistent phase-field models of fracture: Variational principles and multi-field FE implementations. *Int. J. Numer. Methods Engrg*, 83 (2010b) 1273-1311.
- [83] C. Miehe, L.-M. Schanzel, H. Ulmer, Phase field modeling of fracture in multi-physics problems. Part I. Balance of crack surface and failure criteria for brittle crack propagation in thermo-elastic solids. *Comput. Methods Appl. Mech. Engrg*, 294 (2015) 449-485.
- [84] M. Borden, C. Verhoosel, M. Scott, T. Hughes, C. Landis, A phase-field description of dynamic brittle fracture. *Comput. Methods Appl. Mech. Engrg*, 217-220 (2012) 77-95.
- [85] T. Nguyen, J. Yvonnet, M. Bornert, C. Chateau, Initiation and propagation of complex 3D networks of cracks in heterogeneous quasi-brittle materials: Direct comparison between in

situ testing-micro CT experiments and phase field simulations. *J. Mech. Phys. Solids*, 99 (2016) 320-350.

- [86] C. Miehe, F. Welschinger, M. Hofacker. A phase field model of electromechanical fracture. *J. Mech. Phys. Solids*, 58 (2010) 1716-1740.

Appendix A

A.1 Details about the solution of the displacement problem

• Weak form of the displacement problem

Using the variational concept for minimizing the total energy of the solid E with respect to the displacement \mathbf{u} , the weak form corresponding to the displacement problem can be written as:

$$\int_{\Omega} \frac{\partial W_u^e}{\partial \boldsymbol{\varepsilon}_e} : \boldsymbol{\varepsilon}_e(\delta \mathbf{u}) d\Omega + \int_{\Omega} \frac{\partial \Psi^I(\mathbf{w}, \boldsymbol{\chi})}{\partial \mathbf{w}} \delta \mathbf{w} \gamma_{\beta}(\beta, \nabla \beta) d\Omega = \int_{\Omega} \mathbf{f} \cdot \delta \mathbf{u} d\Omega + \int_{\partial \Omega_F} \bar{\mathbf{F}} \cdot \delta \mathbf{u} d\Gamma \quad (\text{A.1})$$

In the absence of body forces, Equation (A.1) can be rewritten as

$$\int_{\Omega} \boldsymbol{\sigma}_e : \boldsymbol{\varepsilon}_e(\delta \mathbf{u}) d\Omega + \int_{\Omega} \mathbf{t}(\mathbf{w}, \boldsymbol{\chi}) \delta \mathbf{w} \gamma_{\beta}(\beta, \nabla \beta) d\Omega - \int_{\Omega} \boldsymbol{\sigma}_e : \nabla^s \delta \mathbf{u} d\Omega = 0 \quad (\text{A.2})$$

where \mathbf{f} and $\bar{\mathbf{F}}$ body forces and prescribed traction over the boundary $\partial \Omega$. And $\boldsymbol{\sigma}_e = \frac{\partial W_u^e}{\partial \boldsymbol{\varepsilon}_e}$ is the Cauchy stress and $\mathbf{t}(\mathbf{w}, \boldsymbol{\chi}) = \frac{\partial \Psi^I(\mathbf{w}, \boldsymbol{\chi})}{\partial \mathbf{w}}$ is the traction vector acting on the interface Γ^I oriented by \mathbf{n}^I and $\delta \mathbf{w} = h \nabla(\delta \mathbf{u}) \mathbf{n}^I$. Using $\boldsymbol{\sigma}_e \mathbf{n} = \mathbf{t}$, the aforementioned expression can be now described as:

$$\int_{\Omega} \boldsymbol{\sigma}_e : \{ \boldsymbol{\varepsilon}_e(\delta \mathbf{u}) + \mathbf{n} \otimes \mathbf{w} \gamma_{\beta}(\beta, \nabla \beta) - \nabla^s \delta \mathbf{u} \} d\Omega \quad (\text{A.3})$$

which is satisfied for a following strain tensor:

$$\boldsymbol{\varepsilon}_e = \nabla^s \mathbf{u} - \mathbf{n} \otimes^s \mathbf{w} \gamma_{\beta}(\beta, \nabla \beta) \quad (\text{A.4})$$

where $(\nabla^s \mathbf{u})_{ij} = (u_{i,j} + u_{j,i})/2$ and $(\mathbf{n} \otimes^s \mathbf{w})_{ij} = (n_i w_j + n_j w_i)$. From (A.4), we set $\tilde{\boldsymbol{\varepsilon}} = \mathbf{n} \otimes^s \mathbf{w} \gamma_{\beta}$

Case 1, from (3.25), we have:

$$\Psi_e^+(\boldsymbol{\varepsilon}_e^+) = \frac{1}{2} \left\{ \frac{1}{\mathcal{D}} \tilde{\mathbf{R}}_e^+ [\text{Tr}(\tilde{\boldsymbol{\varepsilon}}_e)] [\mathbf{1}] + \left(\tilde{\boldsymbol{\varepsilon}}_e - \frac{[\text{Tr}(\tilde{\boldsymbol{\varepsilon}}_e)] [\mathbf{1}]}{\mathcal{D}} \right) \right\} \left\{ \frac{1}{\mathcal{D}} \tilde{\mathbf{R}}_e^+ [\text{Tr}(\tilde{\boldsymbol{\varepsilon}}_e)] [\mathbf{1}] + \left(\tilde{\boldsymbol{\varepsilon}}_e - \frac{[\text{Tr}(\tilde{\boldsymbol{\varepsilon}}_e)] [\mathbf{1}]}{\mathcal{D}} \right) \right\} \quad (\text{A.5})$$

$$\Psi_e^+(\boldsymbol{\varepsilon}_e^+) = \frac{1}{2} \left\{ \frac{\tilde{\mathbf{R}}_e^+}{\mathcal{D}} [\mathbf{1}]^T [\mathbf{1}] + \left(\mathbf{I} - \frac{[\mathbf{1}]^T [\mathbf{1}]}{\mathcal{D}} \right) \right\} : \mathbf{C} : \left\{ \frac{\tilde{\mathbf{R}}_e^+}{\mathcal{D}} [\mathbf{1}]^T [\mathbf{1}] + \left(\mathbf{I} - \frac{[\mathbf{1}]^T [\mathbf{1}]}{\mathcal{D}} \right) \right\} : \boldsymbol{\varepsilon}_e^2 \quad (\text{A.6})$$

and from (3.26), we obtain:

$$\Psi_e^-(\boldsymbol{\varepsilon}_e^-) = \frac{1}{2} \left\{ \frac{1}{\mathcal{D}} \tilde{\mathbf{R}}_e^- [\text{Tr}(\tilde{\boldsymbol{\varepsilon}}_e)] [\mathbf{1}] \right\} \left\{ \frac{1}{\mathcal{D}} \tilde{\mathbf{R}}_e^- [\text{Tr}(\tilde{\boldsymbol{\varepsilon}}_e)] [\mathbf{1}] \right\} \quad (\text{A.7})$$

$$\Psi_e^-(\boldsymbol{\varepsilon}_e^-) = \frac{1}{2} \left\{ \frac{\tilde{\mathbf{R}}_e^-}{\mathcal{D}} [\mathbf{1}]^T [\mathbf{1}] \right\} : \mathbf{C} : \left\{ \frac{\tilde{\mathbf{R}}_e^-}{\mathcal{D}} [\mathbf{1}]^T [\mathbf{1}] \right\} : \boldsymbol{\varepsilon}_e^2 \quad (\text{A.8})$$

we introduce: $\mathbf{R}_e^+ = \left\{ \frac{\tilde{\mathbf{R}}_e^+}{\mathcal{D}} [\mathbf{1}]^T [\mathbf{1}] + \left(\mathbf{I} - \frac{[\mathbf{1}]^T [\mathbf{1}]}{\mathcal{D}} \right) \right\}$ and $\mathbf{R}_e^- = \left\{ \frac{\tilde{\mathbf{R}}_e^-}{\mathcal{D}} [\mathbf{1}]^T [\mathbf{1}] \right\}$, with $\tilde{\mathbf{R}}_e^\pm = \frac{1}{2} \{ \text{sign}\{\pm \text{Tr}(\tilde{\boldsymbol{\varepsilon}}_e)\} + 1 \}$ and $\langle \text{Tr}(\tilde{\boldsymbol{\varepsilon}}_e) \rangle_\pm = \tilde{\mathbf{R}}_e^\pm \text{Tr}(\tilde{\boldsymbol{\varepsilon}}_e)$ (see [18]).

We have the Cauchy stress as:

$$\boldsymbol{\sigma}_e = \{g(d) + k\} \frac{\partial \Psi_e^+(\boldsymbol{\varepsilon}_e^+)}{\partial \boldsymbol{\varepsilon}_e} + \frac{\partial \Psi_e^-(\boldsymbol{\varepsilon}_e^-)}{\partial \boldsymbol{\varepsilon}_e} \quad (\text{A.9})$$

$$\boldsymbol{\sigma}_e = \{ \{g(d) + k\} \mathbf{R}_e^+ : \mathbf{C} : \mathbf{R}_e^+ + \mathbf{R}_e^- : \mathbf{C} : \mathbf{R}_e^- \} : \boldsymbol{\varepsilon}_e = \mathbf{C}(d) : \boldsymbol{\varepsilon}_e \quad (\text{A.10})$$

Case 2, from (3.29) and (3.30), we have:

$$\Psi_e^+(\boldsymbol{\varepsilon}_e^+) = \frac{1}{2} \tilde{\boldsymbol{\varepsilon}}_e^+ : \tilde{\boldsymbol{\varepsilon}}_e^+ = \frac{1}{2} \left(\tilde{\mathbf{P}}_e^+ : \mathbf{C}^{1/2} \right) : \left(\tilde{\mathbf{P}}_e^+ : \mathbf{C}^{1/2} \right) : \boldsymbol{\varepsilon}_e^2 \quad (\text{A.11})$$

$$\Psi_e^-(\boldsymbol{\varepsilon}_e^-) = \frac{1}{2} \tilde{\boldsymbol{\varepsilon}}_e^- : \tilde{\boldsymbol{\varepsilon}}_e^- = \frac{1}{2} \left(\tilde{\mathbf{P}}_e^- : \mathbf{C}^{1/2} \right) : \left(\tilde{\mathbf{P}}_e^- : \mathbf{C}^{1/2} \right) : \boldsymbol{\varepsilon}_e^2 \quad (\text{A.12})$$

Here, $\tilde{\mathbf{P}}_e^\pm = \frac{\partial \tilde{\boldsymbol{\varepsilon}}_e^\pm}{\partial \boldsymbol{\varepsilon}_e}$ can be expressed by [18]

Similar to (A.9), the Cauchy stress now can be analyzed such as:

$$\boldsymbol{\sigma}_e = \left\{ \{g(d) + k\} \left(\tilde{\mathbf{P}}_e^+ : \mathbf{C}^{1/2} \right) : \left(\tilde{\mathbf{P}}_e^+ : \mathbf{C}^{1/2} \right) + \left(\tilde{\mathbf{P}}_e^- : \mathbf{C}^{1/2} \right) : \left(\tilde{\mathbf{P}}_e^- : \mathbf{C}^{1/2} \right) \right\} : \boldsymbol{\varepsilon}_e = \mathbf{C}(d) : \boldsymbol{\varepsilon}_e \quad (\text{A.13})$$

• Model for interface damage

The general form of the traction vector $\mathbf{t}(\mathbf{w}, \boldsymbol{\chi})$ in Equation (A.2) is given by

$$\mathbf{t}(\mathbf{w}, \boldsymbol{\chi}) = [t_n(\mathbf{w}_n, \chi_n), t_t(\mathbf{w}_t, \chi_t)]^T \quad (\text{A.14})$$

where, t_n and t_t are the normal part and tangential part of the traction vector \mathbf{t} across the interface oriented by its normal vector \mathbf{n}^I . Here, we use a simplified nonlinear elastic cohesive model for the interface by taking into account the normal traction only, $\mathbf{t}(\mathbf{w}, \boldsymbol{\chi}) \cdot \mathbf{n}^I = t_n(\mathbf{w}_n, \chi_n)$. The cohesive law in the work of [19] is written as:

$$t_n(\mathbf{w}_n) = g_c^I \frac{w_n}{\delta_n} \exp\left(-\frac{w_n}{\delta_n}\right) \quad (\text{A.15})$$

where $w_n = \mathbf{w} \cdot \mathbf{n}^I$; $\delta_n = \frac{g_c^I}{t_u e}$, and $e = \exp(1)$, the fracture toughness g_c^I at the interfaces (defined as the total area of the traction-opening curve, see in [19]), and t_u is the fracture strength.

The expression of the traction at the interface is given e.g. for the normal traction by

$$t_n(\mathbf{w}, \boldsymbol{\chi}) = \begin{cases} \text{(A.15)} & \text{if } w_n(\mathbf{x}, t) \geq \chi_n(t) \\ \frac{t_n(\chi_n(\mathbf{x}, t))w_n}{\chi_n(\mathbf{x}, t)} & \text{if } w_n(\mathbf{x}, t) < \chi_n(t), \end{cases} \quad (\text{A.16})$$

And, we set:

$$\mathbf{K}_I = \frac{\partial \mathbf{t}(\mathbf{w}, \boldsymbol{\chi})}{\partial \mathbf{w}} = \begin{bmatrix} \frac{\partial t_n(\mathbf{w}, \boldsymbol{\chi})}{\partial w_n} & 0 \\ 0 & 0 \end{bmatrix} \quad (\text{A.17})$$

where $\boldsymbol{\chi}(\mathbf{x}, t) = \max_{\tau \in [0, t]} \{\mathbf{w}(\mathbf{x}, \tau)\} = [\chi_n(\mathbf{x}, t), \chi_t(\mathbf{x}, t)]^T$.

• **FEM discretization of the displacement problem**

Even though the phase field problem is linear in the staggered scheme, ie, for a fixed value to \mathbf{u} , it should be mentioned that for a fixed crack phase field value d , the mechanical problem (A.1) is nonlinear since the computation of eigenvalues of the bulk strain $\boldsymbol{\varepsilon}_e$ and the interface cohesive model in (A.16). A linear procedure to solve this nonlinear problem by the Newton method is introduced in the following. From (A.1), (A.10) and (A.13), the balance equation can be rewritten as

$$\mathcal{R} = \int_{\Omega} \boldsymbol{\sigma}_e : \boldsymbol{\varepsilon}_e(\delta \mathbf{u}) d\Omega + \int_{\Omega} \gamma_{\beta}(\mathbf{x}) \mathbf{t}(\mathbf{w}, \boldsymbol{\chi}) \cdot \delta \mathbf{w} d\Omega - \int_{\Omega} \mathbf{f} \cdot \delta \mathbf{u} d\Omega - \int_{\partial \Omega_F} \bar{\mathbf{F}} \cdot \delta \mathbf{u} d\Gamma = 0 \quad (\text{A.18})$$

where $\boldsymbol{\varepsilon}_e(\delta \mathbf{u}) = \nabla^s \delta \mathbf{u} - \mathbf{n} \otimes^s \delta \mathbf{w} \gamma_{\beta}$. In the Newton method, we solve the following tangent equation by updating the displacement for each loading as:

$$D_{\Delta u} \mathcal{R}(\mathbf{u}_k, d) = -\mathcal{R}(\mathbf{u}_k, d) \quad (\text{A.19})$$

where \mathbf{u}_k is the displacement solution from the k^{th} iteration. The displacements at the current iteration are rewritten by

$$\mathbf{u}_{k+1} = \mathbf{u}_k + \Delta \mathbf{u}_{k+1} \quad (\text{A.20})$$

From (A.19), we obtain

$$D_{\Delta u} \mathcal{R}(\mathbf{u}_k) = \int_{\Omega} \frac{\partial \boldsymbol{\sigma}_e}{\partial \boldsymbol{\varepsilon}_e} : \boldsymbol{\varepsilon}_e(\Delta \boldsymbol{\varepsilon}) : \boldsymbol{\varepsilon}_e(\delta \boldsymbol{\varepsilon}) d\Omega + \int_{\Omega} \gamma_{\beta}(\mathbf{x}) \frac{\partial \mathbf{t}(\mathbf{w}, \boldsymbol{\chi})}{\partial \mathbf{w}} : \Delta \mathbf{w} : \delta \mathbf{w} d\Omega \quad (\text{A.21})$$

with

$$\Delta \mathbf{w}(\mathbf{x}) = h \nabla \Delta \mathbf{u}(\mathbf{x}) \frac{\nabla \phi(\mathbf{x})}{\|\nabla \phi(\mathbf{x})\|} = h \nabla \Delta \mathbf{u}(\mathbf{x}) \mathbf{n}^I \quad (\text{A.22})$$

Similarly, we use FEM approximations for the displacement problem in one element:

$$\mathbf{u} = [\mathbf{N}] \{\mathbf{u}^i\}, \quad \delta \mathbf{u} = [\mathbf{N}] \{\delta \mathbf{u}^i\}, \quad \Delta \mathbf{u} = [\mathbf{N}] \{\Delta \mathbf{u}^i\} \quad (\text{A.23})$$

where \mathbf{N} denotes the shape functions matrix associated to displacement variables and \mathbf{u}^i and $\Delta\mathbf{u}^i$ are nodal displacement components and nodal incremental displacement components in one element. Furthermore, we have:

$$[\boldsymbol{\varepsilon}](\Delta\mathbf{u}) = [\mathbf{B}]\{\Delta\mathbf{u}^i\}, \quad [\boldsymbol{\varepsilon}](\delta\mathbf{u}) = [\mathbf{B}]\{\delta\mathbf{u}^i\} \quad (\text{A.24})$$

where \mathbf{B} is a shape function matrix derivatives. The diffuse jump approximation vector and its incremental counterparts can be discretized as:

$$\mathbf{w} = h[\mathcal{N}][\tilde{\mathbf{B}}]\{\mathbf{u}^i\}, \quad \Delta\mathbf{w} = h[\mathcal{N}][\tilde{\mathbf{B}}]\{\Delta\mathbf{u}^i\}, \quad \delta\mathbf{w} = h[\mathcal{N}][\tilde{\mathbf{B}}]\{\delta\mathbf{u}^i\} \quad (\text{A.25})$$

where

$$[\mathcal{N}] = \begin{bmatrix} n_1 & n_2 & 0 & 0 \\ 0 & 0 & n_1 & n_2 \end{bmatrix} \quad (\text{A.26})$$

$$[\tilde{\mathbf{B}}]\{\mathbf{u}^i\} = \begin{bmatrix} \frac{\partial u_1}{\partial x_1} & \frac{\partial u_1}{\partial x_2} & \frac{\partial u_2}{\partial x_1} & \frac{\partial u_2}{\partial x_2} \end{bmatrix}^T = \begin{bmatrix} \frac{\partial}{\partial x_1} & \frac{\partial}{\partial x_2} & 0 & 0 \\ 0 & 0 & \frac{\partial}{\partial x_1} & \frac{\partial}{\partial x_2} \end{bmatrix}^T [\mathbf{N}]\{\mathbf{u}^i\} \quad (\text{A.27})$$

and n_1 and n_2 are the horizontal component and vertical component of the normal vector \mathbf{n}^I . The smoothed jump strain at the interfaces is defined by:

$$[\bar{\boldsymbol{\varepsilon}}] = \begin{bmatrix} \bar{\varepsilon}_{11} \\ \bar{\varepsilon}_{22} \\ \sqrt{2}\bar{\varepsilon}_{12} \end{bmatrix} = \gamma_\beta(\mathbf{x}) \begin{bmatrix} \mathbf{w}_1 n_1 \\ \mathbf{w}_2 n_2 \\ (\mathbf{w}_1 n_2 + \mathbf{w}_2 n_1)/\sqrt{2} \end{bmatrix} \quad (\text{A.28})$$

Then, it yields

$$[\bar{\boldsymbol{\varepsilon}}](\Delta\mathbf{u}) = h\gamma_\beta(\mathbf{x})[\mathbf{M}][\tilde{\mathbf{B}}]\{\Delta\mathbf{u}^i\}, \quad (\text{A.29})$$

with

$$[\mathbf{M}] = \begin{bmatrix} n_1 & 0 \\ 0 & n_2 \\ \frac{1}{\sqrt{2}}n_2 & \frac{1}{\sqrt{2}}n_1 \end{bmatrix} \quad [\mathcal{N}] = \begin{bmatrix} n_1^2 & n_1 n_2 & 0 & 0 \\ 0 & 0 & n_1 n_2 & n_2^2 \\ \frac{1}{\sqrt{2}}n_1 n_2 & \frac{1}{\sqrt{2}}n_2^2 & \frac{1}{\sqrt{2}}n_1^2 & \frac{1}{\sqrt{2}}n_1 n_2 \end{bmatrix} \quad (\text{A.30})$$

From (A.19) and the aforementioned FEM discretization, the linear tangent problem reduces to the following linear system of algebraic equations:

$$D_{\Delta u} \mathcal{R}(\mathbf{u}_k^i) = [\mathbf{K}_{tan}]\{\Delta\mathbf{u}_{k+1}^i\} = -\{\mathcal{R}(\mathbf{u}_k^i)\} \quad (\text{A.31})$$

$$\begin{aligned} [\mathbf{K}_{tan}] = & \int_{\Omega} \left\{ [\mathbf{B}^T] - h\gamma_\beta(\mathbf{x})[\tilde{\mathbf{B}}^T][\mathbf{M}^T] \right\} [\mathbf{C}(d)] \left\{ [\mathbf{B}] - h\gamma_\beta(\mathbf{x})[\mathbf{M}][\tilde{\mathbf{B}}] \right\} d\Omega \\ & + \int_{\Omega} h^2 \gamma_\beta(\mathbf{x})[\tilde{\mathbf{B}}^T][\mathcal{N}^T][\mathbf{K}_I][\mathcal{N}][\tilde{\mathbf{B}}] d\Omega \end{aligned} \quad (\text{A.32})$$

and

$$\begin{aligned} \{\mathcal{R}(\mathbf{u}_k^i)\} &= \int_{\Omega} \left\{ [\mathbf{B}^T] - h\gamma_{\beta}(\mathbf{x})[\tilde{\mathbf{B}}^T][\mathbf{M}^T] \right\} [\mathbf{C}(d)] \left\{ [\mathbf{B}] - h\gamma_{\beta}(\mathbf{x})[\mathbf{M}][\tilde{\mathbf{B}}] \right\} \{\mathbf{u}_k^i\} d\Omega \\ &+ \int_{\Omega} h\gamma_{\beta}(\mathbf{x})[\tilde{\mathbf{B}}^T][\mathcal{N}^T]\{\mathbf{t}(\mathbf{w}_k)\} d\Omega - \int_{\Omega} \{\mathbf{f}\}[\mathbf{N}^T] d\Omega - \int_{\partial\Omega_F} \{\bar{\mathbf{F}}\}[\mathbf{N}^T] d\Gamma \end{aligned} \quad (\text{A.33})$$

With $\mathbf{C}(d) = \frac{\partial \boldsymbol{\sigma}_e}{\partial \boldsymbol{\varepsilon}_e}$ is the matrix form corresponding to the fourth-order tensor \mathbb{C} .

And then, we solve the following problem:

$$\{\Delta \mathbf{u}_{k+1}^i\} = -[\mathbf{K}_{tan}]^{-1} \cdot \{\mathcal{R}(\mathbf{u}_k^i)\} \quad (\text{A.34})$$

A.2 The solution of the phase field problem in Chapter 4

• Basics of thermodynamics and evolution of phase field

It can be shown that the condition $\mathcal{A}\dot{d} \geq 0$ will be satisfied if either $\mathcal{F} < 0$ and $\dot{d} = 0$ or $\mathcal{F} = 0$ and $\dot{d} > 0$. More precisely, the latter condition leads that, when $\dot{d} > 0$, we have

$$\mathcal{F} = -\frac{\partial W}{\partial d} = 2(1-d)\Psi_e^+ - (1-\beta)g_c\delta_d\gamma^{(p)}(d, \nabla d, \boldsymbol{\omega}^{(p)}) = 0 \quad (\text{A.35})$$

the strain history function introduced in the works [19] is employed, here:

$$\mathcal{H}^e = \max_{\tau \in [0, t]} \{\Psi_e^+(\mathbf{x}, \tau)\} \quad (\text{A.36})$$

and (A.37) is substituted by

$$2(1-d)\mathcal{H}^e - (1-\beta)g_c\delta_d\gamma(d, \nabla d, \boldsymbol{\omega}^{(p)}) = 0 \quad (\text{A.37})$$

• Weak form of the phase field problem

To compute the scalar phase-field parameter $d(\mathbf{x}, t)$, a temporal discretization is carried out at times $0, t_1, \dots, t_n, t_{n+1}, \dots$. By assuming that, at time $t = t_n$, the scalar phase-field parameter $d_n = d(\mathbf{x}, t_n)$ is known. Using (A.37) and (4.4), the weak form used to compute $d_{n+1} = d(\mathbf{x}, t_{n+1})$ is expressed as follows:

$$\int_{\Omega} \left\{ \left(2\mathcal{H}_n^e + (1-\beta)\frac{g_c}{l} \right) d_{n+1}\delta d + (1-\beta)g_c l \nabla d_{n+1} \boldsymbol{\omega}^{(p)} \nabla(\delta d) \right\} d\Omega = \int_{\Omega} 2\mathcal{H}_n^e \delta d d\Omega \quad (\text{A.38})$$

Using FEM, the phase field as well as the phase-field gradient are approximated by:

$$d(\mathbf{x}) = \{\mathbf{N}_d(\mathbf{x})\}\{\mathbf{d}\} \text{ and } \nabla d(\mathbf{x}) = [\mathbf{B}_d(\mathbf{x})]\{\mathbf{d}\} \quad (\text{A.39})$$

$$\delta d(\mathbf{x}) = \{\mathbf{N}_d(\mathbf{x})\}\{\delta \mathbf{d}\} \text{ and } \nabla \delta d(\mathbf{x}) = [\mathbf{B}_d(\mathbf{x})]\{\delta \mathbf{d}\} \quad (\text{A.40})$$

where $\mathbf{N}_d(\mathbf{x})$ and $\mathbf{B}_d(\mathbf{x})$ are the matrix of shape function and matrix of shape function derivative associated with phase-field variable, respectively. By introducing the aforementioned FEM discretization into the weak form (A.38), the phase-field variable $d_{n+1} = d(\mathbf{x}, t_{n+1})$ can be calculated

$$\{\mathbf{d}\} = [\mathbf{K}_d]^{-1} \cdot \{\mathbf{F}_d\} \quad (\text{A.41})$$

where the rigid matrix is determined by

$$[\mathbf{K}_d] = \int_{\Omega} \left\{ \left(\frac{g_c}{l} (1 - \beta) + 2\mathcal{H}_n^e \right) \{\mathbf{N}_d\}^T \{\mathbf{N}_d\} + g_c l (1 - \beta) [\mathbf{B}_d]^T \boldsymbol{\omega}^{(p)} [\mathbf{B}_d] \right\} d\Omega \quad (\text{A.42})$$

and the force vector is defined by

$$\{\mathbf{F}_d\} = \int_{\Omega} 2\{\mathbf{N}_d\}^T \mathcal{H}_n^e d\Omega. \quad (\text{A.43})$$

Appendix B

B.1 Algorithm in chapter 1

1. Set the initial displacement field $\mathbf{u}_0(\mathbf{x})$, the phase field $d_0(\mathbf{x})$ and the strain-history function \mathcal{H}_0 .
 2. **FOR** all displacement increments: (at each time step t_{n+1}), given d_n , \mathbf{u}_n and \mathcal{H}_n .
 - . (a) Determine the new family of degradation functions according to (1.11):
 - . (i) Determine the value of n according to (1.44) or Fig. 1.4
 - . (ii) Determine the value of $m(n)$ according to (1.12)
 - . (b) Compute the history function \mathcal{H}_{n+1} according to (1.21).
 - . (c) Compute the phase field $d_{n+1}(\mathbf{x})$ according to (1.29).
 - . (d) Compute the displacement field $\mathbf{u}_{n+1}(\mathbf{x})$ according to (1.37).
 - . (e) $(\bullet)_n \leftarrow (\bullet)_{n+1}$ and go to (a).
- END

B.2 Algorithms in chapter 2

1. Set the initial displacement field $\mathbf{u}_0(\mathbf{x})$, the phase field $d_0(\mathbf{x})$ and the strain-history function \mathcal{H}_0 .
 2. **FOR** all displacement increments: (at each time step t_{n+1}), given d_n , \mathbf{u}_n and \mathcal{H}_n .
 - . (a) Compute the history function \mathcal{H}_{n+1} that satisfies the condition of the strain orthogonal decompositions according to (2.45) is computed such as:
 - . (i) Equation (2.22) for case 1 .
 - . (ii) Equation (2.38) for case 2.
 - . (b) Compute the phase field $d_{n+1}(\mathbf{x})$ according to (2.53).
 - . (c) Compute the displacement field $\mathbf{u}_{n+1}(\mathbf{x})$ according to (2.71).
 - . (d) $(\bullet)_n \leftarrow (\bullet)_{n+1}$ and go to (a).
- END

B.3 Algorithm in chapter 3 and chapter 4

1. Set the initial displacement field $\mathbf{u}_0(\mathbf{x})$, the phase field $d_0(\mathbf{x})$ and the strain-history function \mathcal{H}_0^e .
 2. Compute the interfacial phase field $\beta(\mathbf{x})$ according to (3.4)
 3. **FOR** all displacement increments: (at each time step t_{n+1}), given d_n , \mathbf{u}_n and \mathcal{H}_n^e .
 - . (a) Compute the history function \mathcal{H}_{n+1}^e that satisfies the condition of the bulk strain orthogonal decompositions according to (3.35) with Ψ_e^+ is computed such as:
 - . (i) Equation (3.25) for case 1
 - . (ii) Equation (3.29) for case 2
 - . (b) Compute the phase field $d_{n+1}(\mathbf{x})$ according to (3.41) (in chapter 3) or (A.41) (in chapter 4).
 - . (c) Compute the displacement field $\mathbf{u}_{n+1}(\mathbf{x})$:
 - . Initialize $\mathbf{u}_k = \mathbf{u}_n$
 - . **WHILE** $\|\Delta\mathbf{u}_{k+1}\| > \epsilon, \epsilon \ll 1$:
 - . (i) Compute $\Delta\mathbf{u}_{k+1}^i$ by (A.34).
 - . (ii) Update $\mathbf{u}_{k+1} = \mathbf{u}_k + \Delta\mathbf{u}_{k+1}^i$.
 - . (iii) $(\bullet)_n \leftarrow (\bullet)_{n+1}$ and go to (i).
 - . **END**
- END**